Interactions Between Nano/Micro-Sized Particles and Microbes for Agricultural and Environmental Applications

Li-Ting Yen
Utah State University

Recommended Citation

INTERACTIONS BETWEEN NANO/MICRO-SIZED PARTICLES AND

MICROBES FOR AGRICULTURAL AND ENVIRONMENTAL

APPLICATIONS

by

Li-Ting Yen

A dissertation submitted in partial fulfillment

of the requirements for the degree

of

DOCTOR of PHILOSOPHY

in

Soil Science

Approved:

_____ _____
Astrid R. Jacobson, Ph.D.   Yao-Tung Lin, Ph.D.
Major Professor   Committee Member

_____ _____
David W. Britt, Ph.D.   Jeanette M. Norton, Ph.D.
Committee Member   Committee Member

_____ _____
Joan E. McLean, M.S.   Youping Sun, Ph.D.
Committee Member   Committee Member

_____
D. Richard Cutler, Ph.D.
Vice Provost of Graduate Studies

UTAH STATE UNIVERSITY
Logan, Utah

2024

ABSTRACT

Interactions between Nano/Micro-sized Particles and Microbes for Agricultural and

Environmental Applications

by

Li-Ting Yen, Doctor of Philosophy

Utah State University, 2024

Major Professor: Dr. Astrid R. Jacobson
Department: Plants, Soils and Climate

In semi-arid regions, high soil pH significantly limits iron (Fe) availability to
plants. Metavivianite (metaVT), an iron phosphate mineral, has been utilized for Fe
supplementation in plants. Previous studies have shown the effectiveness of bulk metaVT
on plants grown on calcareous soil for mitigating Fe efficiency and the extremely low
solubility of bulk metaVT ($Ksp=10^{-36}$) in electrolyte solutions, such as $CaCl_2$. The cause
of the discrepancy between the results of bulk metaVT under pure laboratory conditions
and field application remains unclear. This study explores the applications of nano-sized
metaVT (nano-metaVT) as an Fe amendment for crops, as well as using chitosan (CT) as
a pH-responsive coating on the nano-metaVT amendment. This study examines the
solubilities of nano-metaVT and nano-CT-metaVT in a dilute electrolyte solution and
calcareous soil saturated paste extract (SPE), their impact on wheat growth in silica sand,
and wheat and bean growth in a calcareous soil under salinity stress. The results indicate
that key factors, such as the functional coating on the nano-fertilizers, the presence of soil
microbes, and organic ligands in the soil, affect the solubilities of nano-metaVT and

nano-CT-metaVT. Moreover, beneficial soil microbes, *Pp* Pf-5, mitigate wheat abiotic stress by increasing plant transpiration. Finally, the study confirms that nano-CT-metaVT improves bean root dry mass, and the nano-metaVT treatment resulted in increased chlorophyll content in beans. Nano-metaVT demonstrates retention in the soil and lower concentrations of soluble Fe in leachates than Fe-EDDHA.

Globally, waterborne pathogens pose significant hygiene and health risks to humans. This study also investigates the disinfection efficiency of a heated oyster-shell-derived disinfectant (HOS) against *Staphylococcus aureus* and *Escherichia coli*, highlighting the critical role of singlet oxygen in bacterial inactivation. The HOS disinfectant has the potential to be applied as a universal disinfectant. Furthermore, the study studied the enhanced disinfection efficiency by the immobilization of visible-light-responsive nitrogen-doped titanium dioxide on polymethyl methacrylate (NT-PMMA). This approach shows the increased generation of singlet oxygen, hydroxyl radicals, and hydrogen peroxide with the immobilized material, demonstrating excellent reusability and maintaining a 99% disinfection rate against *Staphylococcus aureus* and *Escherichia coli* over five cycles of disinfection experiment.

(425 pages)

PUBLIC ABSTRACT

Interactions between Nano-Micro-Particles and Microbes for Agricultural and

Environmental Applications

by

Li-Ting Yen, Doctor of Philosophy

Utah State University, 2024

Among the challenges posed by a growing global population, diminishing arable land and water resources affected by climate change are critical for enhancing crop yields, ensuring food security, and maintaining water quality and environmental health.

Iron (Fe), an essential micronutrient, is vital to plant growth. The partially oxidized form of vivianite, metavivianite (metaVT), is reported to be a promising alternative Fe fertilizer. Previous studies have shown the effectiveness of bulk metaVT on plants grown on calcareous soil for mitigating Fe efficiency and the extremely low solubility of bulk metaVT ($Ksp=10^{-36}$) in electrolyte solutions, such as $CaCl_2$. The cause of the discrepancy between the results of bulk metaVT under pure laboratory conditions and field application remains unclear. This study explores the applications of nano-sized metaVT (nano-metaVT) as an Fe amendment for crops, as well as using chitosan (CT) as a pH-responsive coating on the nano-metaVT amendment. This study examines the solubilities of nano-metaVT and nano-CT-metaVT in a dilute electrolyte solution and calcareous soil saturated paste extract (SPE), their impact on wheat growth in silica sand, and wheat and bean growth in a calcareous soil under salinity stress. The results indicate that key factors, such as the functional coating on the nano-fertilizers, the presence of soil

microbes, and organic ligands in the soil, affect the solubilities of nano-metaVT and nano-CT-metaVT. Moreover, beneficial soil microbes, *Pp* Pf-5, mitigate wheat abiotic stress by increasing plant transpiration. Finally, the study confirms that nano-CT-metaVT improves bean root dry mass, and the nano-metaVT treatment resulted in increased chlorophyll content in beans. Nano-metaVT demonstrates retention in the soil and lower concentrations of soluble Fe in leachates than Fe-EDDHA.

Globally, disinfection methods have disadvantages, such as the high cost of raw chemicals, generation of toxic by-products, or low disinfection efficiency. It has been proposed that the disinfection observed using heated oyster-shell-derived disinfectant (HOS) is related to reactive oxygen species (ROSs) generation and protein denaturation. The findings provide evidence that cell permeability is crucial in the HOS disinfection process, and singlet oxygen plays an essential role in the disinfection mechanism. Overall, the HOS disinfectant has a high potential to be applied as a universal disinfectant and mitigate the aquaculture waste pollution problem. Furthermore, the study explores the enhanced disinfection efficiency, focusing on the NT-PMMA. NT-PMMA showed higher intensities of singlet oxygen, hydroxyl radicals, and hydrogen peroxide than NT suspension, implying the greater inactivation efficiency of immobilized NT on PMMA than in NT-suspension. The immobilization approach enhanced the inactivation performances of NT-PMMA, making it superior to NT suspension due to the absence of turbidity interference and the uniform distribution of NT.

ACKNOWLEDGMENTS

I am sincerely grateful to my parents, Ting-Chen Yen and Min-Lien Wang, for their love and support throughout this journey.

CONTENTS

LIST OF TABLES

LIST OF FIGURES

CHAPTER 1

CHAPTER 2

CHAPTER 3

CHAPTER 4

CHAPTER 6

CHAPTER 7

APPENDICES

Appendix A. Copyrights

Appendix B. Supplemental information

TABLE OF ACRONYMS

Abbreviation/ acronyms	Definition
AgrM	Greenville Centennial Research Farm
AAs	Amino acids
CT	chitosan
DMA	deoxymugineic acid
DOM	dissolved organic matter
DTPA	diethylenetriaminepentaacetic acid
EPS	extracellular polymeric substances
FA	fulvic acids
HA	humic acid
HOS	heated oyster shell
ICPMS	inductively coupled plasma mass spectrometry
LMWOAs	low molecular weight organic acids
NA	nutrient agar
nano-CT-metaVT	nano-sized chitosan-coated metavivianite
nano-metaVT	nano-sized metavivianite
NB	nutrient broth
NPs	nanoparticles
*Pc*O6	*Pseudomonas chlororaphis* O6
PMMA	Polymethyl methacrylate
Pp Pf-5	*Pseudomonas protegens* Pf-5
PW	pore water
ROS	reactive oxygen species
SOC	soil organic carbon
SOM	soil organic matter
SPEs	saturation paste extracts
TSA	tryptic soy agar
TSB	tryptic soy broth

CHAPTER 1

INTRODUCTION

With limited arable land and scarce water resources affected by climate change, it is crucial to develop more efficient fertilizers to sustainably improve crop production to feed the increasing population.[1] It has been reported that macronutrient elements, including nitrogen (N), phosphorus (P), and potassium (K), applied to the soil are lost due to leaching or becoming unavailable for plants by 40–70 %, 80–90 %, and 50–90%, respectively, causing a considerable loss of resources.[2] In addition, in an arid and semi-arid area, the availability of most nutrient elements, such as iron (Fe) and P, is significantly affected by high soil pH, dramatically decreasing their availability for plant uptake. Fe is a co-factor for about 140 enzymes, which participate in several metabolic processes, including photosynthesis, chlorophyll biosynthesis, and respiration.[3-5] However, Fe deficiency occurs in plants cultivated in calcareous soils worldwide due to the formation of insoluble complexes in the soil.[6] Nano fertilizers with high surface area to volume ratios exhibit properties distinct from conventional bulk fertilizers. There is a great interest in the use of nano fertilizers in order to increase fertilizer use efficiency, lower the applied dose, and minimize volatilization and leaching losses.[7]

Vivianite ($Fe^{II}(PO_4)_2 \cdot 8H_2O$), a sheet structure formed by chains of octahedra and tetrahedra, is the most common stable iron phosphate mineral in reduced sediments.[8] The partially oxidized form of vivianite, metavivianite ($Fe^{II}Fe_2^{III}(PO_4)_2(OH)_2 \cdot 6H_2O$), is more common in an aerobic environment and used to provide Fe and P for plants.[9] Previous studies have reported the potential of metavivianite as a slow-released Fe and P fertilizer.[10-13] In order to prevent Fe and P applied in nutrient solutions from precipitating

or sorbing to soil solid surfaces in calcareous soils, advanced polymeric materials have the potential to form a pH-responsive coating on nano-sized metaviviantite. Chitosan (CT) has been demonstrated to have beneficial influences on plant growth[14], including triggering the disease-defense abilities of plants toward a wide range of plant pathogenic fungi and bacteria.[15] Therefore, CT has the potential to be used as a protective coating on nano-sized metavivianite in calcareous soil.

Previous studies have demonstrated the effectiveness of bulk VT in mitigating Fe deficiency in plants grown on calcareous soils. However, other research has highlighted its extremely low solubility ($Ksp=10^{-36}$) in electrolyte solutions such as $CaCl_2$. This discrepancy between the results observed under controlled laboratory conditions and those obtained in field applications raises questions about VT solubility and the need for further investigation to bridge this gap in understanding. This study explores the solubilities of nano-metaVT and nano-CT-metaVT in a diluted electrolyte solution (0.003 mol L^{-1} KCl) and calcareous soil saturated paste extract (SPE), which contains compounds relevant to the soil, including LMWOAs, amino acid, fulvic acid, and humic acid. The effects of the presence and absence of two model soil microbes, *Pseudomonas chlororaphis* O6 (*Pc*O6) and *Pseudomonas protegens* Pf-5 (*Pp* Pf-5), on nano-meta VT and nano-CT-metaVT are also investigated. Next, the effectiveness of nano-metaVT and nano-CT-metaVT as an Fe amendment for winter wheat (*Triticum aestivum* L.) growth in silica sand in the presence or absence of salinity stress and presence or absence of *Pp* Pf-5 are studied for salinity mitigation effect and soil microbe inoculation effect. Finally, the effectiveness of nano-metaVT and nano-CT-metaVT on monocot and dicot plants, winter wheat and bean (*Phaseolus vulgaris*), grown in calcareous soil with the presence or

absence of salinity stress is evaluated. The results can provide insight into the effectiveness of nano-metaVT and nano-CT-metaVT and the potential of being the alternative Fe nano fertilizers.

Literature review

1.1 Role of Iron (Fe) in plant health

Iron (Fe) plays a vital role in plant growth as an essential micronutrient.[16] Fe is a co-factor for about 140 enzymes, which participate in several metabolic processes, including photosynthesis, chlorophyll biosynthesis, and respiration.[3-5] However, Fe deficiency is common in plants cultivated in calcareous soils.[6] It is usually recognized by yellow interveinal areas (chlorosis) in young leaves due to the alteration of chlorophyll synthesis. Fe deficiency causes economic losses through persistent leaf chlorosis and the progressive necrosis of young shoots.[17] In order to respond to Fe deficiency, plants have developed two strategies to acquire the nutrient. Strategy I plants (dicots) decrease the rhizosphere pH by releasing more protons, thereby increasing Fe solubility. Strategy-I plants, such as tomato (*Solanum lycopersicum* L.) and *Arabidopsis thaliana* L., release protons via plasma-membrane-localized H^+-ATPases to increase rhizosphere acidification and promote Fe^{3+} solubility.[18] Plants then take up the reduced ferrous ion (Fe^{2+}). Strategy II plants (monocots) produce phytosiderophores, a low molecular weight compound that can chelate Fe^{3+} ions and be taken up as the Fe^{III}-phytosiderophore complex by plants.[4, 19] In addition, an adequate Fe supply is beneficial for plants by mitigating salinity stress. Rabhi et al. (2007) reported that salinity stress on *Medicago ciliaris* L. can be mitigated by adding adequate iron (30 µM Fe) to the growing

medium.[20] Mozafari et al. (2018) further showed that the application of iron nanoparticles (0.8 ppm) increased the content of free proline, total protein, and the enzymatic antioxidant activity of grapes (*Vitis vinifera* L. cv. Merlot 'Khoshnaw') grown under salinity stress.[21]

The disadvantages of conventional Fe fertilizers are related to the availability of Fe decreasing with increasing pH, as shown in Figure 1-1.[22] Inorganic iron will be quickly rendered unavailable by reaction with hydroxide. The free Fe^{3+} concentration of soil-Fe is around $10^{-21.3}$ M in soil with a pH of 8, and total soluble iron is $10^{-10.2}$ M. However, plants require a Fe concentration of 10^{-6} to 10^{-5} M in the soil solution for optimal growth.[23]
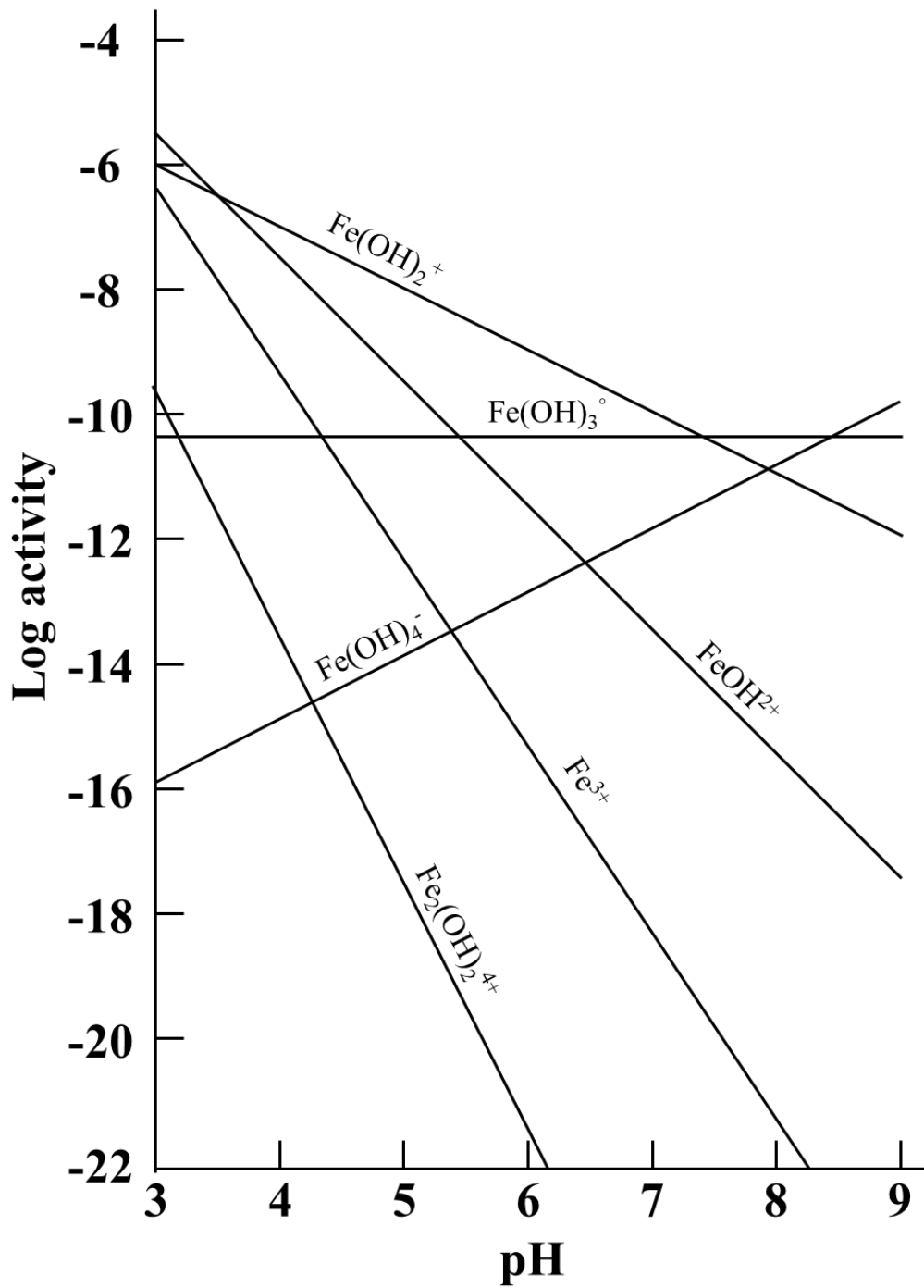
Figure 1-1. Hydrolysis species of Fe (III) in equilibrium with soil-Fe. (Modified from Lindsay, 1979)[22]

Conventional amendment with synthetic Fe-chelates is currently the most effective agricultural practice for preventing Fe deficiencies in calcareous soils.[24] Schenkeveld et al. (2012) studied the effectiveness of Fe-EDDHA chelates under calcareous soil conditions.[25] In the study, the authors found a decline in Fe concentration in soil solution with all Fe-EDDHA treatments within one day, possibly due to adsorption to organic matter, Fe(hydr)oxides, and clay minerals. Moreover, the study also indicated that one of the Fe-EDDHA components, o,p-Fe-EDDHA, revealed the tendency to exchange Fe for Cu. Subsequent leaching of metals implies potential metal mobilization into the groundwater. Therefore, researchers are still looking for natural, high-purity, slow-release Fe fertilizers that are environmentally friendly.[6] Eynard et al. (1992) revealed the effect of vivianite on alleviating Fe deficiency in chickpea (*Cicer arietinum* L.) grown in calcareous soil was competitive compared with Fe chelate (Fe-EDDHA).[11] Bavaresco et al. (2010) investigated the effectiveness of vivianite in alleviating the Fe deficiencies of grapes compared with iron chelate (EDDHA).[26] The results showed that vivianite was competitive in improving the relative chlorophyll content and yield of the grapes. Therefore, vivianite has potential as an environmentally-friendly, Fe-chelate substitute. Fathi et al. (2017) reported that the large specific surface area of nanoparticles improves chemical reaction efficiency, and the application of nano-Fe_2O_3 has positive effects on wheat under salinity stress in soil (pH 7.4-7.9).[27] The literature mentioned above suggests that nano-sized fertilizers could be a good source of phytoavailable Fe in soils relative to Fe-chelate.

1.2 Role of Phosphorus (P) in plant health and the application of metavivinite

Phosphorus (P) is an essential macronutrient for physiological processes during plant growth. Sufficient P improves photosynthesis, nitrogen fixation, flowering, and maturation. Mollier and Pellerin (1999) revealed the P deficiency effects on maize (*Zea mays* L. cv. Volga), such as severe reduction of leaf growth, leaf area, and root growth.[28] However, phosphates (e.g., $H_2PO_4^{-1}$, HPO_4^{-2}, and PO_4^{-3}) chemisorb strongly to variably-charged sites in soils so that insufficient P in soils is common and reduces crop yield globally.[29] Furthermore, the formation of Ca phosphates is promoted under alkaline conditions in the presence of a high Ca concentration. Thus, soluble anions ($H_2PO_4^{-1}$, $HPO_4^{-2,}$ and PO_4^{-3}) tend to form insoluble complexes in alkaline solutions and become unavailable for plant uptake.[30] As shown in Figure 1-2, the solubility of calcium phosphates decreases with increasing pH. P deficiency can result in thin, spindly stems and yield losses. P deficiency influences the root exudate of plants. Carvalhais et al. (2011) showed that maize (*Zea mays* L. var. Surprise) releases a higher amount of γ-aminobutyric acid and carbohydrates under P-deficient conditions, which might affect the nutrient solubility and the attraction of rhizosphere microorganisms.[31] Insufficient P in winter wheat (*Triticum aestivum* L) also results in the plant's vulnerability to abiotic stress, such as salt stress.[32] Agriculture relies on P fertilizer inputs, and rock phosphate is the gold standard P amendment, a non-renewable resource with an estimated reserve of only 50-100 years.[33] Since P can not be synthesized, recovering and reusing P-rich sludge or sediment is critical.[33] Moreover, P leached from soils may lead to the eutrophication of surface waters, adding to global environmental/ecological problems.[34] It is essential to seek environment-friendly techniques for improving P bioavailability in calcareous soils.

Therefore, researchers have started investigating the application of vivianite, which can

be acquired from natural resources or produced from P-rich sewage sludge or sediment,

as a P amendment.[35-36]
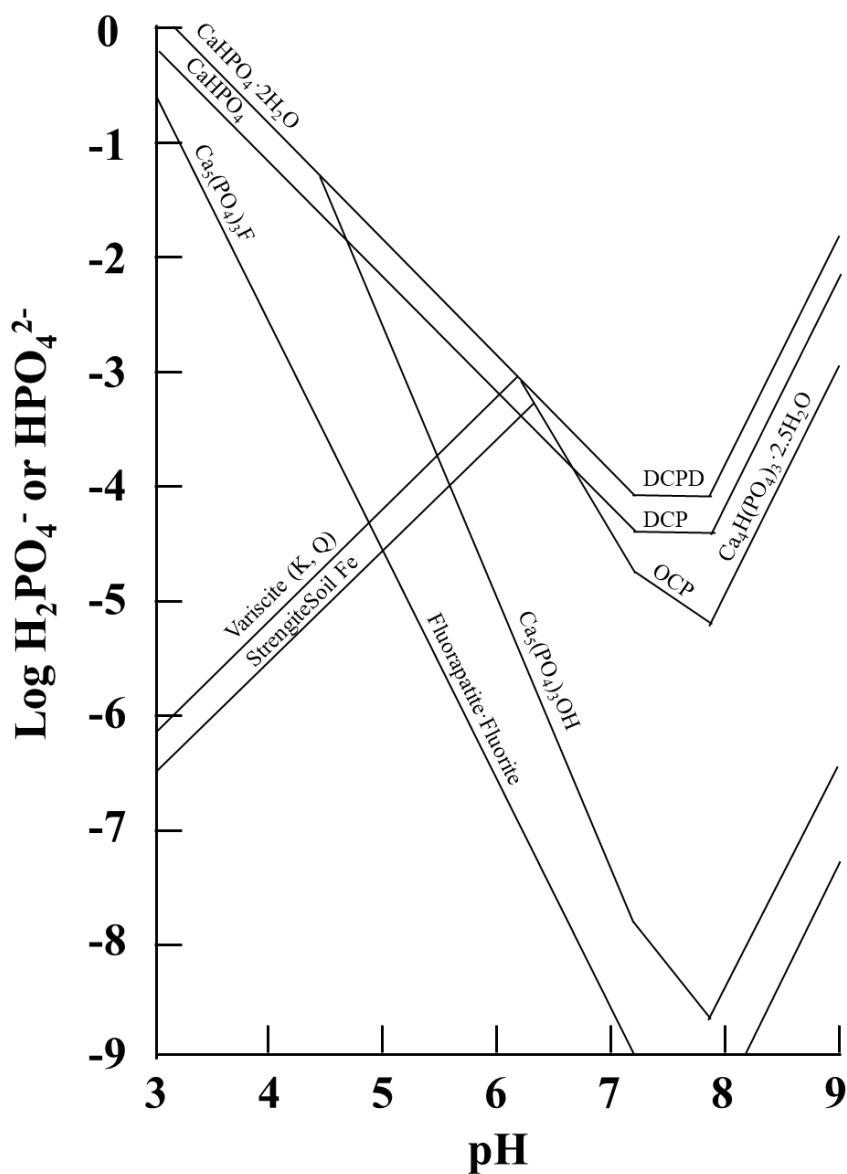
Figure 1-2. Solubility of calcium phosphates compared to strengite and variscite when

Ca^{2+} is $10^{-2.5}$ M or is fixed by calcite and CO_2 (g) at 0.0003 atm. (Modified from Lindsay,

1979)[22]

Vivianite (Fe^{II})$_3$(PO$_4$)$_2$·8H$_2$O, VT) is an iron phosphate mineral that usually

occurs in reduced sediments. The partially oxidized form of vivianite, metavivianite

($Fe^{II}Fe_2^{III}$(PO$_4$)$_2$(OH)$_2$·6H$_2$O, metaVT), is more common in an aerobic environment

where it remains stable for extended periods of time.[37] Secondary sewage effluent often

has a high phosphorus content.[38] Previous studies have demonstrated that 31% of the

phosphorus in sludge can be recovered as vivianite through a chemically enhanced

primary sedimentation process.[39] Jowett et al. (2018) also demonstrated the formation of

vivianite precipitation using low-energy iron electrochemistry in sewage treatment.[40]

Eshun et al. (2024) also reported a formation of biovivianite from the phosphate-solution

in laboratory batch systems using two bacterial strains, *Geobacter sulfurreducens* and

Shewanella putrefaciens.[41] Schütze et al. (2020) used several kinetic models, including

Elovich, Exponential, and Parabolic modes, to describe the slow release of P from bulk

VT compared to hydroxyapatite and bone char in citric acid (0.01-0.1M) and CaCl$_2$

solution (0.01-0.1M) at a pH of 6.[42] The authors concluded that bone char and

hydroxyapatite are more sustainable P sources than bulk VT, because of the poor

solubility of vivinaite in CaCl$_2$ and citric acid solutions. However, Yang et al. (2022)

demonstrated that the simultaneous release of Fe and PO$_4$–P from the dissolution of bulk

VT particles could be induced by citrate effectively at pH 6.[43] The authors further

indicated that the enhancement of bulk VT dissolution was positively correlated to citrate

concentrations, with complete dissolution observed when the citrate concentration was

above 6 mM. Based on the chemical formula of VT, the application of VT as an iron

amendment at a dose of 5 mg Fe per kg of soil results in a coinciding P concentration of

approximately 1.85 mg kg^{-1} in the soil. This level of P supplementation is substantially

lower than what would be required to address P deficiency issues effectively. Thus, VT is primarily utilized as an Fe amendment. The application of bulk VT reduced iron deficiency in different plants, as shown in Table 1-1, including olive trees (*Olea europaea* L.)[13] and lemon trees (*Citrus lemon* L.)[44] growing in calcareous soils. Fodoue et al. (2015) also reported the beneficial effect of applying naturally-occurring vivianite to soils in which beans (*Phaseolus vulgaris* L.) were grown, resulting in leaf densification and extension, improved root system development, and an increase in bean yield.[12] A similar study by Ayeyemi et al. (2023) also highlighted the efficacy of synthetic vivianite, noting that the shoot dry mass of wheat grown in calcareous soil (pH 8.5) treated with 135.25 mg kg^{-1} Fe was significantly higher than that of the control.[45] It is important to note that even though the minerals applied were reported to be VT in publications, based on the authors' descriptions, they likely applied bulk metaVT. In summary, bulk metaVT, which can be recovered from sewage or wastewater, shows promise as an amendment to mitigate iron deficiencies and enhance plant growth in calcareous soils.

Table 1-1. Examples of the effectiveness of (meta)vivianite on various plants grown under high pH or calcareous conditions.

Material	Dose	Growth conditions	Plants	Effectiveness	References
vivianite	1 g/kg	pH 8.2-8.5	Chickpea (*Cicer arietinum* L.)	The chlorophyll content of chickpea leaves was improved with the application of vivianite.	11
vivianite	0.5-2 kg per tree	calcareous, pH 8.1-8.6	Olive trees (*Olea europaea* L.)	Vivianite was almost as effective as Fe chelate in reducing Fe chlorosis in olives, lasting more than two years.	13
vivianite	1.8 g/kg	calcareous, pH 8.0	Kiwifruit (*Actinidia deliciosa* (A.Chev.) C.F.Liang & A.R.Ferguson)	Vivianite enhanced leaf chlorophyll content compared to control treatment under both greenhouse and field conditions.	46
Fe sulfate, vivianite	0.08, 0.16, 0.32 g Fe kg^{-1}	calcareous, pH value: NA	(*Lupinus albus* L.)	Vivianite improved the yield and chlorophyll content with long-term effects and was further enhanced by adding humic substances.	47
vivianite	25 g/L per pot	calcareous, pH 7.3	*Vitis vinifera* L. cv. Merlot grafted on lime-susceptible rootstock	Vivianite was as effective as Fe chelate (Fe-EDDHA) in improving the chlorophyll contents in grapevine leaves.	26
synthetic vivianite	1.0 g/kg	calcareous, pH 8.2	Rooted cuttings of *Vitis berlandieri* Resseguier No. 2 x *Vitis rupestris* Martin	The vines fertilized with vivianite had longer shoots and a higher number of leaves and exhibited higher SPAD values than the control vines. The effectiveness of vivianite lasts through 3 years, indicating the long-term fertilizing effect.	10
synthetic vivianite	0.5-2.0 g/kg	calcareous, pH 7.7	*Eureka lemon* (*Citrus lemon* L.) cuttings grafted on sour orange (*Citrus aurantium* L.)	Vivianite application exhibited a greater leaf Fe concentration and chlorophyll content than untreated plants. The effectiveness of vivianite was comparable to Fe-EDDHA .	44

1.3 Weathering of vivianite and the possible behavior in soil

The oxidation of bulk VT occurs very quickly after being exposed to air. McCammon and Burns (1980) reported the relationship between the crystal structure of bulk VT and its oxidation rate by mechanical grinding the mineral in the air, which generates heat and increases oxygen exposure to the freshly broken edges of bulk VT.[48] The study adopted a model for the oxidation of bulk VT based on experimental results and crystal-chemical principles. The authors further proposed that the Fe^{2+}-Fe^{3+} pair formed after oxidation is more stable than the Fe^{3+}-Fe^{3+} pair. Similar findings were also shown in Rouzies and Millet (1993) study, reporting that the concentration of Fe^{3+} in vivianite determined using Mossbauer spectroscopy remained stable at 50% for at least 375 days.[37] Therefore, the first oxidation stage occurs quickly, and then the structure remains stable for months before complete oxidation. When oxidation occurs, the bulk VT structure is altered due to the elimination of hydrogen bonds by converting H_2O to OH^-. In Roldan et al. (2002), the authors used either water-saturated air or 99.99% pure oxygen at a flow rate of 2 mL s^{-1} to demonstrate the formation of yellowish red (5.1 YR 5.2/6.0) lepidocrocite via complete oxidation of bulk VT.[49] Lepidocrocite (γ-$FeO^{3+}(OH)$) is an iron oxide-hydroxide mineral that consists of layered iron (III) oxide octahedra bonded by hydrogen bonding via hydroxide layers. Weathering rates generally depend on temperature and moisture, mineral particle size, and planes of physical weakness (cleavage) in the crystal in soil. The major reaction process that weathers minerals is the dissolution of mineral-bound ions by water. Unlike the extreme conditions typically described in the literature, such as water-saturated air or 99.99% pure oxygen, the soil environment presents weaker conditions for the weathering of metaVT. In soil

environments, the oxygen availability is about 20% in the atmospheric phase, and the

water content varies depending on irrigation frequency.[50] These factors contribute to

relatively mild weathering conditions compared to those reported in controlled studies.

Consequently, the oxidation process of metaVT in soil is likely to be slower than in the

extreme conditions cited in the literature. This slower oxidation rate could influence the

longevity and effectiveness of metaVT as an Fe amendment in agricultural soils.

1.4 Improving fertilizer efficiency: Nano-sizing and particle coatings

Materials that are less than 100 nanometer in size in at least one dimension are

commonly known as nanomaterials.[51] A substance with the size in nano-scale in one,

two, or three dimensions leads to the structures including a nanosheet, a nanorod, or a

nano-particles.[52] Nano-fertilizers refer to nanomaterials utilized for supporting the

nutrition of plants. The application of nano-fertilizers in crop production is attracting

global interest. Current agricultural production relies on chemical fertilizers to fulfill the

growing demand for food.[53] With limited arable land and scarce water resources affected

by climate change, it is crucial that we develop more efficient fertilizers to sustainably

improve crop production to feed the increasing population.[1] It has been reported that

macronutrient elements, including N, P, and K, applied to the soil are lost via leaching or

runoff by 40–70 %, 80–90 %, and 50–90%, respectively, causing a considerable loss of

resources.[54-55] Low nutrient use efficiency and over-application of chemical fertilizers

may reduce crop yield and increase soil health problems.[1] Therefore, there is a great

interest in applying nano fertilizers to increase fertilizer use efficiency, lower the applied

dose, and minimize volatilization and leaching.[7] With a high surface area to volume ratio,

nano fertilizers exhibit distinct properties from conventional bulk fertilizers. It has been

reported that nano fertilizers modified by polymer coatings can slow down the release of nutrients, improve fertilizer utilization, and reduce leaching losses of fertilizers (Figure 1-3).[56] Therefore, the application of nano fertilizer has the potential to achieve increased sustainability in agriculture.
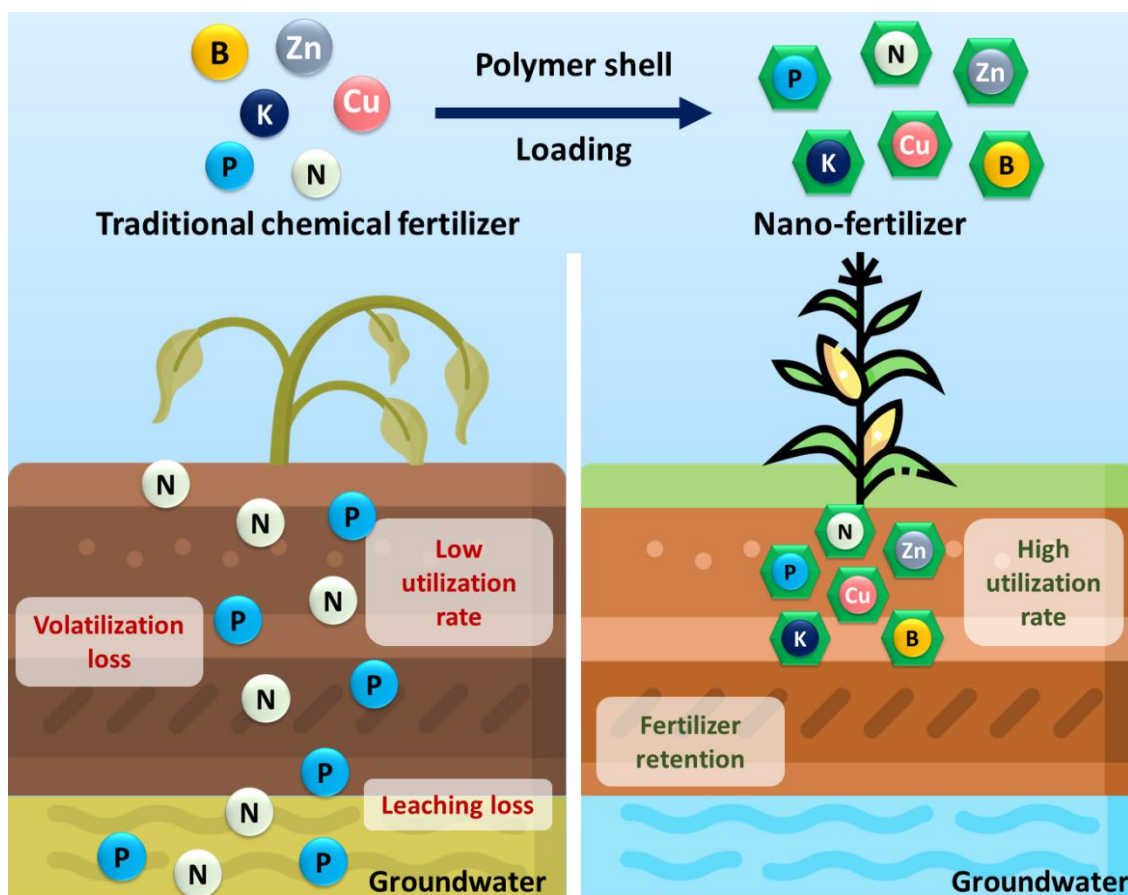
Figure 1-3. Nanomaterials loaded with fertilizers. (Modified from An et al., 2022)[56]

Haydar et al. (2022) showed that the application of 10 mg kg^{-1} iron oxide nanoparticles in soil (pH 4.5) improved the total chlorophyll, total carbohydrates, germination rate, and iron content of mulberry (*Morus alba* L.), as well as increasing plant height, sugar content, and antioxidant enzyme contents of the leaves, compared to the control.[57] The authors further hypothesized that the probable uptake mechanism

involves the conversion of iron nano particles (FeNPs) to bio-available form (Fe^{3+}/Fe^{2+}) and afterward transportation towards the vascular tissues through the apoplastic or symplastic pathways. Likewise, Sabet and Mortazaeinezhad (2018) reported improvement in stem length, yield (130%), and Fe concentration (110%) in cumin (*Cuminum cyminum* L.) amended with 500–1000 mg L^{-1} Fe as nano-iron oxide.[58] The main goals of using these nano fertilizers are to increase nutrient use efficiency and improve precision agriculture. It is generally assumed that nanoparticles of larger size (more than 20 nm) cannot penetrate through cell walls since the cell wall pore sizes vary from 2 to 20 nm.[59] However, using microscopic imaging, Ma et al. (2013) observed that nano-scale zero-valent iron (nZVI) is able to penetrate several layers of epidermal cells of cattail (*Typha latifolia* L.) and hybrid poplars (*Populous deltoids×Populous nigra*).[60] In addition, Serag et al. (2011) reported finding size-dependent distributions of multi-walled carbon nanotubes in the vacuole, plastid, and nucleus of Madagascar periwinkle (*Catharanthus roseus*) protoplasts using confocal imaging and TEM techniques.[61] Based on these results, nano-fertilizer particle transport and translocalization in plants remain unclear. The various aspects of the uptake mechanism of nano-fertilizers result from different factors, such as the morphology of the nanoparticle and the targeted plant.

1.5 Calcareous soils: characteristics and problems

Carbonate-rich soils in the semi-arid West have characteristics rarely found in humid regions.[62] Calcium carbonate accumulation often occurs in these soils, resulting in calcic horizon formation in the soil profile.[63] In addition, the cations released by mineral weathering accumulate instead of leaching out of the profile because of the low precipitation and high evapotranspiration. Therefore, the pH values of soils in arid and

semi-arid environments are generally 7 or above. The cation exchange capacity (CEC) in

these soils is commonly higher than in the acid soils due to the high contents of 2:1-type

clays with high amounts of permanent charge. The cations in the soil solution or the

exchange sites are mainly Ca^{2+}, Mg^{2+}, K^+, and Na^+. Carbonate (CO_3^{2-}) and bicarbonate

(HCO^{3-}) generate hydroxyl ions due to the reaction with water, raising soil pH (Eq. (2) -

(5)).[62]

$$CaCO_3 \rightleftharpoons Ca^{2+} + CO_3^{2-} \tag{2}$$

$$CO_3^{2-} + H_2O \rightleftharpoons HCO_3^- + OH^- \tag{3}$$

$$HCO_2^- + H_2O \rightleftharpoons H_2CO_3 + OH^- \tag{4}$$

$$H_2CO_3 \rightleftharpoons H_2O + CO_2 \tag{5}$$

The availability of most nutrient elements is significantly affected by soil pH, and

calcareous soils reveal the problems of low nutrient solubility. Deficiency of the

macronutrient phosphorus (P) is a widespread problem in arid areas because of the low

solubility of phosphates.[64] Soluble P will react immediately with Ca^{2+} and form insoluble

calcium-phosphate compounds. Moreover, micronutrients, such as iron, zinc, and copper,

are much less available in calcareous soil than in acid soil.[65] Fe and P deficiency in

calcareous soil have been discussed in Sections 1.1 and 1.2.

1.6 Roles of organic compounds in soil rhizosphere

Plant-soil feedback is essential in plant succession, population, community

structure, and diversity. Plants can change the soil microbiota by secreting bioactive

molecules into the rhizosphere. Root exudates are typically comprised of primary

metabolites such as sugars, amino acids, and carboxylic acids, as well as a diverse set of secondary metabolites. Root exudate compounds affect rhizosphere microbes by acting as signaling molecules, attractants, and stimulants. Furthermore, root exudates also affect the solubility of micronutrients in soils. Awad et al. (1999) proposed the influence of phytosiderophores released from winter wheat (*Triticum aestivum* L.) on the mobilization and uptake of iron and zinc in calcareous soils.[66] The authors indicated that the production of phytosiderophores in winter wheat was enhanced under Fe deficiency, compared to Fe sufficiency.

Schütze et al. (2020) compared P release rate from vivianite, hydroxyapatite, and bovine bone char in $CaCl_2$ and citric acid solutions (0.01–0.1 mol L^{-1}, pH 6) over 168 h.[42] The results showed that the released P concentrations in citric acid are 320-466-fold higher than in $CaCl_2$ solution, indicating the critical role of low molecular weight organic acids (LMWOAs) in the solubility of phosphate minerals. Similar results were shown in a Gypser and Freese (2020) study, reporting that the concentrations of P release from vivianite in various solutions after 1,344 h follow the order: citric acid (83.9%) > humic acid (8.1%) > $CaSO_4$ (1.7%) > $CaCl_2$ (1.4%).[67] The release of P bound by organic acids includes the processes of mineral dissolution, direct ligand exchange, and the replacement of P by organic acid anions, the formation of metal–organic complexes, and blocking of P adsorption sites.[68, 69] The results also highlighted the critical roles of LMWOAs and AAs on the solubility of mineral in the soil solution.

Beyond these organic components, soil microbes also play a significant role in influencing solubility. Many rhizobacteria promote plant growth and protect the plant from abiotic stresses by providing access to nutrients otherwise unavailable to roots.[70, 71]

In return, these symbiotic bacteria receive photosynthetically derived carbon in the form of sugars, amino acids, and organic acids from plant root exudates.[72-74] Soil microorganisms, particularly plant growth-promoting rhizobacteria (PGPR), are crucial in the soil ecosystem. They colonize the rhizosphere and enhance plant health and yield through various mechanisms, including improving nutrient bioavailability and producing siderophores.[75] Some PGPR species assimilate iron by producing Fe-chelating compounds known as siderophores, which are essential for transporting iron into their cells and significantly affect the solubility of Fe fertilizers in soil solutions.[76]

1.7 Salinity soil, saline irrigation water, and plant responses to salinity stress

Soil salinity is a global issue because of its negative impact on agricultural production. More than 20% of soils are salt-affected, continuously increasing owing to anthropogenic activities and climate change.[77, 78] Natural and human activities can result in salinity problems, which might occur through pedogenetic or secondary origin due to excessive evaporation, seawater infiltration, or saline water irrigation.[78] With the global demand for water for both drinking and irrigation water increasing, competition for scarce water resources is happening worldwide.[80, 81] Irrigating plants with recycled water that usually contains certain amounts of dissolved salts is one of the ways to ease the water demand.[82] However, this practice may lead to salt accumulation in the soil and result in osmotic and specific ion effects on plants. For example, most sewage effluent has an EC value ranging from 0.30 to 4.7 $dS \cdot m^{-1}$.[38] The electrical conductivity (EC) of secondary municipal effluent ranges from 0.65–0.91 $dS \cdot m^{-1}$, with sodium adsorption ratio (SAR) values ranging from 3.2–7.9.[38, 83] Excess soluble salts lower the osmotic potential of the soil water, inhibiting water uptake by plant roots and resulting in wilting.

Various indicators are used to describe salinity in the soil. The EC of the soil solution provides an indirect measurement of the salt content. Soil saturated paste extracts with ECs (EC_e) greater than 4 dS·m^{-1} are defined as saline, and often interfere with plant growth.[62] SAR is an irrigation water quality parameter used in the management of sodium-affected soils, providing information on the comparative concentrations of Na^+, Ca^{2+}, and Mg^{2+}. The SAR is also used to characterize irrigation water applied to soils. It is calculated as follows:

$$SAR = \frac{[Na+]}{(0.5[Ca^{2+}]+0.5[Mg^{2+}])^{\frac{1}{2}}} \tag{6}$$

where $[Na^+]$, $[Ca^{2+}]$, and $[Mg^{2+}]$ are the concentrations in mmol of charge per liter.

Salinization happens when water-soluble salts in the soil accumulate to a level that negatively affects plant growth. The excess salt accumulation obstructs the growth of crops by limiting their ability to take up water, resulting in an ion imbalance.[84] Thus, plants grown under salinity stress are impacted by osmotic stress, oxidative stress, and altered nutrient balance.[85] Ghassemi et al. (1995) reported that around 20% of irrigated lands worldwide are influenced by salt accumulation, with more than 30% of the countries in arid or semi-arid areas affected.[86] Furthermore, the United Nations reported that the global population is estimated to increase from 7.7 billion in 2019 to 11.2 billion by 2100.[87] To relieve growing population pressures, more drylands will be needed for agricultural production, which will require increased irrigation water. As sources of clean, fresh water dry up, irrigation with slightly saline water is likely, causing further soil salinization. The salinity problems of soils and irrigation water are attracting much

attention, especially in this climate change-influenced environment. It will influence the food crisis problem and the agricultural economy.[86]

1.8 Advanced polymer materials in agriculture and the application of chitosan

Polymers are versatile molecules with repeating structures that can be designed to meet specific applications by modifying the composition of the replicated portion. Examples include varying the type and/or length of side chains or adjusting their polarity or degree of crystallization. In agriculture, polymers and polymeric materials have been used to increase the efficiency of pesticides and control the delivery of agrochemicals (Figure 1-4).[88-91] For example, Jia et al. (2013) prepared a polydopamine film-coated controlled-release fertilizer (PCMCF) and also revealed that the polydopamine film slowed down the release of potassium (K), copper (Cu), and phosphate (P) from PCMCF in two kinds of soil.[91] With the emerging development of nanotechnology, improving the bioavailabilities of nano-agrochemicals by combining the polymer techniques under specific microenvironmental conditions is critical. For instance, Liang et al. (2018) encapsulated the pesticide, avermectin, in a poly-γ-glutamic acid and chitosan polymer, forming a pH-responsive bio-nematocide nanoparticle.[92] Poly-γ-glutamic acid and chitosan encapsulation stabilized avermectin at lower pH but allowed the release of the compound with increasing pH.
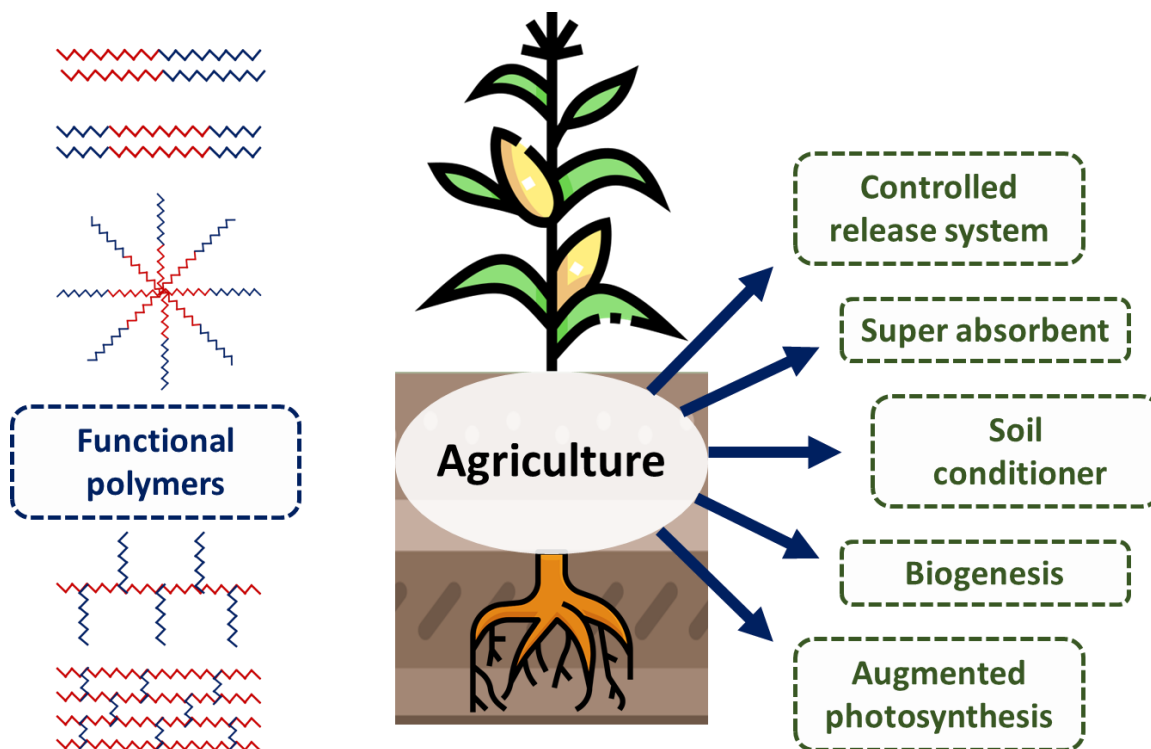
Figure 1-4. The application of functional polymers in agriculture and its benefits. (Modified from Sikder et al., 2021)[87]

Worldwide, approximately 6-8 million shrimp and crab waste shells are produced and discarded every year.[93, 94] Chitin, a major constituent of shrimp and crab shells, is the second most abundant polysaccharide, after cellulose, in the world. Chitosan (CT), the N-deacetylated derivative of chitin, has antifungal and antibacterial properties and has been used in various applications, including cosmetics, food products, agrochemicals, pharmaceuticals, and water treatment.[95, 96] Other studies indicate that CT benefits plant growth. It has been reported that CT treatment improves the disease-defense abilities of plants against a wide range of plant-pathogenic fungi and bacteria.[15] Veroneze et al. (2020) reported that foliar application of chitosan improved the tolerance of maize against water-deficit stress.[97] Similarly, Zhang et al. (2021) reported that the 100 mg L^{-1}

chitosan foliar spray mitigated the negative effect of salinity on romaine lettuce (*Lactuca sativa* L.) and improved its growth attributes, e.g., total leaf area, shoot fresh weight, and shoot and root biomass.[98] Furthermore, Ha et al. (2019) demonstrated that the application of chitosan-encapsulated N, P, and K nano fertilizers in soil improved the yield of cucumber (*Cucumis sativus* L.) and proposed that the positive-charged surface of chitosan and K might contribute to the increased osmotic pressure of stomatal cells, leading to the increased opening of stomatal cells and greater stomatal conductance.[99]

Controlled-release fertilizers are either slowly soluble, slowly released, or held in a natural organic form, compared to the "quick-releasing fertilizers" with higher water solubility. Moreover, controlled-release fertilizers release a small, steady amount of nutrients, staying in the soil longer over time. Due to the need for controlled-release fertilizers, interest in functional coatings is rising. Coating materials are selected based on their biodegrading ability, low cost, and non-toxic properties.[89] Since chitosan has all these characteristics, it has been proposed as a surface coating material. For example, Wu et al. (2008) have utilized chitosan as an external coating on an NPK fertilizer to slow its release.[100] Besides serving as a slow-releasing layer, chitosan coating also has the ability to promote bioavailability in calcareous soils. Chitosan-encapsulated Zn nanoparticles have been reported to promote maize (Surya local, disease susceptible)[101] growth and alleviate the Zn deficiency in an alkaline soil and wheat (MACS 3125, durum wheat cultivars)[102] in sand. However, no study has investigated the effect of the chitosan-coated Fe-P nano-amendment on plant growth and plant tolerance to salinity stress in calcareous soils.

1.9 Soil microbes - *Pseudomonas chlororaphis* O6 (*Pc*O6) and *Pseudomonas protegens* Pf-5

Plant growth-promoting rhizobacteria (PGPR) are often involved in suppressing phytopathogens and have potential as biocontrol agents for the prevention of plant diseases.[103] Use of PGPR as a biocontrol agent requires complete knowledge of how they compete with and protect themselves from other organisms in the rhizosphere. *Pseudomonas chlororaphis* O6 (*Pc*O6) (NCBI taxonomy ID: 1037915; IMG submission ID: 54436) is a beneficial microbe isolated from the root of winter wheat by Dr. Anne Anderson. The genome properties of *Pc*O6 are shown in Table 1-2 and Figure B1-1. Spencer et al. (2003) examined systemic defense induction in tobacco (*Nicotiana tabacum* L.) with roots colonized by *Pc*O6 against two leaf pathogens, *Pseudomonas syringae* and *Erwinia carotovora*.[104] Later, Kim et al. (2004) also demonstrated that *Pc*O6 induced systemic resistance in cucumbers against the pathogen, *Corynespora cassiicola*.[105] *Pc*O6 possesses the ability to help the plant resist both biotic (pathogens) and abiotic stress (drought stress) through different mechanisms. For example, *Pc*O6 was reported to address drought stress in *Arabidopsis thaliana* by triggering the partial closure of stomata.[106] Furthermore, Dimkpa et al. (2012) reported that *Pc*O6 produces a pyoverdine (PVD) siderophore that is regulated by the growth phase of plants and by the presence of metal ions.[107] Overall, this study aims to investigate the interactions among *Pc*O6, wheat plant, and nano-metaVT/nano-CT-metaVT in the soil and the impact on winter wheat grown under salinity stress.

Table 1-2. Genome statistics of *Pseudomonas chlororaphis* O6 (*Pc*O6). Data are obtained from the National Center for Biotechnology Information's Entrez database and the EzGenome database.

Attribute	Value	% of Total
Genome size (bp)	6980251	100.00%
DNA coding region (bp)	6139230	87.95%
DNA G+C content (bp)	4390481	62.90%
Total genes	6356	100.00%
RNA genes	142	2.23%
rRNA operons	10	0.16%
Protein-coding genes	6214	97.77%
Pseudo genes	87	-
Genes with function prediction	5063	79.66%
Genes with internal clusters	890	14.00%
Genes assigned to COGs	4599	72.36%
Genes assigned Pfam domains	5429	85.42%
Genes with signal peptides	677	10.65%
Genes with transmembrane helices	1447	22.77%
CRISPR repeats	1	-

G+C content: guanine + cytosine content; COGs: clusters of orthologous group; CRISPR repeats: clustered regularly interspaced short palindromic repeats.

In order to understand how the decomposition of the chitosan coating on the metaVT particles by a soil organism might affect the solubility of Fe and P, we will use a soil bacterium with the ability to produce chitinase. *Pseudomonas protegens* Pf-5 (*Pp* Pf-

5) (NCBI Taxonomy ID: 220664) is a soil-dwelling bacterium and is a known PGPR. The genome properties are shown in Table 1-3 and Figure B1-2. Loper et al. (2016) were the first researchers to verify that *Pp* Pf-5 is able to produce chitinase by genomic sequence analysis.[108] Rathore et al. (2020) showed that *Pp* Pf-5 inhibited pathogen growth in cumin (*Cuminum cyminum* L.) by producing chitinase, β-1, 3 glucanase, and protease.[109] Ruiu and Mura (2021) also revealed that the productions of *chitinase D*, *pesticin*, and the fluorescent insecticidal toxin *fitD* by *Pp* Pf-5 are key factors in bioinsecticidal action against *Musca domestica* and *Lucilia caesar* larvae.[110] Chitinase is an enzyme that can hydrolyze chitin, which is widely distributed within insect bodies and fungal cell walls, enabling the utilization of the end products as carbon and nitrogen sources. The decomposition of chitin by chitinases is an important step in soil biogeochemical cycling of carbon and nitrogen, playing an essential role in the bactericidal and fungicidal mechanisms of *Pp* Pf-5.[108] Apart from chitinase production, siderophore secretion was triggered in *Pp* Pf-5 under Fe deficiency to scavenge Fe in soil (Mendonca et al., 2020).[111] Furthermore, *Pp* Pf-5 also increased root length (2.3-fold) and root mass (4.5-fold) of trembling aspen (*Populus tremuloides*, "aspen") under low P conditions compared to non-bacterial treatments.[72] Overall, previous studies have shown the potential of *Pp* Pf-5 to mitigate Fe and P deficiency and inhibit the growth of soil pathogens with the production of chitinase and other enzymes.

Table 1-3. Genome statistics of *Pseudomonas protegens* Pf-5 (*Pp* Pf-5). Data are

obtained from the National Center for Biotechnology Information's Entrez database and

the EzGenome database.

Attribute	Value	% of Total
Genome size (bp)	7074893	100.00%
DNA coding region (bp)	6307702	89.16%
DNA G+C content (bp)	4478756	63.30%
Total genes	6257	100.00%
RNA genes	115	1.84%
rRNA operons	16	0.26%
Protein-coding genes	6142	98.16%
Pseudo genes	58	-
Genes with function prediction	4679	74.78%
Genes with internal clusters	4136	66.10%
Genes assigned to COGs	4525	72.32%
Genes assigned Pfam domains	5337	85.3%
Genes with signal peptides	647	10.34%
Genes with transmembrane helices	1448	23.14%
CRISPR repeats	-	

G+C content: guanine + cytosine content; COGs: clusters of orthologous group; CRISPR

repeats: clustered regularly interspaced short palindromic repeats.

1.10 Chitinase in nature and its role

Chitinolytic enzymes have been divided into two main categories: endochitinases (EC 3.2.1.14) and exochitinases. Exochitinases have been classified into two categories, chitobiosidases (EC 3.2.1.29), which catalyze the progressive release of diacetylchitobiose from the terminal nonreducing end, and N-acetylglucosaminidases (EC 3.2.1.30) which cleaves oligomeric products obtained by endochitinases into monomers of N-acetyl glucosamine (GlcNAc). Chitinolytic enzymes can be categorized into families 18, 19, and 20 of glycosyl hydrolases based on the amino acid sequence similarity of chitinases. Family 18 comprises chitinases from viruses, bacteria, fungi, animals, and certain plant chitinases. Family 19 includes some plant chitinases and *Streptomyces* chitinases. Families 18 and 19 do not share amino acid sequence similarity and have entirely different 3D structures. Family 20 involves N-acetylglucosaminidases from bacteria, certain fungi, and humans.[112] Chitinase produced by various organisms plays a critical role in nature. Bacterial chitinase is able to decompose chitin and supply nitrogen and carbon as an energy source.[113] Fungal chitinases are involved in the various stages of growth, including nutrition, morphogenesis, and developmental process.[114] Insect chitinases are used to break down the old cuticle layer during the growth period.

1.11 Summary

Previous studies have indicated the key roles of Fe and P in plant growth. The application of Fe (in section 1.1) and chitosan (in section 1.8) may mitigate salinity stress on plants. Plant tolerance to salinity stress may improve with Fe, P, and chitosan supplements. A novel Fe-P amendment coated by a protective polymer, chitosan, in calcareous soils is needed. With the presence of *Pc*O6 and *Pp* Pf-5, the interactions

among rhizosphere, nano-metaVT, nano-CT-metaVT, and soil bacterium are essential to investigate. This study aims to synthesize nano-metaVT and nano-CT-metaVT and characterize their material properties. The Fe and P phytoavailability of nano-metaVT and nano-CT-metaVT in a dilute electrolyte solution and calcareous soil pore water (saturated paste extract) will be studied. The effects of nano-metaVT and nano-CT-metaVT on mitigating salinity stress in winter wheat grown in sand will be evaluated. Since plants have evolved two different strategies to uptake Fe, we will also investigate both a siderophore-producing monocot (winter wheat) and a rhizosphere-acidifying dicot (bush beans) to investigate whether there is a difference in their abilities to take up Fe from nano-metaVT or nano-CTmetaVT in calcareous soil.

Hypotheses:

CHAPTER 2: Exploring nano-sized metavivianite and nano-sized chitosan-coated metavivianite and their solubility in a calcareous soil saturated paste extract with soil microbe inoculation

1) Nano-metaVT and nano-CT-metaVT have low solubilities in KCl and SPE suspensions.

2) Nano-CT-metaVT is less soluble than nano-metaVT in KCl but more soluble than metaVT in SPE.

3) *Pp* Pf-5 will increase the solubilities of nano-metaVT and nano-CT-metaVT in SPE suspensions.

CHAPTER 3: Investigate *Pseudomonas protegens* Pf-5 mitigating salinity stress in wheat grown with nano-metavivianite and nano-chitosan-coated metavivianite as Fe amendments

1) Fe amendment benefits *Pp* Pf-5 in ½HS suspensions under salinity stress.

2) Nano-metaVT and nano-CT-metaVT improve Fe uptake and mitigate the salinity stress, compared to control, in wheat grown for 14 days.

3) *Pp* Pf-5 improves Fe uptake and mitigates the salinity stress, compared to control, in wheat grown for 14 days.

CHAPTER 4: Exploring meta-vivianite and chitosan-coated meta-vivianite as alternative iron nano-fertilizers for plants growing in calcareous soil and the effects of salinity stress

1) Nano-metaVT and nano-CT-metaVT improve Fe uptake and mitigate the salinity stress in wheat and beans grown for 28 days.

2) Nano-metaVT and nano-CT-metaVT improve Fe uptake in beans grown to maturity (50 days).

1.12 References

(1) Fess, T. L.; Kotcon, J. B.; Benedito, V. A. Crop breeding for low input agriculture: A sustainable response to feed a growing world population. *Sustainability* **2011**, 3 (10), 1742-1772.

(2) Zulfiqar, F.; Navarro, M.; Ashraf, M.; Akram, N. A.; Munné-Bosch, S. Nanofertilizer use for sustainable agriculture: Advantages and limitations. *Plant Sci.* **2019**, 289, 110270. DOI: 10.1016/j.plantsci.2019.110270.

(3) Brittenham, G. M. New advances in iron metabolism, iron deficiency, and iron overload. *Curr Opin Hematol* **1994**, 1 (2), 101-106.

(4) Kobayashi, T.; Nishizawa, N. K. Iron uptake, translocation, and regulation in higher plants. *Annu. Rev. Plant Biol.* **2012**, 63 (1), 131-152. DOI: 10.1146/annurev-arplant-042811-105522.

(5) Morrissey, J.; Guerinot, M. L. Iron uptake and transport in plants: The good, the bad, and the ionome. *Chem. Rev.* **2009**, 109 (10), 4553-4567. DOI: 10.1021/cr900112r.

(6) Abadia, J.; Vazquez, S.; Rellan-Alvarez, R.; El-Jendoubi, H.; Abadia, A.; Alvarez-Fernandez, A.; Lopez-Millan, A. F. Towards a knowledge-based correction of iron chlorosis. *Plant Physiol. Biochem.* **2011**, 49 (5), 471-482. DOI: 10.1016/j.plaphy.2011.01.026.

(7) Seleiman, M. F.; Almutairi, K. F.; Alotaibi, M.; Shami, A.; Alhammad, B. A.; Battaglia, M. L. Nano-fertilization as an emerging fertilization technique: why can modern agriculture benefit from its use? *Plants* **2021**, 10 (1), 2.

(8) Rothe, M.; Frederichs, T.; Eder, M.; Kleeberg, A.; Hupfer, M. Evidence for vivianite formation and its contribution to long-term phosphorus retention in a recent lake sediment: a novel analytical approach. *Biogeosciences* **2014**, 11 (18), 5169-5180. DOI: 10.5194/bg-11-5169-2014.

(9) Wu, Y.; Luo, J. Y.; Zhang, Q.; Aleem, M.; Fang, F.; Xue, Z. X.; Cao, J. S. Potentials and challenges of phosphorus recovery as vivianite from wastewater: A review. *Chemosphere* **2019**, 226, 246-258. DOI: 10.1016/j.chemosphere.2019.03.138.

(10) Diaz, I.; Barron, V.; del Campillo, M. C.; Torrent, J. Testing the ability of vivianite to prevent iron deficiency in pot-grown grapevine. *Sci. Hortic.* **2010**, 123 (4), 464-468. DOI: 10.1016/j.scienta.2009.11.006.

(11) Eynard, A.; Campillo, M. C.; Barrón, V.; Torrent, J. Use of vivianite ($Fe_3(PO_4)_2.8H_2O$) to prevent iron chlorosis in calcareous soils. *Fertil. Res.* **1992**, 31, 61-67. DOI: 10.1007/BF01064228.

(12) Fodoue, Y.; Jean Pierre, N.; Tchameni, R.; Basga, S.; Penaye, J. Assessment of the fertilizing effect of vivianite on the growth and yield of the bean ''*Phaseolus vulgaris*'' on Oxisoils from Ngaoundere (Central North Cameroon). *Int. Res.J. Earth Sci.* **2015**, 3, 18-26.

(13) Rosado, R.; del Campillo, M. C.; Martinez, M. A.; Barron, V.; Torrent, J. Long-term effectiveness of vivianite in reducing iron chlorosis in olive trees. *Plant Soil* **2002**, 241 (1), 139-144. DOI: 10.1023/a:1016058713291.

(14) Uddin, I.; Islam, J. M. M.; Haque, A.; Zubair, A.; Barua, R.; Rahaman, S.; Rahman, L.; Khan, M. A. Significant influence of gamma-radiation-treated chitosan and alginate on increased productivity as well as improved taste and flavor of pineapple. *Int. J. Fruit Sci.* **2020**, 20 (sup2), 455-469. DOI: 10.1080/15538362.2020.1740909.

(15) Lin, Y. C.; Chung, K. R.; Huang, J. W. A synergistic effect of chitosan and lactic acid bacteria on the control of cruciferous vegetable diseases. *Plant Pathol. J.* **2020**, 36 (2), 157-169. DOI: 10.5423/ppj.Oa.01.2020.0004.

(16) Kim, S. A.; Guerinot, M. L. Mining iron: Iron uptake and transport in plants. *Febs Letters* **2007**, 581 (12), 2273-2280. DOI: 10.1016/j.febslet.2007.04.043.

(17) Canasveras, J. C.; Sanchez-Rodriguez, A. R.; del Campillo, M. C.; Barron, V.; Torrent, J. Lowering iron chlorosis of olive by soil application of iron sulfate or siderite. *Agron. Sustain. Dev.* **2014**, 34 (3), 677-684. DOI: 10.1007/s13593-013-0191-4.

(18) Zhang, X.; Zhang, D.; Sun, W.; Wang, T. The adaptive mechanism of plants to iron deficiency via iron uptake, transport, and homeostasis. *Int. J. Mol. Sci.* **2019**, 20 (10). DOI: 10.3390/ijms20102424.

(19) Colombo, C.; Palumbo, G.; He, J. Z.; Pinton, R.; Cesco, S. Review on iron availability in soil: interaction of Fe minerals, plants, and microbes. *J. Soils Sediments* **2014**, 14 (3), 538-548. DOI: 10.1007/s11368-013-0814-z.

(20) Rabhi, M.; Barhoumi, Z.; Ksouri, R.; Abdelly, C.; Gharsalli, M. Interactive effects of salinity and iron deficiency in *Medicago ciliaris*. *C. R. Biol.* **2007**, 330 (11), 779-788. DOI: 10.1016/j.crvi.2007.08.007.

(21) Mozafari, A. A.; Asl, A. G.; Ghaderi, N. Grape response to salinity stress and role of iron nanoparticle and potassium silicate to mitigate salt induced damage under in vitro conditions. *Physiol. Mol. Biol. Plants* **2018**, 24 (1), 25-35. DOI: 10.1007/s12298-017-0488-x.

(22) Lindsay, W. L. Chemical equilibria in soils. In Whiley Interscience, New York, NY., 1979; p 449.

(23) Schenkeveld, W. D. C. Iron fertilization with FeEDDHA : the fate and effectiveness of FeEDDHA chelates in soil-plant systems. **2010**.

(24) Rajaie, M.; Tavakoly, A. R. Iron and/or acid foliar spray versus soil application of Fe-EDDHA for prevention of iron deficiency in Valencia orange grown on a calcareous soil. *J. Plant Nutr.* **2018**, 41 (2), 150-158. DOI: 10.1080/01904167.2017.1382523.

(25) Schenkeveld, W. D. C.; Hoffland, E.; Reichwein, A. M.; Temminghoff, E. J. M.; van Riemsdijk, W. H. The biodegradability of EDDHA chelates under calcareous soil conditions. *Geoderma* **2012**, 173-174, 282-288. DOI: 10.1016/j.geoderma.2011.12.007.

(26) Bavaresco, L.; Goncalves, M.; Civardi, S.; Gatti, M.; Ferrari, F. Effects of traditional and new methods on overcoming lime-induced chlorosis of grapevine. *Am. J. Enol. Vitic.* **2010**, 61 (2), 186-190.

(27) Fathi, A.; Zahedi, M.; Torabian, S. Effect of interaction between salinity and nanoparticles (Fe_2O_3 and ZnO) on physiological parameters of *Zea mays* L. *J. Plant Nutr.* **2017**, 40 (19), 2745-2755. DOI: 10.1080/01904167.2017.1381731.

(28) Mollier, A.; Pellerin, S. Maize root system growth and development as influenced by phosphorus deficiency. *J. Exp. Bot.* **1999**, 50 (333), 487-497. DOI: 10.1093/jexbot/50.333.487.

(29) Elser, J. J.; Bracken, M. E. S.; Cleland, E. E.; Gruner, D. S.; Harpole, W. S.; Hillebrand, H.; Ngai, J. T.; Seabloom, E. W.; Shurin, J. B.; Smith, J. E. Global analysis of nitrogen and phosphorus limitation of primary producers in freshwater, marine and terrestrial ecosystems. *Ecol. Lett.* **2007**, 10 (12), 1135-1142. DOI: DOI: 10.1111/j.1461-0248.2007.01113.x.

(30) Halajnia, A.; Haghnia, G. H.; Fotovat, A.; Khorasani, R. Phosphorus fractions in calcareous soils amended with P fertilizer and cattle manure. *Geoderma* **2009**, 150 (1), 209-213. DOI: 10.1016/j.geoderma.2009.02.010.

(31) Carvalhais, L. C.; Dennis, P. G.; Fedoseyenko, D.; Hajirezaei, M.-R.; Borriss, R.; von Wirén, N. Root exudation of sugars, amino acids, and organic acids by maize as affected by nitrogen, phosphorus, potassium, and iron deficiency. *J. Plant Nutr. Soil Sci.* **2011**, 174 (1), 3-11. DOI: 10.1002/jpln.201000085.

(32) Khan, A.; Ahmad, I.; Shah, A.; Ahmad, F.; Ghani, A.; Nawaz, M.; Shaheen, F.; Fatima, H.; Pervaiz, F.; Javed, S.; et al. Amelioration of salinity stress in wheat (*Triticum aestivum* L) by foliar application of phosphorus. *Phyton-Int. J. Exp. Bot.* **2013**, 82, 281--287.

(33) Cordell, D.; Drangert, J.-O.; White, S. The story of phosphorus: Global food security and food for thought. *Glob. Environ. Change* **2009**, 19 (2), 292-305. DOI: DOI: 10.1016/j.gloenvcha.2008.10.009.

(34) Paerl, H. W. Mitigating harmful cyanobacterial blooms in a human- and climatically-impacted world. *Life* **2014**, 4 (4), 988-1012.

(35) Yuan, Q.; Wang, S.; Wang, X.; Li, N. Biosynthesis of vivianite from microbial extracellular electron transfer and environmental application. *Sci. Total Environ.* **2021**, 762, 143076. DOI: 10.1016/j.scitotenv.2020.143076.

(36) Cosmidis, J.; Benzerara, K.; Morin, G.; Busigny, V.; Lebeau, O.; Jézéquel, D.; Noël, V.; Dublet, G.; Othmane, G. Biomineralization of iron-phosphates in the water column of Lake Pavin (Massif Central, France). *Geochim. Cosmochim. Acta* **2014**, 126, 78-96. DOI: DOI: 10.1016/j.gca.2013.10.037.

(37) Rouzies, D.; Millet, J. M. M. Mössbauer study of synthetic oxidized vivianite at room temperature. *Hyperfine Interact.* **1993**, 77 (1), 19-28. DOI: 10.1007/BF02320295.

(38) Feigin, A.; Ravina, I.; Shalhevet, J. Irrigation with treated sewage effluent: Management for environmental protection; Springer **1991**. DOI: 10.1007/978-3-642-74480-8.

(39) Lin, L.; Li, R.-h.; Li, Y.; Xu, J.; Li, X.-y. Recovery of organic carbon and phosphorus from wastewater by Fe-enhanced primary sedimentation and sludge fermentation. *Process Biochem.* **2017**, 54, 135-139. DOI: 10.1016/j.procbio.2016.12.016.

(40) Jowett, C.; Solntseva, I.; Wu, L.; James, C.; Glasauer, S. Removal of sewage phosphorus by adsorption and mineral precipitation, with recovery as a fertilizing soil amendment. *Water Sci. Technol.* **2018**, 77 (8), 1967-1978. DOI: 10.2166/wst.2018.027.

(41) Eshun, L. E.; Coker, V. S.; Shaw, S.; Lloyd, J. R. Strategies for optimizing biovivianite production using dissimilatory Fe(III)-reducing bacteria. *Environ. Res.* **2024**, 242, 117667. DOI: 10.1016/j.envres.2023.117667.

(42) Schütze, E.; Gypser, S.; Freese, D. Kinetics of phosphorus release from vivianite, hydroxyapatite, and bone char influenced by organic and inorganic compounds. *Soil Syst.* **2020**, 4 (1), 15.

(43) Yang, S. Y.; Yang, X. F.; Zhang, C. Y.; Deng, S. Y.; Zhang, X. R.; Zhang, Y.; Cheng, X. Significantly enhanced P release from vivianite as a fertilizer in rhizospheric soil: Effects of citrate. *Environ. Res.* **2022**, 212, 113567. DOI: 10.1016/j.envres.2022.113567.

(44) Ammari, T. G.; Hattar, B. Effectiveness of vivianite to prevent lime-induced iron deficiency in lemon trees grown on highly calcareous soil. *Commun. Soil Sci. Plant Anal.* **2011**, 42 (21), 2586-2593. DOI: 10.1080/00103624.2011.614034.

(45) Ayeyemi, T.; Recena, R.; Garcia-Lopez, A. M.; Delgado, A. Circular economy approach to enhance soil fertility based on recovering phosphorus from wastewater. *Agronomy-Basel* **2023**, 13 (6), 1513. DOI: 10.3390/agronomy13061513.

(46) Rombola, A. D.; Toselli, M.; Carpintero, J.; Ammari, T.; Quartieri, M.; Torrent, J.; Marangoni, B. Prevention of iron-deficiency induced chlorosis in kiwifruit (*Actinidia deliciosa*) through soil application of synthetic vivianite in a calcareous soil. *J. Plant Nutr.* **2003**, 26 (10-11), 2031-2041. DOI: 10.1081/pln-120024262.

(47) de Santiago, A.; Quintero, J. M.; Carmona, E.; Delgado, A. Humic substances increase the effectiveness of iron sulfate and vivianite preventing iron chlorosis in white lupin. *Biol. Fertil. Soils* **2008**, 44 (6), 875-883. DOI: 10.1007/s00374-008-0272-8.

(48) McCammon, C. A.; Burns, R. G. The oxidation mechanism of vivianite as studied by mossbauer-spectroscopy. *Am. Miner.* **1980**, 65 (3-4), 361-366.

(49) Roldan, R.; Barron, V.; Torrent, J. Experimental alteration of vivianite to lepidocrocite in a calcareous medium. *Clay Min.* **2002**, 37 (4), 709-718. DOI: 10.1180/0009855023740072.

(50) Yu, Z.; Wang, C.; Zou, H.; Wang, H.; Li, H.; Sun, H.; Yu, D. The effects of aerated irrigation on soil respiration and the yield of the maize root zone. *Sustainability* **2022**, 14 (8), 4378.

(51) Powers, K. W.; Palazuelos, M.; Moudgil, B. M.; Roberts, S. M. Characterization of the size, shape, and state of dispersion of nanoparticles for toxicological studies. *Nanotoxicology* **2007**, 1 (1), 42-51.

(52) Hochella, M. F.; Lower, S. K.; Maurice, P. A.; Penn, R. L.; Sahai, N.; Sparks, D. L.; Twining, B. S. Nanominerals, mineral nanoparticles, and earth systems. *Science* **2008**, 319 (5870), 1631-1635. DOI: doi:10.1126/science.1141134.

(53) Zhang, X.; Davidson, E. A.; Mauzerall, D. L.; Searchinger, T. D.; Dumas, P.; Shen, Y. Managing nitrogen for sustainable development. *Nature* **2015**, 528 (7580), 51-59. DOI: 10.1038/nature15743.

(54) Jianjun, C.; Xiangying, W. Controlled-release fertilizers as a means to reduce nitrogen leaching and runoff in container-grown plant production. In Nitrogen in Agriculture, Amanullah, Shah, F. Eds.; IntechOpen, **2018**; p Ch. 3.

(55) Zhu, H.; Zondag, R. H.; Merrick, J.; Demaline, T.; Krause, C. R. Nutrient leaching from container-grown Ornamental tree production. *J. Environ. Hortic.* **2015**, 33 (2), 76-83. DOI: 10.24266/0738-2898-33.2.76.

(56) An, C. C.; Sun, C. J.; Li, N. J.; Huang, B. N.; Jiang, J. J.; Shen, Y.; Wang, C.; Zhao, X.; Cui, B.; Wang, C. X.; et al. Nanomaterials and nanotechnology for the delivery of agrochemicals: strategies towards sustainable agriculture. *J. Nanobiotechnol.* **2022**, 20 (11). DOI: 10.1186/s12951-021-01214-7.

(57) Haydar, M. S.; Ghosh, S.; Mandal, P. Application of iron oxide nanoparticles as micronutrient fertilizer in mulberry propagation. *J. Plant Growth Regul.* **2021**, 41 (4), 1726-1746. DOI: 10.1007/s00344-021-10413-3.

(58) Sabet, H.; Mortazaeinezhad, F. Yield, growth and Fe uptake of cumin (*Cuminum cyminum* L.) affected by Fe-nano, Fe-chelated and Fe-siderophore fertilization in the calcareous soils. *J. Trace Elem. Med. Biol.* **2018**, 50, 154-160. DOI: 10.1016/j.jtemb.2018.06.020.

(59) Martínez-Fernández, D.; Barroso, D.; Komárek, M. Root water transport of *Helianthus annuus* L. under iron oxide nanoparticle exposure. *Environ. Sci. Pollut. Res.* **2016**, 23 (2), 1732-1741. DOI: 10.1007/s11356-015-5423-5.

(60) Ma, X.; Gurung, A.; Deng, Y. Phytotoxicity and uptake of nanoscale zero-valent iron (nZVI) by two plant species. *Sci. Total Environ.* **2013**, 443, 844-849. DOI: 10.1016/j.scitotenv.2012.11.073.

(61) Serag, M. F.; Kaji, N.; Gaillard, C.; Okamoto, Y.; Terasaka, K.; Jabasini, M.; Tokeshi, M.; Mizukami, H.; Bianco, A.; Baba, Y. Trafficking and subcellular localization of multiwalled carbon nanotubes in plant cells. *ACS Nano* **2011**, 5 (1), 493-499. DOI: 10.1021/nn102344t.

(62) Brady, N. C.; Weil, R. R. The nature and properties of soils; Pearson, 2017.

(63) Durand, N.; Monger, H. C.; Canti, M. G.; Verrecchia, E. P. Chapter 9 - Calcium Carbonate Features. In interpretation of micromorphological features of soils and regoliths (Second Edition), Stoops, G., Marcelino, V., Mees, F. Eds.; Elsevier, 2018; pp 205-258.

(64) Basavegowda, N.; Baek, K.-H. Current and future perspectives on the use of nanofertilizers for sustainable agriculture: the case of phosphorus nanofertilizer. *3 Biotech* **2021**, 11 (7), 357. DOI: 10.1007/s13205-021-02907-4.

(65) Lindsay, W. L. Soil and plant relationships associated with iron deficiency with emphasis on nutrient interactions. *J. Plant Nutr.* **1984**, 7 (1-5), 489-500. DOI: 10.1080/01904168409363215.

(66) Awad, F.; Mostafa, M. A.; El-Sebaay, A. S.; El-Ashry, M. S. Effect of wheat root exudates on mobilization of iron and zinc from calcareous soils. *Commun. Soil Sci. Plant Anal.* **1999**, 30 (13-14), 1897-1907. DOI: 10.1080/00103629909370340.

(67) Gypser, S.; Freese, D. Phosphorus release from vivianite and hydroxyapatite by organic and inorganic compounds. *Pedosphere* **2020**, 30 (2), 190-200. DOI: 10.1016/s1002-0160(20)60004-2.

(68) Johnson, S. E.; Loeppert, R. H. Role of organic acids in phosphate mobilization from iron oxide. *Soil Sci. Soc. Am. J.* **2006**, 70 (1), 222-234. DOI: 10.2136/sssaj2005.0012.

(69) Kpomblekou-A, K.; Tabatabai, M. A. Effect of low-molecular weight organic acids on phosphorus release and phytoavailabilty of phosphorus in phosphate rocks added to soils. *Agric. Ecosyst. Environ.* **2003**, 100 (2), 275-284. DOI: 10.1016/S0167-8809(03)00185-3.

(70) Backer, R.; Rokem, J. S.; Ilangumaran, G.; Lamont, J.; Praslickova, D.; Ricci, E.; Subramanian, S.; Smith, D. L. Plant growth-promoting rhizobacteria: Context, mechanisms of action, and roadmap to commercialization of biostimulants for sustainable agriculture. *Front. Plant Sci.* **2018**, 9. DOI: 10.3389/fpls.2018.01473.

(71) Singh, V. K.; Singh, A. K.; Singh, P. P.; Kumar, A. Interaction of plant growth promoting bacteria with tomato under abiotic stress: A review. *Agric. Ecosyst. Environ.* **2018**, 267, 129-140. DOI: 10.1016/j.agee.2018.08.020.

(72) Canarini, A.; Kaiser, C.; Merchant, A.; Richter, A.; Wanek, W. Root exudation of primary metabolites: mechanisms and their roles in plant responses to environmental stimuli. *Front. Plant Sci.* **2019**, 10. DOI: 10.3389/fpls.2019.00157.

(73) Shinde, S.; Cumming, J. R.; Collart, F. R.; Noirot, P. H.; Larsen, P. E. *Pseudomonas fluorescens* transportome is linked to strain-specific plant growth promotion in aspen seedlings under nutrient stress. *Front. Plant Sci.* **2017**, 8. DOI: 10.3389/fpls.2017.00348.

(74) Anderson, A. J.; Hortin, J. M.; Jacobson, A. R.; Britt, D. W.; McLean, J. E. Changes in metal-chelating metabolites induced by drought and a root microbiome in wheat. *Plants* **2023**, 12 (6), 1209.

(75) Bhattacharyya, P. N.; Jha, D. K. Plant growth-promoting rhizobacteria (PGPR): emergence in agriculture. *World J. Microbiol. Biotechnol.* **2012**, 28 (4), 1327-1350. DOI: 10.1007/s11274-011-0979-9.

(76) Phukon, P.; Baruah, J.; Sarmah, D. K.; Bhau, B. S. Green input in agriculture: An overview. In Plant-microbe interactions in agro-ecological perspectives: volume 2: Microbial interactions and agro-ecological impacts, Singh, D. P., Singh, H. B., Prabha, R. Eds.; Springer, 2017; pp 279-305.

(77) Okur, B.; Örçen, N. Chapter 12 - Soil salinization and climate change. In Climate change and soil interactions, Prasad, M. N. V., Pietrzykowski, M. Eds.; Elsevier, 2020; pp 331-350.

(78) Jesus, J. M.; Danko, A. S.; Fiúza, A.; Borges, M.-T. Phytoremediation of salt-affected soils: a review of processes, applicability, and the impact of climate change. *Environ. Sci. Pollut. Res.* **2015**, 22 (9), 6511-6525. DOI: 10.1007/s11356-015-4205-4.

(79) Seleiman, M. F.; Aslam, M. T.; Alhammad, B. A.; Hassan, M. U.; Maqbool, R.; Chattha, M. U.; Khan, I.; Gitari, H. I.; Uslu, O. S.; Roy, R.; et al. Salinity stress in wheat: effects, mechanisms and management strategies. *Phyton-Int. J. Exp. Bot.* **2022**, 91 (4), 667-694. DOI: 10.32604/phyton.2022.017365.

(80) Alcamo, J.; Henrichs, T.; Rosch, T. World water in 2025; World water series report, 2000.

(81) Gleick, P. H. Water and conflict: Fresh water resources and international security. *Int. Secur.* **1993**, 18 (1), 79-112.

(82) Parsons, L. R.; Sheikh, B.; Holden, R.; York, D. W. Reclaimed water as an alternative water source for crop irrigation. *Hortscience* **2010**, 45 (11), 1626-1629. DOI: 10.21273/hortsci.45.11.1626.

(83) Hayes, A.; Mancino, C. F.; Pepper, I. Irrigation of turfgrass with secondary sewage effluent: I. Soil and leachate water quality. *Agron. J.* **1990**, 82 (5), 939-943.

(84) Abdoli, S.; Ghassemi-Golezani, K.; Alizadeh-Salteh, S. Responses of ajowan (*Trachyspermum ammi* L.) to exogenous salicylic acid and iron oxide nanoparticles under salt stress. *Environ. Sci. Pollut. Res.* **2020**, 27 (29), 36939-36953. DOI: 10.1007/s11356-020-09453-1.

(85) Munns, R. Comparative physiology of salt and water stress. *Plant Cell Environ.* **2002**, 25 (2), 239-250. DOI: 10.1046/j.0016-8025.2001.00808.x.

(86) Ghassemi, F.; Jakeman, A. J.; Nix, H. A. Salinisation of land and water resources: Human causes, extent, management and case studies; CAB International, 1995.

(87) Roser, M. Future Population Growth; Published online at OurWorldInData.org, 2019. https://ourworldindata.org/future-population-growth.

(88) Sikder, A.; Pearce, A. K.; Parkinson, S. J.; Napier, R.; O'Reilly, R. K. Recent trends in advanced polymer materials in agriculture related applications. *ACS Appl. Polym. Mater.* **2021**, 3 (3), 1203-1217. DOI: 10.1021/acsapm.0c00982.

(89) Mikula, K.; Izydorczyk, G.; Skrzypczak, D.; Mironiuk, M.; Moustakas, K.; Witek-Krowiak, A.; Chojnacka, K. Controlled release micronutrient fertilizers for precision agriculture - A review. *Sci. Total Environ.* **2020**, 712, 136365. DOI: 10.1016/j.scitotenv.2019.136365.

(90) Sun, C. X.; Shu, K.; Wang, W.; Ye, Z.; Liu, T.; Gao, Y. X.; Zheng, H.; He, G. H.; Yin, Y. H. Encapsulation and controlled release of hydrophilic pesticide in shell cross-linked nanocapsules containing aqueous core. *Int. J. Pharm.* **2014**, 463 (1), 108-114. DOI: 10.1016/j.ijpharm.2013.12.050.

(91) Jia, X.; Ma, Z.-y.; Zhang, G.-x.; Hu, J.-m.; Liu, Z.-y.; Wang, H.-y.; Zhou, F. Polydopamine film coated controlled-release multielement compound fertilizer based on mussel-inspired chemistry. *J. Agric. Food Chem.* **2013**, 61 (12), 2919-2924. DOI: 10.1021/jf3053059.

(92) Liang, W. L.; Yu, A. X.; Wang, G. D.; Zheng, F.; Jia, J. L.; Xu, H. H. Chitosan-based nanoparticles of avermectin to control pine wood nematodes. *Int. J. Biol. Macromol.* **2018**, 112, 258-263. DOI: 10.1016/j.ijbiomac.2018.01.174.

(93) Palmer, J. D.; Brigham, C. J. Feasibility of triacyiglycerol production for biodiesel, utilizing Rhodococcus opacus as a biocatalyst and fishery waste as feedstock. *Renew. Sust. Energ. Rev.* **2016**, 56, 922-928. DOI: 10.1016/j.rser.2015.12.002.

(94) FAO. The state of world fisheries and aquaculture 2018 - Meeting the sustainable development goals; 2018. DOI: ISBN 987-92-5-13053-1.

(95) Jin, X.; Wang, J.; Bai, J. Synthesis and antimicrobial activity of the Schiff base from chitosan and citral. *Carbohydr. Res.* **2009**, 344 (6), 825-829. DOI: DOI: 10.1016/j.carres.2009.01.022.

(96) Younes, I.; Rinaudo, M. Chitin and chitosan preparation from marine sources. Structure, properties and applications. *Mar. Drugs* **2015**, 13 (3). DOI: 10.3390/md13031133.

(97) Veroneze, V.; Martins, M.; Mc Leod, L.; Souza, K. R. D.; Santos, P. R.; Magalhaes, P. C.; Carvalho, D. T.; Santos, M. H.; Souza, T. C. Leaf application of chitosan and physiological evaluation of maize hybrids contrasting for drought tolerance under water restriction. *Braz. J. Biol.* **2020**, 80 (3), 631-640. DOI: 10.1590/1519-6984.218391.

(98) Zhang, G.; Wang, Y. H.; Wu, K.; Zhang, Q.; Feng, Y. N.; Miao, Y.; Yan, Z. M. Exogenous application of chitosan Alleviate salinity stress in lettuce (*Lactuca sativa* L.). *Horticulturae* **2021**, 7 (10). DOI: 10.3390/horticulturae7100342.

(99) Ha, N.; Nguyen, T.; Wang, S.-L.; Dzung, N. Preparation of NPK nanofertilizer based on chitosan nanoparticles and its effect on biophysical characteristics and growth of coffee in green house. *Res. Chem. Intermed.* **2019**, 45. DOI: 10.1007/s11164-018-3630-7.

(100) Wu, L.; Liu, M.; Rui, L. Preparation and properties of a double-coated slow-release NPK compound fertilizer with superabsorbent and water-retention. *Bioresour. Technol.* **2008**, 99 (3), 547-554. DOI: 10.1016/j.biortech.2006.12.027.

(101) Choudhary, R. C.; Kumaraswamy, R. V.; Kumari, S.; Sharma, S. S.; Pal, A.; Raliya, R.; Biswas, P.; Saharan, V. Zinc encapsulated chitosan nanoparticle to promote maize crop yield. *Int. J. Biol. Macromol.* **2019**, 127, 126-135. DOI: 10.1016/j.ijbiomac.2018.12.274.

(102) Deshpande, P.; Dapkekar, A.; Oak, M. D.; Paknikar, K. M.; Rajwade, J. M. Zinc complexed chitosan/TPP nanoparticles: A promising micronutrient nanocarrier suited for foliar application. *Carbohydr. Polym.* **2017**, 165, 394-401. DOI: 10.1016/j.carbpol.2017.02.061.

(103) Beneduzi, A.; Ambrosini, A.; Passaglia, L. M. Plant growth-promoting rhizobacteria (PGPR): their potential as antagonists and biocontrol agents. *Genet. Mol. Biol.* **2012**, 35, 1044-1051.

(104) Spencer, M.; Ryu, C. M.; Yang, K. Y.; Kim, Y. C.; Kloepper, J. W.; Anderson, A. J. Induced defence in tobacco by *Pseudomonas chlororaphis* strain O6 involves at least the ethylene pathway. *Physiol. Mol. Plant Pathol.* **2003**, 63 (1), 27-34. DOI: 10.1016/j.pmpp.2003.09.002.

(105) Kim, M. S.; Kim, Y. C.; Cho, B. H. Gene expression analysis in cucumber leaves primed by root colonization with *Pseudomonas chlororaphis* O6 upon challenge-inoculation with *Corynespora cassiicola*. *Plant Biol.* **2004**, 6 (2), 105-108. DOI: 10.1055/s-2004-817803.

(106) Cho, S. M.; Kang, B. R.; Han, S. H.; Anderson, A. J.; Park, J. Y.; Lee, Y. H.; Cho, B. H.; Yang, K. Y.; Ryu, C. M.; Kirn, Y. C. 2R,3R-butanediol, a bacterial volatile produced by *Pseudomonas chlororaphis* O6, is involved in induction of systemic tolerance to drought in *Arabidopsis thaliana*. *Mol. Plant-Microbe Interact.* **2008**, 21 (8), 1067-1075. DOI: 10.1094/mpmi-21-8-1067.

(107) Dimkpa, C. O.; McLean, J. E.; Britt, D. W.; Anderson, A. J. CuO and ZnO nanoparticles differently affect the secretion of fluorescent siderophores in the beneficial root colonizer, *Pseudomonas chlororaphis* O6. *Nanotoxicology* **2012**, 6 (6), 635-642. DOI: 10.3109/17435390.2011.598246.

(108) Loper, J. E.; Henkels, M. D.; Rangel, L. I.; Olcott, M. H.; Walker, F. L.; Bond, K. L.; Kidarsa, T. A.; Hesse, C. N.; Sneh, B.; Stockwell, V. O.; et al. Rhizoxin analogs, orfamide A and chitinase production contribute to the toxicity of *Pseudomonas protegens* strain Pf-5 to Drosophila melanogaster. *Environ. Microbiol.* **2016**, 18 (10), 3509-3521. DOI: 10.1111/1462-2920.13369.

(109) Rathore, R.; Vakharia, D. N.; Rathore, D. S. In vitro screening of different *Pseudomonas fluorescens* isolates to study lytic enzyme production and growth inhibition during antagonism of *Fusarium oxysporum* f. sp. cumini, wilt causing pathogen of cumin. *Egypt. J. Biol. Pest Control* **2020**, 30 (1), 57. DOI: 10.1186/s41938-020-00259-4.

(110) Ruiu, L.; Mura, M. E. Oral toxicity of *Pseudomonas protegens* against muscoid flies. *Toxins* **2021**, 13 (11), 772. DOI: 10.3390/toxins13110772.

(111) Mendonca, C. M.; Yoshitake, S.; Wei, H.; Werner, A.; Sasnow, S. S.; Thannhauser, T. W.; Aristilde, L. Hierarchical routing in carbon metabolism favors iron-

scavenging strategy in iron-deficient soil Pseudomonas species. *Proc. Natl. Acad. Sci.* **2020**, 117 (51), 32358-32369. DOI: 10.1073/pnas.2016380117.

(112) Rathore, A. S.; Gupta, R. D. Chitinases from bacteria to human: Properties, applications, and future perspectives. *Enzyme Res.* **2015**, 2015, 791907. DOI: 10.1155/2015/791907.

(113) Keyhani, N. O.; Roseman, S. Physiological aspects of chitin catabolism in marine bacteria. *Biochim. Biophys. Acta-Gen. Subj.* **1999**, 1473 (1), 108-122. DOI: DOI: 10.1016/S0304-4165(99)00172-5.

(114) Gortari, M. C.; Hours, R. A. Fungal chitinases and their biological role in the antagonism onto nematode eggs. A review. *Mycol. Prog.* **2008**, 7 (4), 221-238. DOI: 10.1007/s11557-008-0571-3.

CHAPTER 2

Synthesis of nano-sized metavivianite and nano-sized chitosan-coated metavivianite and their solubility in a calcareous soil saturated paste extract with soil microbe inoculation

2.1 Abstract

Iron (Fe) plays a critical role in the metabolic processes of plants, but its deficiency is a common issue in calcareous soils, primarily due to high pH and carbonate levels. Traditional approaches to mitigate Fe deficiency often involve the use of synthetic Fe-chelates, which are effective but have raised concerns regarding their potential for mobilization and leaching. This leaching can reduce both the efficiency and cost-effectiveness of these fertilizers as well as threaten groundwater. In response, there is growing interest in nano-sized fertilizers designed to target the rhizosphere more effectively. In this context, nano-metavivianite ($Fe^{II}Fe_2^{III}(PO_4)_2(OH)_2 \cdot 6H_2O$; metaVT) has emerged as a promising alternative for Fe supplementation in plants. Previous studies have shown the effectiveness of bulk metaVT on plants grown on calcareous soil for mitigating Fe efficiency. However, other studies have reported the extremely low solubility of bulk metaVT ($Ksp=10^{-36}$) in dilute electrolyte solutions, such as $CaCl_2$. The cause of the discrepancy in the results of bulk metaVT from pure laboratory conditions and field application remains unclear. Since the solubility of Fe in soils is strongly affected by pH and the chelation of Fe^{III} with organic ligands, the current study explores the solubility of nano-sized metavivianite (nano-metaVT) and nano-sized chitosan-coated metaVT (nano-CT-metaVT) in a diluted electrolyte solution (KCl) and a calcareous soil-saturated paste extract (SPE). SPE contains compounds relevant to the soil, including

LMWOAs, amino acid, fulvic acid, and humic acid. The effects of inoculation with

beneficial soil microbes, specifically *Pseudomonas chlororaphis* O6 (*Pc*O6) and

Pseudomonas protegens Pf-5 (*Pp* Pf-5) were also investigated. Our findings highlight the

key factors that affect the solubility of nano-metaVT and nano-CT-metaVT, including the

CT coating on the nano-fertilizers, the presence of soil microbes, and organic ligands.

The presence of CT coating enhanced the solubility of nano-CT-metaVT in SPE

suspensions. Moreover, *Pp* Pf-5 inoculation significantly influences the solubilities of

both nano-metaVT and nano-CT-metaVT, increasing the total soluble Fe concentration in

SPE suspensions by not only lowering the environmental pH but also involving other

mechanisms, which remain unclear. The study provides insights into the potential

application of nano-metaVT and nano-CT-metaVT by analyzing the characterization,

solubility, and impact of soil microbe inoculation on both nano-metaVT and nano-CT-

metaVT in SPE suspension.

Keywords: calcareous soil, chitosan coating, metavivianite, *Pseudomonas chlororaphis*

O6, *Pseudomonas protegens* Pf-5, solubility

2.2 Introduction

Iron (Fe) is a critical micronutrient in plant growth and is involved in key

metabolic processes, including photosynthesis, chlorophyll biosynthesis, and respiration.

[1-3] Fe deficiency frequently occurs in calcareous soils due to the rapid formation of iron

hydroxides.[4] Currently, the most common agricultural approach is to apply synthetic Fe-

chelates to alleviate the Fe deficiency. However, when Hernandez-Apaolaza and Lucena

(2011) evaluated the soluble and retained fractions of Fe-EDDHA in a 50-cm long soil

column (sandy loam, pH 7.7), they found that over 25% of Fe-o,o-EDDHA was leached

from the soil columns within ten days.[5] Thus, the search for eco-friendly Fe fertilizers continues. [4] Metavivianite ($Fe^{II}Fe_2^{III}(PO_4)_2(OH)_2 \cdot 6H_2O$; metaVT), a partially-oxidized iron phosphate mineral, is stable in aerobic conditions[6] and can be recovered from phosphorus-rich secondary sewage effluent. [7-9] MetaVT is gaining attention for its potential to supply bioavailable Fe in calcareous soils. [10-12]

Besides the Fe deficiency in calcareous soils, the inefficiency of nutrient use and overuse of chemical fertilizers cause problems such as diminished crop yields and soil health degradation worldwide.[13] Nano-fertilizers have emerged as a possible solution, offering increased efficiency, reduced dosing, and minimized leaching and volatilization risks.[14] Nano-fertilizers, with their high surface area-to-volume ratio, present unique properties compared to bulk fertilizers, potentially enhancing sustainable agricultural practices. Adding a functional coating on the nano-fertilizer particles is another approach to improve their utilization efficiency. Chitosan (CT) is a polysaccharide that can be extracted from crustacean shells, insect shells, and fungi and is being used in diverse fields due to its biodegradability, cost-effectiveness, and biocompatibility. [15, 16] CT coatings can enhance nutrient release control, improve utilization, and reduce fertilizer loss, making CT an ideal coating material for nano fertilizers. [17] This study modified nano-metaVT's surface with CT to provide an insoluble coating in alkaline conditions and create a positively charged surface that might enhance the retention of nano-CT-metaVT in soil.

Previous studies have highlighted the low solubility ($Ksp = 10^{-36}$) of bulk VT in suspension systems, such as $CaCl_2$ and $CaSO_4$ solutions.[18] Interestingly, when applied to calcareous soil, bulk VT has been effective in addressing iron deficiencies in various

plants, including olive (*Olea europaea* L.) trees[19] and lemon trees (*Citrus lemon* L.).[10] The apparent discrepancy between the solubility in pure electrolyte suspensions and real soil applications, as reported in previous studies, may be due to the influence of organic compounds such as humic acid, fulvic acid, low molecular weight organic acids, and amino acids, which are present in soil solutions and known to impact the solubility of metals.[20, 21]

Beyond these organic components, soil microbes also play a significant role in influencing solubility. Soil microorganisms, particularly plant growth-promoting rhizobacteria (PGPR), are crucial in the soil ecosystem. They colonize the rhizosphere and enhance plant health and yield through various mechanisms, including improving nutrient bioavailability and producing siderophores.[22] Some PGPR species assimilate iron by producing Fe-chelating siderophores, which transport iron into their cells and significantly affect Fe solubility in soil solutions.[23] *Pseudomonas chlororaphis* O6 (*Pc*O6) and *Pseudomonas protegens* Pf-5 (*Pp* Pf-5) are PGPRs that are reported to have several beneficial effects on plant growth and health and are known for producing the siderophore, pyoverdine (Pvd). *Pp* Pf-5 also produces the siderophore, enantio-pyochelin (E-Pch)[24], though it has a lower Fe affinity ($K_a = 2 \times 10^5$ M^{-1} for E-Pch vs. $K_a = 10^{32}$ M^{-1} for Pvd).[25-27] Moreover, Loper et al. (2016) verified by genomic sequence analysis that *Pp* Pf-5 can produce the enzyme chitinase, which degrades chitin.[28] This study adopted *Pc*O6 and *Pp* Pf-5 to compare nano-metaVT and nano-CT-metaVT solubility since they both acquire Fe and have the ability to produce siderophores. In addition, *Pp* Pf-5 has been reported to produce chitinase, which might affect the CT coating by decomposing chitosan, then alter the solubilities of nano-metaVT and nano-CT-metaVT.

In summary, several key aspects of nano-metaVT and nano-CT-metaVT are yet to be fully understood, including 1) the influence of CT coating on solubility of nano-metaVT, 2) the impact of organic compounds relevant to soil on solubilities of nano-metaVT and nano-CT-metaVT, and 3) the effects of soil microbe inoculation, on solubilities of nano-metaVT and nano-CT-metaVT. The SPE-suspension system is used to investigate the key factors that might affect the solubilities of the nano-metaVT and nano-CT-metaVT. We hypothesize that nano-metaVT and nano-CT-metaVT have low solubility in KCl and SPE suspensions. Moreover, nano-CT-metaVT is less soluble than nano-metaVT in KCl but more soluble than nano-metaVT in SPE because of the characteristics of CT coating. Lastly, Pp Pf-5 and *Pc*O6 affect the solubilities of nano-metaVT and nano-CT-metaVT in SPE suspensions. This investigation aims to gain insight into the preliminary application of nano-metaVT and nano-CT-metaVT and the potential effects of soil-dwelling microbes.

2.3 Materials and Methods

2.3.1 Chemical reagents

Monoammonium phosphate $[(NH_4)H_2PO_4]$, iron (II) sulfate heptahydrate $(FeSO_4 \cdot 7H_2O)$ (ACS reagent, $\geq 99.0\%$), and chitosan (from shrimp shells, $\geq 75\%$ deacetylated) were purchased from MilliporeSigma (Burlington, MA, USA). Sodium hydroxide (NaOH) was purchased from Mallinckrodt (UK). All reagents used in this study were reagent grade or better.

2.3.2 Synthesis of nano-metaVT and nano-CT-metaVT

Nano-metaVT was synthesized based on the protocols described by Ammari and Hattar (2011).[10] The synthesis was conducted in an ice bath in an argon gas chamber to eliminate oxygen and allow ferrous ions to be present. Five-gram monoammonium phosphate [$(NH_4)H_2PO_4$] was dissolved in 200 mL deionized water to form a solution with a PO_4^{3-} concentration of 0.217 mol L^{-1}. After stirring for 30 min, 15 g ferrous sulfate ($FeSO_4 \cdot 7H_2O$) was slowly added to the solution to create a solution with a Fe concentration of 0.270 mol L^{-1}. The solution was kept stirring for 30 min. Then, the pH of the suspension was adjusted to pH 6.5 by dropwise additions of 0.00125 mol L^{-1} NaOH. A pale-blue, vivianite precipitate was washed several times with deionized water until the EC of the mixture was below 0.2 dS·m^{-1}. The precipitate was then centrifuged at 6,000 × g for 15 min, the supernatant liquid decanted, and the pellet dried in a freeze-dryer (FreeZone Benchtop Freeze Dryer, Labconco, Kansas City, MO, USA).

A chitosan (CT) solution was prepared by dissolving one gram of CT in 200 mL 0.1 mol L^{-1} acetic acid (CH_3COOH) while stirring. After 12 h, four grams of metavivianite powder was slowly added to the CT solution and stirred for an additional 30 min. The pH of the suspension was adjusted to 6.5 by adding 0.00125 mol L^{-1} NaOH. The nano-CT-metaVT precipitate was then rinsed with deionized water until salt-free ($<$ 0.2 dS·m^{-1}). Finally, the precipitate was centrifuged at 6,000 × g for 15 min, the supernatant liquid was decanted, and the pellet freeze-dried.

2.3.3 Nano-MetaVT and nano-CT-metaVT characterization

2.3.3.1 Particle thickness, morphology, and elemental presence

The nano-metaVT and nano-CT-metaVT powders were fixed onto aluminum stubs for scanning electron microscopy (SEM) analysis using copper tape. The samples were sputter-coated with a 10-nm layer of gold and palladium using a rotary sputter coater system EMS150R ES (Electron Microscopy Sciences, Hatfield, PA, USA). The morphology and the thickness of the particles were viewed with a SEM (Quanta FEG 650, Field Electron and Ion Company, Hillsboro, OR, USA) under a high vacuum at an accelerating voltage of 20 kV. The thickness of the nano-metaVT and nano-CT-metaVT crystals was measured with image processing software (Image J, version 1.53). Three images each were used to measure the thickness of nano-metaVT and nano-CT-metaVT when viewed at ten random locations. The instrument was equipped with energy-dispersive X-ray spectroscopy (EDS, Oxford Instruments, Abingdon-on-Thames, UK) using an X-Max detector at an accelerating voltage of 5 kV to identify elements present.

2.3.3.2 Zeta potential

The zeta potentials of the nano-metaVT and nano-CT-metaVT particles were measured using an electrophoretic light scattering instrument (Zetaplus, Brookhaven Instruments Corporation, Holtsville, NY, USA). Samples were prepared in 0.0001 mol/L KCl, forming a 0.4 g L^{-1} suspension, and analyzed at 25 °C in triplicate.

2.3.3.3 Crystalline structure

X-ray diffraction (XRD) patterns were obtained using X-ray Diffractometers. The 0-year nano-metaVT and nano-CT-metaVT were analyzed at Utah State University

(Panalytical X'Pert Pro X-ray diffraction spectrometer, Malvern Panalytical, Malvern, UK), and 1-year and 2-year nano-mataVT and nano-CT-metaVT were analyzed at the University of Utah (D8 Discover diffraction spectrometer, Bruker, Billerica, MA, USA). The fine nano-metaVT and nano-CT-metaVT powders were kept on a zero-diffraction plate for analysis. XRD data were collected with a 2θ diffraction angle from 20° to 80°, with a 0.02° step size, 0.4 seconds per step count time.

2.3.3.4 Elemental analysis

The N, C, H, and O compositions of the nano-metaVT and nano-CT-metaVT nanoparticles were analyzed with an elemental analyzer (Vario EL cube, Elementar, Cheadle, UK). A 1–1.5 mg sample was packed into a tin capsule and placed in the automated sampler of the device. The sample was burned in a flow of oxygen at temperatures up to 1200 °C. The gases formed were successively passed through oxidizing and reducing tubes and adsorption columns, each of which was intended to identify the gas mixture components (CO_2, H_2O, and SO_2).

2.3.3.5 Surface analysis

To identify nano-metaVT and nano-CT-metaVT surface elements, X-ray photoelectron spectroscopy (XPS) was performed with a photoelectron spectroscopy system (PHI 5000 Versa Probe II, ULVAC-PHI, Kanagawa, Japan). Monochromated Al Kα (1486.6 eV) radiation with an operating power of 50 W (15 kV voltage) was used for all the XPS measurements. The XPS survey spectra were measured with a pass energy of 117.4 and 0.125 eV energy steps. For the measurement of each atomic element, a pass energy of 23.5 with 0.025 eV energy steps was used.

2.3.3.6 Specific surface area

The specific surface area was analyzed by nitrogen adsorption according to the Brunauer-Emmett-Teller (BET) equation (ASAP 2020, Micromeritics, Norcross, GA, USA). The de-gas temperature was set at 60 ℃ for 12 h (Colombo et al., 2017; Oliveira et al., 2017).

2.3.4 Characterization of soil

A Millville series soil (coarse-silty, carbonatic, mesic Typic Haploxerolls) soil was used in this study. The soil (0–10 cm depth) was collected from USU Greenville Research Farm in North Logan, UT, USA, in April 2020, from conventionally managed wheat breeding plots irrigated and planted in a wheat-alfalfa rotation. We refer to the soil as AgrM (Agricultural Milleville) in this article and previous publications.[29-31] The soil characteristics, including soil texture, particle size distribution, pH, EC, organic matter content, calcium carbonate equivalent, dissolved organic carbon (DOC), cation exchange capacity, phosphorus, potassium, ammonium, nitrate, sulfate, and other element concentrations were analyzed using Standard Methods for the Western Region.[32] Soil characteristics are provided in Table 2-1. The AgrM soil is not typically characterized as Fe-deficient, with a DTPA-extractable Fe concentration of 6 mg kg^{-1} soil, which is above the generally recommended Fe level of 5 mg kg^{-1} soil for winter wheat. However, Gerwing and Gelderman (2023) noted that Fe deficiencies can become more pronounced when the soil is wet and cold.[33] Therefore, a DTPA-extractable Fe concentration close to the recommended dose, may still be marginal for crops particularly sensitive to Fe deficiency, like beans, or seasonally following early spring snowmelt.

Table 2-1. Characteristics of soil sampled from 0–10 cm.

Characteristics	
Location	N 41.76346° W 111.81396°
Elevation	1369 m
Soil abbreviation	AgrM
Soil series, texture	Millville, silt loam
Taxonomic class	Coarse-silty, carbonatic, mesic Typic Haploxerolls
Particle size distribution (% sand/silt/clay)	22/56/23
Management	Irrigated commercial-style production
Crops	Winter wheat and small grain breeding trials in rotation with alfalfa
pH$_{saturated\ paste\ extract}$	8.4
EC$_e$ (dS·m^{-1})	0.4
DTPA – Fe (mg kg^{-1})	6.0
DTPA – Cu (mg kg^{-1})	1.0
DTPA – Mn (mg kg^{-1})	12.3
DTPA – Zn (mg kg^{-1})	1.1

EC$_e$: Electrical conductivity of saturated paste extract

2.3.5 Preparation and characterization of soil saturated paste extracts (SPE)

About 90 mL double-deionized water (resistance >18 MΩ cm) was added to 250 g soil in a 250 mL polycarbonate centrifuge bottle (Nalgene™) to form a saturated paste. The mixture was mixed well with a spatula and allowed to stand for 18 hours. Then water was added as necessary, and the soil paste was centrifuged at 4,608 × g for 25 min. The supernatant was filtered through a 25 mm nylon syringe filter with a pore size of 0.22 µm (Thermo Scientific, Waltham, MA, USA). Characteristics of the SPE after 0.2-micron filter sterilization are presented in Tables 2-2, 2-3, and 2-4. The cations were analyzed by an inductively coupled plasma mass spectrometer (Agilent 7700x, Agilent Technologies, Santa Clara, CA, USA). Anions were analyzed by ion chromatography (Dionex method 123) with a Dionex ICS-3000 (ThermoFisher Scientific). Amino acids (AAs) were analyzed by liquid chromatography triple quadrupole mass spectrometry (LC-QqQ-MS) (Agilent 1290 LC coupled with Agilent 6490 QqQ-MS, Agilent Technologies, Santa Clara, CA, USA) with an Imakt amino acid column (50 x 3 mm). Soluble elements were analyzed using the EPA method 6020 on an inductively coupled plasma mass spectrometer (Agilent 7700x, Agilent Technologies, Santa Clara, CA, USA).

Table 2-2. Total soluble elemental analysis of initial SPE (Day 0) and various SPE suspensions after 7 days.

Total soluble elements	Day 0	Day 7			
	SPE	metaVT-SPE	CT-metaVT-SPE	metaVT-SPE with *Pp* Pf-5	CT-metaVT-SPE with *Pp* Pf-5
Al (μg L^{-1})	17.5 ± 4.5	5.3 ± 2.6	5.9 ± 4.8	9.7 ± 3.2	8.9 ± 3.4
As (μg L^{-1})	6.1 ± 0.4	3.7 ± 0.3	3.6 ± 0.2	3.8 ± 0.1	3.8 ± 0.1
Ba (μg L^{-1})	47.4 ± 3.9	1.3 ± 0.2	1.1 ± 0.1	1.1 ± 0.3	1.0 ± 0.2
Ca (mg L^{-1})	73.8 ± 6.1	68.7 ± 5.5	69.6 ± 2.7	70.1 ± 3.8	71.7 ± 0.5
Cd (μg L^{-1})	0.1 ± 0.03	< DL	< DL	< DL	< DL
Co (μg L^{-1})	2.1 ± 0.5	1.1 ± 0.1	1.1 ± 0.1	1.3 ± 0.2	1.2 ± 0.1
Cr (μg L^{-1})	0.9 ± 0.05	0.7 ± 0.04	0.6 ± 0.02	0.6 ± 0.03	0.7 ± 0.02
Cu (μg L^{-1})	23.4 ± 5.6	16.8 ± 1.6	15.1 ± 1.6	18.7 ± 4.3	16.9 ± 4.2
Fe (μg L^{-1})	21.3 ± 7.2	30.3 ± 3.0	33.8 ± 4.2	36.7 ± 3.4	44.6 ± 7.0
K (mg L^{-1})	4.6 ± 0.5	4.0 ± 1.8	5.2 ± 0.4	3.2 ± 0.2	5.0 ± 0.7
Mg (mg L^{-1})	10.6 ± 0.8	10.2 ± 0.6	10.3 ± 0.5	9.8 ± 0.5	9.7 ± 0.8
Mn (μg L^{-1})	94.1 ± 41.5	0.5 ± 0.3	1.0 ± 1.0	0.8 ± 0.3	2.2 ± 1.9
Na (mg L^{-1})	5.3 ± 0.4	3.6 ± 0.3	3.9 ± 0.1	3.7 ± 0.1	3.9 ± 0.1
Ni (μg L^{-1})	7.5 ± 1.6	5.8 ± 0.3	5.7 ± 1.8	7.1 ± 2.4	5.3 ± 0.2
P (μg L^{-1})	556 ± 49	576 ± 40	665 ± 49	596 ± 36	653 ± 32
Pb (μg L^{-1})	0.10 ± 0.08	0.04 ± 0.03	0.03 ± 0.04	0.04 ± 0.02	0.04 ± 0.03
Sb (μg L^{-1})	2.3 ± 0.4	2.3 ± 0.3	2.3 ± 0.3	2.3 ± 0.4	2.4 ± 0.2
Si (mg L^{-1})	14.0 ± 1.3	12.9 ± 1.1	13.0 ± 0.7	15.0 ± 0.3	15.3 ± 0.5
Sr (μg L^{-1})	100.4 ± 4.4	81.5 ± 7.1	81.6 ± 4.7	76.2 ± 5.6	76.4 ± 5.6
Tl (μg L^{-1})	0.04 ± 0.01	0.02 ± 0.01	0.01 ± 0.01	0.01 ± 0.01	0.01 ± 0.002
V (μg L^{-1})	6.4 ± 0.5	3.5 ± 0.5	3.2 ± 0.4	3.7 ± 0.1	3.5 ± 0.1
Zn (μg L^{-1})	16.5 ± 7.3	9.3 ± 5.4	7.2 ± 4.6	15.9 ± 2.8	13.9 ± 3.6

< DL: lower than the detection limit

Table 2-3. LMWOAs and AAs analyses of initial SPE (Day 0) and various SPE suspensions after 7 days.

LMWOAs	Day 0	Day 7			
	SPE	metaVT-SPE	CT-metaVT-SPE	metaVT-SPE with *Pp* Pf-5	CT-metaVT-SPE with *Pp* Pf-5
Humic acids (mg L^{-1} C)	27.4 ± 3.1	16.0 ± 1.3	16.0 ± 3.1	12.2 ± 5.0	9.3 ± 4.4
Fulvic acids (mg L^{-1} C)	73.4 ± 8.1	66.9 ± 5.5	71.6 ± 4.1	68.5 ± 2.3	69.1 ± 3.9
Gluconate (mg L^{-1})	2.52 ± 0.11	2.51 ± 0.05	2.56 ± 0.08	2.65 ± 0.15	2.59 ± 0.07
Oxalate (mg L^{-1})	0.05 ± 0.02	0.04 ± 0.01	0.20 ± 0.27	0.17 ± 0.24	0.04 ± 0.01
Arginine (mg L^{-1})	0.07 ± 0.01	0.08 ± 0.01	0.06 ± 0.00	0.06 ± 0.00	0.06 ± 0.01

< DL: lower than the detection limit

2.3.6 Solubility of nano-metaVT and nano-CT-metaVT in a suspension system

This experiment evaluated the solubilities of nano-metaVT and nano-CT-metaVT in a dilute KCl solution and SPE. *Pc*O6 is a soil bacterium isolated from field-grown winter wheat in Logan, Utah. *Pp* Pf-5 (ATCC BAA-477) was purchased from the American Type Culture Collection (ATCC). All the experiments were conducted in a continuous suspension system on a shaker table. Measurements for each sample bottle and structured were collected daily using a randomized complete block design (RCBD) with three trials (block) per treatment. Each trial (block) contained three replicates, yielding nine experimental units (n = 9). s

The variables were KCl electrolyte/SPE, nano-metaVT/ nano-CT-metaVT, and the presence/absence of *Pc*O6/*Pp* Pf-5 in SPE. The 0.003 mol L^{-1} KCl solution was autoclaved, and SPE was filter-sterilized through a 0.2 µm nylon filter. The doses of nano-metaVT and nano-CT-metaVT were 0.6 g L^{-1} in solution based on total particle mass. We calculated the amount of mass CT contributes to the overall mass from the particle digestion results. The result shows that CT contributes about 1.8% of the overall mass of nano-CT-metaVT. In the treatments with soil microbes, *Pc*O6 and *Pp* Pf-5 were added to the 99 mL KCl electrolyte or SPE as 1.0 mL aliquots of a 2×10^6 CFU mL^{-1} bacterial suspension. The final bacterial concentration was about 2×10^4 CFU mL^{-1}. All the reaction suspensions in sterile polypropylene 250-mL bottles were placed in a cardboard box on an end-to-end shaker and kept shaking at 100 rpm in the dark throughout the reaction process. At each sampling time point (0, 1, 2, 3, 4, 5, 6, and 7 days), each bottle was placed on a magnetic stirrer and mixed to keep the particles in suspension. One mL of the sample with *Pc*O6/*Pp* Pf-5 treatments was series-diluted and

cultured on Luria–Bertani agar (LB) or tryptic soy agar (TSA) plates, respectively, to verify the bacterial concentrations. Then, a 10 mL suspension was placed in a polyallomer centrifuge tube (Nalgene™, Thermo Fisher Scientific, Waltham, MA, USA), and pH and EC were measured. Then, the suspension was centrifuged at $20,800 \times g$ for 30 minutes to remove the particle larger than 30 nm, filtering through a 25 mm nylon syringe filter with a pore size of 0.22 µm (Thermo Scientific) and acidifying to 0.5% HNO_3. Since the particle sizes of both nano-metaVT and nano-CT-metaVT are micro-sized in two dimensions and nano-sized in one dimension, the centrifugation and filtration processes likely removed any nano-metaVT and nano-CT-metaVT particles. Finally, the total soluble Fe and P concentrations of the samples were analyzed by an inductively coupled plasma mass spectrometer (Agilent 7700x, Agilent Technologies).

2.3.7 Geochemical modeling

We used the geochemical speciation software, Visual MINTEQ Ver. 3.1 [32], to investigate the comparison between the experimental and predicted solubility, the potential chemical complexes in SPE suspension, and how pH changes affect VT solubility predicted by the software. Both FA and HA were simulated using the NICA-Donnan FA/HA model, which is an integral component of Visual MINTEQ Ver. 3.1. Sparks (2023) previously expanded the geochemical database's stability constants, which were taken into account.[30] The composition of the SPE served as the basis for the model's input solution phase. This simulated solution phase was then employed to predict potential ligand complexes in the SPE. The input information is shown in Table 2-4.

Table 2-4. The input in the geochemical modeling for vivianite-KCl and vivianite-SPE solubilities and potential chemical complexes prediction.

Input	Values
Solution	KCl
pH	pH value measured on Day 7
Ionic strength	To be calculated
CO_2	42 ppm
Total soluble elements	Table B2-1
Finite solid	Vivianite 0.001196 mol/L
Settings	Oversaturated solids are not allowed to precipitate
	(Exceptions: Solid specified as infinite, finite, or possible)
Solution	SPE
pH	pH value measured on Day 7
Ionic strength	To be calculated
CO_2	42 ppm
Total soluble elements	Table 2-2
LMWOAs and AAs	Table 2-3
DOC parameters	NICA Donnan for SPE
Finite solid	Vivianite 0.001196 mol/L
Settings	Oversaturated solids are not allowed to precipitate
	(Exceptions: Solid specified as infinite, finite, or possible)

We utilized the geochemical speciation model Visual MINTEQ Ver. 3.1 [32] to simulate the solution phase when undergoing the titration process. The input information is shown in Table 2-5.

Table 2-5. The input in the geochemical modeling for predicting the pH effect on vivianite-SPE solubility.

Input	Values
pH	Calculated from the mass and charge balance
Ionic strength	To be calculated
CO_2	42 ppm

DOC parameters	NICA Donnan for SPE
Total soluble elements	Table 2-2
LMWOAs and AAs	Table 2-4
Finite solid	Vivianite 0.001196 mol/L
Settings	Oversaturated solids are not allowed to precipitate (Exceptions: Solid specified as infinite, finite, or possible)
Volume of solution to be titrated	100 a.u.
Volume of titrant	0.1
Concentration unit of titrant	mol L^{-1}
Titrant composition	0.1 mol L^{-1} HNO$_3$

2.3.8 Data Analyses

We evaluated the changes in pH, EC, and total soluble Fe and P concentrations over time under each treatment using a mixed-effects model with repeated measures. In the mixed model treatment, time and its interactions are fixed effects, while block is a random effect. Correlations among the repeated measurements were estimated with compound symmetry structure. The rate of change (slope) due to time was estimated for each treatment and compared. Treatment difference at each experimented time point was also tested for significance. The significance level was set at 0.05. Diagnostics of residuals did not reveal a departure from normality and nonconstant variances. All statistical analyses were performed using SAS® Studio (release 3.81, SAS Inc., Cary, NC, USA).

2.4 Results and Discussions

2.4.1 Characterization of nano-metaVT and nano-CT-metaVT

The X-ray diffraction (XRD) patterns of nano-metaVT and nano-CT-metaVT are depicted in Figs. 2-1a and 2-1b, showing distinct major diffraction peaks. These peaks occur at 2θ angles of 11.2°, 13.2°, 18.1°, 19.4°, 23.1°, 27.8°, and 29.9° and correspond to the (110), (020), (200), (-101), (101), (031), and (-301) crystal faces of $Fe_3(PO_4)_2 \cdot 8H_2O$. These data confirm the crystalline nature and specific crystallographic structure of the nano-metaVT and nano-CT-metaVT materials. Repeated XRD analyses of the nano-metaVT and nano-CT-metaVT particles at the end of all the experiments (0, 1, and 2 years) reveal no significant changes in particle composition. As shown in Fig. 2-1c and 1d, SEM images reveal that nano-metaVT and nano-CT-metaVT particles possess feather-like structures comprising a multilayered, nano-plate composite. The specific surface area of nano-metaVT and nano-CT-metaVT are 13.9 and 14.5 m^2 g^{-1}, respectively. To analyze these structures further, ten spots on the nano-plates were randomly selected for thickness measurements. The measurements were conducted using Image J software (version 1.53). The analyses show that the average thickness of the nano-plates in nano-metaVT is 24.9 ± 5.4 nm, while for nano-CT-metaVT, it is 38.9 ± 7.6 nm. The increased thickness of the nano-CT-metaVT is attributable to the chitosan coating, which adds to the overall dimensions of the nano-plates.
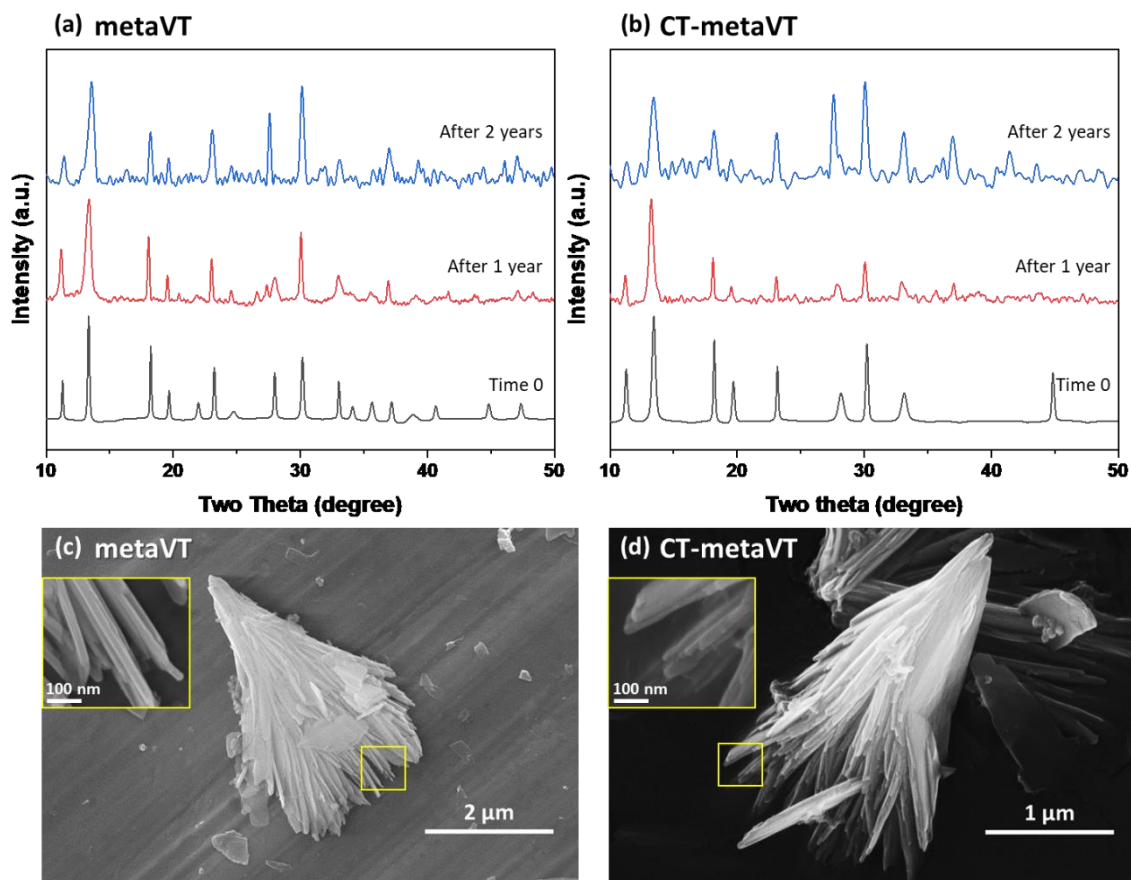
Figure 2-1. XRD pattern of nano-metaVT (a) and nano-CT-metaVT (b) analyzed at different times (0, 1, and 2 years). The 0-year samples were analyzed at Utah State University (Panalytical X'Pert Pro X-ray diffraction spectrometer, Malvern Panalytical Ltd, England), and 1-year and 2-year samples were analyzed at the University of Utah (D8 Discover diffraction spectrometer, Bruker, Billerica, MA, USA). SEM images of nano-metaVT (c) and nano-CT-metaVT (d) were observed after being freeze-dried.

Table 2-6 presents the analyses of nitrogen (N), carbon (C), hydrogen (H), and

oxygen (O) in the studied materials. It is observed that nano-CT-metaVT exhibits an

approximately 2.3 times higher N content and 21.8 times higher C content than uncoated

nano-metaVT. This significant increase in the N and C contents of nano-CT-metaVT can

be attributed to the presence of glucosamine in the CT coating. Additionally, surface

charge measurements reveal that nano-metaVT displays a negatively charged surface,

with a zeta potential of -14.6 ± 5.6 mV, whereas nano-CT-metaVT exhibits a positively

charged surface of 22.0 ± 2.8 mV. This difference in the surface charges of the two

particles further supports that CT coated the nano-metaVT surface. The design of nano-

CT-metaVT, with its positively charged surface, is intended to enhance its persistence in

a soil environment through electrostatic attraction to the typically negatively charged soil

particles. This characteristic could be critical for the prolonged availability of nutrients in

the soil and to slow potentially high leaching rates. Furthermore, the CT coating on the

nano-CT-metaVT may serve as a carbon source for soil microorganisms, potentially

influencing the subsequent microbial degradation processes in the soil ecosystem. This

aspect of the nano-CT-metaVT particles could have significant implications for its role in

nutrient cycling and soil health.

Table 2-6. N, C, H, and O contents and the zeta potential of nano-metaVT and nano-CT-metaVT.

	Elemental analysis (%)				Zeta potential (mV)
	N	C	H	O	
nano-metaVT	0.14	0.06	2.26	22.90	-14.6 ± 5.6
nano-CT-metaVT	0.32	1.31	2.59	24.61	22.0 ± 2.8

The results from the XPS and zeta potential analyses provide compelling evidence for the presence of a CT coating on nano-metaVT. These methods effectively identify the surface chemical composition and the positive surface charge characteristic of the chitosan coating. The specific XPS signals of the N 1s region, presented in Fig. 2-1a, elucidate peaks at 399.0–399.3 eV, corresponding to the assignments of -NH$_2$ and NH groups, respectively.[34, 35] Fig. 2-2b displays the XPS signals of the Fe 2p region for both nano-metaVT and nano-CT-metaVT and the peak of Fe 2p3/2 at 711–712 eV, which indicates that both Fe^{2+} and Fe^{3+} are present in the nano-metaVT and nano-CT-metaVT.[36] In Fig. 2-2c, the observable peaks at 135 eV are attributed to P-O.[37] These Fe 2p3 and P 2p spectra reveal an overall higher intensity of Fe and P signals for nano-metaVT compared to nano-CT-metaVT. This difference in signal intensity can be attributed to the variation in surface composition due to the CT coating. This reduction in spectral intensity suggests a screening effect caused by the CT coating. In essence, the presence of the CT layer on the surface of the nano-metaVT particles partially obscures the underlying Fe and P elements, leading to a diminished intensity in their respective spectral peaks.
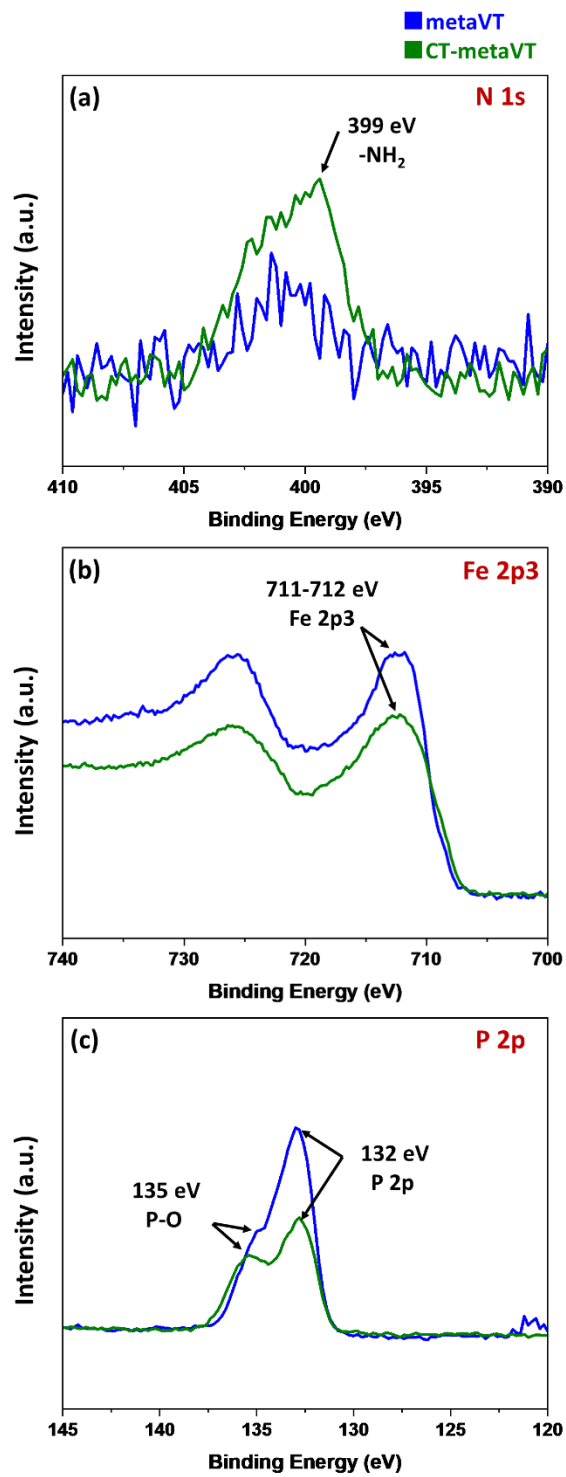
Figure 2-2. XPS spectra of N 1s (a), Fe 2p3 (b), and P 2p (c) in nano-metaVT and nano-CT-metaVT.

2.4.2 Solubility of nano-metaVT and nano-CT-metaVT

2.4.2.1 Solubility in KCl and SPE suspensions

The solubility of Fe in soils is strongly affected by pH and the chelation of Fe^{III} with organic ligands. In this experiment, a dilute electrolyte solution was prepared with KCl at the same EC as the SPE, 0.4 dS·m^{-1}. The differences between the KCl and SPE solutions include chemical composition and pH. The SPE solution contains the soluble components extracted from the soil solution with a pH$_{saturated\ paste\ extract}$ of 8.4, while the KCl solution was prepared at a concentration of 0.003 mol L^{-1} at a pH of 5.9. The kinetic results over seven days were analyzed with a generalized linear mixed model, and the slope and the intercept are attached to a table in the graph. The total soluble Fe concentrations of both nano-metaVT and nano-CT-metaVT in the KCl suspension (pH 5.9) increase from 683 to 1,146 and 527 to 654 μg L^{-1}, respectively (Fig. 2-3a). The total soluble Fe concentrations in the nano-metaVT-KCl suspensions are significantly higher over time, with a slope of 57.6, greater than that of the nano-CT-metaVT-KCl suspensions (23.3). This difference can be attributed to the solubility characteristics of CT, which is known to dissolve in dilute acidic solutions below a pH of 6.0, as noted by Rouhani Shirvan et al. (2019).[38] Even though the pH of the 0.003 mol L^{-1} KCl solution is 5.9, CT becomes soluble, yet it is only partially protonated under this condition. Moreover, the total soluble Fe concentrations of nano-metaVT and nano-CT-metaVT in the SPE suspensions (Fig. 2-3b) are significantly lower, about 30 μg L^{-1}, in SPE suspension (pH 8.4) compared to Fe solubility in the KCl suspensions and remain stable throughout the reaction period.

The total soluble P concentrations in the nano-metaVT-KCl and nano-CT metaVT-KCl suspensions also increase over time from 302 and 310 µg L^{-1} to 630 and 698 µg L^{-1}, respectively. Total soluble P concentrations in both the nano-metaVT and nano-CT-metaVT suspensions increase over time in KCl (Fig. 2-3c) but not in the SPE suspensions (Fig. 2-1d). Schütze et al. (2020) found that P release from vivianite in calcium chloride ($CaCl_2$) suspensions (0.01 mol L^{-1}, pH 6) reached 0.0005 mg m^{-2} in 168 h.[39] By comparison, under similar pH conditions (pH 5.9) but a lower electrolyte concentration (0.003 mol L^{-1} KCl), our nano-metaVT and nano-CT-metaVT suspensions exhibited higher total soluble P concentrations of 0.076 and 0.080 mg m^{-2}, respectively, representing a 152-160 fold increase on a specific surface area basis. Additionally, on a weight basis, while only 0.02 mg P is dissolved from each gram of VI according to Schütze et al., 1.05 and 1.17 mg P are dissolved from each gram of nano-metaVT and nano-CT-metaVT in our study, equating to 53-59 times higher solubility. Still, the experimental conditions in Schütze et al.'s (2020) study are not identical to those in the current research, and some factors might affect the solubility, such as the ionic strength of the solution and mineral crystallinity. However, the results suggest a possible nano-size effect, resulting in the increased solubility of the nano-sized metaVT and CT-metaVT over bulk VT.

The pH and EC of the suspensions were measured daily, and the findings are presented in Fig. 2-4. While the nano-metaVT-KCl suspension displays higher total soluble Fe concentrations than the nano-CT-metaVT-KCl suspension (Fig. 2-3a), the pH of the nano-metaVT-KCl suspension is consistently lower (Fig. 2-4a). Similarly, the nano-CT-metaVT-SPE suspension exhibits higher total soluble Fe concentrations and

lower pH than those in nano-metaVT-SPE suspension (Fig. 2-3b). The results reflect the proton release during the hydrolysis processes of both nano-metaVT and nano-CT-metaVT suspensions (Eq. (1) - (4)). The initial decrease in pH observed from day 0 to day 2 in both nano-metaVT-SPE and nano-CT-metaVT-SPE suspensions, as shown in Figure 2-4b, followed by a subsequent increase, suggests that the protons released during the hydrolysis process are being buffered by the hydroxyl groups present in the SPE suspensions. No significant differences in EC were observed between the nano-metaVT and nano-CT-metaVT suspensions, as indicated in Figures 2-4c and 2-4d.

$$Fe^{3+} + H_2O \rightarrow Fe(OH)^{2+} + H^+ \tag{1}$$

$$Fe(OH)^{2+} + H_2O \rightarrow Fe(OH)_2{}^+ + H^+ \tag{2}$$

$$Fe(OH)_2{}^+ + H_2O \rightarrow Fe(OH)_3 + H^+ \tag{3}$$

$$Fe(OH)_3 + H_2O \rightarrow Fe(OH)_4{}^- + H^+ \tag{4}$$
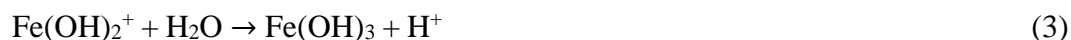
Although the chelation and complexation of organic compounds in SPE were expected to enhance the solubility of both nano-metaVT and nano-CT-metaVT compared to the KCl suspension, this was not the case. Moreover, the nano-CT-metaVT-SPE demonstrated higher total solubility than the nano-metaVT-SPE, although both were significantly lower than their respective solubilities in the nano-CT-metaVT-KCl and nano-metaVT-KCl suspensions. This observation suggests that the interactions influencing solubility in SPE suspensions, containing compounds relevant to the soil, including LMWOAs, amino acid, fulvic acid, and humic acid, may differ substantially from those in KCl suspensions, a dilute electrolyte solution.

	metaVT	CT-metaVT	P value
Slope	57.6	23.3	<0.0001
Intercept	789.9	496.8	<0.0001
R^2	0.87	0.91	-

	metaVT	CT-metaVT	P value
Slope	0.2	0.3	0.5033
Intercept	30.2	32.6	0.0074
R^2	0.12	0.43	-

	metaVT	CT-metaVT	P value
Slope	39.6	48.8	0.0562
Intercept	392.2	408.1	0.4260
R^2	0.81	0.83	-

	metaVT	CT-metaVT	P value
Slope	0.8	4.3	0.3728
Intercept	544.0	616.1	<0.0001
R^2	0.01	0.09	-
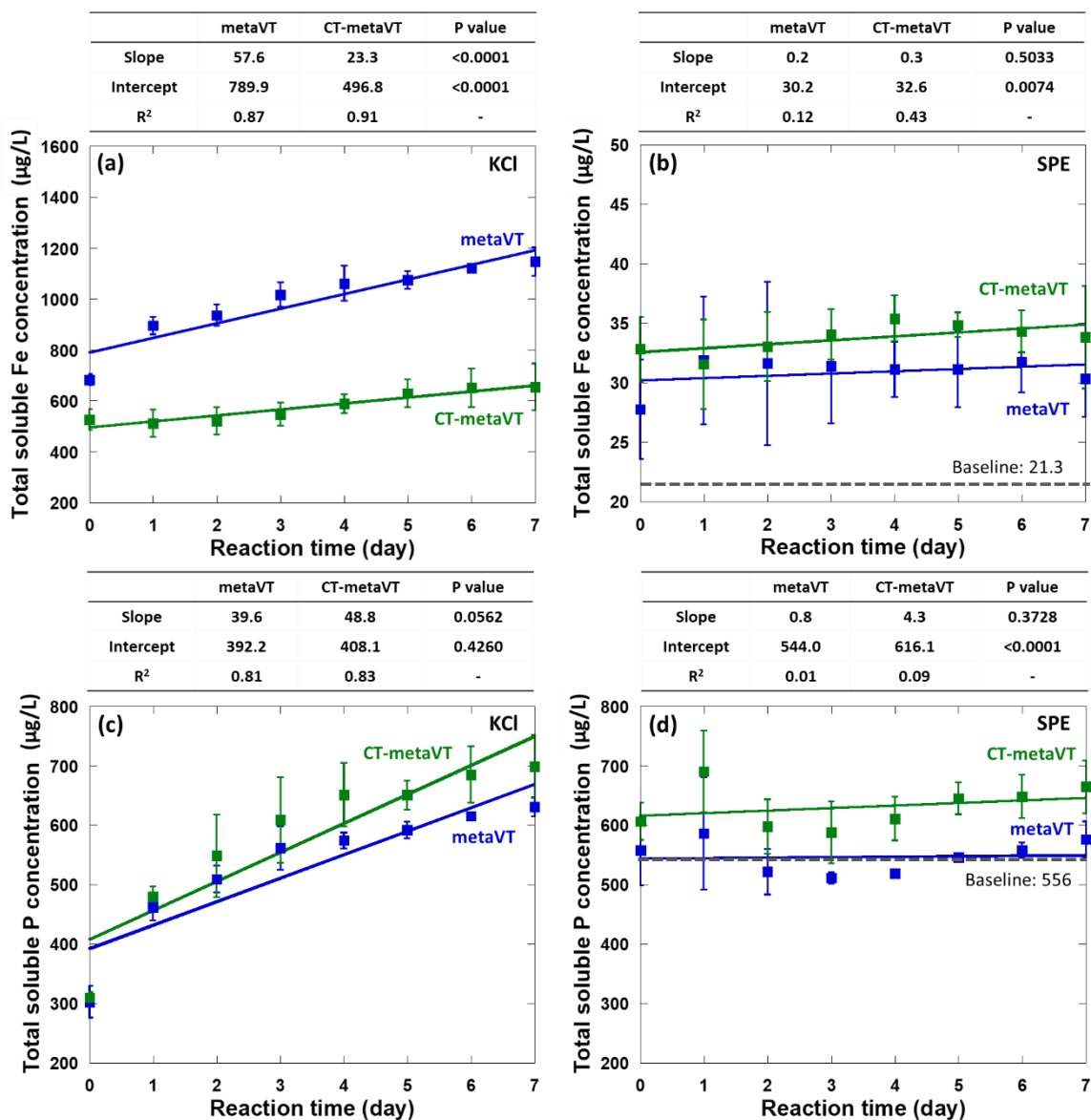
Figure 2-3. Total soluble Fe concentration in 0.003 mol L^{-1} KCl suspension (a) and SPE suspension (b). Total soluble P concentration in 0.003 mol L^{-1} KCl suspension (c) and SPE suspension (d). Condition: [nano-metaVT/ nano-CT-metaVT] = 0.6 g L^{-1}. Baseline: The initial total soluble Fe and P concentrations in SPE before adding the treatment.

	metaVT	CT-metaVT	P value
Slope	-0.0211	-0.0135	0.1912
Intercept	5.3	5.7	<0.0001
R^2	0.37	0.30	-

	metaVT	CT-metaVT	P value
Slope	0.0324	0.0254	0.5540
Intercept	8.0	8.0	0.3591
R^2	0.33	0.16	-

	metaVT	CT-metaVT	P value
Slope	0.0021	0.0017	0.3002
Intercept	0.4238	0.4271	0.0880
R^2	0.76	0.56	-

	metaVT	CT-metaVT	P value
Slope	-0.0028	-0.0017	0.4678
Intercept	0.4021	0.4051	0.6298
R^2	0.28	0.17	-
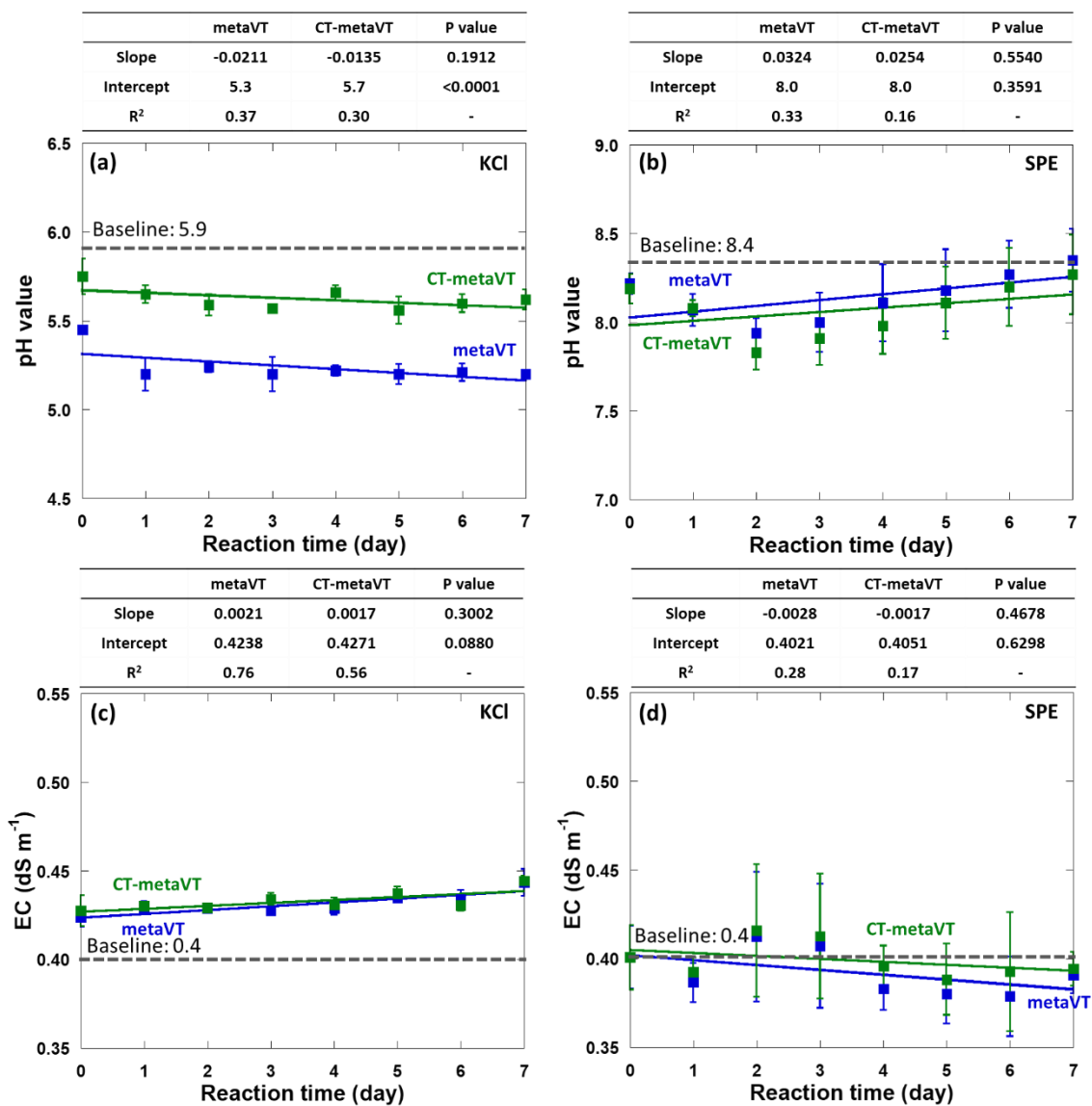
Figure 2-4. The pH of 0.003 mol L^{-1} KCl suspension (a) and SPE suspension (b) changed over time. The EC of 0.003 mol L^{-1} KCl suspension (c) and SPE suspension (d) changed over time. Condition: [nano-metaVT/ nano-CT-metaVT] = 0.6 g L^{-1}. Baseline: The initial pH and EC of SPE before adding the treatment.

2.4.2.2 *Pc*O6 inoculation effect

To investigate the impact of soil microbes on the solubility of nano-metaVT and nano-CT-metaVT, suspensions containing these nanoparticles in SPE were inoculated with beneficial soil microbes known for Pvd production and incubated for seven days. The specific microbe studied first was *Pc*O6. The concentrations of total soluble Fe and P P in both nano-metaVT-SPE and nano-CT-metaVT-SPE suspensions inoculated with *Pc*O6 are depicted in Fig. 2-5. Analysis using a generalized linear mixed model reveals no significant difference in the slope or intercept of total soluble Fe concentrations between the *Pc*O6 and the no-microbe treatments for the nano-metaVT-SPE suspension (Fig. 2-5a). However, in the nano-CT-metaVT-SPE suspension, the *Pc*O6 treatment results in a higher total soluble Fe concentration than the no-microbe treatment. The total soluble P concentrations are not significantly influenced by *Pc*O6 inoculation in either the nano-metaVT-SPE (Fig. 2-5c) or nano-CT-metaVT-SPE (Fig. 2-5d) suspensions.

Interestingly, the pH levels in the nano-CT-metaVT-SPE suspension inoculated with *Pc*O6 are consistent with those in suspensions without *Pc*O6 treatment (Fig. 2-6b). This observation contrasts with the results from Figs. 2-4a and 2-4b, indicating that while the *Pc*O6 treatment increased total soluble Fe in the nano-CT-metaVT-SPE, it did not significantly affect the pH. Additionally, no significant differences in EC were observed between the nano-metaVT and nano-CT-metaVT suspensions (Figs. 2-6c and 2-6d). These findings suggest that the impact of *Pc*O6 on Fe solubility is specific to the nano-CT-metaVT under the conditions tested without affecting the overall pH or EC of the suspensions.

	No microbe	PcO6	P value
Slope	0.2	0.4	0.4122
Intercept	30.2	30.2	0.1597
R²	0.12	0.35	-

	No microbe	PcO6	P value
Slope	0.3	0.4	0.8299
Intercept	32.6	35.1	0.0275
R²	0.43	0.53	-

	No microbe	PcO6	P value
Slope	0.8	13.7	0.0010
Intercept	544.0	511.3	0.0453
R²	0.01	0.47	-

	No microbe	PcO6	P value
Slope	4.3	8.5	0.3180
Intercept	616.1	620.4	0.1556
R²	0.09	0.23	-
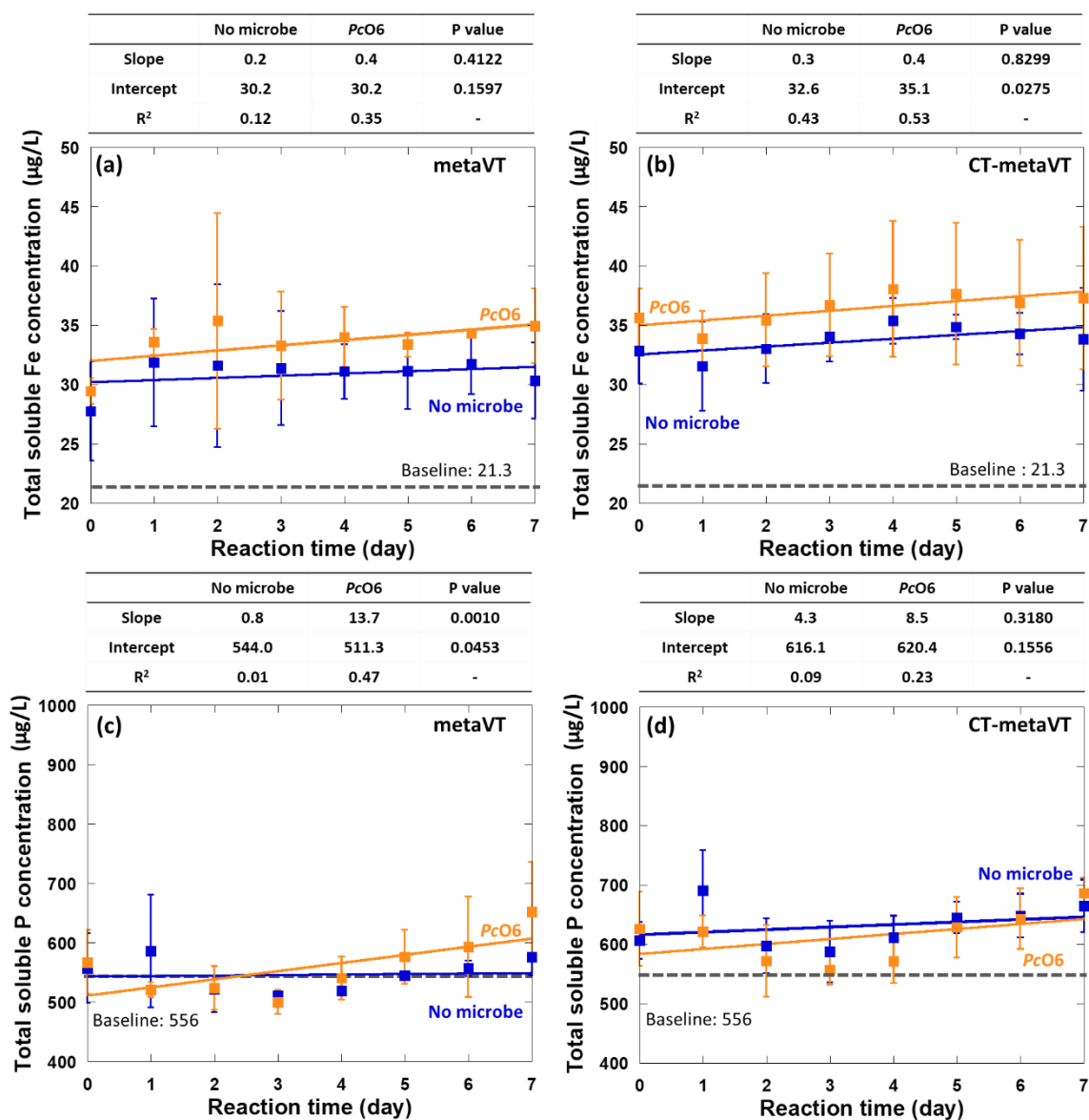
Figure 2-5. Effects of *Pc*O6 inoculation on total soluble Fe concentrations in nano-metaVT-SPE (a) and nano-CT-metaVT-SPE (b) suspensions. The effects of *Pc*O6 inoculation on total soluble P concentrations in nano-metaVT-SPE (c) and nano-CT-metaVT-SPE (d) suspensions. Baseline: The initial total soluble Fe and P concentrations in SPE before adding the treatment.

	No microbe	*Pc*O6	P value
Slope	0.0324	0.0174	0.3820
Intercept	8.0	8.0	0.9435
R^2	0.33	0.09	-

	No microbe	*Pc*O6	P value
Slope	0.0254	0.0275	0.8829
Intercept	8.0	8.0	0.9435
R^2	0.16	0.20	-

	No microbe	*Pc*O6	P value
Slope	-0.0028	-0.0026	0.9151
Intercept	0.4021	0.4036	0.8242
R^2	0.28	0.29	-

	No microbe	*Pc*O6	P value
Slope	-0.0017	-0.0018	0.9496
Intercept	0.4021	0.4036	0.8242
R^2	0.17	0.13	-
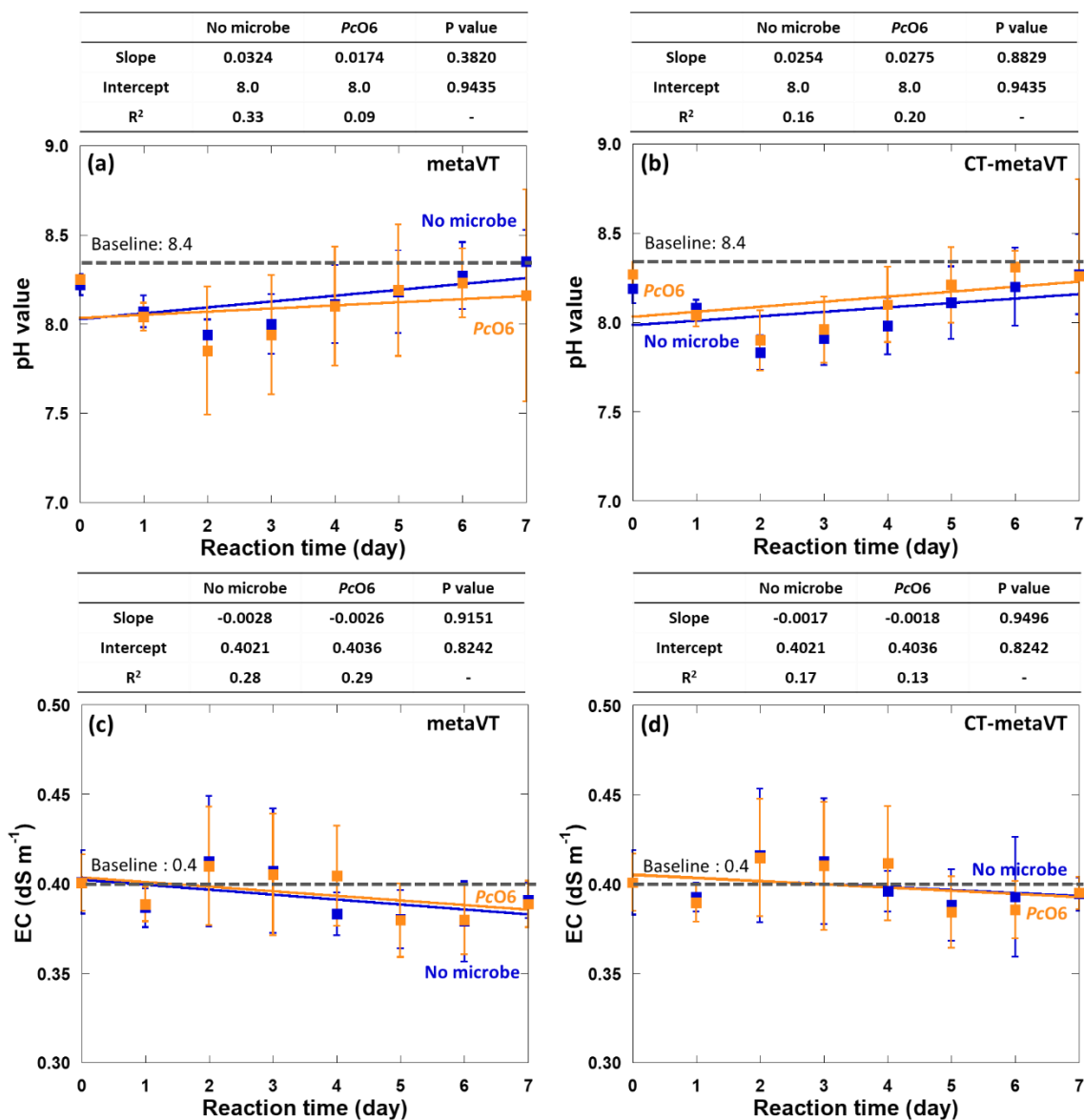
Figure 2-6. Effects of *Pc*O6 inoculation on pH in nano-metaVT-SPE (a) and nano-CT-metaVT-SPE (b) suspensions. The effects of *Pc*O6 inoculation on EC in nano-metaVT-SPE (c) and nano-CT-metaVT-SPE (d) suspensions. Baseline: The initial pH and EC of SPE before adding the treatment.

2.4.2.3 *Pp* Pf-5 inoculation effect

Pp Pf-5, recognized as a plant PGPR, is notable for its ability to protect plants by producing a variety of siderophores and enzymes. This bacterium synthesizes several types of siderophores, including Pvd and E-Pch, with E-Pch being a yellow-green siderophore that is structurally distinct from Pvd and exhibits a lower affinity for Fe.[24, 40, 41] Loper et al. (2016) have also reported that *Pp* Pf-5 produces chitinase, an enzyme that breaks down chitin found in insect exoskeletons and fungal cell walls, thus facilitating the use of these degradation products as carbon and nitrogen sources.[28]

Figs. 2-7a and 2-7b illustrate that inoculation with *Pp* Pf-5 significantly enhances the total soluble Fe concentrations in both nano-metaVT-SPE and nano-CT-metaVT-SPE suspensions compared to the no-microbe treatment. Specifically, *Pp* Pf-5 inoculation resulted in intercept values 22.5- and 29.1-fold higher than those of the no-microbe treatments in the nano-metaVT-SPE and nano-CT-metaVT-SPE suspensions, respectively. However, the levels of soluble P remained unchanged with *Pp* Pf-5 inoculation in both types of suspensions (Figs. 2-7c and 2-7d).

Furthermore, the pH levels in the suspensions inoculated with *Pp* Pf-5 are higher than those without the bacterium (Figs. 2-8a and 2-8b). This aligns with earlier findings (Figs. 2-4a and 2-4b). Additionally, the EC values are lower in both nano-metaVT and nano-CT-metaVT suspensions treated with *Pp* Pf-5 (Figs. 2-8c and 2-8d). These results suggest that the *Pp* Pf-5 treatment distinctly influences Fe solubility under the tested conditions, concurrently leading to the decreasing pH and EC of the suspensions.

The effects of *Pp* Pf-5 inoculation on total soluble Fe concentrations, pH, and EC are unlikely to be related to chitinase production since similar trends are observed in both the nano-metaVT and nano-CT-metaVT treatments. Even though both *Pc*O6 and *Pp* Pf-5 produce Pvd, no significant effects on total soluble Fe, pH, and EC are observed with *Pc*O6 treatment, indicating that Pvd is not the primary mechanism by which *Pp* Pf-5 enhances total soluble Fe. Moreover, E-Pch, another siderophore produced by *Pp* Pf-5, has a significantly lower iron-binding affinity (Ka = 2×10^5 M^{-1}) than Pvd (Ka = 10^{32} M^{-1}), reflecting its lower Fe chelation capacity.[25-27] Moreover, the presence of Fe in solution might inhibit the production of bacterial siderophores. This suggests that the mechanisms underlying the effects of *Pp* Pf-5 inoculation may involve complex interactions beyond chelation by the siderophore.

	No microbe	Pp Pf-5	P value
Slope	0.2	0.2	0.9091
Intercept	30.2	37.0	<0.0001
R^2	0.12	0.12	-

	No microbe	Pp Pf-5	P value
Slope	0.3	0.2	0.5816
Intercept	32.6	42.1	<0.0001
R^2	0.43	0.21	-

	No microbe	Pp Pf-5	P value
Slope	0.8	3.6	0.4019
Intercept	544.0	561.8	0.2069
R^2	0.01	0.08	-

	No microbe	Pp Pf-5	P value
Slope	4.3	-3.5	0.0260
Intercept	616.1	655.7	0.0070
R^2	0.09	0.07	-
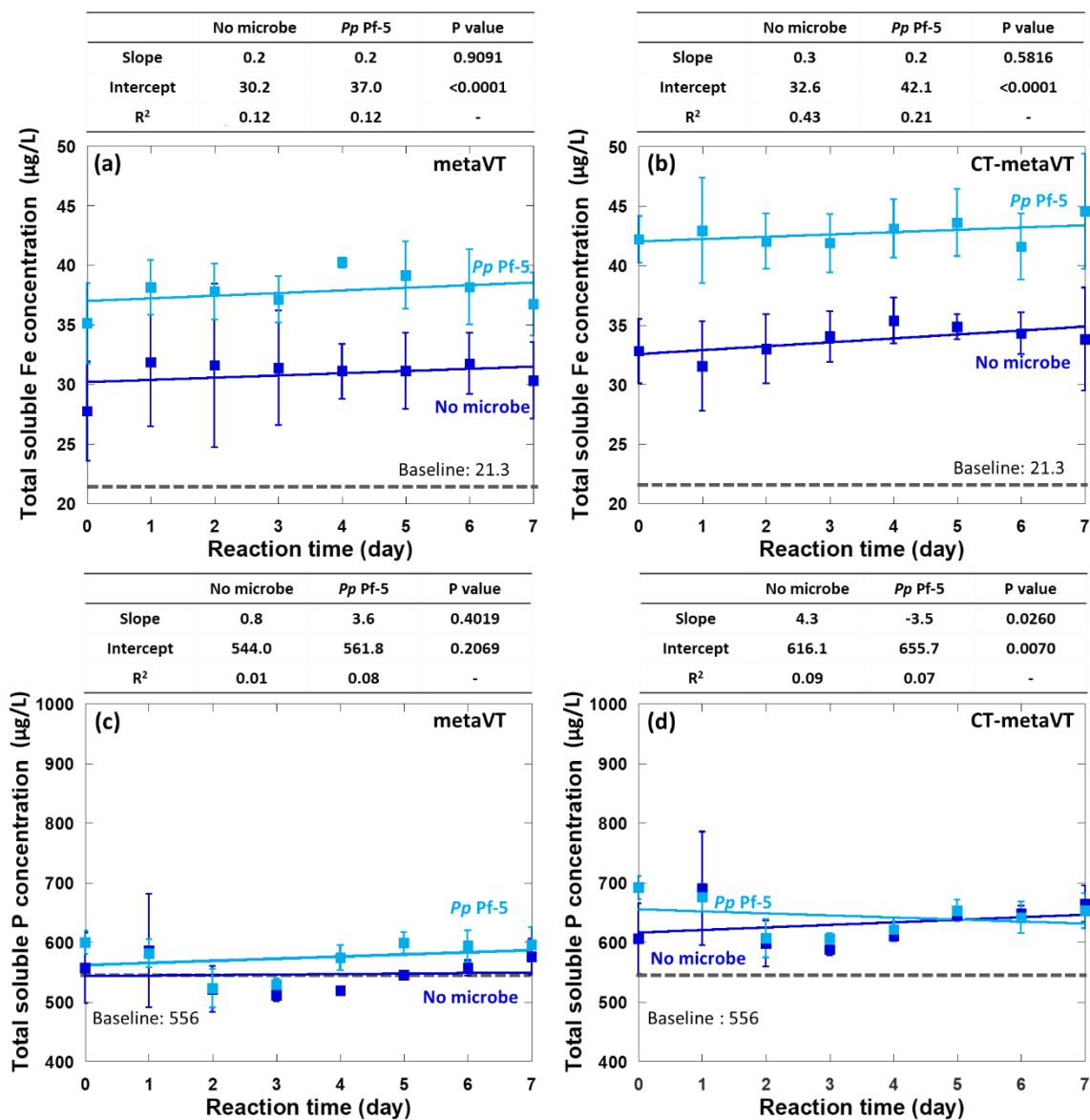
Figure 2-7. Effect of *Pp* Pf-5 inoculation on total soluble Fe concentrations in nano-metaVT-SPE (a) and nano-CT-metaVT-SPE (b) suspensions. The impact of *Pp* Pf-5 inoculation on total soluble P concentrations in nano-metaVT-SPE (c) and nano-CT-metaVT-SPE (d) suspensions. Error bars represent the standard deviation of the nine replicates. Baseline: The initial total soluble Fe and P concentrations in SPE before adding the treatment.

	No microbe	Pp Pf-5	P value
Slope	0.0324	0.0153	0.1720
Intercept	8.0	7.8	<0.0001
R²	0.33	0.11	-

	No microbe	Pp Pf-5	P value
Slope	0.0254	0.0244	0.9515
Intercept	8.0	7.6	<0.0001
R²	0.16	0.12	-

	No microbe	Pp Pf-5	P value
Slope	-0.0028	0.0015	0.0038
Intercept	0.4021	0.3502	<0.0001
R²	0.28	0.20	-

	No microbe	Pp Pf-5	P value
Slope	-0.0017	0.0008	0.1134
Intercept	0.4051	0.3570	<0.0001
R²	0.17	0.08	-
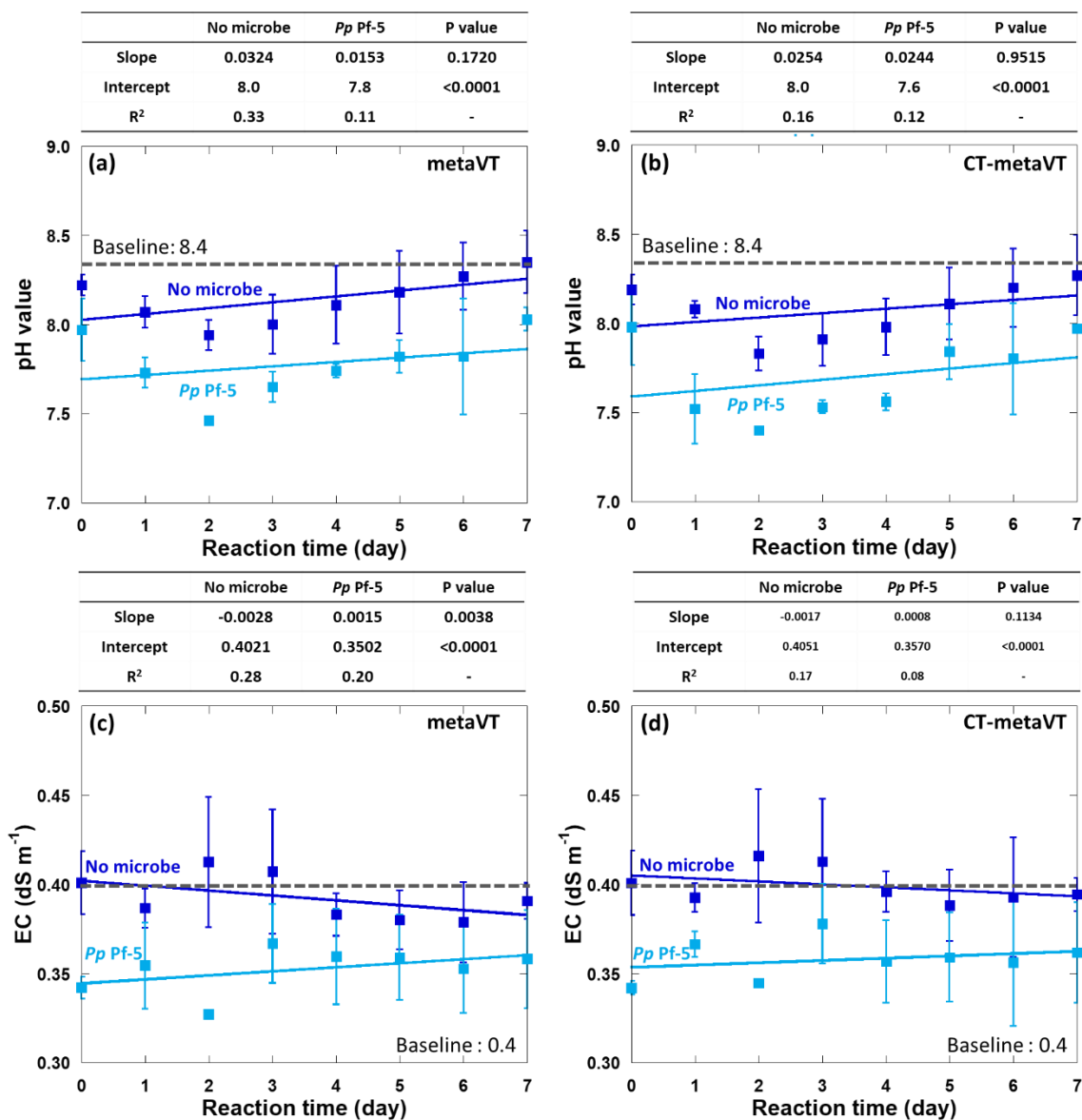
Figure 2-8. Effect of *Pp* Pf-5 inoculation on pH in nano-metaVT-SPE (a) and nano-CT-metaVT-SPE (b) suspensions. The impact of *Pp* Pf-5 inoculation on EC in nano-metaVT-SPE (c) and nano-CT-metaVT-SPE (d) suspensions. Error bars represent the standard deviation of the nine replicates. Baseline: The initial pH and EC of SPE before adding the treatment.

Inoculation with *Pp* Pf-5 causes a decrease in pH levels in both the nano-metaVT-SPE and nano-CT-metaVT-SPE suspensions compared to the suspensions without microbial presence, which results in higher soluble Fe concentrations. To assess the impact of this pH reduction on solubility, the Visual MINTEQ model was utilized. The pH levels in nano-metaVT-SPE and nano-CT-metaVT-SPE suspensions without *Pp* Pf-5 inoculation are recorded at 7.9 and 7.8 on Day 0, while those with inoculation measured 7.5 and 7.4 after 7 days, respectively (Figures 2-8a and 2-8b). In Figure 2-9b, nano-metaVT-SPE with *Pp* Pf-5 shows a 19.6% increase in total soluble Fe concentration compared to the suspension without microbes, while the model predicts only a 11.1% increase when the pH decreases from 7.9 to 7.5. Similarly, nano-CT-metaVT-SPE with *Pp* Pf-5 inoculation exhibits a 27.3% increase in total soluble Fe concentration compared to the non-inoculated, with a pH reduction from 7.8 to 7.4. However, the predicted increase in total soluble Fe concentration is only 12.0%. The discrepancies between the experimental results and model predictions suggest that the increase in Fe concentrations due to *Pp* Pf-5 inoculation is not solely attributable to the pH decrease. *Pp* Pf-5 may produce other compounds not analyzed in this study that enhance Fe dissolution from both nano-metaVT and nano-CT-metaVT minerals. Conversely, the differences between the experimental and predicted increases in total P concentrations are relatively modest, suggesting that the observed increase in total P concentrations is largely due to the reduction in pH observed in the suspensions.

The findings found that different bacterial strains have varied effects on the solubility of nano-metaVT and nano-CT-metaVT. Furthermore, the interactions observed with *Pp* Pf-5 provide deeper insights into the solubilities of nano-metaVT and nano-CT-

metaVT within SPE suspensions, offering a more realistic approximation of actual soil

environmental conditions than results from simpler electrolyte suspensions like KCl.

Previous studies have primarily focused on the solubility of vivianite in relatively simple

suspension systems such as electrolytes (e.g., $CaCl_2$) or solutions of LMWOAs, e.g.,

citric acid, often overlooking the critical role of soil microbes in soil solution

chemistry.[21, 39, 42] Therefore, the mechanisms by which *Pp* Pf-5 enhances the

solubilization of nano-metaVT and nano-CT-metaVT than no-microbe treatments in

more complex environments warrant further detailed investigation.
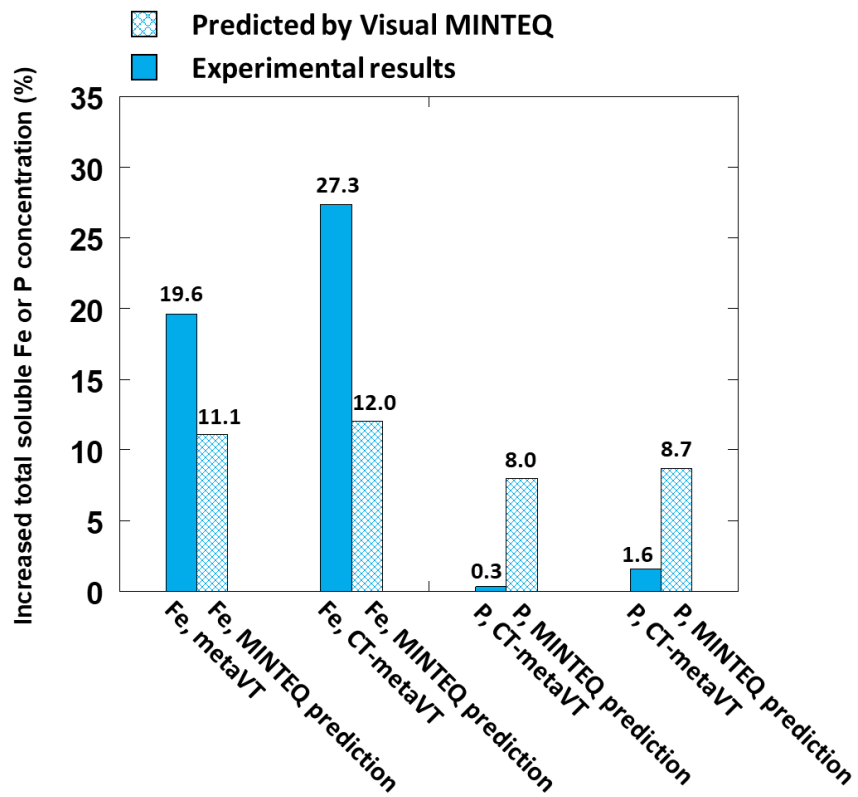
Figure 2-9. The increased total soluble Fe and P concentrations of nano-metaVT-SPE and nano-CT-metaVT-SPE suspensions with *Pp* Pf-5 inoculation are compared to the increased total soluble Fe and P concentrations in vivianite-SPE suspension predicted by Visual MINTEQ.

2.4.2.4 Role of chitosan coating

Fig. 2-9 highlights the impact of the CT coating on nano-metaVT solubility by comparing the total soluble Fe and P concentrations in nano-metaVT- and nano-CT-metaVT-SPE suspensions. Figs. 2-9a and 2-9b demonstrate that nano-CT-metaVT-SPE suspensions consistently display significantly higher total soluble Fe concentrations than those of nano-metaVT-SPE, regardless of the presence of *Pp* Pf-5. Analyses using a generalized linear mixed model indicate higher intercept values for nano-CT-metaVT-SPE suspensions, both without and with *Pp* Pf-5 inoculation, at 32.6 and 42.1 respectively. A similar trend is observed for total soluble P concentrations, as depicted in Figs. 2-9c and 2-9d. Specifically, the intercept values for nano-CT-metaVT-SPE suspensions are 616.1 without *Pp* Pf-5 inoculation and 655.7 with it, both significantly higher than those recorded for nano-metaVT-SPE. Thus the CT coating enhances the solubilities of both Fe and P in the nano-CT-metaVT in SPE suspension in seven days even though the pH of the nano-CT-metaVT-SPE suspensions are not different from those in nano-metaVT-SPE suspensions, as shown in Figs. 2-10a and 2-10b. Similarly, the EC values are consistent between the two types of materials, as shown in Figs. 2-10c and 2-10d.

CT, being a linear polysaccharide, is typically insoluble under alkaline conditions (pH > 6.0), which raises questions regarding its behavior in the SPE solution (pH 8.4). The purpose of modifying nano-metaVT's surface with CT was to provide an insoluble coating under alkaline conditions and create a positively charged surface that might enhance the retention of nano-CT-metaVT in soil. For example, Ha et al. (2019) showed that CT-encapsulated N, P, and K nano fertilizers increased cucumber yield, suggesting

that the positive charge of chitosan and K might increase stomatal cell osmotic pressure, leading to greater stomatal conductance.[43] Similarly, Wu et al. (2008) used CT as a coating on NPK fertilizers to slow their release.[17] CT not only acts as a slow-release layer but also enhances bioavailability in calcareous soils. For instance, CT-encapsulated Zn nanoparticles have been shown to promote maize growth, alleviate Zn deficiency in alkaline soils[44], and enhance wheat growth in sandy soils.[45] In this study, however, the CT coating in nano-CT-metaVT does not slow Fe and P release compared to un-coated nano-metaVT but does lead to higher total soluble Fe concentrations in the alkaline SPE.

	metaVT	CT-metaVT	P value
Slope	0.2	0.3	0.5033
Intercept	30.2	32.6	0.0074
R^2	0.12	0.43	-

	metaVT	CT-metaVT	P value
Slope	0.2	0.2	0.8906
Intercept	37.0	42.1	<0.0001
R^2	0.12	0.21	-

	metaVT	CT-metaVT	P value
Slope	0.8	4.3	0.3728
Intercept	544.0	616.1	<0.0001
R^2	0.01	0.09	-

	metaVT	CT-metaVT	P value
Slope	3.6	-3.5	0.0123
Intercept	561.8	655.7	<0.0001
R^2	0.08	0.07	-
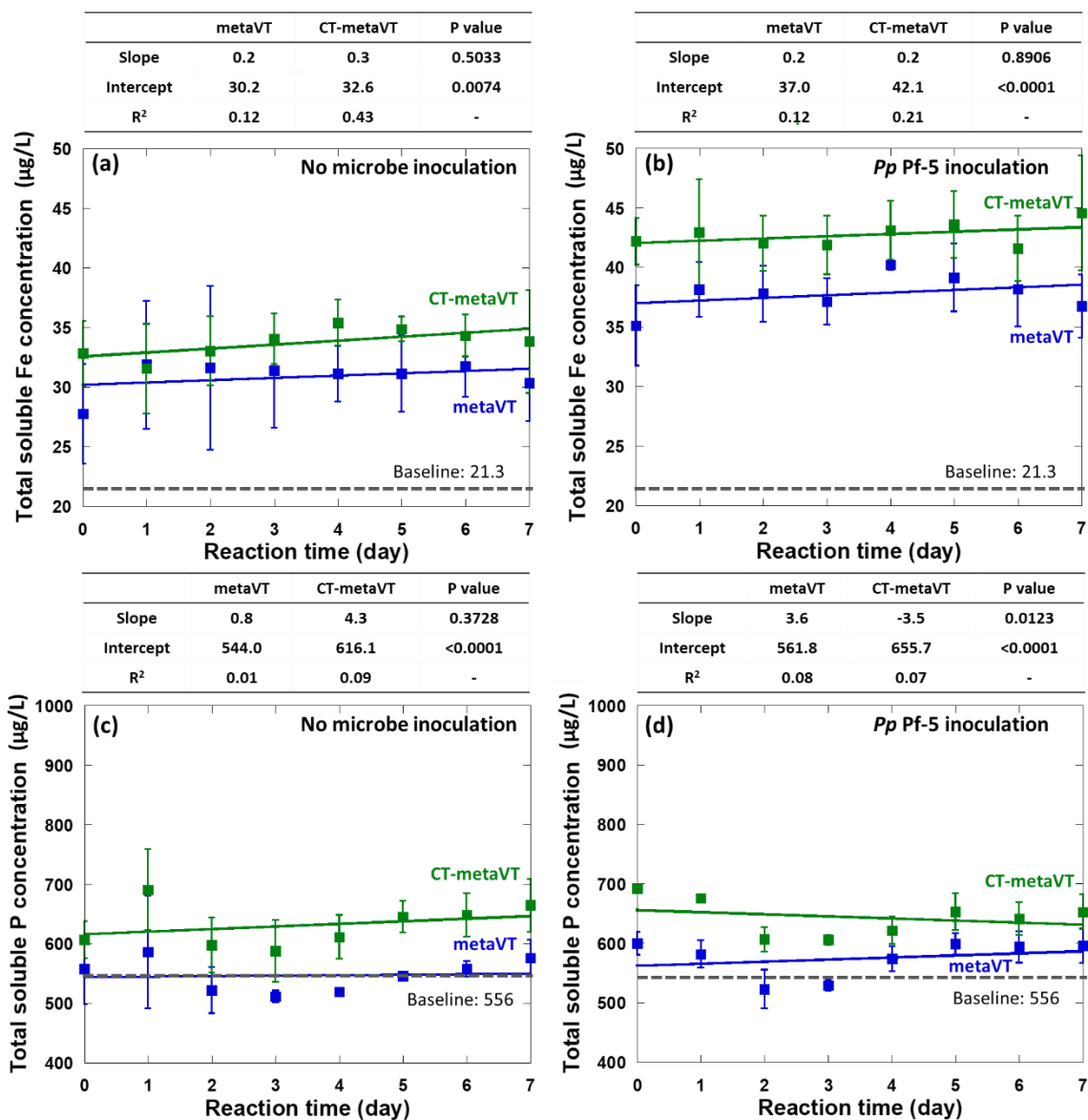
Figure 2-10. Total soluble Fe concentrations in nano-metaVT-SPE and nano-CT-metaVT-SPE suspensions without (a) and with (b) *Pp* Pf-5 inoculation. Total soluble P concentrations in nano-metaVT-SPE and nano-CT-metaVT-SPE suspensions without (c) and with (d) *Pp* Pf-5 inoculation. Error bars represent the standard deviation of the nine replicates. Baseline: The initial total soluble Fe and P concentrations in SPE before adding the treatment.

	metaVT	CT-metaVT	P value
Slope	0.0324	0.0254	0.5540
Intercept	8.0	8.0	0.3591
R^2	0.33	0.16	-

	metaVT	CT-metaVT	P value
Slope	0.0145	0.0234	0.5682
Intercept	7.8	7.6	0.1009
R^2	0.11	0.12	-

	metaVT	CT-metaVT	P value
Slope	-0.0028	-0.0017	0.4678
Intercept	0.4021	0.4051	0.6298
R^2	0.28	0.17	-

	metaVT	CT-metaVT	P value
Slope	0.0014	0.0007	0.5061
Intercept	0.3508	0.3579	0.1273
R^2	0.20	0.08	-
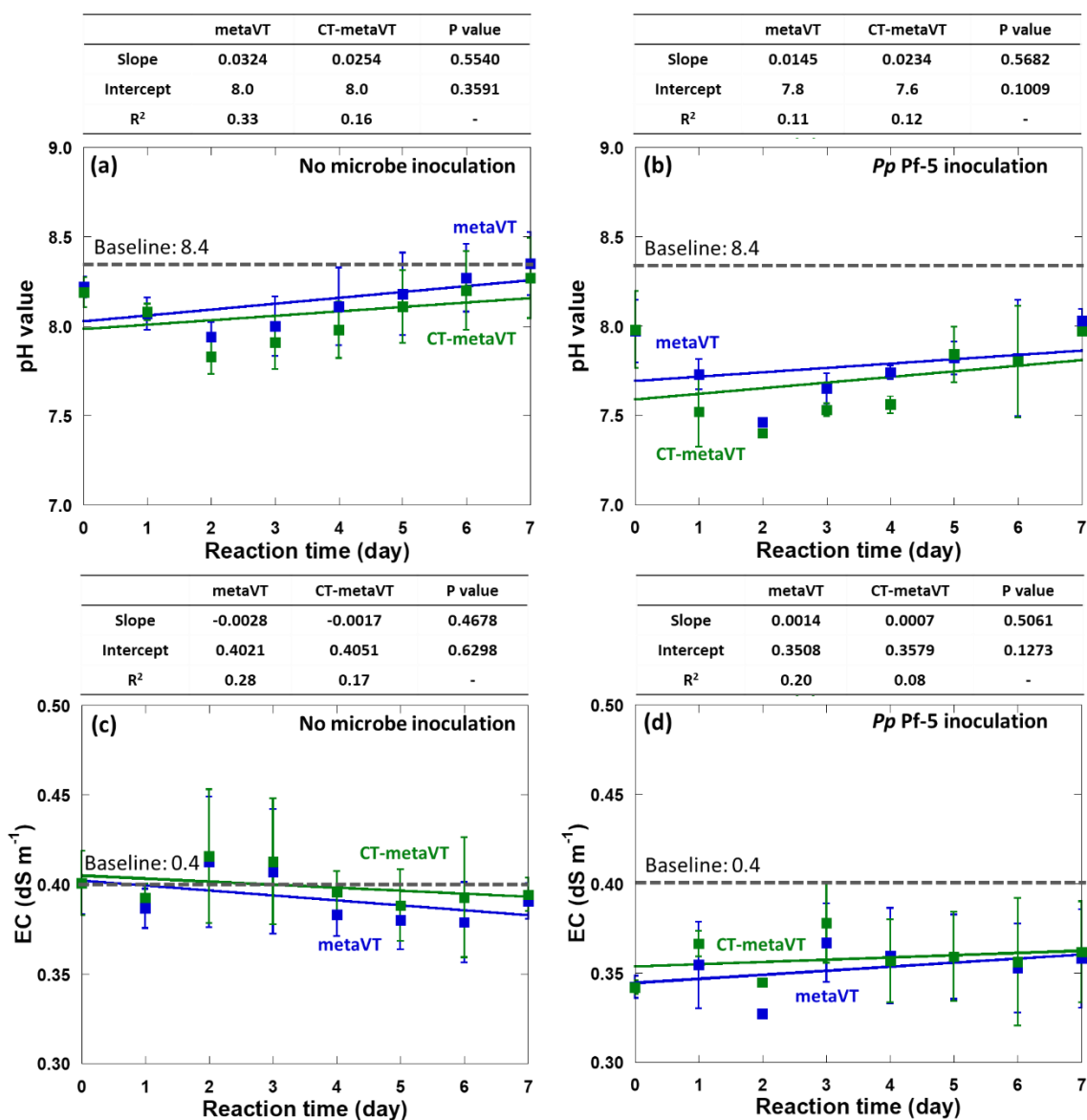
Figure 2-11. The pH of nano-metaVT-SPE and nano-CT-metaVT-SPE suspensions changed over time without (a) and with (b) *Pp* Pf-5 inoculation. The EC of nano-metaVT-SPE and nano-CT-metaVT-SPE suspensions changed over time without (c) and with (d) *Pp* Pf-5 inoculation. Error bars represent the standard deviation of the nine replicates. Baseline: The initial pH and EC of SPE before adding the treatment.

2.4.3 Geochemical modeling

LMWOAs exudated by plant roots and bacteria in soils contribute to the enhanced solubility of metals and improved nutrient assimilation. Additionally, AAs secreted into the rhizosphere also influence metal interactions. A SPE contains soluble LMWOAs and AAs in the suspension, which can simulate, though not identically, the chemical reaction with nano-metaVT and nano-CT-metaVT occurring in a soil solution. Naturally occurring soluble organic compounds in soils, such as fulvic acids (FAs), which contain ligand functional groups, are recognized for their capacity to bind to iron within the system. This interaction has a consequential effect on the dissolution rate and bioavailability of iron in the environment.

In Fig. 2-11a, the nano-metaVT-KCl and nano-CT-metaVT-KCl suspensions without microbe inoculation show a total soluble Fe concentration of 1147 ± 55 $\mu g\ L^{-1}$ and 654 ± 92 $\mu g\ L^{-1}$, respectively, and total soluble P concentration of 630 ± 16 $\mu g\ L^{-1}$ and 699 ± 53 $\mu g\ L^{-1}$ after seven days, respectively. The empirical results in the nano-metaVT-KCl suspension are lower than the total dissolved Fe concentration (11,698 μg L^{-1}) and total dissolved P concentration predicted (4107 $\mu g\ L^{-1}$) by the Visuall MINTEQ speciation model (Fig. 2-12a). Similarly, the nano-CT-metaVT-KCl suspensions resulted in lower than predicted total dissolved Fe concentration, 5,202 $\mu g\ L^{-1}$, and predicted total dissolved P concentration, 1,910 $\mu g\ L^{-1}$.

In Fig. 2-11b, the total soluble Fe concentration of nano-metaVT-SPE and nano-CT-metaVT-SPE suspensions with *Pp* Pf-5 inoculation are higher than in the suspensions without microbes. However, the measured total soluble Fe concentrations in the suspensions are about 28-38-fold lower than the concentrations predicted by the

MINTEQ model. The total soluble P concentrations in thenano-CT-metaVT-SPE suspensions are higher overall than in the nano-metaVT-SPE suspensions. Thus, the experimental results of total soluble P concentrations in SPE suspensions are closer to the total dissolved P concentrations predicted by the MINTEQ model, compared to total soluble Fe concentrations. The results suggested that incongruent dissolution of nano-metaVT and nano-CT-metaVT occurs in SPE suspension.

Overall, the total soluble Fe concentrations in both the nano-metaVT and nano-CT-metaVT suspensions in either KCl or SPE are significantly lower than the Visual MINTEQ prediction values. However, there are limitations to the visual MINTEQ model, which must be taken into account. First, thermodynamic constants are only available for pure vivianite in which all the Fe is present as Fe^{II}, unlike the mixed redox state of nano-metaVT. At a given pH, Fe^{III} is less soluble than Fe^{II}, suggesting that metaVT (more oxidized than VT) is likely less soluble than pure VT. The thermodynamic constant of nano-metaVT, a partially oxidized form of vivianite, is undefined and understudied due to the complexity arising from its various possible oxidation states. Another significant limitation is the modeling of reaction time. Visual MINTEQ predicts outcomes based on fully completed reactions, but in reality, nano-metaVT and nano-CT-metaVT in this study only have seven days for weathering.
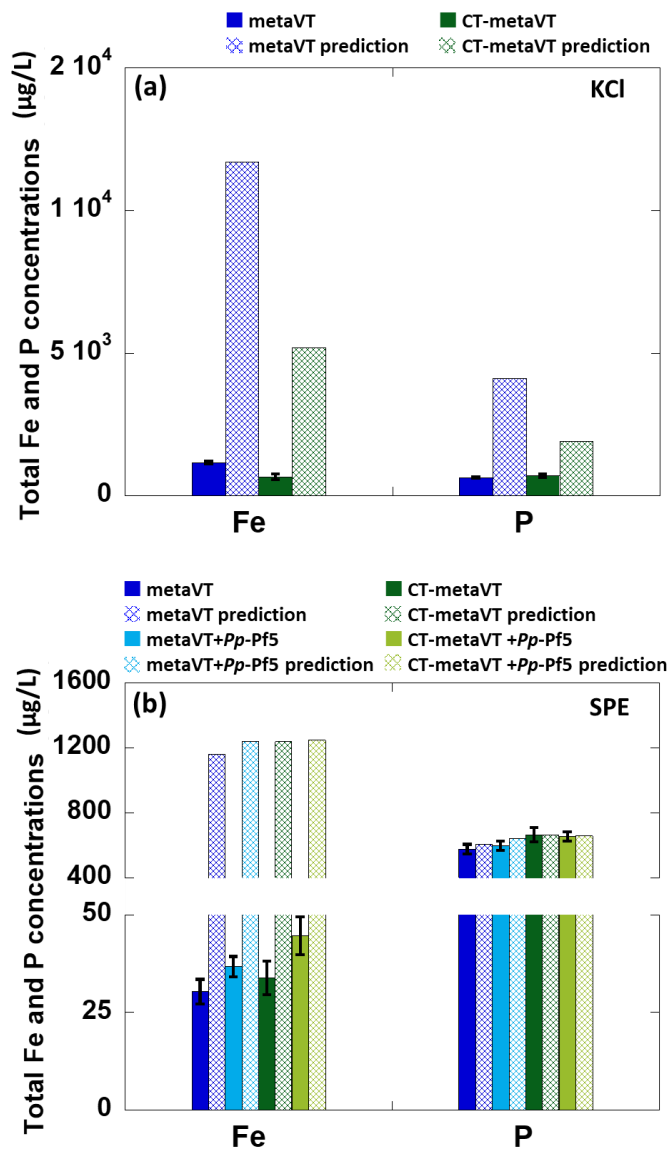
Figure 2-12. The total Fe and P concentrations in nano-metaVT-KCl and nano-CT-metaVT-KCl suspensions after seven days (a). The solid color bars represent experimental results, and the dotted yellow lines represent the Visual MINTEQ predicted values. The total Fe and P concentrations in nano-metaVT-SPE and nano-CT-metaVT-SPE after seven days (b), including the microbial inoculation treatments. The solid color bars represent experimental results, and the pattern-filled bars represent the values predicted by Visual MINTEQ.

Schütze et al. (2020) compared the P release rate from vivianite in $CaCl_2$ and citric acid solutions (0.01–0.1 mol L^{-1}, pH 6) in seven days.[39] The results showed that the released P concentrations in citric acid are 320-466-fold higher than in $CaCl_2$ solution, indicating the critical role of LMWOAs in the solubility of phosphate minerals. Similar results were shown in a Gypser and Freese (2020) study, reporting that the concentrations of P release from vivianite in various solutions after 1,344 h follow the order: citric acid (83.9%) > humic acid (8.1%) > $CaSO_4$ (1.7%) > $CaCl_2$ (1.4%).[21] The release of P bound by organic acids includes the processes of mineral dissolution, direct ligand exchange, and the replacement of P by organic acid anions, the formation of metal–organic complexes, and the blocking of P adsorption sites.[20, 46] We did not detect citric acid in the SPE, which might be due to its rapid consumption by soil microbes during SPE preparation process. The complete secondary metabolite analyses, including siderophores secreted by soil organisms, are difficult to quantify based on the current technology. Still, they play an important role in the solubility of Fe-minerals. There are other compounds reacting with Fe from nano-metaVT and nano-CT-metaVT in this system. From Table 2-8, it is clear that 99.98% Fe^{3+} and 82.24% Fe^{2+} are bound by FA and that there are 54.93% HPO_4^{-2} and 20.38% $CaHPO_4$ in the nano-vivianite-SPE suspensions, as predicted by visual MINTEQ. The results indicate that FA is the predominant ligand complexing Fe in the SPE suspensions.

Table 2-7. The Fe and P speciation in metaVT-SPE and CT-metaVT-SPE suspensions predicted by visual MINTEQ.

		metaVT-SPE	CT-metaVT-SPE
Component	Species name	% of total concentration	
Fe^{3+}	$FA2\text{-}Fe^{III}(7)(aq)$	100	100
Fe^{2+}	Fe^{2+}	2.1	2.0
	$FeOH^+$	0.15	0.12
	$FeHPO_4$ (aq)	0.05	0.05
	$FeHCO_3^+$	0.03	0.02
	$(6)Fe^+2D(aq)$	0.03	0.02
	$(7)Fe^+2D(aq)$	0.20	0.20
	$HA1\text{-}Fe^{II}(6)(aq)$	9.5	9.0
	$HA2\text{-}Fe^{II}(6)(aq)$	2.7	2.4
	$FA1\text{-}Fe^{II}(7)(aq)$	85.2	86.1
	$FA2\text{-}Fe^{II}(7)(aq)$	0.06	0.06
PO_4^{3-}	HPO_4^{-2}	55.4	55.9
	H_2PO^{4-}	3.1	3.8
	$FeHPO_4$ (aq)	0.05	0.06
	$MgPO_4\text{-}$	0.05	0.04
	$MgHPO_4$ (aq)	7.0	7.1
	$CaHPO_4$ (aq)	20.8	21.4
	$CaPO_4^-$	13.4	11.4
	$CaH_2PO_4^+$	0.08	0.10
	$NaHPO_4^-$	0.08	0.08
	$KHPO_4^-$	0.03	0.04

2.5 Conclusions

In this study, we investigated the solubilities of nano-metaVT and nano-CT-metaVT in a simple electrolyte solution (0.003 mol L^{-1} KCl) and in a calcareous SPE, which contains LMWOAs, amino acid, fulvic acid, and humic acid, and a solid surface. In KCl solution, the total soluble Fe concentration of nano-CT-metaVT suspensions is significantly lower than that of nano-metaVT suspensions after 7 days, which might be due to the insoluble CT coating limiting the solubilization of nano-CT-metaVT. Conversely, the nano-CT-metaVT resulted in significantly higher total Fe concentrations than nano-metaVT in SPE after 7 days. This result suggests that the CT coating effectively increases Fe solubility. On the other hand, *Pp* Pf-5, a beneficial soil microbe, significantly influences the solubilities of both nano-metaVT and nano-CT-metaVT, increasing the total soluble Fe concentration in SPE suspensions by not only lowering the environmental pH but also involving other mechanisms, which remains unclear. The total soluble P concentrations of both nano-metaVT and nano-CT-metaVT in a KCl solution are found to be 152-160 times higher than bulk vivianite in a $CaCl_2$ solution, as reported in the previous study, suggesting a significant impact of particle size on solubility. Even though the total soluble Fe concentration of nano-metaVT and nano-CT-metaVT in the SPE suspensions (pH 8.4) are still much lower than in the KCl suspensions (pH 5.9), our findings highlight the key factors that affect the solubilities of nano-metaVT and nano-CT-metaVT, including functional coating on the nano-fertilizers and the presence of soil microbes, LMWOAs, and AAs. Future research could explore the mechanisms behind the interactions between the nano-metaVT and nano-CT-metaVT, potentially leading to more refined and efficient alternative Fe amendments.

2.6 References

(1) Kobayashi, T.; Nishizawa, N. K. Iron uptake, translocation, and regulation in higher plants. *Annu. Rev. Plant Biol.* **2012**, *63* (1), 131-152. DOI: 10.1146/annurev-arplant-042811-105522.

(2) Morrissey, J.; Guerinot, M. L. Iron uptake and transport in plants: The good, the bad, and the ionome. *Chem. Rev.* **2009**, *109* (10), 4553-4567. DOI: 10.1021/cr900112r.

(3) Brittenham, G. M. New advances in iron metabolism, iron deficiency, and iron overload. *Curr. Opin. Hematol.* **1994**, *1* (2), 101-106.

(4) Abadia, J.; Vazquez, S.; Rellan-Alvarez, R.; El-Jendoubi, H.; Abadia, A.; Alvarez-Fernandez, A.; Lopez-Millan, A. F. Towards a knowledge-based correction of iron chlorosis. *Plant Physiol. Biochem.* **2011**, *49* (5), 471-482. DOI: 10.1016/j.plaphy.2011.01.026.

(5) Hernandez-Apaolaza, L.; Lucena, J. J. Influence of the soil/solution ratio, interaction time, and extractant on the evaluation of iron chelate sorption/desorption by soils. *J. Agric. Food Chem.* **2011**, *59* (6), 2493-2500. DOI: 10.1021/jf104120e.

(6) Rouzies, D.; Millet, J. M. M. Mössbauer study of synthetic oxidized vivianite at room temperature. *Hyperfine Interact.* **1993**, *77* (1), 19-28. DOI: 10.1007/BF02320295.

(7) Feigin, A.; Ravina, I.; Shalhevet, J. *Irrigation with treated sewage effluent management for environmental protection*; Springer, 1991. DOI: 10.1007/978-3-642-74480-8.

(8) Jowett, C.; Solntseva, I.; Wu, L.; James, C.; Glasauer, S. Removal of sewage phosphorus by adsorption and mineral precipitation, with recovery as a fertilizing soil amendment. *Water Sci. Technol.* **2018**, *77* (8), 1967-1978. DOI: 10.2166/wst.2018.027 (acccessed 11/28/2022).

(9) Lin, L.; Li, R.-h.; Yang, Z.-y.; Li, X.-y. Effect of coagulant on acidogenic fermentation of sludge from enhanced primary sedimentation for resource recovery: Comparison between $FeCl_3$ and PACl. *Chem. Eng. J.* **2017**, *325*, 681-689. DOI: 10.1016/j.cej.2017.05.130.

(10) Ammari, T. G.; Hattar, B. Effectiveness of vivianite to prevent lime-induced iron deficiency in lemon trees grown on highly calcareous soil. *Commun. Soil Sci. Plant Anal.* **2011**, *42* (21), 2586-2593. DOI: 10.1080/00103624.2011.614034.

(11) Diaz, I.; Barron, V.; del Campillo, M. C.; Torrent, J. Testing the ability of vivianite to prevent iron deficiency in pot-grown grapevine. *Sci. Hortic.* **2010**, *123* (4), 464-468. DOI: 10.1016/j.scienta.2009.11.006.

(12) Bavaresco, L.; Goncalves, M.; Civardi, S.; Gatti, M.; Ferrari, F. Effects of traditional and new methods on overcoming lime-induced chlorosis of grapevine. *Am. J. Enol. Vitic.* **2010**, *61* (2), 186-190.

(13) Fess, T. L.; Kotcon, J. B.; Benedito, V. A. Crop breeding for low input agriculture: A sustainable response to feed a growing world population. *Sustainability* **2011**, *3* (10), 1742-1772.

(14) Seleiman, M. F.; Almutairi, K. F.; Alotaibi, M.; Shami, A.; Alhammad, B. A.; Battaglia, M. L. Nano-fertilization as an emerging fertilization technique: why can modern agriculture benefit from its use? *Plants* **2021**, *10* (1), 2.

(15) An, C. C.; Sun, C. J.; Li, N. J.; Huang, B. N.; Jiang, J. J.; Shen, Y.; Wang, C.; Zhao, X.; Cui, B.; Wang, C. X.; et al. Nanomaterials and nanotechnology for the delivery of agrochemicals: strategies towards sustainable agriculture. *J. Nanobiotechnol.* **2022**, *20* (11). DOI: 10.1186/s12951-021-01214-7.

(16) Mikula, K.; Izydorczyk, G.; Skrzypczak, D.; Mironiuk, M.; Moustakas, K.; Witek-Krowiak, A.; Chojnacka, K. Controlled release micronutrient fertilizers for precision agriculture - A review. *Sci. Total Environ.* **2020**, *712*, 136365. DOI: 10.1016/j.scitotenv.2019.136365.

(17) Wu, L.; Liu, M.; Rui, L. Preparation and properties of a double-coated slow-release NPK compound fertilizer with superabsorbent and water-retention. *Bioresour. Technol.* **2008**, *99* (3), 547-554. DOI: 10.1016/j.biortech.2006.12.027.

(18) Nriagu, J. O. Stability of vivianite and ion-pair formation in the system $Fe_3(PO_4)_2$-H_3PO_4-H_2O. *Geochim. Cosmochim. Acta* **1972**, *36* (4), 459-470. DOI: 10.1016/0016-7037(72)90035-X.

(19) Rosado, R.; del Campillo, M. C.; Martinez, M. A.; Barron, V.; Torrent, J. Long-term effectiveness of vivianite in reducing iron chlorosis in olive trees. *Plant Soil* **2002**, *241* (1), 139-144. DOI: 10.1023/a:1016058713291.

(20) Johnson, S. E.; Loeppert, R. H. Role of organic acids in phosphate mobilization from iron oxide. *Soil Sci. Soc. Am. J.* **2006**, *70* (1), 222-234. DOI: 10.2136/sssaj2005.0012.

(21) Gypser, S.; Freese, D. Phosphorus release from vivianite and hydroxyapatite by organic and inorganic compounds. *Pedosphere* **2020**, *30* (2), 190-200. DOI: 10.1016/s1002-0160(20)60004-2.

(22) Bhattacharyya, P. N.; Jha, D. K. Plant growth-promoting rhizobacteria (PGPR): emergence in agriculture. *World J. Microbiol. Biotechnol.* **2012**, *28* (4), 1327-1350. DOI: 10.1007/s11274-011-0979-9.

(23) Phukon, P.; Baruah, J.; Sarmah, D. K.; Bhau, B. S. Green input in agriculture: An overview. In *Plant-microbe interactions in agro-ecological perspectives: volume 2: Microbial interactions and agro-ecological impacts*, Singh, D. P., Singh, H. B., Prabha, R. Eds.; Springer, 2017; pp 279-305.

(24) Drehe, I.; Simonetti, E.; Ruiz, J. A. Contribution of the siderophores pyoverdine and enantio-pyochelin to fitness in soil of *Pseudomonas protegens* Pf-5. *Curr. Microbiol.* **2018**, *75* (12), 1560-1565. DOI: 10.1007/s00284-018-1560-7.

(25) Meyer, J. M.; Abdallah, M. A. The fluorescent pigment of *Pseudomonas fluorescens*: biosynthesis, purification and physicochemical properties. *Microbiology* **1978**, *107* (2), 319-328. DOI: 10.1099/00221287-107-2-319.

(26) Albrecht-Gary, A.-M.; Blanc, S.; Rochel, N.; Ocaktan, A. Z.; Abdallah, M. A. Bacterial iron transport: coordination properties of pyoverdin PaA, a peptidic

siderophore of *Pseudomonas aeruginosa*. *Inorg. Chem.* **1994**, *33* (26), 6391-6402. DOI: 10.1021/ic00104a059.

(27) Braud, A.; Hannauer, M.; Mislin, G. L.; Schalk, I. J. The *Pseudomonas aeruginosa* pyochelin-iron uptake pathway and its metal specificity. *J Bacteriol* **2009**, *191* (11), 3517-3525. DOI: 10.1128/jb.00010-09

(28) Loper, J. E.; Henkels, M. D.; Rangel, L. I.; Olcott, M. H.; Walker, F. L.; Bond, K. L.; Kidarsa, T. A.; Hesse, C. N.; Sneh, B.; Stockwell, V. O.; et al. Rhizoxin analogs, orfamide A and chitinase production contribute to the toxicity of *Pseudomonas protegens* strain Pf-5 to Drosophila melanogaster. *Environ. Microbiol.* **2016**, *18* (10), 3509-3521. DOI: 10.1111/1462-2920.13369.

(29) Yen, L.-T. Evaluation of nano-metavivianite and nano-chitosan-coated metavivianite for alleviating salt stress in winter wheat and bean. Utah State University, 2024.

(30) Sparks, D. CuO nanoparticles solubility as influenced by soil pore water, native microorganisms, and wheat rhizosphere chemistry in a sand matrix. Utah State University, All Graduate Theses and Dissertations, 2023.

(31) Hortin, J. M.; Anderson, A. J.; Britt, D. W.; Jacobson, A. R.; McLean, J. E. Copper oxide nanoparticle dissolution at alkaline pH is controlled by dissolved organic matter: influence of soil-derived organic matter, wheat, bacteria, and nanoparticle coating. *Environ.-Sci. Nano* **2020**, *7* (9), 2618-2631. DOI: 10.1039/d0en00574f.

(32) Gavlak, R. G.; Horneck, D. A.; Miller, R. O.; Center, W. R. D.; Fertilizer, F. W.; Association, A. *Plant, soil, and water reference methods for the western region*; Western Rural Development Center, 2013.

(33) Gerwing, J.; Gelderman, R. *Fertilizer Recommendations Guide*; Department of Agronomy, Horticulture & Plant Science, College of Agriculture, Food & Environmental Sciences, South Dakota State University, 2023. https://www.nrcs.usda.gov/sites/default/files/2023-06/EC750_2023.pdf.

(34) Li, P.-C.; Liao, G. M.; Kumar, S. R.; Shih, C.-M.; Yang, C.-C.; Wang, D.-M.; Lue, S. J. Fabrication and characterization of chitosan nanoparticle-incorporated quaternized poly(vinyl alcohol) composite membranes as solid electrolytes for direct methanol alkaline fuel cells. *Electrochim. Acta* **2016**, *187*, 616-628. DOI: 10.1016/j.electacta.2015.11.117.

(35) Liao, G.-M.; Yang, C.-C.; Hu, C.-C.; Pai, Y.-L.; Lue, S. J. Novel quaternized polyvinyl alcohol/quaternized chitosan nano-composite as an effective hydroxide-conducting electrolyte. *J. Membr. Sci.* **2015**, *485*, 17-29. DOI: 10.1016/j.memsci.2015.02.043.

(36) Yamashita, T.; Hayes, P. Analysis of XPS spectra of Fe^{2+} and Fe^{3+} ions in oxide materials. *Appl. Surf. Sci.* **2008**, *254* (8), 2441-2449. DOI: 10.1016/j.apsusc.2007.09.063.

(37) Peng, B.; Xu, Y.; Liu, K.; Wang, X.; Mulder, F. M. High-performance and low-cost sodium-ion anode based on a facile black phosphorus−carbon nanocomposite. *ChemElectroChem* **2017**, *4* (9), 2140-2144. DOI: 10.1002/celc.201700345.

(38) Rouhani Shirvan, A.; Shakeri, M.; Bashari, A. Recent advances in application of chitosan and its derivatives in functional finishing of textiles. In *The Impact and Prospects of Green Chemistry for Textile Technology*, Shahid ul, I., Butola, B. S. Eds.; Woodhead Publishing, 2019; pp 107-133.

(39) Schütze, E.; Gypser, S.; Freese, D. Kinetics of phosphorus release from vivianite, hydroxyapatite, and bone char influenced by organic and inorganic compounds. *Soil Syst.* **2020**, *4* (1), 15.

(40) Michavila, G.; Adler, C.; De Gregorio, P. R.; Lami, M. J.; Caram Di Santo, M. C.; Zenoff, A. M.; de Cristobal, R. E.; Vincent, P. A. *Pseudomonas protegens* CS1 from the lemon phyllosphere as a candidate for citrus canker biocontrol agent. *Plant Biol.* **2017**, *19* (4), 608-617. DOI: 10.1111/plb.12556.

(41) Mendonca, C. M.; Yoshitake, S.; Wei, H.; Werner, A.; Sasnow, S. S.; Thannhauser, T. W.; Aristilde, L. Hierarchical routing in carbon metabolism favors iron-scavenging strategy in iron-deficient soil *Pseudomonas* species. *Proc. Natl. Acad. Sci.* **2020**, *117* (51), 32358-32369. DOI: 10.1073/pnas.2016380117.

(42) Yang, S. Y.; Yang, X. F.; Zhang, C. Y.; Deng, S. Y.; Zhang, X. R.; Zhang, Y.; Cheng, X. Significantly enhanced P release from vivianite as a fertilizer in rhizospheric soil: Effects of citrate. *Environ. Res.* **2022**, *212*, 113567. DOI: 10.1016/j.envres.2022.113567.

(43) Ha, N.; Nguyen, T.; Wang, S.-L.; Dzung, N. Preparation of NPK nanofertilizer based on chitosan nanoparticles and its effect on biophysical characteristics and growth of coffee in green house. *Res. Chem. Intermed.* **2019**, *45*. DOI: 10.1007/s11164-018-3630-7.

(44) Choudhary, R. C.; Kumaraswamy, R. V.; Kumari, S.; Sharma, S. S.; Pal, A.; Raliya, R.; Biswas, P.; Saharan, V. Zinc encapsulated chitosan nanoparticle to promote maize crop yield. *Int. J. Biol. Macromol.* **2019**, *127*, 126-135. DOI: 10.1016/j.ijbiomac.2018.12.274.

(45) Deshpande, P.; Dapkekar, A.; Oak, M. D.; Paknikar, K. M.; Rajwade, J. M. Zinc complexed chitosan/TPP nanoparticles: A promising micronutrient nanocarrier suited for foliar application. *Carbohydr. Polym.* **2017**, *165*, 394-401. DOI: 10.1016/j.carbpol.2017.02.061.

(46) Kpomblekou-A, K.; Tabatabai, M. A. Effect of low-molecular weight organic acids on phosphorus release and phytoavailabilty of phosphorus in phosphate rocks added to soils. *Agric. Ecosyst. Environ.* **2003**, *100* (2), 275-284. DOI: 10.1016/S0167-8809(03)00185-3.

CHAPTER 3

***Pseudomonas protegens* Pf-5 mitigate salinity stress in wheat grown with nano-metavivianite and nano-chitosan-coated metavivianite as Fe amendments**

3.1 Abstract

In arid and semi-arid regions, soil salinity and iron (Fe) deficiency significantly hinder agricultural productivity. Fe, essential for plant and microbial growth, is often applied in agriculture as soluble chelated Fe, which is prone to leaching in high-pH calcareous soils. This study explores the use of nano-sized metavivianite ($Fe^{II}Fe_2^{III}$ $(PO_4)_2(OH)_2 \cdot 6H_2O$; metaVT) as an alternative Fe amendment. In an attempt to optimize the efficacy of the amendment, we employed chitosan (CT), recognized for its biocompatibility and non-toxicity, as a positively charged coating for nano-metaVT. In a modified half-strength Hoagland solution (½HS), the culturability of *Pseudomonas protegens* Pf-5 (*Pp* Pf-5) improved with Fe-EDDHA and nano-metaVT addition and even more so under saline conditions with nano-metaVT. Wheat was grown in sand with ½HS and supplemented with *Pp* Pf-5 to model nutrient competition and growth enhancement by the soil microbe. The salinity stress (EC= 10 dS·m^{-1}; pH= 8.4) was imposed by added sodium (Na) and calcium (Ca) salts. The results show that nano-CT-metaVT and Fe-EDDHA-treated wheat have longer shoot lengths than the controls. Wheat inoculated with *Pp* Pf-5 exhibits approximately 2.3 to 2.9 times higher transpiration rates than wheat grown without microbial inoculation. This elevated transpiration rate suggests mitigation of salinity stress with microbial colonization of the wheat plants. However, Fe additions do not have any effect despite wheat root colonization and nano-CT-metaVT particle's presence on the roots, as confirmed via EDS analyses. While the various iron sources had

minimal impacts on wheat growth over the 14-day study, the findings highlight the potential of *Pp* Pf-5 inoculation as a strategy to mitigate salinity stress in wheat, warranting further investigation in future studies.

Keywords: chitosan coating, iron deficiency, metavivianite, *Pseudomonas protegens* Pf-5, salinity stress, wheat

3.2 Introduction

Soil salinity is a global issue because of its negative impact on agricultural production, especially in arid and semi-arid areas. More than 20% of soils worldwide are salt-affected, with levels continuously increasing owing to anthropogenic activities and climate change (Jesus et al., 2015; Okur and Örçen, 2020). Excess salt accumulation obstructs the growth of crops by limiting their ability to take up water, resulting in an ion imbalance (Abdoli et al., 2020). An adequate iron (Fe) supply is beneficial for plants experiencing salinity stress (Rabhi et al., 2007). For example, Mozafari et al. (2018) showed that the application of Fe nanoparticles (0.8 ppm) to grapes (*Vitis vinifera* L. cv. Merlot' Khoshnaw') growing under salinity stress increased their contents of free proline and total protein as well as their enzymatic antioxidant activity.

In arid and semi-arid regions, Fe deficiency is a common problem (Abadia et al., 2011). Carbonate-rich soils in the semi-arid Western U.S. have characteristics rarely found in humid regions (Weil and Brady, 2017). Calcium carbonate accumulation often occurs in these soils, forming calcic horizon in the soil profile (Durand et al., 2018). In addition, the cations released by mineral weathering accumulate instead of leaching out of the profile because of the low precipitation and high evapotranspiration. Therefore, the

pH values of soils in arid and semi-arid environments are generally 7 or above. Inorganic

Fe is quickly rendered unavailable due to the rapid formation of iron hydroxides in a

$pH_{\text{saturated paste extract}}$ 8 soil, the free Fe^{3+} concentration is around $10^{-21.3}$ M, and the total

soluble Fe is around $10^{-10.2}$ M (Kim and Guerinot, 2007). Microbes require total soluble

Fe concentrations of 10^{-7}–10^{-5} M, and plants require 10^{-9}–10^{-4} M in the soil solution for

optimal growth (Lemanceau et al., 2009; Schenkeveld, 2010), which is approximately

10^1–10^6 higher than the total soluble Fe concentration in alkaline soil solution. Fe

participates in essential metabolic processes (Brittenham, 1994; Kobayashi and

Nishizawa, 2012; Morrissey and Guerinot, 2009). Plants and microbes acquire Fe via

different strategies, such as the production of siderophores or through rhizosphere

acidification. Conventional amendment with synthetic Fe-chelates is commonly used to

prevent Fe deficiencies in calcareous soils (Rajaie and Tavakoly, 2018). However, within

one day of application, a decline in Fe concentration was found in soil solutions treated

with Fe-EDDHA, and one of the Fe-EDDHA components, *o,p*-Fe-EDDHA, revealed the

tendency to exchange Fe for Cu (Schenkeveld et al., 2012). The high solubility of Fe-

chelates also implies potentially high-risk mobilization and subsequent leaching of metals

into groundwater. Therefore, researchers are still looking for natural, high-purity, slow-

release Fe fertilizers that are environmentally friendly (Abadia et al., 2011).

Vivianite ($Fe^{II})_3(PO_4)_2 \cdot 8H_2O$; VT) is an Fe phosphate mineral that usually occurs

in reduced sediments. The partially oxidized form of vivianite, metavivianite

($Fe^{II}Fe_2^{III}(PO_4)_2(OH)_2 \cdot 6H_2O$; metaVT), is more common in an aerobic environment

where it remains stable for extended periods of time (Rouzies and Millet, 1993). MetaVT

can also be recovered from secondary sewage effluent, which often has a high

phosphorus content (Feigin et al., 1991; Jowett et al., 2018). Lin et al. (2017) demonstrated that 31% of the phosphorus in sludge can be recovered as vivianite through a chemically enhanced primary sedimentation process. MetaVT has shown the potential to provide Fe in calcareous soil (Ammari and Hattar, 2011; Bavaresco et al., 2010; Diaz et al., 2010).

Current agricultural production relies on chemical fertilizers to fulfill the growing demand for food (Zhang et al., 2015), however, low nutrient use efficiency and over-application of chemical fertilizers compromise soil health (Fess et al., 2011). Therefore, there is great interest in applying nano fertilizers to increase fertilizer use efficiency, lower applied fertilizer doses, and minimize volatilization and leaching (Seleiman et al., 2021). With a high surface area to volume ratio, nano-sized particles exhibit properties distinct from conventional bulk fertilizers. Thus, the application of nano fertilizer has the potential to promote sustainability in agriculture. Additional attempts to improve the efficiency of Fe amendments in soils focus on modifying the nano-fertilizer surface. Nano fertilizers modified by polymer coatings can slow down the release of nutrients, improve fertilizer utilization, and reduce leaching losses of fertilizers (An et al., 2022). Our goal is to maximize interaction between plant roots and the nano-fertilizer in the rhizosphere and minimize losses due to sorption to soil particle surfaces or leaching. Since nano-metaVT has a negative surface charge, we investigated positively-charged chitosan (CT), the N-deacetylated derivative of chitin, as a possible surface coating. CT was selected based on its biodegrading ability, low cost, non-toxic properties (Mikula et al., 2020), and insolubility under alkaline conditions ($>$ pH 6). CT was used as a surface coating material for nano-metaVT in this study. Both nano-metaVT and nano-CT-

metaVT prepared in this study have one dimension in the nano-size range, and their effectiveness was evaluated and compared to a conventional Fe-chelate, Fe-EDDHA, in a sand culture pot system.

Many rhizobacteria promote plant growth and protect the plant from abiotic stresses by providing access to nutrients otherwise unavailable to roots (Backer et al., 2018; Singh et al., 2018). In return, these symbiotic bacteria receive photosynthetically derived carbon in the form of sugars, amino acids, and organic acids from plant root exudates (Anderson et al., 2023; Canarini et al., 2019; Shinde et al., 2017). *Pseudomonas protegens* is a gram-negative, soil-dwelling bacterium with biological control activity (Balthazar et al., 2022; Ruiu and Mura, 2021). *Pseudomonas protegens* (*Pp* Pf-5) produces several types of siderophores for Fe chelation, including pyoverdines (Pvds) and enantio-pyochelin (E-Pch) (Drehe et al., 2018). Previous studies have shown the potential of *Pp* Pf-5 to promote the growth of plants by producing siderophores and enzymes that can inactivate pathogens (Ruiu and Mura, 2021). Additionally, there is an overexpression of certain genes and proteins associated with the synthesis of secondary metabolites under Fe-limited conditions. *Pp* Pf-5 is also reported to produce chitinase which can degrade fungal cell walls and cause the cell lysis of fungal pathogens (Lim et al., 2012). However, understanding the effect of salinity stress on *Pp* Pf-5 and plants supplied with various sources of Fe remains unclear.

This study investigates the effect of *Pp* Pf-5 inoculation on wheat grown in a sand matrix amended with nano-metaVT, nano-CT-metaVT, or commercial Fe-EDDHA. A gnotobiotic growing system using silica sand as the growth matrix was used in this experiment to avoid the complexity of working with intact soils. The pH of the modified

(Fe-deficient) half-strength Hoagland solution was adjusted to pH 8.4 to simulate the pH value in calcareous soil. Salinity stress (EC = 10 dS·m^{-1}) was also applied to the wheat system to explore the interaction between *Pp* Pf-5 and wheat under abiotic stress with the presence of different Fe sources. We hypothesize that Fe amendment benefits *Pp* Pf-5 in ½HS suspensions under salinity stress. Moreover, compared to the negative control, nano-metaVT and nano-CT-metaVT improve Fe uptake and mitigate the salinity stress in wheat grown for 14 days. Finally, *Pp* Pf-5 improves Fe uptake and mitigates the salinity stress, compared to control, in wheat grown for 14 days. Our study provides insight into the effectiveness of nano-metaVT and nano-CT-metaVT for Fe supply and the effects of root colonization by *Pp* Pf-5 on wheat growth under salinity stress.

3.3 Materials and Methods

3.3.1 Bacterial culturability with various Fe sources under salinity stress

To evaluate the effects of Fe and salinity on culturable *Pp* Pf-5 (CFU mL^{-1}) in modified half-strength Hoagland solution (½HS), treatments with triplicates were conducted in sterile polypropylene 250-mL bottles in a 4×2 factorial design with eight treatments. The treatments were unamended controls; the presence/absence of the Fe sources, including nano-metaVT, nano-CT-metaVT, and Fe-EDDHA, at 33.3 mg Fe L^{-1}; and the presence/absence of salinity stress. The growth broth was ½HS with 1 g L^{-1} sucrose added as a carbon source. The initial bacterial concentration of *Pp* Pf-5 was 1.0×10^6 CFU mL^{-1}. The cultures were shaken at 100 rpm in the dark throughout the reaction. Aliquots were removed at 0 and 72 h, and culturable cells were determined by plating serial dilutions onto tryptic soy agar (TSA) plates to determine the bacterial CFU mL^{-1}.

Sterilized double-deionized water (resistance > 18 MΩ cm) was used to prepare a

½HS solution. The ½HS with the composition reported in Potter et al. (2021) was

modified by the omission of ferric chloride ($FeCl_3 \cdot 6H_2O$) (Table B3-1) and had a pH of

5.3 and EC of 1.3 dS·m^{-1} adjusted to pH 8.4 with 0.5 M KOH.

3.3.2 Wheat growth experiment

3.3.2.1 Wheat (*Triticum aestivum*)

Winter wheat (*Triticum aestivum* cv. Juniper) seeds harvested in 2018 were

surface-disinfected in fresh 10% H_2O_2 for 15 minutes, then rinsed ten times using sterile

double-deionized water. Ten seeds selected at random were placed on LB plates, then

sealed with a parafilm and incubated at 23 °C for 48 h to confirm the absence of

microbial contaminants. Quartz sand (4075; Unimin Corp; New Canaan, CT, USA) was

washed with double-deionized water, then heated at 550 °C in a muffle furnace for 8 h to

remove residual organic matter and to sterilize. Then sand matrix, 300 g, was mixed with

nano-metaVT, nano-CT-metaVT, or Fe-EDDHA (Sequestrene$^{™}$ 138, $C_{18}H_{16}FeN_2O_6 \cdot Na$)

at a dose of 5 mg Fe kg^{-1} and transferred to acid-washed, sterile, magenta boxes (V8505,

$10 \times 7 \times 7$ cm, Sigma-Aldrich, St Saint Louis, MO, USA). The treatments with triplicates

were conducted in magenta boxes using a $4 \times 2 \times 2$ factorial design with 16 treatments.

The treatments were the presence/absence of the Fe sources, nano-metaVT, nano-CT-

metaVT, or Fe-EDDHA, each at 5 mg Fe kg^{-1}; the presence/absence of *Pp* Pf-5; and the

presence/absence of salinity stress. The effectiveness of nano-metaVT and nano-CT-

metaVT is expected to be better than that of the positive control (without Fe) and

comparable to that of the positive control, Fe-EDDHA.

3.3.2.2 Growth conditions and the salinity stress treatment

In this study, salinity stress was induced by adding NaCl and CaCl$_2$, at a molar concentration ratio of 2:1, to the ½HS (pH 8.4), achieving EC values of 10 dS·m^{-1}. This specific salinity level, 10 dS·m^{-1}, was selected based on preliminary experiments identifying it as a concentration that significantly impairs Juniper wheat growth. The saline ½HS contained 42 mM NaCl and 21 mM CaCl$_2$. Each growth box was filled with 45 mL sterilized, ½HS (EC = 1.3 dS·m^{-1}) or saline ½HS (EC = 10 dS·m^{-1}) to achieve 150% of its field capacity (0.15 g H$_2$O g^{-1} sand). Field capacity was measured with a soil tensiometer. The matrix is considered to be at field capacity when the water potential in the sand is at -33 kPa. Ten surface-sterilized seeds were placed in the sand matrix at an approximate depth of 5 mm and lightly covered with sand. The treatments with the added soil microbe, *Pp* Pf-5, were inoculated by injecting 0.45 mL aliquots of a 2×10^6 CFU mL^{-1} bacterial suspension into the box, making an initial bacterial concentration in each magenta box of about 2.0×10^4 CFU mL^{-1}.

Wheat was grown for 14 d in an environmental growth chamber at 25 ± 2 °C, under high-energy sodium lights (Yescom USA Inc., City of Industry, CA, USA) and fluorescent lamps (F54W/T5/841/ECO, GE 46761) with 16/8 h light/dark photocycle periods. The light panels were fixed at approximately 70 cm above the base of the pots with an average photon flux of 350 µmol^{-1} m^{-2} s^{-1}. After growing for 9 d, the lids of the magenta boxes were removed when the shoot tips were about to hit the top of the boxes. Plants were watered daily with sterile double-deionized water to replace water lost through evapotranspiration gravimetrically. The masses of the magenta boxes were recorded every day after removing the lid to calculate the water lost from evaporation

(W_E) and plant transpiration (W_T). Another set of experiments was conducted with the same condition, but with no plants growing in the magenta boxes to calculate the water loss from the nonplanted growth matrix via evaporation (W_E), then the water loss from plant transpiration (W_T) was estimated as:

$$W_T = W_{Total} - W_E$$

where W_{Total} represents the total water loss (g) in the magenta boxes with wheat growing; W_E represents the average of water loss via evaporation (g) in the magenta boxes without wheat growing.

3.3.2.3 Harvesting methods and determination of growth attributes

At day 14 after seed planting, sterile deionized water was added to each Magenta box to bring the sand water content to 300% of sand field capacity and allowed to equilibrate for 15 minutes. This process resulted in a total of 90 mL of solution in each box, ensuring a sufficient volume of sand pore water for subsequent analyses. The shoot tissue was cut above the coleoptiles, and the shoot length and the fresh mass were measured. The roots were carefully removed from the sand, and root-adhering sand was returned to the sand retained in the box. After uprooting the wheat root tissue from the growth box, the sand pore water of the sand with *Pp* Pf-5 inoculated treatments was extracted and was serially diluted and cultured on the TSA medium. The root tissue was rinsed with sterilized deionized water and placed on tissue paper to absorb the excess water before measuring the root length and root fresh mass. The shoot and root tissues were oven-dried at 60 °C for at least 48 h before the determination of the dry mass.

3.3.3 Elemental analysis of plant tissue

To analyze root and shoot tissue for Fe and P concentrations, the dried plant tissue was weighed (about 0.2 g) and digested with nitric and perchloric acids based on the method described by Zasoski and Burau (1977). The samples were filtered through a 25 mm nylon syringe filter with a 0.22 µm pore size (Thermo Scientific, Waltham, MA, USA) and stored in scintillation vials. The Fe, P, Na, and K concentrations in the digested solution were determined by an inductively coupled plasma mass spectrometer (Agilent 7700x Agilent technologies, Santa Clara, CA, USA).

3.3.4 Root tissue observation via SEM and EDS

The wheat root with *Pp* Pf-5 inoculated treatments was further observed by scanning electron microscopy (SEM, Quanta FEG 650, Field Electron and Ion Company, Hillsboro, OR, USA) and energy dispersive X-ray spectroscopy (EDS, Oxford Instruments, Abingdon-on-Thames, UK) for microbe colonization. The root tissue was prepared following the protocol described by Neinhuis and Edelmann (1996) and observed by SEM. Briefly, root sections from the fine root were immersed in 100% dry methanol for 10 minutes, followed by 100% dry ethanol for 30 minutes, and then transferred to a fresh ethanol solution for 30 min. The samples were critical-point-dried with ethanol as the transitional fluid before being sputter-coated with a 10-nm layer of gold and palladium using a rotary sputter coater system EMS150R ES (Electron Microscopy Sciences, Hatfield, PA). The coated samples were viewed in a SEM under a high vacuum at an accelerating voltage of 20 kV. The nano-metaVT and nano-CT-metaVT particles on the root surface with and without salinity stress were analyzed for elemental composition via EDS using an X-Max detector.

3.3.5 Data analysis

The experimental design for the wheat growth study was structured according to a randomized complete block design (RCBD) with three trials (blocks) per treatment. Three trials (blocks) were conducted, resulting in nine experimental units (n = 9) per treatment. This design allowed for the control of variability within the experimental blocks. Plant growth parameters, physiological measurements, and elemental analyses were subjected to statistical evaluation using a three-way Analysis of Variance (ANOVA) performed with SAS software (SAS® Studio, release 3.81, Enterprise Edition, Madison, WI, USA). Diagnostics of residuals did not reveal a departure from normality and nonconstant variances, except for the shoot and root sodium (Na) concentrations. Shoot and root sodium (Na) concentrations were log-converted before the data analysis. The adjusted Tukey-Kramer multiple comparison procedure was employed to discern significant differences between treatment means, with a significance level set at 0.05.

For the bacterial culturability experiment, a completely randomized design (CRD) was implemented with three replications (n = 3). The bacterial concentration data obtained were log-transformed and statistically analyzed using two-way ANOVA with SAS software (SAS® Studio). Significant differences among treatment means were determined using the adjusted Tukey-Kramer multiple comparison procedure, with the level of significance maintained at $\alpha \leq 0.05$.

3.4 Results and Discussions

3.4.1 Bacterial culturability with various Fe sources

Previous results show that *Pp* Pf-5 inoculation increased the total soluble Fe in the nano-metaVT-soil saturated paste extract (SPE) and nano-CT-metaVT-SPE compared with wheat grown without *Pp* Pf-5 (section 2.4.2.3). Fig. 3-1 shows the *Pp* Pf-5 culturability results of shaken liquid culture studies investigating the effect of Fe sources on the growth of *Pp* Pf-5 in ½HS with sucrose as a carbon source. Overall, the higher bacterial culturability at 72 h, about 10–100 times than culturability at 0 h, can be observed with the absence of salinity stress (EC = 1.3 dS·m^{-1}) (Fig. 3-1a). Significantly, higher culturable cell numbers occur in the presence of nano-metaVT, 7.9-log CFU mL^{-1}, and to a greater extent Fe-EDDHA, 8.3-log CFU mL^{-1}, but the addition of nano-CT-metaVT failed to boost growth. In Fig. 3-1b, the bacterial culturability of the control treatments drops from 6.0-log to 5.3-log CFU mL^{-1} at 72 h under salinity stress (EC = 10 dS·m^{-1}), while Fe treatments have a significantly higher bacterial culturability of about 7-log CFU mL^{-1}, regardless the type of Fe sources. This finding is consistent with the essential role of Fe in bacterial metabolism. The positive effect of nano-metaVT and Fe-EDDHA on the soil bacterium culturability in suspension might also extend to the soil environment, but this has yet to be determined.
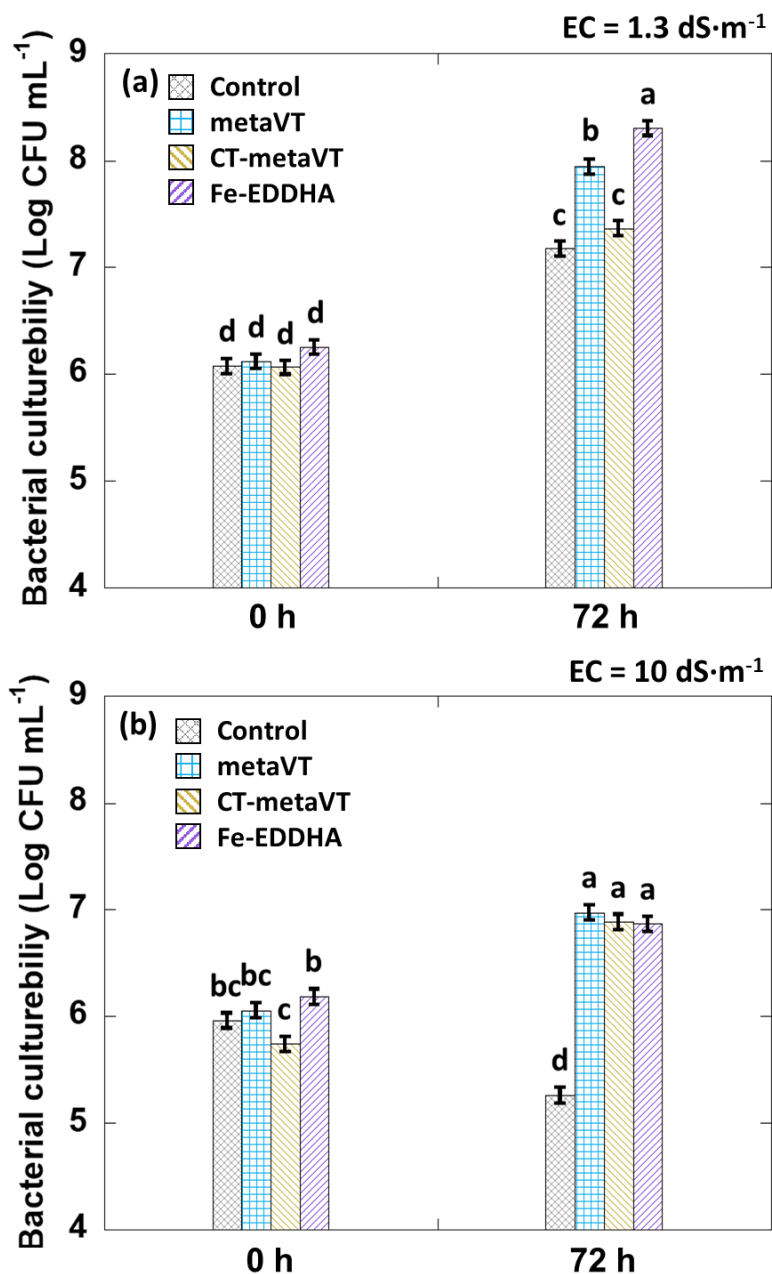
Fig. 3-1. Bacterial culturability of *Pp* Pf-5 with various Fe sources with a dose of 33.3 mg Fe L^{-1} without salinity stress (EC = 1.3 dS·m^{-1}) (a), and under salinity stress (EC = 10 dS·m^{-1}) (b). A two-way ANOVA was performed. Different letters above the columns represent significant differences based on the Tukey-Kramer test ($\alpha \leq 0.05$). Error bars represent the standard error calculated from the statistical model.

3.4.2 Effect of *Pp* Pf-5 inoculation on wheat with the presence of different Fe sources

Salinity stress adversely impacts plant growth through mechanisms such as the accumulation of Na^+ in plant tissues, leading to nutrient imbalances and affecting critical physiological processes, such as transpiration (Harris et al., 2010; Pour-Aboughadareh et al., 2021; Saqib et al., 2013). Fig. 3-2 depicts the effects of various Fe sources, salinity levels, and the presence of *Pp* Pf-5 on the wheat growth. Fig. 3-2a shows that the shoot length of the wheat is affected by the different Fe sources, salinity stress, and *Pp* Pf-5 inoculation, but there is no interaction between the three factors. Both the nano CT-metaVT and Fe-EDDHA treatments have longer shoot lengths than the negative control; *Pp* Pf-5 inoculated wheat has longer shoot lengths than the no-microbe treatment. Moreover, the Fe-EDDHA treatment exhibits greater shoot dry mass than the negative control (Fig. 3-2b) but not the nano-metaVT and nano-CT-metaVT treatments. Similarly, there is no significant difference in shoot dry mass between *Pp* Pf-5 inoculation and the no-microbe treatments.

Wheat under salinity stress transpired less than wheat grown without salinity stress across all the Fe treatments. Interestingly, wheat inoculated with *Pp* Pf-5 exhibits approximately 2.3 to 2.9 times higher transpiration rates than wheat grown without microbial inoculation. However, Fe additions do not have any effect (Fig. 3-2c). This elevated transpiration rate suggests mitigation of salinity stress with microbial colonization of the wheat plants. Previous research by Harris et al. (2010) reported that salinity at an EC of 15 dS·m^{-1} resulted in a lower grain yield in wheat, primarily due to the reduced biomass associated with decreased transpiration. In contrast, the current

study's observation of higher transpiration and increased shoot length in *Pp* Pf-5 inoculated wheat suggests a mitigating effect on the salinity stress.

Research on other *P. protegens* isolates, SN15-2 and CHA0, suggests multiple adaptive strategies to hyperosmotic conditions, including cytoplasmic K^+ accumulation, compatible solute synthesis, Na^+ ion exclusion, and membrane alteration (Wang et al., 2020). The isolate *P. protegens* CHA0 also significantly improves the growth of pea and its salinity tolerance under hydroponic conditions (Patel et al., 2023). Despite extensive research on the anti-pathogen ability of *Pp* Pf-5 (Rathore et al., 2020; Sexton et al., 2017), anti-fungal (Balthazar et al., 2022), and bio-control (Loper et al., 2016; Ruiu and Mura, 2021) properties, studies specifically investigating *Pp* Pf-5's salt tolerance are limited (see Table 3-1). It is promising to explore further the mechanisms that *Pp* Pf-5 contributes to reduced Na uptake in wheat shoot tissues, thereby alleviating salt stress.
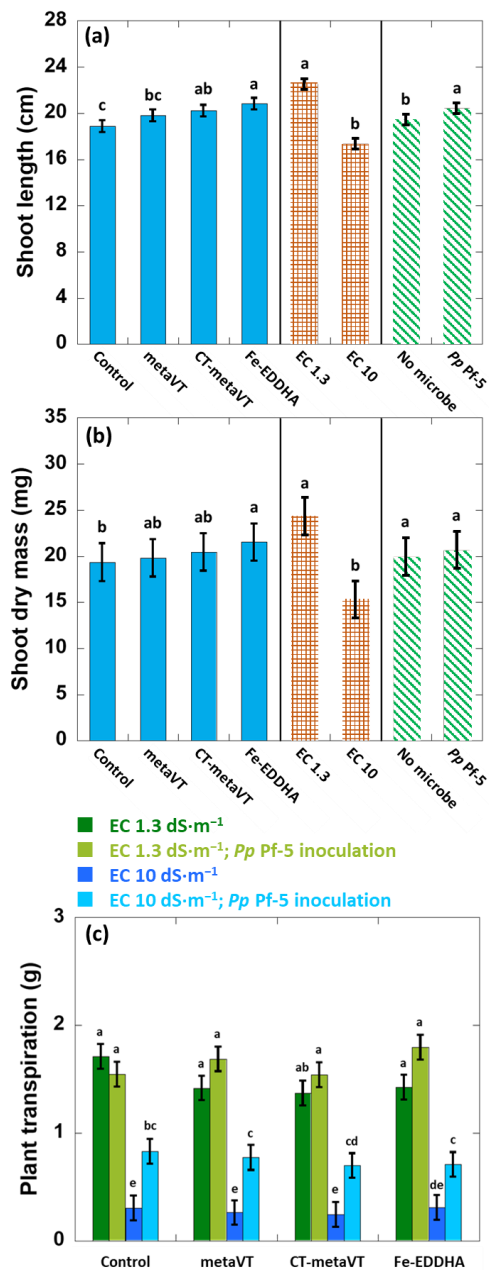
Fig. 3-2. Shoot length (a), dry mass (b), and plant transpiration (c) of wheat grown in the sand with the four Fe treatments (control, nano-metaVT, nano-CT-metaVT, and Fe-EDDHA). A three-way ANOVA was performed. Different letters above columns represent significant differences based on the Tukey test ($\alpha \le 0.05$). Error bars represent the standard error calculated from the statistical mix model.

Table 3-1. Summarization of recent studies related to *Pseudomonas protegens*.

Microbe	Bacterial concentration	Target	Performance	References
Improve the plant growth				
Pseudomonas protegens Pf-5	10^4 CFU ml^{-1}	Wheat (*Triticum aestivum* v. Juniper, winter wheat)	Wheat grown in the sand at pH 8.4 and inoculated with *Pp* Pf-5 showed the potential to mitigate the salinity stress (42 mM NaCl and 21 mM CaCl$_2$) by increasing the plant transpiration **(see section 3.4.1)**.	**This study**
Pseudomonas protegens CHA0	2.4×10^8 CFU ml^{-1}	Pea (*Pisum sativum*)	*Pp* CHA0 greatly improved the growth and tolerance against salinity of pea plants grown in hydroponic conditions.	(Patel et al., 2023)
Pseudomonas protegens Pf-5	NA	Cumin (*Cuminum cyminum* L)	*Pp* Pf-5 exhibited the highest *in vitro* growth inhibition (82 %) against *Fusarium oxysporum* f. sp. *cumini* (*Foc*), the causal pathogen of cumin wilt. *Pp* Pf-5 produced high protease and chitinase activities. *Pp* Pf-5 antagonism of *Foc* growth correlated with decreased production of cellulase and polygalacturonase, enzymes important in plant cell wall degradation.	(Rathore et al., 2020)
Pseudomonas protegens Pf-5	4×10^9 CFU ml^{-1}	Aspen seeds (*Populus tremuloides* Michx.)	*Pp* Pf-5 colonization increased root length (2.3-fold) and root mass (4.5-fold) under low P compared to growth without microbial inoculation.	(Shinde et al., 2017)
Bio-control for pathogens				
Pseudomonas protegens Pf-5	10^5 CFU ml^{-1}	Cannabis crops (*Cannabis sativa* L.)	*Pp* Pf-5 has biocontrol activity against cannabis fungal pathogens, including *Botrytis cinerea*.	(Balthazar et al., 2022)
Pseudomonas protegens Pf-5	NA	*Pseudomonas aeruginosa* PAO1	The success of *Pp* Pf-5 against inter-species competitor *P. aeruginosa* PAO1 was contingent on its production of a pyoverdine siderophore for Fe chelation.	(Sexton et al., 2017)
Pseudomonas protegens Pf-5	NA	genus *Fusarium*	Secretion of the siderophore pyoverdine was observed when *Pp* Pf-5 was grown in the presence of fusaric acid. Fe sequestration partly accounts for the resistant mechanism against the mycotoxin in *Pp* Pf-5.	(Ruiz et al., 2015)

Bio-control for insects				
Pseudomonas protegens Pf-5	10^8 CFU ml^{-1}	*Musca domestica* and *Lucilia caesar* larvae	*Pp* Pf-5 caused 100% mortality toward *Musca domestica* and *Lucilia Caesar*.	(Ruiu and Mura, 2021)
Pseudomonas protegens Pf-5	NA	*Drosophila melanogaster*	Extracellular chitinase, the secretion of rhizoxin analogs, and orfamide A contribute to this oral toxicity of *Pp* Pf-5 to the common fruit fly, *D. melanogaster*.	(Loper et al., 2016)
Pseudomonas protegens bacterium studies				
Pseudomonas protegens SN15-2	NA	NA	Results indicated *P. protegens* SN15-2 utilizes multiple strategies for adaptation to hyperosmotic growth environments (450 mM NaCl), including (i) accumulating high cytoplasmic concentrations of K$^+$, (ii) accumulating low molecular mass compatible solutes, (iii) exclusion of excess Na$^+$ ion in cells, (iv) altering membrane composition.	(Wang et al., 2020)
Pseudomonas protegens Pf-5	NA	NA	Biosynthesis of secondary metabolites with biocontrol activity. 2,4-diacetylphloroglucinol (DAPG), or famine A and pyrrolnitrin, as well as a chitinase, were over-expressed under the Fe-limited condition.	(Lim et al., 2012)

3.4.3 Elemental analysis of plant tissue

Elemental analysis of wheat shoot tissues, both under normal and salinity stress conditions, shows that growth with Fe-EDDHA consistently results in significantly higher Fe concentrations in the shoot tissues compared to the control, with or without *Pp* Pf-5 inoculation (Fig. 3-3a). Interestingly, such an increase in Fe concentration is not observed in the wheat shoots treated with nano-metaVT and nano-CT-metaVT over the 14-day growth period. This could be attributed to the nature of nano-metaVT and nano-CT-metaVT as mineral forms of Fe that require weathering or dissolution before plant uptake, suggesting the 14 d period in the sand growth matrix may have been insufficient to observe notable differences in shoot Fe content. Regarding Na uptake, significantly higher levels than nano-metaVT and nano-CT-metaVT were detected in the Fe-EDDHA treatment combined with *Pp* Pf-5 inoculation (Fig. 3-3b) at EC of 1.3 dS·m^{-1}. This might be due to the presence of Na in the Fe-EDDHA (Sequestrene 138, $C_{18}H_{16}FeN_2O_6 \cdot Na$).

Fig. 3-3c presents the elemental analysis of wheat root tissues grown under both non-saline and saline conditions and with and without *Pp* Pf-5 inoculation. At low EC, wheat treated with Fe-EDDHA exhibits significantly higher concentrations of Fe in root tissues compared to the control, regardless of *Pp* Pf-5 inoculation. However, under salinity stress, Fe concentrations in root tissues are not notably influenced by either the Fe amendments or the presence of *Pp* Pf-5, as compared to the control. This observation parallels the findings in shoot tissues (Fig. 3-2a), where increases in Fe concentrations with nano-metaVT and nano-CT-metaVT treatments were not detected over the 14-day growth period. This lack of increase could be attributed to the slow weathering or dissolution of the nano-metaVT and nano-CT-metaVT amendments within this relatively

short timeframe. According to the Utah Fertilizer Guide, the critical nutrient concentrations for wheat at the early boot stage are 0.15-0.20% P and 1.5-2.0% K on a dry weight basis, with foliar tissue requiring 50-60 mg Fe kg^{-1} dry weight basis. Elemental analysis of wheat shoot tissues, as shown in Fig. 3-3a (Fe), and appendix Figs. B3-5a (P), and B3-6a (K), indicate that the wheat plants maintained adequate levels of Fe, P, and K at this stage. This sufficiency indicates that Fe deficiency was not evident in the negative controls, suggesting that the wheat plants were still utilizing nutrients stored in the seed.

Interestingly, wheat roots (Fig. 3-3d) treated with Fe-EDDHA show significantly higher Na concentrations compared to the control, both with and without *Pp* Pf-5 inoculation at EC of 1.3 dS·m^{-1}, and are not different from that under salinity stress. Based on the shoot and root dry masses, as well as shoot and root Na concentrations, it has been observed that wheat grown with Fe-EDDHA treatments takes up more Na, approximately 0.008 to 0.011 mg, in each magenta box compared to the negative controls. Moreover, the total additional Na contributed by Fe-EDDHA treatments is around 0.6 mg per magenta box, which is greater than the extra amount of Na uptake observed in wheat with these treatments. This suggests potential Na accumulation by the Fe-EDDHA (Sequestrene 138, $C_{18}H_{16}FeN_2O_6 \cdot Na$) treated wheat tissue.
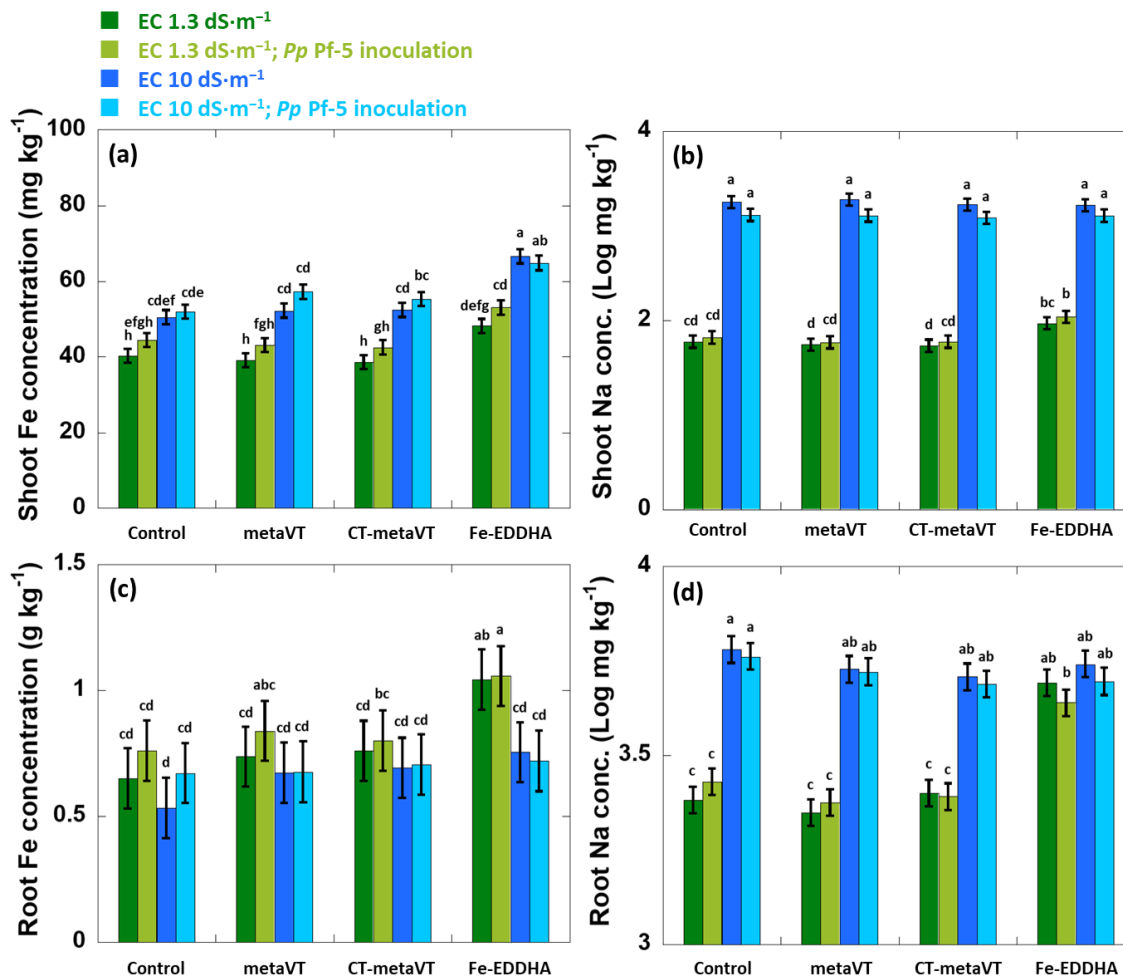
Fig. 3-3. Shoot Fe (a), Na (b), root Fe (c), and Na (d) concentrations of wheat grown in the sand with four Fe treatments, control, nano-metaVT, nano-CT-metaVT, and Fe-EDDHA with and without inoculation by *Pp* Pf-5, with EC of 1.3 and 10 dS·m^{-1}. A three-way ANOVA was performed. Different letters above columns represent significant differences based on the Tukey test ($\alpha \le 0.05$). Error bars represent the standard error calculated from the statistical mix model.

3.4.4 *Pp* Pf-5 colonization on root tissue observed via SEM

The influence of nano-metaVT and nano-CT-metaVT on the attachment of nano-metaVT and nano-CT-metaVT to the root surface and *Pp* Pf-5 colonization of the root

were observed by SEM. In Fig. 3-4, rod-shaped bacterial cells adhering to the surface of 14-day-old wheat roots inoculated with this bacterium are consistent with expectations for *Pp* Pf-5. These cells form clumps on all roots across different Fe and salinity treatments. In wheat grown with the control, nano-metaVT, and nano-CT-metaVT treatments under both normal and salinity stress conditions, the bacterial cells were linked to fine strands and small, rounded particles less than 100 nm in diameter, potentially extracellular vesicles as suggested by Potter et al. (2020). These vesicles might contain siderophores for scavenging Fe and other vital metals, similar to the cargo structures in extracellular vesicles of *P. aeruginosa* reported by Augustyniak et al. (2022), Couto et al. (2015), and Lin et al. (2017). It is also possible that the fine strands are drying artifacts from the extracellular polymeric substance (EPS). Bacterial cells and aggregates were also noted on roots treated with nano-metaVT and nano-CT-metaVT, as shown in Figs. 3-4b, 3-4c, 3-4f, and 3-4g, but were absent in roots treated with Fe-EDDHA. The study also revealed the presence of endophytes originating from within the wheat seeds, indicating a diverse microbial interaction in the growth system across the treatments (e.g., red arrows in Figs. 3-4d and 3-4h). EDS analyses of root particulate structures grown with nano-CT-metaVT under both normal and saline conditions (Figs. 3-4i and 3-4j) confirmed the presence of both Fe and P, consistent with the nano-CT-metaVT composition. However, this study does not observe the adherent of nano-metaVT or Fe-EDDHA on the root surface. These findings suggest that nano-metaVT, nano-CT-metaVT, and Fe-EDDHA would have a minimal impact on *Pp* Pf-5 root colonization under salinity stress.
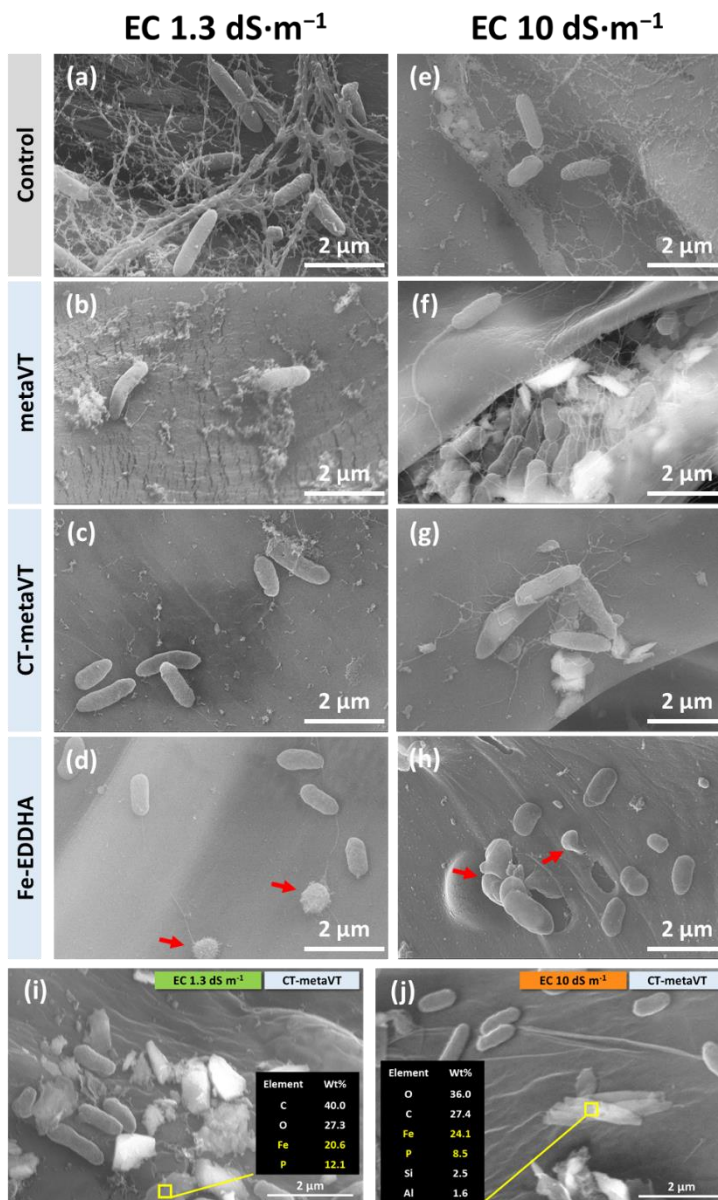
Fig. 3-4. SEM images of the *Pp* Pf-5 colonization of wheat root surfaces when grown in sand with and without three different Fe sources and with and without salinity stress (EC = 1.3 dS·m^{-1} versus (EC = 10 dS·m^{-1}) (a–h). Red arrows point out the presence of endophytes. EDS analyses for particles of nano-CT-metaVT attached to the root surface without salinity stress (i) and under salinity stress (j) are shown. The yellow squares are the targeted spots for EDS analyses.

The pore water of the sand inoculated with *Pp* Pf-5 was extracted, serially diluted, and cultured on a TSA medium. The bacterial colonies represent the number of bacterial cells living in the rhizosphere and released from the root surface if possible. The resulting bacterial concentrations (log CFU mL^{-1}) are depicted in Fig. 3-5, showing *Pp* Pf-5 levels ranging from 7-log to 8-log CFU mL^{-1}. Notably, wheat treated with nano-metaVT exhibited higher *Pp* Pf-5 concentrations than the control without salinity stress (EC = 1.3 dS·m^{-1}). Under saline conditions, however, nano-metaVT and nano-CT-metaVT treatments displayed no significant differences in *Pp* Pf-5 viable counts compared to the control.

Despite the presence of one or more endophyte(s) within the wheat seed (Figs. 3-4d and 3-4h), which persisted even after surface sterilization before sowing, the sand pore water cultures on TSA medium (Figs. B3-7a and B3-7b) exclusively showed *Pp* Pf-5 colonies. Siderophores are known to play a key role in enhancing the rhizosphere competence of root-colonizing bacteria (Roberto et al., 2007). This outcome suggests a competitive interaction between the *Pp* Pf-5 and endophyte, consistent with the root colonization patterns observed in Fig. 3-4. The findings suggest that the *Pp* Pf-5 population in the rhizosphere in the presence of nano-metaVT is higher than that of the negative control and not different from those of the nano-CT-metaVT and Fe-EDDHA treatments. However, the Fe-EDDHA treatment resulted in a higher bacterial concentration under salinity stress.
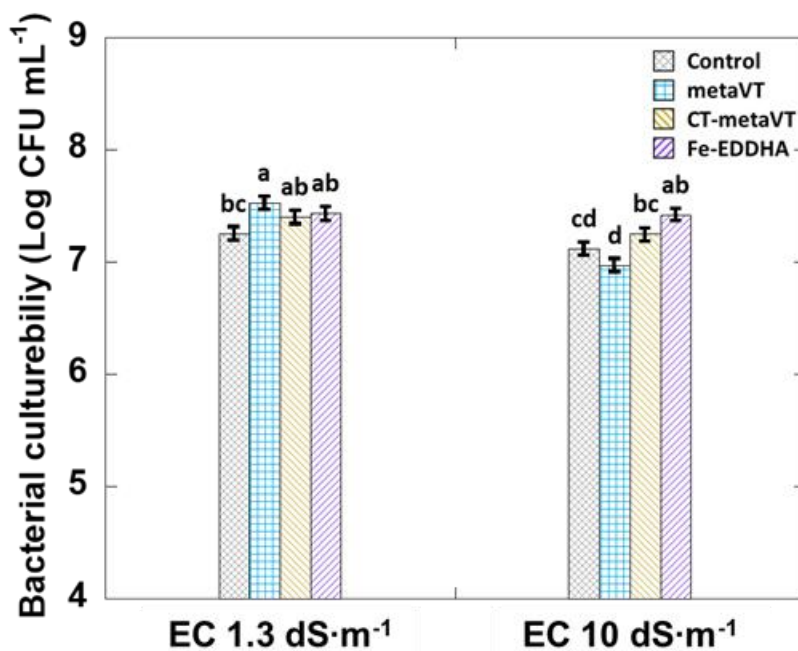
Fig. 3-5. Bacterial culturability of *Pp* Pf-5 in sand pore water extraction without salinity stress (EC = 1.3 dS·m^{-1}) and under salinity stress (EC = 10 dS·m^{-1}). A two-way ANOVA was performed. Different letters above columns represent significant differences based on the Tukey-Kramer test ($\alpha \leq 0.05$). Error bars represent the standard error calculated from the statistical mix model.

3.5 Conclusions

This study evaluates the role of *Pp* Pf-5 in supporting wheat growth in sand with high pH and salinity. Results show that nano-CT-metaVT and Fe-EDDHA treatments have longer shoots than the negative control; *Pp* Pf-5 inoculated wheat has longer shoots than wheat without microbial inoculation. Under salinity stress, *Pp* Pf-5 inoculated wheat has significantly higher transpiration rates than wheat grown without the microbe, suggesting mitigation of the salinity stress. Root colonization by *Pp* Pf-5 was evident, with bacterial cells forming clumps on roots and potentially extracellular vesicles that

might contain siderophores. Other wheat growth attributes, such as shoot/root dry mass and shoot/root Fe concentrations, resulted in no significant differences across Fe treatments, likely due to reliance on seed nutrients during the initial 14-day growth period. Still, these findings revealed the potential of multifunctional traits of *Pp* Pf-5, particularly in mitigating salinity stress in wheat growth under alkaline conditions. Future studies could further investigate the impact and mechanism of *Pp* Pf-5 inoculation on wheat growth under abiotic stress over an extended period.

3.6 References

1. Abadia, J., Vazquez, S., Rellan-Alvarez, R., El-Jendoubi, H., Abadia, A., Alvarez-Fernandez, A., & Lopez-Millan, A. F. (2011). Towards a knowledge-based correction of iron chlorosis. *Plant Physiol. Biochem.*, *49*(5), 471-482. https://doi.org/10.1016/j.plaphy.2011.01.026

2. Abdoli, S., Ghassemi-Golezani, K., & Alizadeh-Salteh, S. (2020). Responses of ajowan (*Trachyspermum ammi* L.) to exogenous salicylic acid and iron oxide nanoparticles under salt stress. *Environ. Sci. Pollut. Res.*, *27*(29), 36939-36953. https://doi.org/10.1007/s11356-020-09453-1

3. Ammari, T. G., & Hattar, B. (2011). Effectiveness of vivianite to prevent lime-induced iron deficiency in lemon trees grown on highly calcareous soil. *Commun. Soil Sci. Plant Anal.*, *42*(21), 2586-2593. https://doi.org/10.1080/00103624.2011.614034

4. An, C. C., Sun, C. J., Li, N. J., Huang, B. N., Jiang, J. J., Shen, Y., Wang, C., Zhao, X., Cui, B., Wang, C. X., Li, X. Y., Zhan, S. S., Gao, F., Zeng, Z. H., Cui, H. X., & Wang, Y. (2022). Nanomaterials and nanotechnology for the delivery of agrochemicals: strategies towards sustainable agriculture. *J. Nanobiotechnol.*, *20*(11). https://doi.org/10.1186/s12951-021-01214-7

5. Anderson, A. J., Hortin, J. M., Jacobson, A. R., Britt, D. W., & McLean, J. E. (2023). Changes in metal-chelating metabolites induced by drought and a root microbiome in wheat. *Plants*, *12*(6), 1209. https://www.mdpi.com/2223-7747/12/6/1209

6. Augustyniak, D., Olszak, T., & Drulis-Kawa, Z. (2022). Outer membrane vesicles (OMVs) of *Pseudomonas aeruginosa* provide passive resistance but not sensitization to LPS-specific phages. *Viruses*, *14*(1), 121. https://www.mdpi.com/1999-4915/14/1/121

7. Backer, R., Rokem, J. S., Ilangumaran, G., Lamont, J., Praslickova, D., Ricci, E., Subramanian, S., & Smith, D. L. (2018). Plant growth-promoting rhizobacteria: Context, mechanisms of action, and roadmap to commercialization of biostimulants for sustainable agriculture. *Front. Plant Sci.*, *9*. https://doi.org/10.3389/fpls.2018.01473

8. Balthazar, C., Novinscak, A., Cantin, G., Joly, D. L., & Filion, M. (2022). Biocontrol activity of *Bacillus* spp. and *Pseudomonas* spp. against *Botrytis cinerea* and other Cannabis fungal pathogens. *Phytopathology*, *112*(3), 549-560. https://doi.org/10.1094/phyto-03-21-0128-r

9. Bavaresco, L., Goncalves, M., Civardi, S., Gatti, M., & Ferrari, F. (2010). Effects of traditional and new methods on overcoming lime-induced chlorosis of grapevine. *Am. J. Enol. Vitic.*, *61*(2), 186-190.

10. Brittenham, G. M. (1994). New advances in iron metabolism, iron deficiency, and iron overload. *Curr. Opin. Hematol.*, *1*(2), 101-106.

11. Canarini, A., Kaiser, C., Merchant, A., Richter, A., & Wanek, W. (2019). Root exudation of primary metabolites: mechanisms and their roles in plant responses to environmental stimuli. *Front. Plant Sci*, *10*. https://doi.org/10.3389/fpls.2019.00157

12. Couto, N., Schooling, S. R., Dutcher, J. R., & Barber, J. (2015). Proteome profiles of outer membrane vesicles and extracellular matrix of *Pseudomonas aeruginosa* biofilms. *J. Proteome Res.*, *14*(10), 4207-4222. https://doi.org/10.1021/acs.jproteome.5b00312

13. Diaz, I., Barron, V., del Campillo, M. C., & Torrent, J. (2010). Testing the ability of vivianite to prevent iron deficiency in pot-grown grapevine. *Sci. Hortic.*, *123*(4), 464-468. https://doi.org/10.1016/j.scienta.2009.11.006

14. Drehe, I., Simonetti, E., & Ruiz, J. A. (2018). Contribution of the siderophores pyoverdine and enantio-pyochelin to fitness in soil of *Pseudomonas protegens* Pf-5. *Curr. Microbiol.*, *75*(12), 1560-1565. https://doi.org/10.1007/s00284-018-1560-7

15. Durand, N., Monger, H. C., Canti, M. G., & Verrecchia, E. P. (2018). *Chapter 9 - Calcium carbonate features*. Elsevier. https://doi.org/10.1016/B978-0-444-63522-8.00009-7

16. Feigin, A., Ravina, I., & Shalhevet, J. (1991). *Irrigation with treated sewage effluent management for environmental protection* (1st 1991. ed.). Springer. https://doi.org/10.1007/978-3-642-74480-8

17. Fess, T. L., Kotcon, J. B., & Benedito, V. A. (2011). Crop breeding for low input agriculture: A sustainable response to feed a growing world population. *Sustainability*, *3*(10), 1742-1772. https://doi.org/10.3390/su3101742

18. Harris, B. N., Sadras, V. O., & Tester, M. (2010). A water-centred framework to assess the effects of salinity on the growth and yield of wheat and barley. *Plant Soil*, *336*(1-2), 377-389. https://doi.org/10.1007/s11104-010-0489-9

19. Jesus, J. M., Danko, A. S., Fiúza, A., & Borges, M.-T. (2015). Phytoremediation of salt-affected soils: a review of processes, applicability, and the impact of climate change. *Environ. Sci. Pollut. Res.*, *22*(9), 6511-6525. https://doi.org/10.1007/s11356-015-4205-4

20. Jowett, C., Solntseva, I., Wu, L., James, C., & Glasauer, S. (2018). Removal of sewage phosphorus by adsorption and mineral precipitation, with recovery as a fertilizing soil amendment. *Water Sci. Technol.*, *77*(8), 1967-1978. https://doi.org/10.2166/wst.2018.027

21. Kobayashi, T., & Nishizawa, N. K. (2012). Iron uptake, translocation, and regulation in higher plants. *Annu. Rev. Plant Biol.*, *63*(1), 131-152. https://doi.org/10.1146/annurev-arplant-042811-105522

22. Lemanceau, P., Bauer, P., Kraemer, S., & Briat, J.-F. (2009). Iron dynamics in the rhizosphere as a case study for analyzing interactions between soils, plants and microbes. *Plant Soil*, *321*(1), 513-535. https://doi.org/10.1007/s11104-009-0039-5

23. Lim, C. K., Hassan, K. A., Tetu, S. G., Loper, J. E., & Paulsen, I. T. (2012). The effect of iron limitation on the transcriptome and proteome of *Pseudomonas*

fluorescens Pf-5. *PLoS One*, *7*(6), e39139.
https://doi.org/10.1371/journal.pone.0039139

24. Lin, J., Zhang, W., Cheng, J., Yang, X., Zhu, K., Wang, Y., Wei, G., Qian, P.-Y., Luo, Z.-Q., & Shen, X. (2017). A *Pseudomonas* T6SS effector recruits PQS-containing outer membrane vesicles for iron acquisition. *Nat. Commun.*, *8*(1), 14888. https://doi.org/10.1038/ncomms14888

25. Lin, L., Li, R.-h., Yang, Z.-y., & Li, X.-y. (2017). Effect of coagulant on acidogenic fermentation of sludge from enhanced primary sedimentation for resource recovery: Comparison between FeCl₃ and PACl. *Chem. Eng. J.*, *325*, 681-689. https://doi.org/10.1016/j.cej.2017.05.130

26. Loper, J. E., Henkels, M. D., Rangel, L. I., Olcott, M. H., Walker, F. L., Bond, K. L., Kidarsa, T. A., Hesse, C. N., Sneh, B., Stockwell, V. O., & Taylor, B. J. (2016). Rhizoxin analogs, orfamide A and chitinase production contribute to the toxicity of *Pseudomonas protegens* strain Pf-5 to Drosophila melanogaster. *Environ. Microbiol.*, *18*(10), 3509-3521. https://doi.org/10.1111/1462-2920.13369

27. Mikula, K., Izydorczyk, G., Skrzypczak, D., Mironiuk, M., Moustakas, K., Witek-Krowiak, A., & Chojnacka, K. (2020). Controlled release micronutrient fertilizers for precision agriculture - A review. *Sci. Total Environ.*, *712*, 136365. https://doi.org/10.1016/j.scitotenv.2019.136365

28. Morrissey, J., & Guerinot, M. L. (2009). Iron uptake and transport in plants: The good, the bad, and the ionome. *Chem. Rev.*, *109*(10), 4553-4567. https://doi.org/10.1021/cr900112r

29. Mozafari, A. A., Asl, A. G., & Ghaderi, N. (2018). Grape response to salinity stress and role of iron nanoparticle and potassium silicate to mitigate salt induced damage under in vitro conditions. *Physiol. Mol. Biol. Plants*, *24*(1), 25-35. https://doi.org/10.1007/s12298-017-0488-x

30. Neinhuis, C., & Edelmann, H. G. (1996). Methanol as a rapid fixative for the investigation of plant surfaces by SEM. *J. Microsc.*, *184*(1), 14-16. https://doi.org/https://doi.org/10.1046/j.1365-2818.1996.d01-110.x

31. Okur, B., & Örçen, N. (2020). Chapter 12 - Soil salinization and climate change. In M. N. V. Prasad & M. Pietrzykowski (Eds.), *Climate Change and Soil Interactions* (pp. 331-350). Elsevier. https://doi.org/10.1016/B978-0-12-818032-7.00012-6

32. Patel, J. S., Selvaraj, V., More, P., Bahmani, R., Borza, T., & Prithiviraj, B. (2023). A plant biostimulant from Ascophyllum nodosum potentiates plant growth promotion and stress protection activity of *Pseudomonas protegens* CHA0. *Plants-Basel*, *12*(6), 1208. https://doi.org/10.3390/plants12061208

33. Potter, M., Deakin, J., Cartwright, A., Hortin, J., Sparks, D., Anderson, A. J., McLean, J. E., Jacobson, A., & Britt, D. W. (2021). Absence of nanoparticle-induced drought tolerance in nutrient sufficient wheat seedlings. *Environ. Sci. Technol.*, *55*(20), 13541-13550. https://doi.org/10.1021/acs.est.1c00453

34. Potter, M., Hanson, C., Anderson, A. J., Vargis, E., & Britt, D. W. (2020). Abiotic stressors impact outer membrane vesicle composition in a beneficial rhizobacterium:

Raman spectroscopy characterization. *Sci Rep*, *10*(1), 21289. https://doi.org/10.1038/s41598-020-78357-4

35. Pour-Aboughadareh, A., Mehrvar, M. R., Sanjani, S., Amini, A., Nikkhah-Chamanabad, H., & Asadi, A. (2021). Effects of salinity stress on seedling biomass, physiochemical properties, and grain yield in different breeding wheat genotypes. *Acta Physiol. Plant.*, *43*(7), 98. https://doi.org/10.1007/s11738-021-03265-7

36. Rabhi, M., Barhoumi, Z., Ksouri, R., Abdelly, C., & Gharsalli, M. (2007). Interactive effects of salinity and iron deficiency in *Medicago ciliaris*. *C. R. Biol.*, *330*(11), 779-788. https://doi.org/10.1016/j.crvi.2007.08.007

37. Rajaie, M., & Tavakoly, A. R. (2018). Iron and/or acid foliar spray versus soil application of Fe-EDDHA for prevention of iron deficiency in Valencia orange grown on a calcareous soil. *J. Plant Nutr.*, *41*(2), 150-158. https://doi.org/10.1080/01904167.2017.1382523

38. Rathore, R., Vakharia, D. N., & Rathore, D. S. (2020). In vitro screening of different *Pseudomonas fluorescens* isolates to study lytic enzyme production and growth inhibition during antagonism of *Fusarium oxysporum* f. sp. cumini, wilt causing pathogen of cumin. *Egypt. J. Biol. Pest Control*, *30*(1), 57. https://doi.org/10.1186/s41938-020-00259-4

39. Roberto Pinton, Zeno Varanini, & Nannipieri, P. (2007). *The rhizosphere: Biochemistry and organic substances at the soil-plant* (2nd Edition). CRC Press. https://doi.org/10.1201/9781420005585

40. Rouzies, D., & Millet, J. M. M. (1993). Mössbauer study of synthetic oxidized vivianite at room temperature. *Hyperfine Interact.*, *77*(1), 19-28. https://doi.org/10.1007/BF02320295

41. Ruiu, L., & Mura, M. E. (2021). Oral toxicity of *Pseudomonas protegens* against muscoid flies. *Toxins 13*(11), 772. https://doi.org/10.3390/toxins13110772

42. Saqib, M., Akhtar, J., Abbas, G., & Nasim, M. (2013). Salinity and drought interaction in wheat (*Triticum aestivum* L.) is affected by the genotype and plant growth stage. *Acta Physiol. Plant.*, *35*(9), 2761-2768. https://doi.org/10.1007/s11738-013-1308-8

43. Schenkeveld, W. D. C. (2010). *Iron fertilization with FeEDDHA : the fate and effectiveness of FeEDDHA chelates in soil-plant systems* Wageningen University. https://edepot.wur.nl/155619

44. Schenkeveld, W. D. C., Hoffland, E., Reichwein, A. M., Temminghoff, E. J. M., & van Riemsdijk, W. H. (2012). The biodegradability of EDDHA chelates under calcareous soil conditions. *Geoderma*, *173-174*, 282-288. https://doi.org/10.1016/j.geoderma.2011.12.007

45. Seleiman, M. F., Almutairi, K. F., Alotaibi, M., Shami, A., Alhammad, B. A., & Battaglia, M. L. (2021). Nano-fertilization as an emerging fertilization technique: why can modern agriculture benefit from its use? *Plants*, *10*(1), 2. https://doi.org/10.3390/plants10010002

46. Sexton, D. J., Glover, R. C., Loper, J. E., & Schuster, M. (2017). *Pseudomonas protegens* Pf-5 favours self-produced siderophore over free-loading in interspecies competition for iron. *Environ. Microbiol.*, *19*(9), 3514-3525. https://doi.org/10.1111/1462-2920.13836

47. Shinde, S., Cumming, J. R., Collart, F. R., Noirot, P. H., & Larsen, P. E. (2017). *Pseudomonas fluorescens* transportome is linked to strain-specific plant growth promotion in aspen seedlings under nutrient stress. *Front. Plant Sci.*, *8*. https://doi.org/10.3389/fpls.2017.00348

48. Singh, V. K., Singh, A. K., Singh, P. P., & Kumar, A. (2018). Interaction of plant growth promoting bacteria with tomato under abiotic stress: A review. *Agric. Ecosyst. Environ.*, *267*, 129-140. https://doi.org/10.1016/j.agee.2018.08.020

49. Wang, X., Tang, D., & Wang, W. (2020). Adaptation strategies of *Pseudomonas protegens* SN15-2 to hyperosmotic growth environment. *J. Appl. Microbiol.*, *128*(6), 1720-1734. https://doi.org/10.1111/jam.14582

50. Weil, R. R., & Brady, N. C. (2017). *The nature and properties of soils.* (15th ed.). Pearson Education.

51. Zhang, X., Davidson, E. A., Mauzerall, D. L., Searchinger, T. D., Dumas, P., & Shen, Y. (2015). Managing nitrogen for sustainable development. *Nature*, *528*(7580), 51-59. https://doi.org/10.1038/nature15743

CHAPTER 4

Exploring meta-vivianite and chitosan-coated meta-vivianite as alternative iron

nano-fertilizers for plants growing in calcareous soil and the effects of salinity stress

4.1 Abstract

Calcareous soils are subject to several challenges, including high soil pH that leads to low iron (Fe) bioavailability and the constant threat of soil salinization due to low precipitation, high evapotranspiration, and repeated fertilization. Conventional synthetic Fe-chelates, such as Fe-EDDHA, are of concern due to their potential mobilization and leaching to groundwater. Metavivianite ($Fe^{II}Fe_2^{III}(PO_4)_2(OH)_2 \cdot 6H_2O$; metaVT) has been applied to supply Fe to crops successfully. To enhance its efficacy, we propose applying nano-sized metaVT and coupling it with a beneficial surface coating, chitosan (CT), the second most abundant polysaccharide in the world. In this study, we examine the potential of nano-metaVT and nano-chitosan-coated metaVT (nano-CT-metaVT) as Fe sources for winter wheat (*Triticum aestivum* cv. Juniper) as the monocot and bush beans (*Phaseolus vulgaris*) as the dicot in calcareous soil. Our findings show that nano-CT-metaVT improves bean root dry mass, and nano-metaVT treatment increases the chlorophyll content of bean leaves. Nano-CT-metaVT results in lower Na uptake in shoot than Fe-EDDHA treatment, indicating a potential for salinity stress mitigation. Additionally, after 50 days, bean plants treated with nano-CT-metaVT showed increased flower and bud formation compared to controls. Fe mobility assessments revealed the retention of nano-metaVT in the top layer of soil, with a significantly higher DTPA-extractable Fe concentration than in the control soil. Notably, soluble Fe in the leachate was markedly lower for metaVT and CT-metaVT than for Fe-

EDDHA treatments, indicating less Fe leaching out from the soil column. The stability of metaVT and CT-metaVT in soil was confirmed over four weeks with wheat cultivation and confirmed with energy-dispersive X-ray spectroscopy (EDS). These findings suggest that metaVT and CT-metaVT are promising Fe fertilizers, offering environmental benefits and improved wheat and beans growth.

Keywords: beans, chitosan coating, iron deficiency, salinity stress, metavivianite, wheat

4.2 Introduction

Calcareous soils are subject to several challenges, including high soil pH that leads to low nutrient bioavailability and the constant threat of soil salinization due to low precipitation, high evapotranspiration, and the application of fertilizers and other soil amendments. Current agricultural production relies on chemical fertilizers to fulfill the growing demand for food (Zhang et al., 2015); however, low nutrient use efficiency and over-application of chemical fertilizers reduce crop yields and threaten soil health (Fess et al., 2011). For this reason, there is great interest in investigating nano fertilizers. With a high surface area to volume ratio, nano fertilizers exhibit distinct properties from conventional bulk fertilizers and are purported to increase fertilizer use efficiency by reducing required doses by minimizing volatilization and leaching losses (El-Ghany et al., 2021; Sadati Valojai et al., 2021; Solanki et al., 2015).

Iron (Fe) is an essential micronutrient (Kim and Guerinot, 2007). It is a co-factor for about 140 enzymes participating in metabolic processes such as photosynthesis, chlorophyll biosynthesis, and respiration (Brittenham, 1994; Kobayashi and Nishizawa, 2012; Morrissey and Guerinot, 2009). In calcareous soils, however, Fe deficiency is

common in plants (Abadia et al., 2011) because it is quickly rendered unavailable by reaction with hydroxide as pH increases. The free Fe^{3+} concentration in aerated-soil solutions is around $10^{-21.3}$ M at pH 8, and total soluble iron is $10^{-10.2}$ M, which is orders of magnitude less than the concentration required by crops (10^{-6} to 10^{-5} M in the soil solution) for optimal growth (Schenkeveld, 2010).

Conventional amendment with synthetic Fe-chelates is currently the most effective agricultural practice for preventing Fe deficiencies in calcareous soils (Rajaie and Tavakoly, 2018). However, a study by Hernandez-Apaolaza and Lucena (2011) using a 50 cm-long soil column (sandy loam, pH 7.7) to evaluate the soluble and retained fractions of Fe-EDDHA moving through soil found that over 25% of Fe-o,o-EDDHA was leached from the soil columns within ten days. Schenkeveld et al. (2012) found a 65% decline in the Fe concentration of soil solutions in extracts of Fe-EDDHA amended soils within one day, likely due to its sorption to organic matter, Fe(hydr)oxides, and clay minerals. Moreover, one of the Fe-EDDHA components, *o,p*-Fe-EDDHA, revealed a tendency to exchange Fe for Cu. This implies potentially high-risk mobilization and subsequent leaching of metals into the groundwater. Therefore, researchers are still looking for alternative Fe fertilizers that are environmentally friendly (Abadia et al., 2011).

In recent years, there has been a growing interest in vivianite due in part to its recoverability from wastewater and its potential as a Fe amendment for crop cultivation (Ammari and Hattar, 2011; Fodoue et al., 2015; Liu et al., 2018). Vivianite ($Fe^{II})_3(PO_4)_2 \cdot 8H_2O$; VT) is an iron phosphate mineral that usually occurs in reduced sediments. The partially oxidized form of vivianite, metavivianite

($Fe^{II}Fe_2^{III}(PO_4)_2(OH)_2 \cdot 6H_2O$; metaVT), is more common in aerobic environments where the mixed oxidation state of Fe remains stable for extended periods of time (Rouzies and Millet, 1993). MetaVT is reported to be a promising alternative Fe fertilizer, as seen in studies with chickpeas (*Cicer arietinum* L.) and grapes (*Vitis vinifera*) growing in calcareous soils that reported similar leaf chlorophyll contents and yields as the Fe-EDDHA treated crops and significantly higher amounts than the controls (Bavaresco et al., 2010; Eynard et al., 1992).

Since nano-metaVT has a negative surface charge, we coated the nano-metaVT with chitosan (CT), a biodegradable, low-cost, non-toxic biopolymer that has been used as a beneficial surface coating on other nanoparticles (NPs) to impart a positive surface charge to the particles (Mikula et al., 2020; Modi et al., 2021; Sikder et al., 2021). We investigated how the CT coating affects Fe uptake by plants, Fe transport, and the weathering of the NPs applied in soil environments. In addition to simply correcting a nutrient deficiency, supplying crops with Fe has been shown to mitigate salinity stress in crops resulting, for example, in greater shoot and dry masses of *Medcago cilaris* L. or increasing the protein and antioxidant activity of grapes (Rabhi et al., 2007; Mozafari et al., 2018). Therefore, we investigate whether the use of nano-meta-VT and nano-CT-metaVT are also effective at mitigating salinity stress in plants.

Finally, since plants have evolved two different strategies to uptake Fe, we will investigate both a siderophore-producing monocot (strategy 2) and a rhizosphere-acidifying dicot (strategy 1) to investigate whether there is a difference in their abilities to take up Fe from nano-metaVT or nano-CTmetaVT. We study winter wheat (*Triticum aestivum* cv. Juniper) as the monocot due to its agricultural importance in semi-arid

regions and bush beans (*Phaseolus vulgaris*) as the dicot due to its sensitivity to iron

deficiency. We hypothesize that nano-metaVT and nano-CT-metaVT will improve Fe

uptake growth attributes such as shoot length and root biomass, and mitigate the salinity

stress in wheat and beans grown for 28 days. Results indicated that nano-CT-metaVT

improves bean root dry mass, and nano-metaVT treatment increases the chlorophyll

content of bean leaves. Nano-CT-metaVT results in lower Na uptake in shoot than Fe-

EDDHA treatment, indicating a potential for salinity stress mitigation. Additionally,

nano-metaVT and nano-CT-metaVT increased flower and bud formation in beans grown

to maturity (50 days) compared to controls. This study provides insight into the

effectiveness of nano-metaVT and nano-CT-metaVT as potential Fe fertilizers for wheat

and beans growing in calcareous soils typical of semi-arid to arid regions.

4.3 Materials and Methods

4.3.1 Characterization of soil

The soil used in this study is from the Millville soil series (coarse-silty,

carbonatic, mesic Typic Haploxerolls), collected from the Utah Agricultural Experiment

Station Greenville Research Farm in North Logan, UT, USA, in April 2020 and internally

designated as AgrM. The soil was collected from conventionally-managed wheat

breeding plots planted and irrigated in a wheat-alfalfa rotation. The soil characteristics,

including soil texture, particle size distribution, pH, EC, organic matter content, calcium

carbonate equivalent, cation exchange capacity, phosphorus, potassium, ammonium,

nitrate, sulfate, and other element concentrations, were analyzed using standard methods

for the western region (Gavlak et al. 2005) and. are provided in Table 4-1.

Table 4-1. Characteristics of soil sampled from 0–10 cm.

Characteristics	
Location	N 41.76346° W 111.81396°
Elevation	1369 m
Soil abbreviation	AgrM
Soil series, texture	Millville, silt loam
Taxonomic class	Coarse-silty, carbonatic, mesic Typic Haploxerolls
Particle size distribution (% sand/silt/clay)	22/56/23
Management	Irrigated commercial-style production
Crops	Winter wheat and small grain breeding trials in rotation with alfalfa
$pH_{saturated\ paste\ extract}$	8.4
EC_e (dS·m^{-1})	0.4
Phosphorus (mg kg^{-1})	12.0
Potassium (mg kg^{-1})	93.9
Ammonium (mg kg^{-1} N)	2.4
Nitrate (mg kg^{-1} N)	7.1
Sulfate (mg kg^{-1} S)	3.6
Organic matter (% of whole soil)	3.0
Cation exchange capacity (cmol kg^{-1})	20
Calcium carbonate (%)	14.1
Saturation point (%)	41.0
DTPA – Fe (mg kg^{-1})	6.0
DTPA – Cu (mg kg^{-1})	1.0
DTPA – Mn (mg kg^{-1})	12.3
DTPA – Zn (mg kg^{-1})	1.1

EC_e: Electrical conductivity of saturated paste extract

4.3.2 Wheat and beans grown in a growth chamber

4.3.2.1 Preparation of plant seeds and growth pots

Winter wheat (*Triticum aestivum* v. Juniper) and bean (*Phaseolus vulgaris*) seeds were surface-disinfected in fresh 10% H_2O_2 for 15 minutes, then rinsed ten times using sterile double-deionized water (resistance >18 MΩ cm). Ten seeds selected at random were placed on LB plates, sealed with Parafilm, and incubated at 23 °C for 48 h to confirm the absence of microbial contaminants. Soil was mixed with nano-metaVT, nano-CT-metaVT, and Fe-EDDHA (Sequestrene™ 138 Fe) at a dose of 5 mg/kg Fe and fertilized with 71.4 mg kg^{-1} NH_4NO_3, 47.9 mg kg^{-1} KH_2PO_4, and 52.9 mg kg^{-1} KCl based on Utah Fertilizer Guide (James and Topper, 1993), to provide sufficient N, P, and K for the 28-day growth period. Each pot was filled with 2 kg of the amended soil. The experiment was conducted in pots (height: 18 cm; diameter: 15 cm) using a 4×2 factorial design with 8 treatments for each plant, wheat and bean, and three replicates. The variables were unamended controls; the presence/absence of the Fe sources metaVT, CT-metaVT, or Fe-EDDHA, each at 5 mg Fe kg^{-1}; wheat (monocot)/bean (dicot); and the presence/absence of salinity stress. The effectiveness of nano-metaVT and nano-CT-metaVT is expected to be better than that of the positive control (without Fe) and comparable to the positive control, Fe-EDDHA.

4.3.2.2 Growth conditions and the salinity stress treatment

Ten (wheat) and two (bean) sterilized seeds were placed in soil at an approximate depth of 5 mm. Wheat and beans were grown for 28 d at 25 ± 2 °C in a growth chamber under high-energy sodium lights (Yescom USA Inc.; City of Industry, CA, USA) and

fluorescent lamps (F54W/T5/841/ECO, GE 46761) with 16/8 h photocycle periods. The light panels were fixed at approximately 70 cm above the base of the pots, resulting in an average photon flux of 280 μmol m^{-2} s^{-1} at the top of the pot. The plants were irrigated with deionized water to field capacity gravimetrically for the first seven days; after that, the non-salinity treatments were watered with deionized water, and salinity treatments were watered with a saline solution containing 33.6 mM NaCl and 16.8 mM CaCl$_2$ (EC = 4 dS·m^{-1}) for the next 21 days. The field capacity was measured with a soil tensiometer. The matrix is considered to be at field capacity when the water potential in the soil is at -33 kPa.

4.3.2.3 Determination of growth attributes

At 28 days post-sowing, plants were carefully uprooted from the soil. The root-adhering soil, referred to as rhizosphere soil, was distinguished from the bulk soil for subsequent analyses. To separate the rhizosphere soil from the root tissues, the roots were immersed in 100 mL of double-deionized water (resistivity >18 MΩ·cm) in a 250-mL polycarbonate centrifuge bottle for one minute. Subsequently, the roots were placed on a clean paper towel to remove excess water. The wet weights of the shoot and root tissues were determined immediately after the lengths were measured. The shoot and root tissues were oven-dried at 60 °C for at least 48 h before the dry masses were weighed and recorded. The pH and EC of the oven-dried (60 °C) rhizosphere soil were measured in a soil suspension (soil: water = 1:1) prepared with double-deionized water (resistance > 18 MΩ cm). The pH and EC of air-dried bulk soil were measured in a soil-saturated paste (0.36 g H$_2$O g^{-1} soil) extract prepared with double-deionized water.

4.3.2.4 Leaf chlorophyll relative content

Non-destructive estimation of the leaf chlorophyll concentration was made with a handheld chlorophyll meter (SPAD 502, Minolta Co. LTD, Osaka, Japan) on six leaves per pot on the 27th day after sowing.

4.3.2.5 Elemental analysis of plant tissue

To analyze shoot and root tissue for Fe, P, Na, and K concentrations, the dried plant tissue was weighed (about 0.2 g) and digested with nitric and perchloric acids based on the method described by Zasoski and Burau (1977). The digested samples were filtered through a 25 mm nylon syringe filter with a 0.22 µm pore size (Thermo Scientific, Waltham, MA, USA) and stored in scintillation vials. The Fe, P, Na, and K concentrations in the digested solution were determined by inductively coupled plasma mass spectrometry (Agilent 7700x Agilent Technologies, Santa Clara, CA, USA).

4.3.3 Fe mobility and leaching through the soil columns

To examine the Fe mobility of nano-metaVT, nano-CT-metaVT, and Fe-EDDHA through the calcareous AgrM soil, a polypropylene plastic cylinder (diameter = 5 cm; height = 15 cm) connected to a polyethylene support at the bottom with a drainage hole was used to hold soil (Fig. 4-1). A sheet of nylon mesh filter with a pore size of 30 µm was placed between the soil and the drainage hole. The columns were filled with 310 g of soil amended with 71.4 mg N kg^{-1}, 47.9 mg P kg^{-1}, and 100.8 mg K kg^{-1}. A subsample of Fe-enriched soil was prepared by adding nano-metaVT, nano-CT-metaVT, or Fe-EDDHA to a dose of 160 mg Fe kg^{-1} soil. Ten grams of the Fe-enriched soil was placed on the top (0.4 cm thick) of each 310 g soil column, resulting in an overall dose of 5 mg

Fe/kg per soil column (total mass 320 g). Half of the soil columns were planted with three surface-sterilized wheat seeds, half were left fallow, and all were watered daily to 1.2 times the field capacity of soil (166.7 g H_2O kg^{-1} soil) based on the weight of the whole column. No liquid leached out from the soil columns during days 1 to 9. On days 9 to 14, the soil columns were watered to 2.25 times the field capacity of soil (312.5 g H_2O kg^{-1} soil), and leachates were collected from days 10 to 15. The leachate was filtered through a 25 mm nylon syringe filter with a 0.22 µm pore size (Thermo Scientific) and stored in scintillation vials. The total soluble Fe in the leachate was determined by an inductively coupled plasma mass spectrometer (Agilent 7700x, Agilent Technologies). On Day 15, the soil was extruded from the plastic sleeves and divided into five layers with a thickness of 3 cm. Soil from each layer was analyzed for total and plant-available (DTPA extractable) iron.
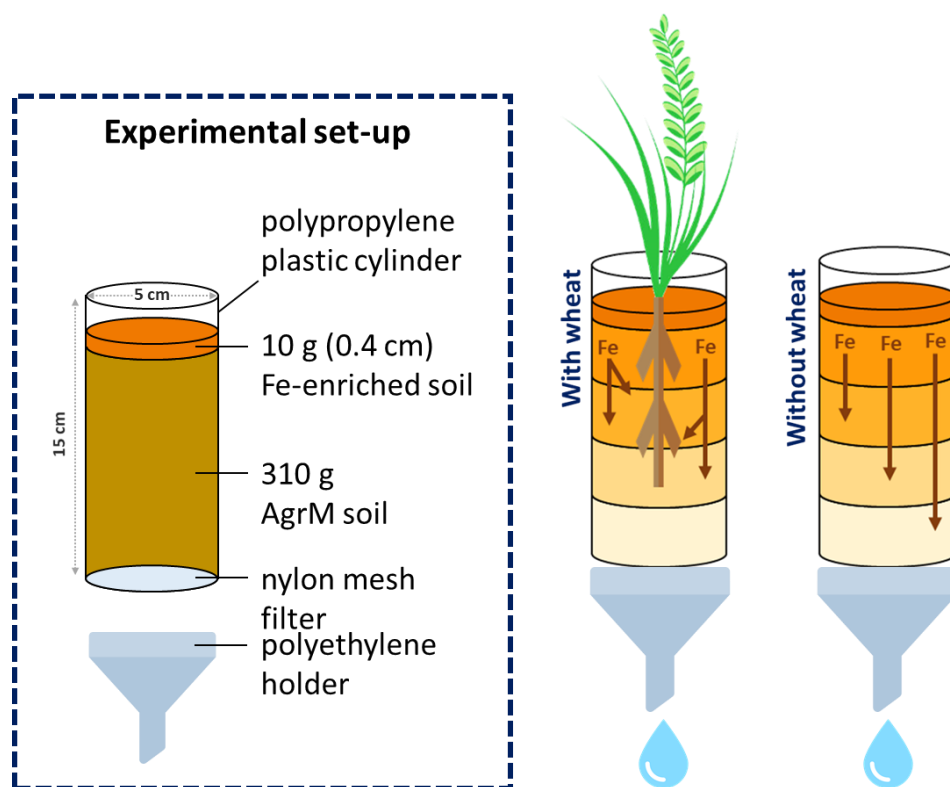
Fig. 4-1. Illustration for the experimental set-up to examine Fe mobility and leaching through the soil columns.

The DTPA extract solution was prepared by dissolving 7.45 g triethanolamine (TEA), 0.985 g diethylenetriaminepentaacetic acid (DTPA), and 0.735 g $CaCl_2 \cdot 2H_2O$ in 20 mL ddH_2O. Then, the solution was diluted to about 400 mL with ddH_2O, adjusted to pH 7.3 ± 0.05 with 1.0 M HCl, and diluted to 500 mL with ddH_2O. Then, 10 g of soil was weighed into 50 mL centrifuge bottles, and 20 mL DTPA extract solution was added to each tube. Samples were shaken for 2 h at 180 rpm and then centrifuged at 17,000 × g for 25 minutes. After centrifuging, the supernatant from each sample was filtered through a 0.22 μm nylon filter into a separate scintillation vial. The solution was analyzed for Fe

using an atomic absorption spectroscopy (AAS, Varian AA240, Agilent Technologies, Santa Clara, CA, USA), with a wavelength of 248.3 nm, slit width of 0.2 nm.

4.3.4 Weathering of nano-metaVT and nano-CT-metaVT in soil

The weathering of nano-metaVT and nano-CT-metaVT in the soil with the presence of wheat roots was investigated by scanning electron microscopy (SEM). A small piece of double-sided carbon tape was adhered to an aluminum specimen stub (diameter = 125 mm) and sprinkled with nano-metaVT or nano-CT-metaVT powder (Fig. 4-2). The treated stubs were then buried in a 50-mL conical centrifuge tube filled with soil. One sterilized wheat seed was planted in each tube and watered daily. At 1, 2, 3, and 4 weeks after sowing, the stub in each treatment was excavated, air-dried, and readied for SEM examination. The samples were sputter-coated gold and palladium to form a 10-nm layer using a rotary sputter coater system EMS150R ES (Electron Microscopy Sciences, Hatfeld, PA, USA). The morphology of the particles was viewed in a SEM (Quanta FEG 650, Field Electron and Ion Company, Hillsboro, OR, USA) under a high vacuum at an accelerating voltage of 20 kV. The Fe/P weight ratio of nano-metaVT and nano-CT-metaVT in soil was identified by EDS.
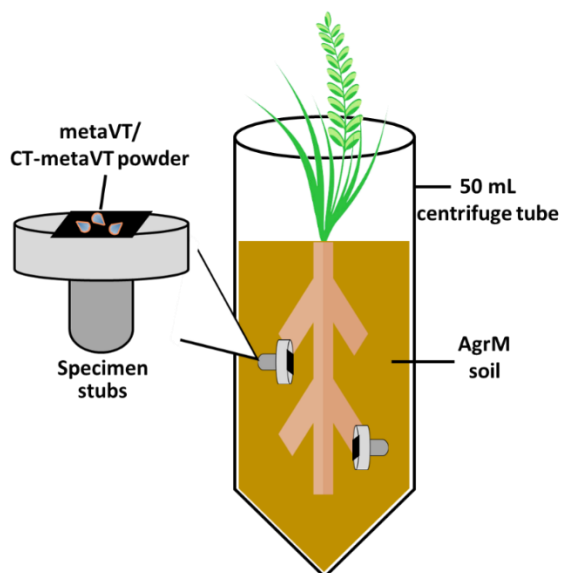
Fig. 4-2. The experimental set-up for examining the weathering of nano-metaVT and nano-CT-metaVT in a calcareous soil planted with wheat.

4.3.5 Data analysis

The experimental design for the wheat and bean growth study was structured according to a randomized complete block design (RCBD) with three trials (block) per treatment. Three trials (block) were conducted, resulting in nine experimental units (n = 9) per treatment. Plant growth parameters, physiological measurements, and elemental analyses were subjected to statistical evaluation using a two-way Analysis of Variance (ANOVA) performed with SAS software (SAS® Studio, release 3.81, Enterprise Edition, Madison, WI, USA). Diagnostics of residuals did not reveal a departure from normality and nonconstant variances, except for EC values of the rhizosphere and bulk soils, shoot and root Na concentration, and wheat root dry masses, which were all log-converted prior to the data analysis. The adjusted Tukey-Kramer multiple comparison procedure was

employed to discern significant differences between treatment means, with a significance level set at 0.05.

For the beans grown to maturity (50 days), the Fe mobility and leaching experiment, and the nano-metaVT and nano-CT-metaVT weathering experiments, a completely randomized design (CRD) was implemented with three replications (n = 3). Diagnostics of residuals did not reveal a departure from normality and nonconstant variances. The adjusted Tukey-Kramer multiple comparison procedure was employed to discern significant differences between treatment means, with a significance level set at 0.05.

4.4. Results and Discussions

4.4.1 Growth attributes of wheat and bean grown in soil

After 28 days of soil cultivation, the growth attributes (shoot/root dry masses, shoot water content, and chlorophyll content) of wheat and beans grown with the nano-metaVT, nano-CT-metaVT, and Fe-EDDHA treatments were assessed. Figs. 4-3a and 4-3b show no significant effect of Fe sources on shoot dry masses of wheat and beans, including the positive control, Fe-EDDHA. On the other hand, Fe-EDDHA treatment shows a greater wheat root dry mass than the control without the salinity stress but not under the salinity stress (Fig. 4-3c). In Fig. 4-3d, the nano-CT-metaVT treatment resulted in a higher root dry mass of beans than the control and was not different from Fe-EDDHA. The results indicate the effect of different Fe sources is more significant in wheat/bean root tissue than in shoot tissue.
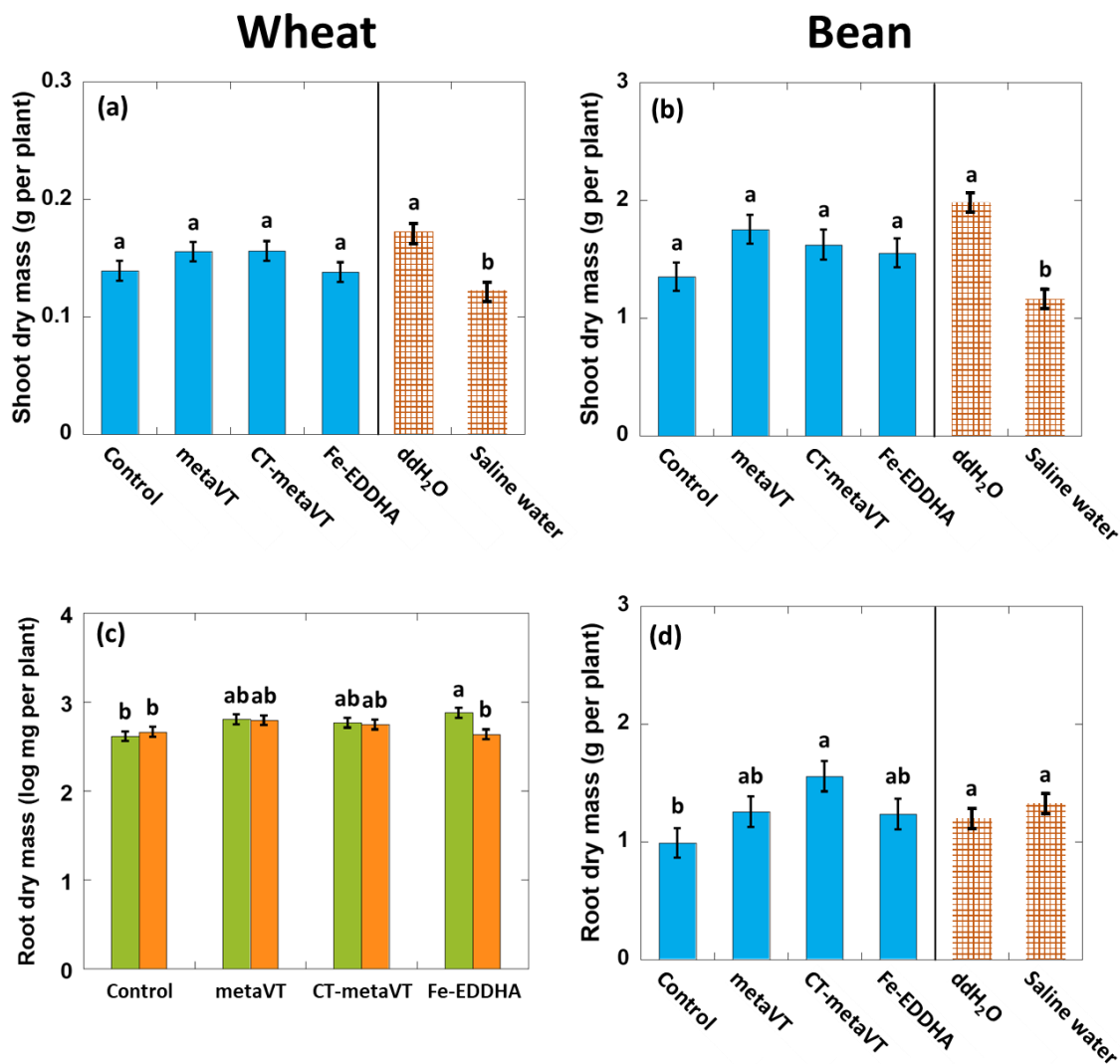
Fig. 4-3. Shoot dry mass (a, b) and root dry mass (c, d) of wheat and beans grown with four Fe treatments, control, nano-metaVT, nano-CT-metaVT, and Fe-EDDHA, and irrigated with ddH$_2$O or saline water (EC = 4 dS·m^{-1}). A two-way ANOVA was performed. Different letters above columns represent significant differences between treatments based on the Tukey-Kramer test ($\alpha \leq 0.05$). Error bars represent the standard error calculated with the statistical mix model.

Wheat grown with the nano-metaVT amendment displays superior shoot water content compared to the Fe-EDDHA treatment (Fig. 4-4a). According to previous research, shoot water contents measured four weeks after sowing wheat correlate positively to grain yields (Tahara et al., 1990). The consequences of the various Fe treatments on the relative chlorophyll content of beans are presented in Fig. 4-4d. Beans treated with nano-metaVT exhibit increased chlorophyll contents compared to the control. In a similar study using a dicotyledon plant, Rosado et al. (2002) assessed the impact of vivianite on olive trees (*Olea europaea* L.) cultivated in calcareous soil (pH 8.1–8.6) with doses of vivianite (not nano-sized) ranging from 0.5 to 2 kg tree^{-1}. Their results indicate that vivianite is nearly as effective as Fe chelate in mitigating Fe chlorosis in olive trees, with the effects lasting over two years. In contrast, the chlorophyll contents of wheat remain consistent, about 36.6 ± 3.6, across all treatments (Fig. 4-4c). This observation aligns with the findings of Naz et al. (2023), who treated wheat grown in calcareous soil (pH 7.7; DTPA-extractable Fe: 5.23 mg Fe kg^{-1}) with $FeSO_4.7H_2O$ at agriculturally relevant concentrations of 5.7 and 8.5 mg Fe kg^{-1}, but found no significant difference in chlorophyll content. In summary, applying nano-metaVT demonstrates the potential to increase the chlorophyll contents of beans but not wheat.
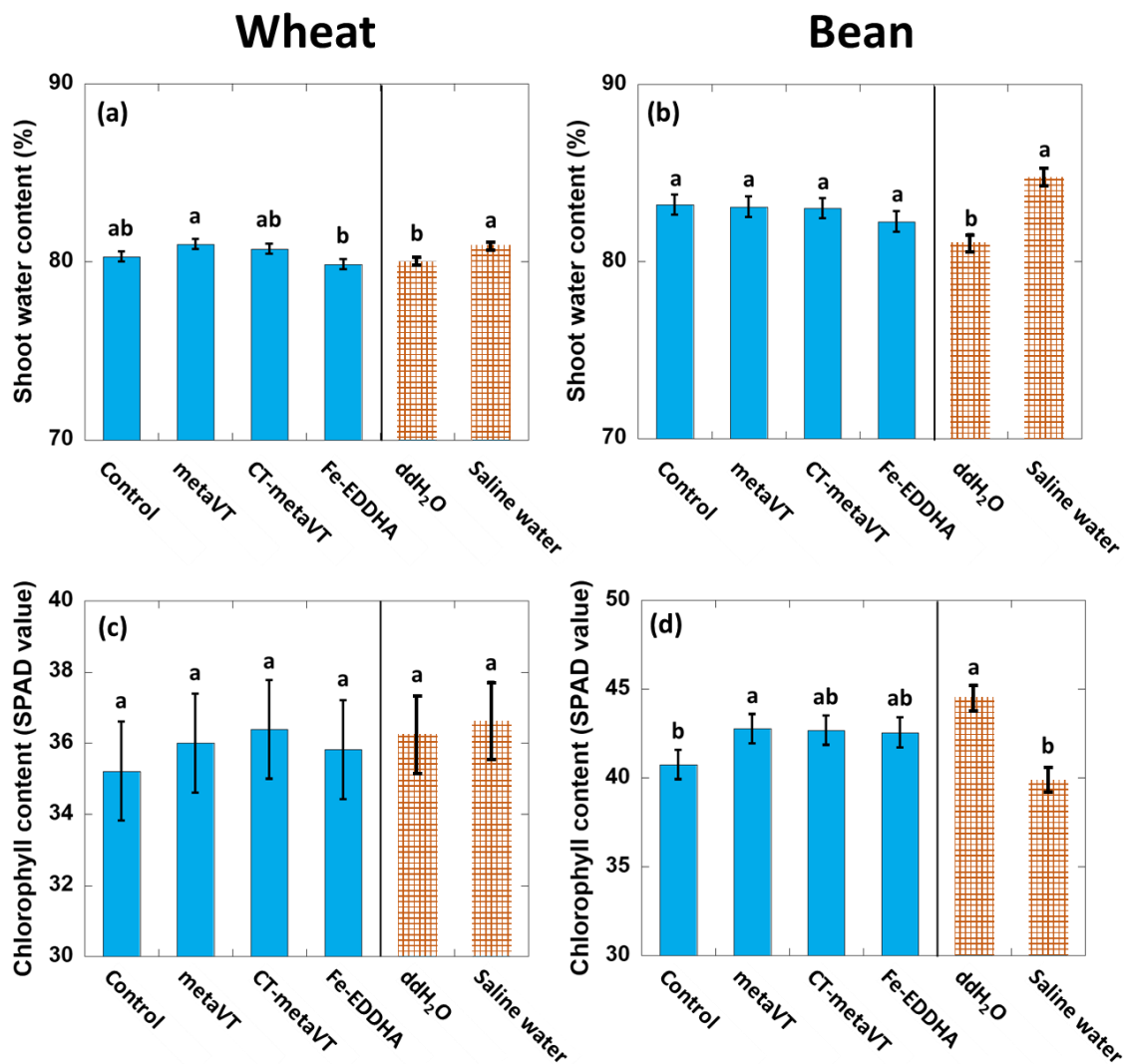
Fig. 4-4. Shoot water content (a, b) and relative chlorophyll content (c, d) of wheat and beans grown with four Fe treatments: control, nano-metaVT, nano-CT-metaVT, and Fe-EDDHA, and irrigated with ddH_2O or saline water (EC = 4 dS·m^{-1}). A two-way ANOVA was performed. Different letters above columns represent significant differences between treatments based on the Tukey-Kramer test ($\alpha \leq 0.05$). Error bars represent the standard error calculated with the statistical mix model.

4.4.2 Elemental analysis of plant tissue

As seen in Fig. 4-5a, for wheat grown for 29 days, the applications of various Fe amendments did not significantly affect shoot Fe concentrations. However, the nano-metaVT treatment resulted in a higher shoot P concentration than the Fe-EDDHA treatment. Interestingly, the salinity treatment results in higher Fe but not P concentrations in wheat shoots (Figs. 4-5b and 4-5c). In beans, on the other hand, the Fe-EDDHA treatment results in higher shoot Fe but not P concentrations, and the salinity treatment did not affect shoot Fe nor P concentration s (Figs. 4-5 b and 4-5d).
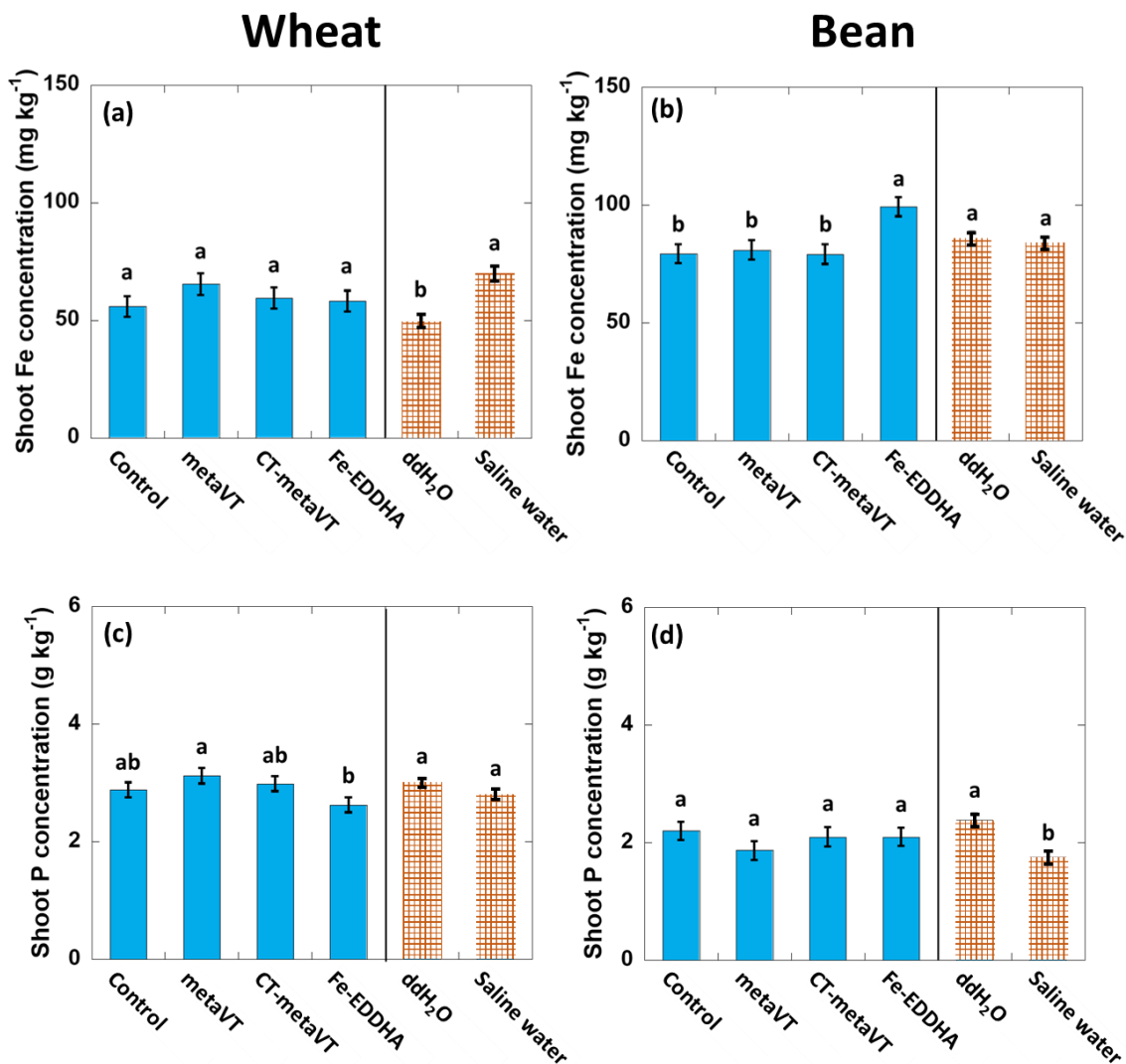
Fig. 4-5. Shoot Fe (a, b) and P (c, d) concentrations of wheat (a, c) and beans (b, d) grown in soil with four Fe treatments, control, nano-metaVT, nano-CT-metaVT, and Fe-EDDHA, and irrigated with ddH_2O and saline water ($EC = 4 \ dS \cdot m^{-1}$). A two-way ANOVA was performed. Different letters above columns represent significant differences between treatments based on the Tukey-Kramer test ($\alpha \leq 0.05$). Error bars represent the standard error calculated with the statistical mix model.

Figs. 4-6a and 4-6c show that the nano-CT-metaVT-treated wheat resulted in a significantly lower shoot Na concentration and a higher shoot K concentration than the Fe-EDDHA treatment. However, the shoot Na concentration in beans is not affected by the different Fe sources. CT-metaVT-treated beans had a lower shoot K concentration than the control. The connection between Fe availability and K uptake is highlighted by Milashi et al. (2020), who suggest that enhanced Fe uptake promotes K absorption, leading to increased K uptake. Na^+ and K^+ ions engage in competitive interactions for absorption via shared transport mechanisms. This competition is frequently skewed in favor of Na^+ due to its typically higher extracellular concentration relative to K^+ in saline conditions, which enhances the uptake efficiency of Na^+ over K^+. This reduction potentially facilitates the activation of defense pathways, including antioxidative enzymatic systems, such as catalase and superoxide dismutase (Naz et al., 2023).
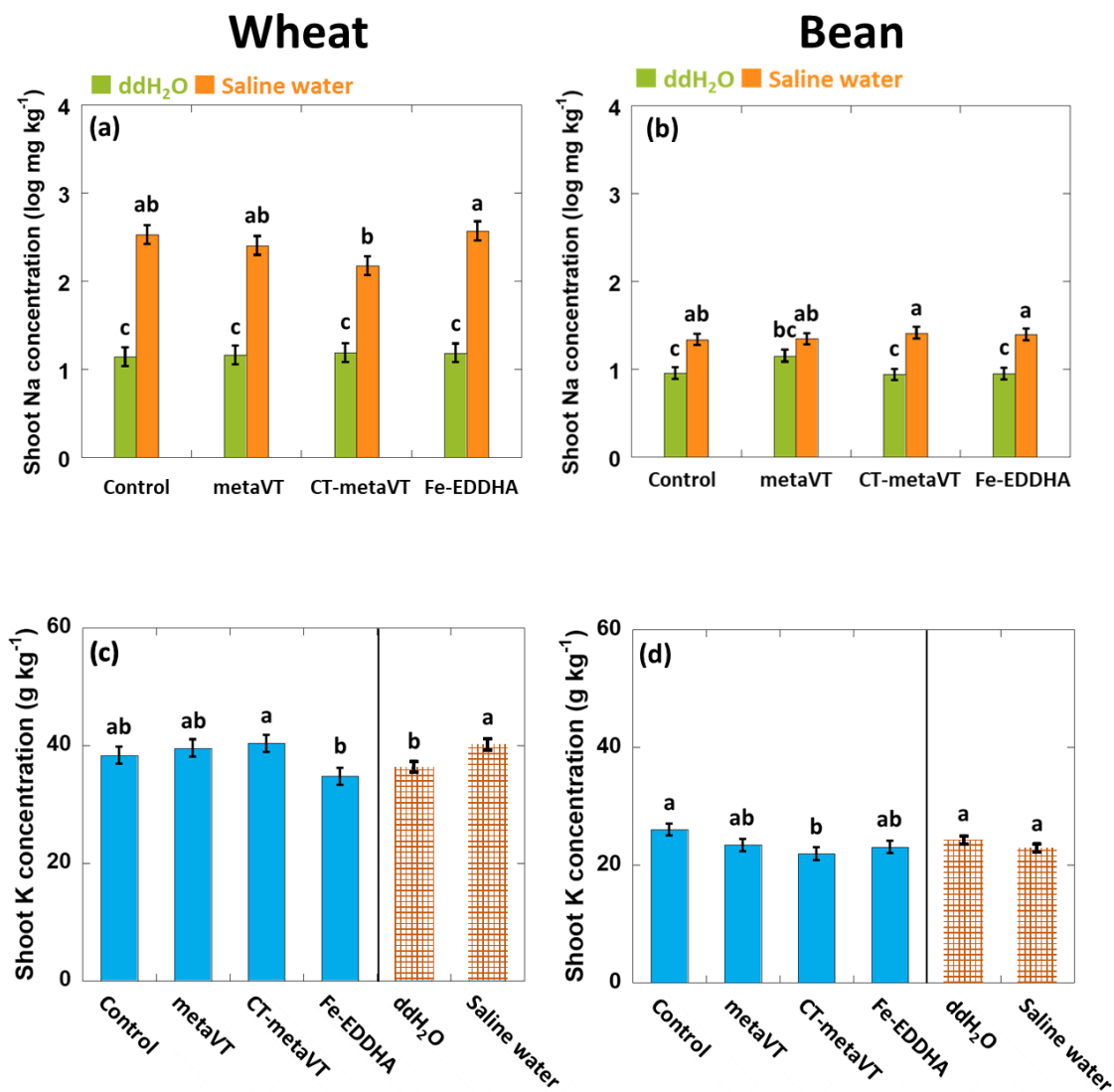
Fig. 4-6. Shoot Na (a, b) and K (c, d) concentrations of wheat (a, c) and beans (b, d) grown in soil with four Fe treatments, control, nano-metaVT, nano-CT-metaVT, and Fe-EDDHA, and irrigated with ddH$_2$O and saline water (EC = 4 dS·m^{-1}). A two-way ANOVA was performed. Different letters above columns represent significant differences between treatments based on the Tukey-Kramer test ($\alpha \leq 0.05$). Error bars represent the standard error calculated with the statistical mix model.

The root-associated Fe concentrations of the nano-metaVT and nano-CT-metaVT-treated wheat are significantly higher than those treated with Fe-EDDHA t (Fig. 4-7a) though none of the root-associated Fe concentrations of the Fe-treated wheat were significantly different than the negative control. Thus, the Fe sources do not affect the root-associated Fe in beans. Moreover, no significant changes are observed in root-associate P, Na, and K concentrations with any of the Fe treatments (nano-metaVT, nano-CT-metaVT, and Fe-EDDHA) of wheat and bean (Fig. B4-1). In this study, employing a highly calcareous soil, the effects of Fe treatments on shoot and root-associated Fe are more significant in wheat (monocot), which employs siderophores to acquire Fe, than for the rhizosphere-acidifying beans (dicot). In addition, decreased Na and increased K uptake in shoot compared to Fe-EDDHA treatment are observed in the nano-CT-metaVT-treated wheat but not in beans. The effects of nano-(meta)vivianite on wheat and beans under salinity stress have not been explored before, based on the literature summarized in Table 4-2, and warrant further investigation.
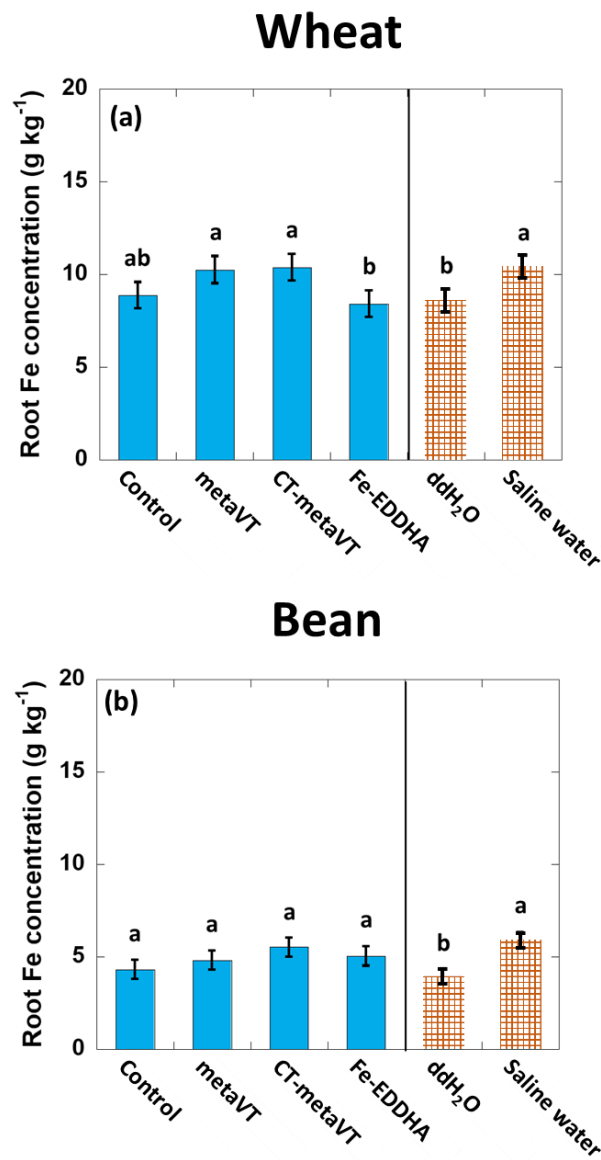
Wheat

Bean

Fig. 4-7. Root-associate Fe (a, b) of wheat and beans grown with four Fe treatments, control, nano-metaVT, nano-CT-metaVT, and Fe-EDDHA, and irrigated with ddH$_2$O or saline water (EC = 4 dS·m^{-1}). A two-way ANOVA was performed. Different letters above columns represent significant differences between treatments based on the Tukey-Kramer test ($\alpha \leq 0.05$). Error bars represent the standard error calculated with the statistical mix model.

Table 4-2. Examples of the effectiveness of (meta)vivianite on various plants grown under high pH or calcareous conditions.

Material	Dose	Growth conditions	Plants	Effectiveness	References
Nano-metaVT, Nano-CT-nano-metaVT	5 mg Fe kg^{-1}	calcareous, pH 8.4	Winter wheat (*Triticum aestivum* v. Juniper) and bean (*Phaseolus vulgaris*)	Nano-CT-metaVT showed an increase in root dry mass and relative chlorophyll content of beans. In addition, there are higher numbers of flowers and buds in nano-CT-metaVT-treated beans grown for 50 days than in the negative control.	**This study**
vivianite	1 g kg^{-1}	pH 8.2-8.5	Chickpea (*Cicer arietinum* L.)	The chlorophyll content of chickpea leaves was improved with the application of vivianite.	(Eynard et al., 1992)
vivianite	0.5-2 kg per tree	calcareous, pH 8.1-8.6	Olive trees (*Olea europaea* L.)	Vivianite was almost as effective as Fe chelate in reducing Fe chlorosis in olives, lasting more than two years.	(Rosado et al., 2002)
vivianite	1.8 g kg^{-1}	calcareous, pH 8.0	Kiwifruit (*Actinidia deliciosa* (A.Chev.) C.F.Liang and A.R.Ferguson)	Vivianite enhanced leaf chlorophyll content compared to control treatment under both greenhouse and field conditions.	(Rombola et al., 2003)
Fe sulfate, vivianite	0.08, 0.16, 0.32 g Fe kg^{-1}	calcareous, pH value: NA	(*Lupinus albus* L.)	Vivianite improved the yield and chlorophyll content with long-term effects and was further enhanced by adding humic substances.	(de Santiago et al., 2008)
vivianite	25 g/L per pot	calcareous, pH 7.3	*Vitis vinifera* L. cv. Merlot grafted on lime-susceptible rootstock	Vivianite was as effective as Fe chelate (Fe-EDDHA) in improving the chlorophyll contents in grapevine leaves.	(Bavaresco et al., 2010)
synthetic vivianite	1.0 g kg^{-1}	calcareous, pH 8.2	Rooted cuttings of *Vitis berlandieri* Resseguier No. 2 x *Vitis rupestris* Martin	The vines fertilized with vivianite had longer shoots and a higher number of leaves and exhibited higher SPAD values than the control vines. The effectiveness of vivianite lasts through 3 years, indicating the long-term fertilizing effect.	(Diaz et al., 2010)
synthetic vivianite	0.5-2.0 g kg^{-1}	calcareous, pH 7.7	*Eureka lemon* (*Citrus lemon* L.) cuttings grafted on sour orange (*Citrus aurantium* L.)	Vivianite application exhibited a greater leaf Fe concentration and chlorophyll content than untreated plants. The effectiveness of vivianite was comparable to Fe-EDDHA.	(Ammari and Hattar, 2011)

4.4.3 Beans grown to maturity

The results presented in sections 4.4.1, 4.4.2, and 4.4.3 focus on beans cultivated for 28 days. Since a different growth duration might lead to different responses to the Fe treatments, the experiment was replicated with beans over a longer growth period of 50 days, and the outcomes are presented in Fig. 4-8. Both the nano-metaVT and nano-CT-metaVT treatments significantly influenced the flowering phase, leading to a noticeable rise in the number of flowers and buds compared to untreated controls (Fig. 4-8a). Additionally, beans subjected to the nano-CT-metaVT treatment manifested greater shoot lengths than the control (Fig. 4-8b). Moreover, the Fe-EDDHA-treated bean shows a greater root dry mass than the control (Fig. 4-8c). Interestingly, beans treated with nano-metaVT for 50 days exhibit a higher Fe concentration in shoot tissue relative to all other treatments (Fig. 4-8d). In contrast, on Day 50 of this experiment, the Fe-EDDHA treatment resulted in significantly higher Fe concentrations in the bean pods and the root tissues compared to the control. This study highlights the promising potential of nano-metaVT and nano-CT-metaVT treatments in boosting flowering and possibly future yield in beans. The results spanning over the 28 and 50-day growth periods accentuated that the distinctions in overall growth become more pronounced with prolonged growth duration. At the 50-day mark, the beans were observed to be in the flowering stage, with promising bean pods.
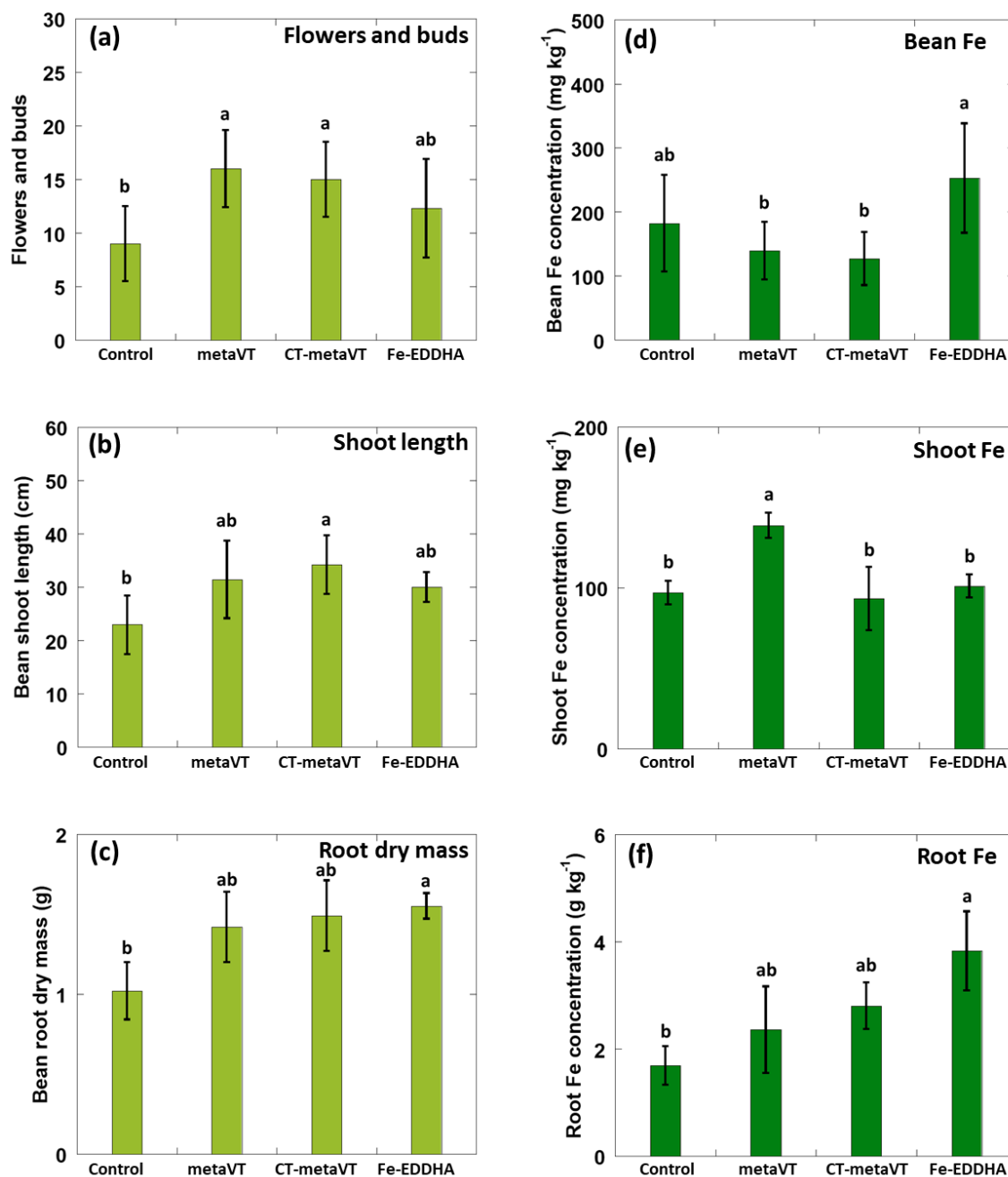
Fig. 4-8. Beans grown in soil with four Fe treatments (control, nano-metaVT, nano-CT-metaVT, and Fe-EDDHA) for 50 days. A one-way ANOVA was performed. Different letters above columns represent significant differences between treatments based on the Tukey-Kramer test ($\alpha \leq 0.05$). Error bars represent the standard deviation of the three replicates.

4.4.4 Fe mobility and leaching through the soil columns

We confirmed the decreased mobility of nano-metaVT and nano-CT relative to Fe-EDDHA using soil columns planted with wheat. Since the calcareous soil has a high total Fe concentration, DTPA-extractable Fe (defined as plant-available Fe) was used to investigate differences in the treated soil columns. Table 4-3 presents the DTPA-extractable Fe concentrations across various depths of the soil columns separated into five layers. The initial DTPA-extractable Fe concentration of the untreated soil is 6.0 ± 0.2 mg kg^{-1}. The surface layer treated with Fe-EDDHA exhibits a tenfold higher DTPA-extractable Fe concentration (114.7 ± 10.9 mg kg^{-1}) than those treated with nano-metaVT (10.0 ± 0.7 mg kg^{-1}) and nano-CT-metaVT (10.6 ± 0.3 mg kg^{-1}). This notable disparity is attributed to the high solubility of iron chelates. After 14 days, columns treated with both nano-metaVT and nano-CT-metaVT show the highest DTPA-extractable Fe concentrations at the surface layer, surpassing those in the deeper soil layers. In contrast, Fe-EDDHA treated columns display no significant variation in DTPA-extractable Fe concentrations among the different layers, with values ranging from 6.5 to 7.5 mg kg^{-1}. These findings also highlight the rapid depletion of DTPA-extractable Fe in the Fe-EDDHA-treated columns compared to the high initial DTPA-extractable Fe concentration in the top layer.

Fig. 4-9 shows that the total soluble Fe in the leachate from columns treated with nano-metaVT is 0.57 μg accumulated over D11 to D15. The total soluble Fe concentration in the nano-CT-metaVT treated column leachate is 1.01 μg accumulated over D11 to D15, which is not different from nano-metaVT treatment. In comparison, the total soluble Fe is 23.57 μg in the leachate of the Fe-EDDHA-treated column

accumulated over D11 to D15, significantly higher than the control, nano-metaVT, and nano-CT-metaVT treated column leachates. The results confirm that Fe-EDDHA leaches more readily from the soil profile than nano-metaVT and nano-CT-metaVT. A study by Hernandez-Apaolaza and Lucena (2011) used soil (sandy loam, pH 7.7) in a 50 cm-long column to evaluate the soluble and retained fractions of Fe-EDDHA moving through soil. A single 2 mL dose of 500 mg Fe L^{-1} solutions of Fe-EDDHA was poured onto the top of the columns at the beginning of the experiment, and over 25% of Fe-o,o-EDDHA was leached from the soil columns within ten days. The results imply potentially high-risk mobilization and subsequent leaching of Fe-EDDHA into the groundwater, resulting in inefficient plant utilization rates and an increased risk of environmental pollution.

Table 4-3. The mobility of DTPA-extractable Fe in the soil columns with wheat. Two-way ANOVA with differing letters represents a significant difference based on the Tukey-Kramer test ($\alpha \leq 0.05$).

unit: mg kg^{-1}	control	metaVT	CT- metaVT	Fe-EDDHA
Initial DTPA-Fe concentrations in the top layers (0.4 cm; 160 mg Fe kg^{-1})	6.0 ± 0.2	10.0 ± 0.7	10.6 ± 0.3	114.7 ± 10.9
Layer 1	6.9 ± 0.4^{bcd}	8.2 ± 0.3^{a}	7.9 ± 0.3^{ab}	7.5 ± 0.6^{abc}
Layer 2	6.0 ± 0.2^{d}	6.5 ± 0.2^{cd}	6.7 ± 0.2^{cd}	6.5 ± 0.1^{cd}
Layer 3	6.0 ± 0.3^{d}	6.4 ± 0.2^{cd}	6.5 ± 0.1^{cd}	6.7 ± 0.2^{cd}
Layer 4	6.2 ± 0.1^{d}	6.7 ± 0.4^{cd}	6.7 ± 0.1^{cd}	7.4 ± 0.9^{abc}
Layer 5	6.2 ± 0.2^{d}	6.9 ± 0.4^{bcd}	6.6 ± 0.0^{cd}	7.5 ± 0.7^{abc}
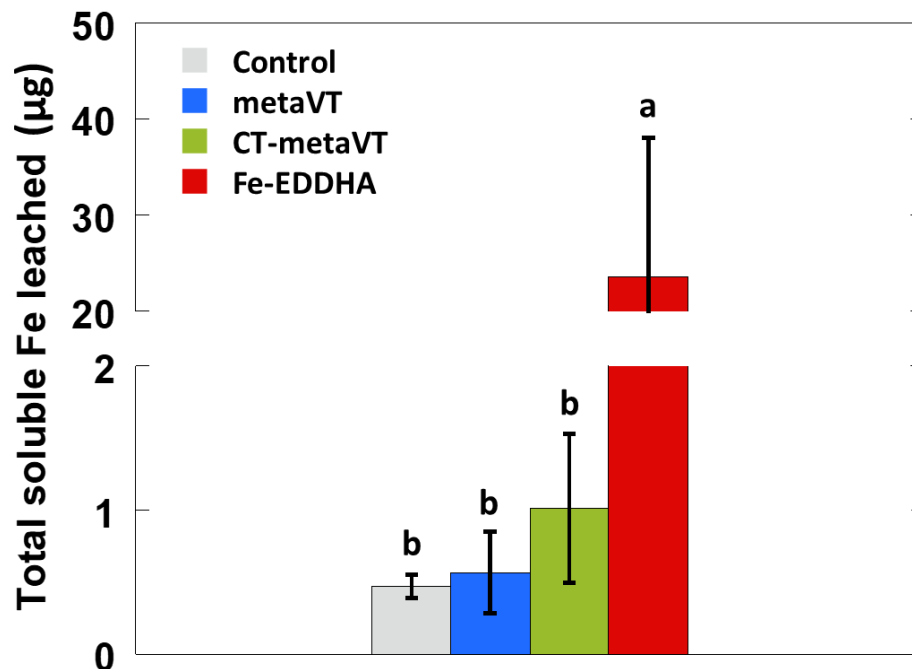
Fig. 4-9. The total soluble Fe leached from day 11 to day 15 through soil columns planted with wheat. A one-way ANOVA was performed. Different letters above the columns represent significant differences based on the Tukey-Kramer test ($\alpha \leq 0.05$). Error bars represent the standard deviation of the three replicates.

4.4.5 Weathering of nano-metaVT and nano-CT-metaVT in soil

Fig. 4-10 illustrates the weathering profiles of nano-metaVT and nano-CT-metaVT in soil from one to four weeks after planting with wheat. Both nano-metaVT and nano-CT-metaV retained their morphology throughout the four weeks, displaying no significant dissolution or breakdown. The Fe/P mass ratio of both nano-metaVT and nano-CT-metaVT in soils was determined by EDS, with results displayed in Fig. B4-4. Initially, the Fe/P atomic weight ratio of the applied nano-metaVT and nano-CT-metaVT was 2.7 (3Fe/2P). Over the four weeks, this ratio ranged between 3 and 4, aligning more closely with a ratio of 3.6 (2Fe/P). However, as the nano-metaVT and nano-CT-metaVT were in contact with soil and plant roots for several weeks, the potential attachment of other particles or compounds might have affected the semi-quantification of Fe or P by EDS. This uncertainty means that while the values appeared stable, the specific weathering reactions that occurred cannot be precisely determined.

Previous studies, such as that by Roldan et al. (2002), used 99.99% pure oxygen saturated with water to verify the final weathering product of bulk VT, as lepidocrocite (γ-FeO(OH)), an iron oxide-hydroxide mineral. The present findings show that neither nano-metaVT nor nano-CT-metaVT achieved complete oxidation within four weeks in planted and watered soil as indicated by the presence of P remaining in nano-metaVT and nano-CT-metaVT minerals. This suggests their potential for long-term effectiveness when applied as a soil amendment. Although the exact weathering rates of nano-metaVT and nano-CT-metaVT in soil remain unclear, our incubation results suggest they provide a stable source of Fe, potentially benefiting plant iron nutrition over extended periods.

These results support findings by Rosado et al. (2002), who documented the enduring positive impacts of vivianite in combating chlorosis in olive trees for up to two years.
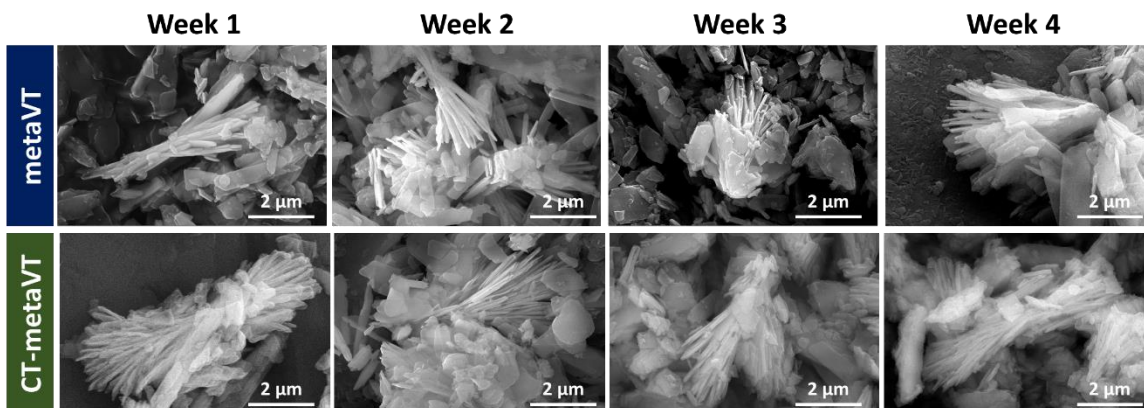
Fig. 4-10. Morphology of nano-metaVT and nano-CT-metaVT weathered in soil planted with wheat for one to four weeks.

4.5 Conclusions

This study investigates mitigating the dual agricultural challenges of Fe deficiency and soil salinity in arid and semi-arid calcareous soils where inorganic Fe bioavailability is limited. The study confirms that nano-CT-metaVT improves bean root dry mass, and nano-metaVT treatment increases the chlorophyll content in beans. Compared with Fe-EDDHA treated plants, nano-CT-metaVT lowers Na uptake in shoot, indicating a potential for salinity stress mitigation. A notable increase in reproductive potential, as indicated by a higher number of flowers and buds, was observed for beans to maturity (50 days), with a higher number of flowers and buds. Nano-metaVT demonstrates superior environmental performance by minimizing Fe leaching, as evidenced by its retention in the soil and lower concentrations of soluble Fe than Fe-EDDHA leachates. Stability tests over four weeks further validate the utilization of nano-

metaVT and nano-CT-metaVT as stable and subject to less loss via leaching the

FeEDDHA.

4.6 References

1. Abadia, J., Vazquez, S., Rellan-Alvarez, R., El-Jendoubi, H., Abadia, A., Alvarez-Fernandez, A., & Lopez-Millan, A. F. (2011). Towards a knowledge-based correction of iron chlorosis. *Plant Physiol. Biochem.*, *49*(5), 471-482. https://doi.org/10.1016/j.plaphy.2011.01.026

2. Ammari, T. G., & Hattar, B. (2011). Effectiveness of vivianite to prevent lime-induced iron deficiency in lemon trees grown on highly calcareous soil. *Commun. Soil Sci. Plant Anal.*, *42*(21), 2586-2593. https://doi.org/10.1080/00103624.2011.614034

3. Bavaresco, L., Goncalves, M., Civardi, S., Gatti, M., & Ferrari, F. (2010). Effects of traditional and new methods on overcoming lime-induced chlorosis of grapevine. *Am. J. Enol. Vitic.*, *61*(2), 186-190.

4. Brittenham, G. M. (1994). New advances in iron metabolism, iron deficiency, and iron overload. *Curr. Opin. Hematol.*, *1*(2), 101-106.

5. El-Ghany, M. F. A., El-Kherbawy, M. I., Abdel-Aal, Y. A., El-Dek, S. I., & Abd El-Baky, T. (2021). Comparative study between traditional and nano calcium phosphate fertilizers on growth and production of snap bean (*Phaseolus vulgaris* L.) plants. *Nanomaterials*, *11*(11). https://doi.org/10.3390/nano11112913

6. Eynard, A., Campillo, M. C., Barrón, V., & Torrent, J. (1992). Use of vivianite ($Fe_3(PO_4)_2.8H_2O$) to prevent iron chlorosis in calcareous soils. *Fertil. Res.*, *31*, 61-67. https://doi.org/10.1007/BF01064228

7. Fodoue, Y., Jean Pierre, N., Tchameni, R., Basga, S., & Penaye, J. (2015). Assessment of the fertilizing effect of vivianite on the growth and yield of the bean ''*Phaseolus vulgaris*'' on Oxisoils from Ngaoundere (Central North Cameroon). *Int. Res.J. Earth Sci.*, *3*, 18-26.

8. Gavlak, R. G., Horneck, D. A., Miller, R. O., Center, W. R. D., Fertilizer, F. W., & Association, A. (2013). *Plant, soil, and water reference methods for the western region* (4th ed.). Western Rural Development Center. https://books.google.com/books?id=DytlHQAACAAJ

9. Hernandez-Apaolaza, L., & Lucena, J. J. (2011). Influence of the soil/solution ratio, interaction time, and extractant on the evaluation of iron chelate sorption/desorption by soils. *J. Agric. Food Chem.*, *59*(6), 2493-2500. https://doi.org/10.1021/jf104120e

10. James, D. W., & Topper, K. F. (1993). *Utah Fertilizer Guide*. U. S. U. Extension.

11. Kim, S. A., & Guerinot, M. L. (2007). Mining iron: Iron uptake and transport in plants. *FEBS Letters*, *581*(12), 2273-2280. https://doi.org/10.1016/j.febslet.2007.04.043

12. Kobayashi, T., & Nishizawa, N. K. (2012). Iron uptake, translocation, and regulation in higher plants. *Annu. Rev. Plant Biol.*, *63*(1), 131-152. https://doi.org/10.1146/annurev-arplant-042811-105522

13. Liu, J. Q., Cheng, X., Qi, X., Li, N., Tian, J. B., Qiu, B., Xu, K. N., & Qu, D. (2018). Recovery of phosphate from aqueous solutions via vivianite crystallization: Thermodynamics and influence of pH. *Chem. Eng. J.*, *349*, 37-46. https://doi.org/10.1016/j.cej.2018.05.064

14. Mikula, K., Izydorczyk, G., Skrzypczak, D., Mironiuk, M., Moustakas, K., Witek-Krowiak, A., & Chojnacka, K. (2020). Controlled release micronutrient fertilizers for precision agriculture - A review. *Sci. Total Environ.*, *712*, 136365. https://doi.org/10.1016/j.scitotenv.2019.136365

15. Milashi, L. R., Javid, M. G., Alahdadi, I., & Darbandi, A. I. (2020). Alleviation of salt stress and improvement of Fe accumulation in wheat grain, using slow-release fertilizer enriched with Fe. *J. Plant Nutr.*, *43*(20), 2990-3001. https://doi.org/10.1080/01904167.2020.1799007

16. Modi, S., Kumar, S., & Dubey, P. K. (2021). Dynamics of chitosan based NPK-nanofertilizers in greenhouse cucumber production system. *J.Environ.Biol.*, *42*(1), 162-168. https://doi.org/10.22438/eb/42/1/MRN-1251

17. Morrissey, J., & Guerinot, M. L. (2009). Iron uptake and transport in plants: The good, the bad, and the ionome. *Chem. Rev.*, *109*(10), 4553-4567. https://doi.org/10.1021/cr900112r

18. Mozafari, A. A., Asl, A. G., & Ghaderi, N. (2018). Grape response to salinity stress and role of iron nanoparticle and potassium silicate to mitigate salt induced damage under in vitro conditions. *Physiol. Mol. Biol. Plants*, *24*(1), 25-35. https://doi.org/10.1007/s12298-017-0488-x

19. Naz, T., Iqbal, M. M., Fahad, S., Akhtar, J., Saqib, M., Alamri, S., Siddiqui, M. H., Saud, S., Khattak, J. Z. K., Ali, S., Hassan, S., Nawaz, T., Hammad, H. M., Banout, J., Wu, C., Wang, D. P., Datta, R., Danish, S., & Nasim, W. (2023). Bio-fortification of two wheat cultivars with iron and zinc through their soil and foliar application in salt-factored soil: growth, ionic, physiological, and biochemical modifications. *J. Plant Growth Regul.*. https://doi.org/10.1007/s00344-023-10955-8

20. Rabhi, M., Barhoumi, Z., Ksouri, R., Abdelly, C., & Gharsalli, M. (2007). Interactive effects of salinity and iron deficiency in *Medicago ciliaris*. *C. R. Biol.*, *330*(11), 779-788. https://doi.org/10.1016/j.crvi.2007.08.007

21. Rajaie, M., & Tavakoly, A. R. (2018). Iron and/or acid foliar spray versus soil application of Fe-EDDHA for prevention of iron deficiency in Valencia orange grown on a calcareous soil. *J. Plant Nutr.*, *41*(2), 150-158. https://doi.org/10.1080/01904167.2017.1382523

22. Roldan, R., Barron, V., & Torrent, J. (2002). Experimental alteration of vivianite to lepidocrocite in a calcareous medium. *Clay Min.*, *37*(4), 709-718. https://doi.org/10.1180/0009855023740072

23. Rosado, R., del Campillo, M. C., Martinez, M. A., Barron, V., & Torrent, J. (2002). Long-term effectiveness of vivianite in reducing iron chlorosis in olive trees. *Plant Soil*, *241*(1), 139-144. https://doi.org/10.1023/a:1016058713291

24. Rouzies, D., & Millet, J. M. M. (1993). Mössbauer study of synthetic oxidized vivianite at room temperature. *Hyperfine Interact.*, *77*(1), 19-28. https://doi.org/10.1007/BF02320295

25. Sadati Valojai, S. T., Niknejad, Y., Fallah Amoli, H., & Barari Tari, D. (2021). Response of rice yield and quality to nano-fertilizers in comparison with conventional fertilizers. *J. Plant Nutr.*, *44*(13), 1971-1981. https://doi.org/10.1080/01904167.2021.1884701

26. Schenkeveld, W. D. C. (2010). *Iron fertilization with FeEDDHA : the fate and effectiveness of FeEDDHA chelates in soil-plant systems* Wageningen University. https://edepot.wur.nl/155619

27. Schenkeveld, W. D. C., Hoffland, E., Reichwein, A. M., Temminghoff, E. J. M., & van Riemsdijk, W. H. (2012). The biodegradability of EDDHA chelates under calcareous soil conditions. *Geoderma*, *173-174*, 282-288. https://doi.org/10.1016/j.geoderma.2011.12.007

28. Sikder, A., Pearce, A. K., Parkinson, S. J., Napier, R., & O'Reilly, R. K. (2021). Recent trends in advanced polymer materials in agriculture related applications. *ACS Appl. Polym. Mater.*, *3*(3), 1203-1217. https://doi.org/10.1021/acsapm.0c00982

29. Solanki, P., Bhargava, A., Chhipa, H., Jain, N., & Panwar, J. (2015). Nano-fertilizers and their smart delivery system. In M. Rai, C. Ribeiro, L. Mattoso, & N. Duran (Eds.), *Nanotechnologies in Food and Agriculture* (pp. 81-101). Springer International Publishing. https://doi.org/10.1007/978-3-319-14024-7_4

30. Tahara, M., Carver, B. F., Johnson, R. C., & Smith, E. L. (1990). Relationship between relative water-content during reproductive development and winter-wheat grain-yield. *Euphytica*, *49*(3), 255-262.

CHAPTER 5

LITERATURE REVIEW II

5.1 Development of current disinfection approaches

Effective disinfection approaches are crucial in environmental management and water treatment.[1] Disinfection can control the spread of infectious diseases by eliminating harmful microorganisms from water, surfaces, and air.[2] In medical and healthcare settings, it is essential to prevent hospital-acquired infections and ensure the sterility of medical instruments.[3] In water treatment, disinfection is vital to ensure safe drinking water free from pathogens such as bacteria, viruses, and protozoa, thereby preventing waterborne diseases.[4] Conventional disinfection methods, including chlorination, UV light, and ozonation, have been well established. However, these methods also have disadvantages, such as the high cost of the raw chemicals, the generation of toxic byproducts, or low disinfection efficiency.[5, 6] In addition, pathogens develop resistance to traditional disinfectants, necessitating the ongoing development of effective disinfectants and promising new disinfection methods.[7-9] Examples of conventional disinfection approaches and their disadvantages are listed below:

(a) Chlorine:

Chlorine is widely recognized as one of the most cost-effective and potent disinfectants for neutralizing microorganisms and maintaining residual concentration to inhibit microbial growth in water supply systems.[10] Its affordability and widespread availability have established it as a mainstay in numerous municipal water treatment processes.[11] However, despite its apparent efficacy, chlorine has significant drawbacks. A

primary concern is the formation of disinfection byproducts.[10] The interaction of chlorine with organic matter in water leads to the creation of harmful compounds such as trihalomethanes and haloacetic acids.[12] Epidemiological studies have associated prolonged exposure to these byproducts with various health issues, including the potential for carcinogenic effects.[13]

(b) UV radiation:

UV disinfection has gained popularity due to several advantages, such as its efficacy in inactivating pathogens, absence of disinfectant residuals, minimal formation of disinfection byproducts, and the ease with which it can be integrated into existing water treatment processes, or to sterilize surfaces such as medical equipment, the inside of biosafety cabinets and hoods, etc.[14] However, it faces certain limitations. The complexity of substances in the treated water and economic constraints mean that UV doses might not always ensure the complete inactivation of antibiotic-resistant microbes. Additionally, UV disinfection lacks prolonged residual effects, and the possibility of photoreactivation and dark repair mechanisms can undermine its overall effectiveness.[15] Consequently, in most practical applications, a combined approach is often necessary, where UV disinfection is used alongside another method that provides lasting residual protection to ensure comprehensive water safety.[16]

(c) Silver:

Silver (Ag) has a long-standing history of water disinfection, tracing centuries.[17, 18] Ag nanoparticles extend to various domains such as air and water purification, biomedical sector as therapeutic agents, consumer products in textiles, and wound

dressing applications.[17] However, concerns have been raised regarding the leaching of Ag, particularly from fabric products, when exposed to various liquids like water, milk, sweat, and urine. Quadros et al. (2013) reported that leaching levels of Ag were higher with sweat and urine than with tap water.[19] The potential for accumulation and concerns about human toxicity and environmental impacts from continuous Ag release necessitates careful management. Moreover, Ag has a strong affinity for binding with sulfur (S), both organic and inorganic, particularly in wastewater treatment plants.[20] As a result, most silver nanoparticles (Ag NPs) are effectively concentrated and subsequently removed during the treatment process.[21] These factors limit the unrestricted use of Ag and emphasize the need for cautious application, especially in consumer products.[22]

(d) Photocatalyst:

Photocatalysis has the potential to serve as an alternative technology due to its emerging ability to degrade persistent organic pollutants and inactivate pathogens effectively.[23] Because of its large band gap, titanium dioxide (TiO_2) is one of the most popular photocatalysts. Its versatility in water disinfection is impressive for degrading organic pollutants and inactivating bacteria, viruses, and other pathogens. The popularity of TiO_2 can be attributed to its cost-effectiveness and high oxidative potential. When illuminated by UV light, TiO_2 can produce reactive oxygen species (ROSs), which are highly reactive and can oxidize a wide range of contaminants. However, conventional TiO_2 can only be activated under radiation with wavelengths below 350 nm.[24] Moreover, photocatalysts have typically been used in suspension systems for photooxidation. The TiO_2 suspension process often suffers from the adverse effects of particle aggregation and turbidity shading in the catalyst suspension, thereby reducing its photocatalytic activity.

Another concern with using nano-sized photocatalysts is the difficulty of completely removing these particles from water after treatment, posing potential environmental and health risks.

(e) Waste-derived disinfection agents:

Waste-derived disinfection agents are gaining attention in a world grappling with increasing waste generation and the dire need for sustainable solutions. The idea is to utilize certain waste materials with antimicrobial properties as disinfection agents. For instance, waste from fishery sources, such as oyster shells or shrimp shells, can be processed to produce disinfection materials, which has shown potential in water disinfection. These agents function either by releasing antimicrobial substances or interrupting bacterial metabolism to inactivate pathogens. Beyond the obvious environmental advantage of repurposing waste, these agents can be cost-effective, especially in regions with abundant waste material. However, studies are needed to ensure the consistency of the waste-derived agent and optimize efficiency to match or surpass conventional disinfectants.

5.2 Role of titanium dioxide (TiO$_2$)

Advanced oxidation processes are popular technologies that utilize ROSs to degrade various contaminants in water.[25] Advanced oxidation processes have been indicated as one of the promising approaches in water purification from persistent organic pollutants[26], pharmaceutical residues[27], and even microorganisms. The procedures rely on the production of ROSs such as singlet oxygen ($^1O_2$), hydroxyl radicals ($\cdot$OH), and hydrogen peroxide (H_2O_2). These strong oxidants can degrade recalcitrant compounds

through reactions involving, for example, Fenton catalysis[28, 29], ozonation[30], and sulfate radical-based reactions.[31, 32] Hydroxyl radicals can also be initiated by photons in the presence of catalysts or oxidants. The most common catalyst is titanium dioxide (TiO_2).

TiO_2 functions as a semiconductor, and its photocatalytic activity is initiated by absorbing photons with adequate energy. This absorption causes electrons in the valence band (e_{vb}^-) of TiO_2 to be excited to the conduction band (e_{cb}^-), leaving behind positively charged holes in the valence band (h_{vb}^+).[24] The band gap energy of anatase, a form of TiO_2, is around 3.2 eV, indicating that photocatalysis is triggered by photons with wavelengths below approximately 385 nm, which falls within the UVA spectrum.[33] There are two possible pathways for these excited electrons and holes. They may undergo bulk recombination, a process where they simply recombine without contributing to photocatalytic activity, which is considered an unproductive reaction. Alternatively, when these electrons and holes reach the TiO_2 surface, they can participate in reactions that generate ROSs, such as superoxide anion radicals ($O_2^-\cdot$), $\cdot OH$, and H_2O_2 radicals.[34] These ROS are highly reactive and play a crucial role in the photocatalytic degradation of contaminants and inactivation of pathogens.

5.3 Improve the photocatalysis effectiveness

(a) Element doping

Much effort has been made to enhance the photocatalytic efficiencies of photocatalysts, such as doping and surface modification. Element doping of TiO_2 is one approach that can further narrow the bandgap, allowing it to utilize the full spectrum of visible light in sunlight.[35, 36] Elemental doping involves introducing foreign atoms into

the TiO₂ lattice, which can modify its electronic structure and optical properties.[37] For example, doping with metals like iron (Fe)[38], Ag[39], and copper (Cu)[40] has been shown to narrow the band gap of TiO₂, allowing it to absorb visible light more effectively than the pure material, which primarily absorbs ultraviolet light. Metal doping can introduce new recombination centers, while non-metal doping might decrease photocatalytic activity under certain conditions.

Non-metal doping, with elements such as nitrogen (N)[35], carbon (C)[41], and sulfur (S)[42], also shows promise. The choice of dopant depends on the desired application and the specific properties required for the photocatalyst. Overall, elemental-doped TiO₂ has shown improved performance in various environmental and energy applications, including air and water purification, self-cleaning surfaces, and hydrogen production. It also extends the range of light that TiO₂ can utilize, enhancing its photocatalytic activity under solar illumination.

(b) Immobilization

Photocatalysts are commonly used in suspension systems for photooxidation, but TiO₂ suspensions often face challenges such as particle aggregation and turbidity shading, which diminish photocatalytic activity. Immobilizing photocatalysts onto surfaces can effectively mitigate these issues.[43] Immobilization involves fixing the catalyst powder onto a support material, offering a sustainable and cost-effective disinfection solution without the need for post-treatment steps, thus reducing operational costs.[44] Additionally, immobilized photocatalysts can be reused without the need for recovery or separation from the suspension, addressing ecotoxicity concerns.[45, 46] Previous research has demonstrated the potential of immobilized TiO₂ for bacterial

inactivation. Cantarella et al. (2016) embedded TiO_2 in polymethyl methacrylate (PMMA) at a concentration of 150 g L^{-1}, achieving a 4.8-log reduction in *E. coli* in one hour under UV light.[47] Varnagiris et al. (2021) immobilized carbon-doped TiO_2 on high-density polyethylene (HDPE) beads, resulting in a 2.5-log reduction in *Salmonella typhimurium* in one hour under UV light (5 mW cm^{-2}).[48] However, the efficiency of immobilized photocatalysts against bacteria under visible light and their comparison to suspension systems have not been extensively explored.

Poly-methyl-methacrylate (PMMA) has excellent impact strength, UV resistance, and high transparency to visible light. It is also the most frequently used commercial polymer in architecture, electronics, and furniture.[49, 50] By sprinkling a layer of TiO_2 on PMMA fabricating a TiO_2/PMMA film, Ounas et al. (2020) showed that the photocatalytic degradation of methylene blue with UV light irradiation remained merely only 60% after 250 min because the sprinkling method reduced PMMA light transmittance by 50%.[51] To improve the light transmittance, other researchers have adopted methods to functionalize the PMMA polymer matrix with the minimum influence on its original properties, including dip-coating[52], vapor-deposition[53], and magnetron sputtering.[54] Dip-coating is an economical and facile approach to fabricating nanocoating on a polymer matrix that is easy to scale up with a uniform thickness.[52]

5.4 Role of waste-derived disinfection agents

Recently, a novel disinfection method has been reported to take advantage of waste oyster shells. A benefit of using oyster shells as a raw material is their abundance. Global oyster yield in 2019 was around 6.1×10^6 tons, and the yield increases yearly.[55] With the escalating yield, oyster shell waste becomes a greater environmental problem

impacting shorelines and fisheries worldwide. Using waste oyster shells as a disinfectant material would be a win-win strategy, providing a cost-effective material source and alleviating the environmental issue. Research has shown that pulverized oyster and scallop shells heated to over 700 °C exhibit bactericidal activity due to the conversion of calcium carbonate ($CaCO_3$) to calcium oxide (CaO).[56, 57] Oikawa et al. (2000) conducted the first study investigating the disinfection efficacy of heated oyster shells against *Staphylococcus aureus* (*S. aureus*), *Escherichia coli* (*E. coli*), and *Pseudomonas aeruginosa*, achieving 0.6-log-inactivation, 0.75-log-inactivation, and 3.8-log-inactivation with 1 g L^{-1} oyster shell solution in 1 h, respectively.[58] Later, Sawai *et al.* conducted several studies demonstrating that the heated scallop shells could effectively inactivate *S. aureus* and *E. coli*.[59]

It has been proposed that the disinfection observed with the use of heated oyster shell is related to ROS generation and protein denaturation.[60-64] For example, Chen et al. (2015), Sadeghi et al. (2020), and Park et al. (2021) have suggested that the disinfection mechanism of shell-derived disinfectants is related to the generation of $HO_2^•$, $^•O_2$, and H_2O_2.[60, 63, 65] In addition, several researchers have reported the presence of $HO_2^•$, $^•O_2$, and H_2O_2 in solutions containing shell-derived disinfectants.[56, 66-69] However, the presence of $^1O_2$ has not been reported, and no direct mechanistic evidence has been provided; thus, the disinfection mechanism remains unclear. Nevertheless, knowing how or why a disinfectant deactivates microorganisms is critical for understanding how efficiently the disinfectant removes viable microorganisms. It also provides information towards improvements in the production and efficacy of new disinfectants and the prediction of types of organisms the disinfectant could inactivate.

5.5 Different resistance of gram-positive and gram-negative bacteria towards ROSs

The literature has consistently highlighted the significant health risks posed by food contamination with pathogenic bacteria, such as *S. aureus* and *E. coli*.[70-72] *S. aureus* is predominantly associated with food poisoning and is also responsible for severe conditions like toxic shock syndrome, endocarditis, and infections in post-operative wounds. On the other hand, *E. coli*, commonly found in human intestines, is known to cause various infections, including urinary tract infections, cholecystitis, and septicemia. Moreover, *S. aureus* is a gram-positive bacteria, whereas *E. coli* is classified as a gram-negative bacteria. The cell wall of gram-positive bacteria like *S. aureus* is relatively thicker than gram-negative bacteria, measuring 20–80 nm.[73] It consists predominantly of a multilayered peptidoglycan structure, accounting for about 90% of its composition. This peptidoglycan forms a dense, three-dimensional lattice due to the glycans being extensively cross-linked. In contrast, the cell wall of gram-negative bacteria such as *E. coli* is thinner, only 10-15 nm, but structurally more complex.[74] The outer membrane of gram-negative bacteria is primarily composed of lipopolysaccharide (LPS) and includes a few layers of peptidoglycan, approximately 2 nm thick. This outer membrane is characterized by the presence of various lipoproteins, including porins, which are proteins that create pores in the outer membrane.[75]

This distinction in cell wall structure is crucial as it dictates their interaction with ROSs generated in various disinfection processes.[76] ROSs can damage cellular components due to their oxidative nature, leading to bacterial inactivation. With their outer lipid membrane, gram-negative bacteria can sometimes offer more resistance against ROSs than gram-positive counterparts.[23] This lipid barrier can impede the

penetration of ROSs, necessitating higher ROS concentrations or prolonged exposure for effective disinfection.[77] This inherent difference in resistance has significant implications for water disinfection strategies.

5.6 Summary

In summary, searching for an ideal disinfectant remains an ongoing and complex challenge. Previous research has underscored the importance of photocatalysis as an effective approach for decomposing organic pollutants and inactivating pathogens, primarily through the generation of ROSs like $^1O_2$ and $OH^.$. This study will introduce a surface-functionalized, nitrogen-doped TiO_2-coated polymethyl methacrylate composite (NT-PMMA) created using a dip-coating technique to boost photocatalytic activity through immobilization. It will explore the efficiency of NT-PMMA against both *S. aureus* and *E. coli* under visible light, and compare to the conventional suspension system. Moreover, this study will also investigate the efficacy of an oyster-shell-derived disinfectant against two bacteria, *S. aureus* and *E. coli*, examining its impact on bacterial permeability, morphology, and biophysical properties. The bacterial susceptibility to various disinfectants will be investigated by focusing on *Staphylococcus aureus* and *Escherichia coli* as representative models for gram-positive and gram-negative bacteria. This study will advance our understanding of pathogen inactivation by photocatalyst-immobilized polymers and shell-derived disinfectants, and advocates for applying innovative and environmentally sustainable approaches to pathogen inactivation.

5.7 References

(1) Ilyas, S.; Srivastava, R. R.; Kim, H. Disinfection technology and strategies for COVID-19 hospital and bio-medical waste management. *Sci. Total Environ.* **2020**, *749*, 141652. DOI: 10.1016/j.scitotenv.2020.141652.

(2) Exner, M.; Kramer, A.; Lajoie, L.; Gebel, J.; Engelhart, S.; Hartemann, P. Prevention and control of health care–associated waterborne infections in health care facilities. *Am. J. Infect. Control* **2005**, *33* (5, Supplement), S26-S40. DOI: 10.1016/j.ajic.2005.04.002.

(3) ICAN, C. a. *Best practices for environmental cleaning in healthcare facilities in resource-limited settings*; US Department of Health and Human Services, CDC, 2019.

(4) Ashbolt, N. J. Microbial contamination of drinking water and human health from community water systems. *Curr. Environ. Health Rep.* **2015**, *2* (1), 95-106. DOI: 10.1007/s40572-014-0037-5.

(5) Dalrymple, O. K.; Stefanakos, E.; Trotz, M. A.; Goswami, D. Y. A review of the mechanisms and modeling of photocatalytic disinfection. *Appl. Catal. B-Environ.* **2010**, *98* (1-2), 27-38. DOI: 10.1016/j.apcatb.2010.05.001.

(6) Moazzami, M.; Fernstrom, L. L.; Hansson, I. Reducing Campylobacter jejuni, Enterobacteriaceae and total aerobic bacteria on transport crates for chickens by irradiation with 265-nm ultraviolet light (UV-C LED). *Food Control* **2021**, *119*. DOI: 10.1016/j.foodcont.2020.107424.

(7) Abu-Shkara, F.; Neeman, I.; Sheinman, R.; Armon, R. The effect of fatty acid alteration in coliform bacteria on disinfection resistance and/or adaptation. *Water Sci. Technol.* **1998**, *38* (12), 133-139. DOI: 10.1016/s0273-1223(98)00814-2.

(8) Childress, H.; Sullivan, B.; Kaur, J.; Karthikeyan, R. Effects of ultraviolet light disinfection on tetracycline-resistant bacteria in wastewater effluents. *J. Water Health* **2014**, *12* (3), 404-409. DOI: 10.2166/wh.2013.257.

(9) Hsu, I. L.; Yeh, F. H.; Chin, Y.-C.; Cheung, C. I.; Chia, Z. C.; Yang, L.-X.; Chen, Y.-J.; Cheng, T.-Y.; Wu, S.-P.; Tsai, P.-J.; et al. Multiplex antibacterial processes and risk in resistant phenotype by high oxidation-state nanoparticles: New killing process and mechanism investigations. *Chem. Eng. J.* **2021**, *409*, 128266. DOI: 10.1016/j.cej.2020.128266.

(10) Mazhar, M. A.; Khan, N. A.; Ahmed, S.; Khan, A. H.; Hussain, A.; Rahisuddin; Changani, F.; Yousefi, M.; Ahmadi, S.; Vambol, V. Chlorination disinfection by-products in municipal drinking water – A review. *J. Clean Prod.* **2020**, *273*, 123159. DOI: 10.1016/j.jclepro.2020.123159.

(11) Deborde, M.; von Gunten, U. Reactions of chlorine with inorganic and organic compounds during water treatment—Kinetics and mechanisms: A critical review. *Water Res.* **2008**, *42* (1), 13-51. DOI: 10.1016/j.watres.2007.07.025.

(12) Rodriguez, M. J.; Serodes, J.; Roy, D. Formation and fate of haloacetic acids (HAAs) within the water treatment plant. *Water Res.* **2007**, *41* (18), 4222-4232. DOI: 10.1016/j.watres.2007.05.048.

(13) Pan, S.; An, W.; Li, H.; Su, M.; Zhang, J.; Yang, M. Cancer risk assessment on trihalomethanes and haloacetic acids in drinking water of China using disability-adjusted life years. *J. Hazard. Mater.* **2014**, *280*, 288-294. DOI: 10.1016/j.jhazmat.2014.07.080.

(14) Chen, J.; Loeb, S.; Kim, J.-H. LED revolution: fundamentals and prospects for UV disinfection applications. *Environ. Sci.-Wat. Res. Technol.* **2017**, *3* (2), 188-202. DOI: 10.1039/C6EW00241B.

(15) Zhang, G.; Li, W.; Chen, S.; Zhou, W.; Chen, J. Problems of conventional disinfection and new sterilization methods for antibiotic resistance control. *Chemosphere* **2020**, *254*, 126831. DOI: 10.1016/j.chemosphere.2020.126831.

(16) Wolfe, R. L. Ultraviolet disinfection of potable water. *Environ. Sci. Technol.* **1990**, *24* (6), 768-773. DOI: 10.1021/es00076a001.

(17) Deshmukh, S. P.; Patil, S. M.; Mullani, S. B.; Delekar, S. D. Silver nanoparticles as an effective disinfectant: A review. *Mater. Sci. Eng. C-Mater. Biol. Appl.* **2019**, *97*, 954-965. DOI: 10.1016/j.msec.2018.12.102.

(18) Thurman, R. B.; Gerba, C. P.; Bitton, G. The molecular mechanisms of copper and silver ion disinfection of bacteria and viruses. *Crit. Rev. Environ. Sci. Technol.* **1989**, *18* (4), 295-315. DOI: 10.1080/10643388909388351.

(19) Quadros, M. E.; Pierson, R. I. V.; Tulve, N. S.; Willis, R.; Rogers, K.; Thomas, T. A.; Marr, L. C. Release of silver from nanotechnology-based consumer products for children. *Environ. Sci. Technol.* **2013**, *47* (15), 8894-8901. DOI: 10.1021/es4015844.

(20) Bell, R. A.; Kramer, J. R. Structural chemistry and geochemistry of silver-sulfur compounds: Critical review. *Environ. Toxicol. Chem.* **1999**, *18* (1), 9-22. DOI: 10.1002/etc.5620180103.

(21) Kaegi, R.; Voegelin, A.; Sinnet, B.; Zuleeg, S.; Hagendorfer, H.; Burkhardt, M.; Siegrist, H. Behavior of metallic silver nanoparticles in a pilot wastewater treatment Plant. *Environ. Sci. Technol.* **2011**, *45* (9), 3902-3908. DOI: 10.1021/es1041892.

(22) Bahcelioglu, E.; Unalan, H. E.; Erguder, T. H. Silver-based nanomaterials: A critical review on factors affecting water disinfection performance and silver release. *Crit. Rev. Environ. Sci. Technol.* **2021**, *51* (20), 2389-2423. DOI: 10.1080/10643389.2020.1784666.

(23) Tzeng, J.-H.; Weng, C.-H.; Yen, L.-T.; Gaybullaev, G.; Chang, C.-J.; de Luna, M. D. G.; Lin, Y.-T. Inactivation of pathogens by visible light photocatalysis with nitrogen-doped TiO_2 and tourmaline-nitrogen co-doped TiO_2. *Sep. Purif. Technol.* **2021**, *274*, 118979. DOI: 10.1016/j.seppur.2021.118979.

(24) Schneider, J.; Matsuoka, M.; Takeuchi, M.; Zhang, J.; Horiuchi, Y.; Anpo, M.; Bahnemann, D. W. Understanding TiO_2 photocatalysis: mechanisms and materials. *Chem. Rev.* **2014**, *114* (19), 9919-9986. DOI: 10.1021/cr5001892.

(25) Mukherjee, J.; Lodh, B. K.; Sharma, R.; Mahata, N.; Shah, M. P.; Mandal, S.; Ghanta, S.; Bhunia, B. Advanced oxidation process for the treatment of industrial wastewater: A review on strategies, mechanisms, bottlenecks and prospects. *Chemosphere* **2023**, *345*, 140473. DOI: 10.1016/j.chemosphere.2023.140473.

(26) Zhao, Q.; Zhao, X.; Cao, J. Advanced nanomaterials for degrading persistent organic pollutants. In *Advanced Nanomaterials for Pollutant Sensing and Environmental Catalysis*, Zhao, Q. Ed.; Elsevier, 2020; pp 249-305.

(27) Klavarioti, M.; Mantzavinos, D.; Kassinos, D. Removal of residual pharmaceuticals from aqueous systems by advanced oxidation processes. *Environ. Int.* **2009**, *35* (2), 402-417. DOI: 10.1016/j.envint.2008.07.009.

(28) Roy, K.; Moholkar, V. S. Sulfadiazine degradation using hybrid AOP of heterogeneous Fenton/persulfate system coupled with hydrodynamic cavitation. *Chem. Eng. J.* **2020**, *386*, 121294. DOI: 10.1016/j.cej.2019.03.170.

(29) Wang, A. Q.; Wang, H.; Deng, H.; Wang, S.; Shi, W.; Yi, Z. X.; Qiu, R. L.; Yan, K. Controllable synthesis of mesoporous manganese oxide microsphere efficient for photo-Fenton-like removal of fluoroquinolone antibiotics. *Appl. Catal. B-Environ.* **2019**, *248*, 298-308. DOI: 10.1016/j.apcatb.2019.02.034.

(30) Guo, Y.; Zhang, Y. X.; Yu, G.; Wang, Y. J. Revisiting the role of reactive oxygen species for pollutant abatement during catalytic ozonation: The probe approach versus the scavenger approach. *Appl. Catal. B-Environ.* **2021**, *280*. DOI: 10.1016/j.apcatb.2020.119418.

(31) Gao, P.; Tian, X.; Nie, Y.; Yang, C.; Zhou, Z.; Wang, Y. Promoted peroxymonosulfate activation into singlet oxygen over perovskite for ofloxacin degradation by controlling the oxygen defect concentration. *Chem. Eng. J.* **2019**, *359*, 828-839. DOI: 10.1016/j.cej.2018.11.184.

(32) Giannakis, S.; Lin, K.-Y. A.; Ghanbari, F. A review of the recent advances on the treatment of industrial wastewaters by sulfate radical-based advanced oxidation processes (SR-AOPs). *Chem. Eng. J.* **2021**, *406*, 127083. DOI: 10.1016/j.cej.2020.127083.

(33) Dette, C.; Pérez-Osorio, M. A.; Kley, C. S.; Punke, P.; Patrick, C. E.; Jacobson, P.; Giustino, F.; Jung, S. J.; Kern, K. TiO_2 anatase with a bandgap in the visible region. *Nano Lett.* **2014**, *14* (11), 6533-6538. DOI: 10.1021/nl503131s.

(34) Nosaka, Y.; Nosaka, A. Y. Generation and detection of reactive oxygen species in photocatalysis. *Chem. Rev.* **2017**, *117* (17), 11302-11336. DOI: 10.1021/acs.chemrev.7b00161.

(35) Lin, Y.-H.; Weng, C.-H.; Srivastav, A. L.; Lin, Y.-T.; Tzeng, J.-H. Facile synthesis and characterization of N-doped TiO_2 photocatalyst and its visible-light activity for

photo-oxidation of ethylene. *J. Nanomater.* **2015**, 807394. DOI: 10.1155/2015/807394.

(36) Lin, Y. T.; Weng, C. H.; Chen, F. Y. Key operating parameters affecting photocatalytic activity of visible-light-induced C-doped TiO_2 catalyst for ethylene oxidation. *Chem. Eng. J.* **2014**, *248*, 175-183. DOI: 10.1016/j.cej.2014.02.085.

(37) Fei, H.; Aihua, Y.; Hui, Z. Influences of doping on photocatalytic properties of TiO_2 photocatalyst. In *Semiconductor Photocatalysis*, Wenbin, C. Ed.; IntechOpen, 2016; p Ch. 2.

(38) Moradi, V.; Jun, M. B. G.; Blackburn, A.; Herring, R. A. Significant improvement in visible light photocatalytic activity of Fe doped TiO_2 using an acid treatment process. *Appl. Surf. Sci.* **2018**, *427*, 791-799. DOI: 10.1016/j.apsusc.2017.09.017.

(39) Chokesawatanakit, N.; Jutakridsada, P.; Boonlue, S.; Knijnenburg, J. T. N.; Wright, P. C.; Sillanpää, M.; Kamwilaisak, K. Ag-doped Cobweb-like structure of TiO_2 nanotubes for antibacterial activity against Methicillin-resistant *Staphylococcus aureus* (MRSA). *J. Environ. Chem. Eng.* **2021**, *9* (5), 105843. DOI: 10.1016/j.jece.2021.105843.

(40) Guo, F.; Liu, J.; Zhang, W.; Yu, Z.; Liu, Y.; Liang, W. Synthesis of Cu,N-doped TiO_2 nanotube by a novel magnetron sputtering method and its photoelectric property. *Vacuum* **2019**, *165*, 223-231. DOI: 10.1016/j.vacuum.2019.04.032.

(41) Huang, S.-M.; Weng, C.-H.; Tzeng, J.-H.; Huang, Y.-Z.; Anotai, J.; Yen, L.-T.; Chang, C.-J.; Lin, Y.-T. Kinetic study and performance comparison of TiO_2-mediated visible-light-responsive photocatalysts for the inactivation of *Aspergillus niger*. *Sci. Total Environ.* **2019**, *692*. DOI: 10.1016/j.scitotenv.2019.07.329.

(42) Han, C.; Pelaez, M.; Likodimos, V.; Kontos, A. G.; Falaras, P.; O'Shea, K.; Dionysiou, D. D. Innovative visible light-activated sulfur doped TiO_2 films for water treatment. *Appl. Catal. B-Environ.* **2011**, *107* (1), 77-87. DOI: 10.1016/j.apcatb.2011.06.039.

(43) Terra, J. C. S.; Desgranges, A.; Amara, Z.; Moores, A. Photocatalysis on magnetic supports for singlet oxygen generation: Role of immobilization and photobleaching. *Catal. Today* **2023**, *407*, 52-58. DOI: 10.1016/j.cattod.2022.05.042.

(44) Goutham, R.; Badri Narayan, R.; Srikanth, B.; Gopinath, K. P. Supporting materials for immobilisation of nano-photocatalysts. In *Nanophotocatalysis and Environmental Applications : Materials and Technology*, Inamuddin, Sharma, G., Kumar, A., Lichtfouse, E., Asiri, A. M. Eds.; Springer International Publishing, 2019; pp 49-82.

(45) Wood, D.; Shaw, S.; Cawte, T.; Shanen, E.; Van Heyst, B. An overview of photocatalyst immobilization methods for air pollution remediation. *Chem. Eng. J.* **2020**, *391*, 123490. DOI: 10.1016/j.cej.2019.123490.

(46) Zhang, L. X.; Rao, L.; Wang, P. F.; Shi, Z. Y. Durable, strong, and flexible superhydrophobic N-TiO_2 silicone composite aerogels with unique air-liquid-solid

triphase photocatalytic properties. *Appl. Surf. Sci.* **2023**, *609*. DOI: 10.1016/j.apsusc.2022.155348.

(47) Cantarella, M.; Sanz, R.; Buccheri, M. A.; Ruffino, F.; Rappazzo, G.; Scalese, S.; Impellizzeri, G.; Romano, L.; Privitera, V. Immobilization of nanomaterials in PMMA composites for photocatalytic removal of dyes, phenols and bacteria from water. *J. Photochem. Photobiol. A-Chem.* **2016**, *321*, 1-11. DOI: 10.1016/j.jphotochem.2016.01.020.

(48) Varnagiris, S.; Urbonavicius, M.; Sakalauskaite, S.; Demikyte, E.; Tuckute, S.; Lelis, M. Photocatalytic inactivation of *Salmonella typhimurium* by floating carbon-doped TiO₂ photocatalyst. *Materials* **2021**, *14* (19), 5681. DOI: 10.3390/ma14195681.

(49) El-Newehy, M. H.; Kim, H. Y.; Khattab, T. A.; El-Naggar, M. E. Production of photoluminescent transparent poly(methyl methacrylate) for smart windows. *Luminescence* **2022**, *37* (1), 97-107. DOI: 10.1002/bio.4150.

(50) Khaled, S. M.; Sui, R.; Charpentier, P. A.; Rizkalla, A. S. Synthesis of TiO₂−PMMA nanocomposite: using methacrylic acid as a coupling agent. *Langmuir* **2007**, *23* (7), 3988-3995. DOI: 10.1021/la062879n.

(51) Ounas, O.; El Foulani, A. A.; Lekhlif, B.; Jamal-Eddine, J. Immobilization of TiO2 into a poly methyl methacrylate (PMMA) as hybrid film for photocatalytic degradation of methylene blue. *Mater. Today Proc.* **2020**, *22*, 35-40. DOI: 10.1016/j.matpr.2019.08.068.

(52) Wu, T.-T.; Guo, S.; Li, B.; Li, J.-Y.; Zhang, H.-S.; Ma, P.-Z.; Zhang, X.; Shen, C.-Y.; Liu, X.-H.; Cao, A.-M. Facile construction of nanofilms from a dip-coating process to enable high-performance solid-state batteries. *ACS Appl. Mater. Interfaces* **2022**, *14* (28), 32026-32034. DOI: 10.1021/acsami.2c07292.

(53) Peng, X.; Lv, Y.; Zhao, S. Chemical vapor deposition and thermal oxidation of cuprous phosphide nanofilm. *Coatings* **2022**, *12* (1), 68. DOI: 10.3390/coatings12010068.

(54) Hao, B.; Guo, J.; Zhang, L.; Ma, H. Cr-doped TiO₂/CuO photocatalytic nanofilms prepared by magnetron sputtering for wastewater treatment. *Ceram. Int.* **2022**, *48* (5), 7106-7116. DOI: 10.1016/j.ceramint.2021.11.270.

(55) Botta, R.; Asche, F.; Borsum, J. S.; Camp, E. V. A review of global oyster aquaculture production and consumption. *Mar. Pol.* **2020**, *117*. DOI: 10.1016/j.marpol.2020.103952.

(56) Shimamura, N.; Irie, F.; Yamakawa, T.; Kikuchi, M.; Sawai, J. Heated scallop-shell powder treatment for deactivation and removal of Listeria sp biofilm formed at a low temperature. *Biocontrol Sci.* **2015**, *20* (2), 153-157. DOI: 10.4265/bio.20.153.

(57) Xing, R.; Qin, Y.; Guan, X.; Liu, S.; Yu, H.; Li, P. Comparison of antifungal activities of scallop shell, oyster shell and their pyrolyzed products. *Egypt. J. Aquat. Res.* **2013**, *39* (2), 83-90. DOI: 10.1016/j.ejar.2013.07.003.

(58) Oikawa, K.; Asada, T.; Yamamoto, K.; Wakabayashi, H.; Sasaki, M.; Sato, M.; Matsuda, J. Antibacterial activity of calcined shell calcium prepared from wild surf clam. *J. Health Sci.* **2000**, *46* (2), 98-103.

(59) Sawai, J.; Shiga, H.; Kojima, H. Kinetic analysis of the bactericidal action of heated scallop-shell powder. *Int. J. Food Microbiol.* **2001**, *71* (2-3), 211-218. DOI: 10.1016/s0168-1605(01)00619-5.

(60) Sadeghi, K.; Thanakkasaranee, S.; Lim, I. J.; Seo, J. Calcined marine coral powders as a novel ecofriendly antimicrobial agent. *Mater. Sci. Eng. C-Mater. Biol. Appl.* **2020**, *107*, 6. DOI: 10.1016/j.msec.2019.110193.

(61) Sawai, J.; Kawada, E.; Kanou, F.; Igarashi, H.; Hashimoto, A.; Kokugan, T.; Shimizu, M. Detection of active oxygen generated from ceramic powders having antibacterial activity. *J. Chem. Eng. Jpn.* **1996**, *29* (4), 627-633. DOI: 10.1252/jcej.29.627.

(62) Sato, Y.; Ishihara, M.; Nakamura, S.; Fukuda, K.; Kuwabara, M.; Takayama, T.; Hiruma, S.; Murakami, K.; Fujita, M.; Yokoe, H. Comparison of various disinfectants on bactericidal activity under organic matter contaminated environments. *Biocontrol Sci.* **2019**, *24* (2), 103-108. DOI: 10.4265/bio.24.103.

(63) Chen, Y. C.; Lin, C. L.; Li, C. T.; Hwang, D. F. Structural transformation of oyster, hard clam, and sea urchin shells after calcination and their antibacterial activity against foodborne microorganisms. *Fish. Sci.* **2015**, *81* (4), 787-794. DOI: 10.1007/s12562-015-0892-5.

(64) Alsohaimi, I. H.; Nassar, A. M.; Elnasr, T. A. S.; Cheba, B. A novel composite silver nanoparticles loaded calcium oxide stemming from egg shell recycling: A potent photocatalytic and antibacterial activities. *J. Clean Prod.* **2020**, *248*. DOI: 10.1016/j.jclepro.2019.119274.

(65) Park, K.; Sadeghi, K.; Thanakkasaranee, S.; Park, Y. I.; Park, J.; Nam, K. H.; Han, H.; Seo, J. Effects of calcination temperature on morphological and crystallographic properties of oyster shell as biocidal agent. *Int. J. Appl. Ceram. Technol.* **2021**, *18* (2), 302-311. DOI: 10.1111/ijac.13647.

(66) Sawai, J.; Miyoshi, H.; Kojima, H. Sporicidal kinetics of Bacillus subtilis spores by heated scallop shell powder. *J. Food Prot.* **2003**, *66* (8), 1482-1485. DOI: 10.4315/0362-028x-66.8.1482.

(67) Sawai, J. Antimicrobial characteristics of heated scallop shell powder and its application. *Biocontrol Sci.* **2011**, *16* (3), 95-102. DOI: 10.4265/bio.16.95.

(68) Watanabe, T.; Fujimoto, R.; Sawai, J.; Kikuchi, M.; Yahata, S.; Satoh, S. Antibacterial characteristics of heated scallop-shell nano-particles. *Biocontrol Sci.* **2014**, *19* (2), 93-97. DOI: 10.4265/bio.19.93.

(69) Nomoto, Y.; Sawada, S.; Abe, S.; Wakazawa, J.; Kikuchi, M.; Sawai, J. Sorbitol minimizes calcium carbonate scale generation while maintaining the disinfection

effect of heated scallop-shell powder for fresh produce. *Biocontrol Sci.* **2018**, *23* (4), 157-165. DOI: 10.4265/bio.23.157.

(70) Poolman, J. T.; Anderson, A. S. *Escherichia coli* and *Staphylococcus aureus*: leading bacterial pathogens of healthcare associated infections and bacteremia in older-age populations. *Expert Rev. Vaccines* **2018**, *17* (7), 607-618. DOI: 10.1080/14760584.2018.1488590.

(71) Haque, M.; Sartelli, M.; McKimm, J.; Bakar, M. A. Health care-associated infections – an overview. *Infect. Drug Resistance* **2018**, *11* (null), 2321-2333. DOI: 10.2147/IDR.S177247.

(72) Stone, P. W. Economic burden of healthcare-associated infections: an American perspective. *Expert Rev. Pharmacoecon. Outcomes Res.* **2009**, *9* (5), 417-422. DOI: 10.1586/erp.09.53.

(73) Rohde, M. The gram-positive bacterial cell wall. *Microbiol. Spectr.* **2019**, *7* (3), 10.1128/microbiolspec.gpp1123-0044-2018. DOI: 10.1128/microbiolspec.gpp3-0044-2018.

(74) Huang, K. C.; Mukhopadhyay, R.; Wen, B.; Gitai, Z.; Wingreen, N. S. Cell shape and cell-wall organization in Gram-negative bacteria. *Proc. Natl. Acad. Sci.* **2008**, *105* (49), 19282-19287. DOI: doi:10.1073/pnas.0805309105.

(75) Beveridge, T. J. Structures of gram-negative cell walls and their derived membrane vesicles. *J. Bacteriol.* **1999**, *181* (16), 4725-4733. DOI: doi:10.1128/jb.181.16.4725-4733.1999.

(76) Zhang, J.; Su, P.; Chen, H.; Qiao, M.; Yang, B.; Zhao, X. Impact of reactive oxygen species on cell activity and structural integrity of Gram-positive and Gram-negative bacteria in electrochemical disinfection system. *Chem. Eng. J.* **2023**, *451*, 138879. DOI: 10.1016/j.cej.2022.138879.

(77) Huang, M.; Zhuang, H.; Zhao, J.; Wang, J.; Yan, W.; Zhang, J. Differences in cellular damage induced by dielectric barrier discharge plasma between Salmonella Typhimurium and Staphylococcus aureus. *Bioelectrochemistry* **2020**, *132*, 107445. DOI: 10.1016/j.bioelechem.2019.107445.

CHAPTER 6

Mode of inactivation of *Staphylococcus aureus* and *Escherichia coli* by heated oyster-shell powder

6.1 Abstract[1]

Bacterial infection and subsequent disinfection of microorganisms are ongoing issues around the world. Bio-calcium oxide derived from heated oyster-shell (HOS) waste product has been shown to be an effective disinfectant and has the additional advantage of the marketing use of utilizing waste materials that would otherwise contribute to environmental problems; however, its mode of inactivation is unknown. In this research, fluorescence microscopy (FM), transmission electron microscopy (TEM), atomic force microscopy (AFM), and electron spin resonance (ESR) spectrometer techniques were used to characterize the mode of inactivation of *S. aureus* and *E. coli* via HOS. This is the first work to provide insight into the three-dimensional morphology and biophysical properties of the inactivated *S. aureus* and *E. coli* cells via HOS. Noteworthy, the presence of singlet oxygen in HOS suspension altered bacterial cell permeability, leading to sustained inactivation. The HOS exhibited excellent disinfection capacity and achieved a 5-log-inactivation *E. coli* within 60 min with a dose of 0.2 g/L, superior to other shell-derived disinfectants. Thus, HOS provides a cost-effective disinfectant for the application of controlling pathogens.

Keywords: singlet oxygen, disinfection, heated oyster shell, *Staphylococcus aureus,*

Escherichia coli singlet oxygen, pathogens

6.2 Introduction

Bacterial infection is a serious issue worldwide [1]. Conventional disinfection

methods, including chlorination, UV light, and ozonation, have been well established.

However, these methods also have disadvantages, such as the high cost of the raw

chemicals, generation of toxic by-products, or low disinfection efficiency [2, 3]. In

addition, pathogens develop resistance to traditional disinfectants necessitating the

ongoing development of effective disinfectants and promising disinfection methods [4-6].

Recently, a novel disinfection method has been reported that takes advantage of waste

oyster shells. A benefit of using oyster shells as a raw material is their abundance. Global

oyster yield in 2019 was around 6.1×10^6 tons, and the yield is increasing every year [7,

8]. With the escalating yield, oyster shell waste becomes a greater environmental problem

impacting shorelines and fisheries worldwide. Using waste oyster shells as a disinfectant

material would be a win-win strategy, providing a cost-effective material source and

alleviating the environmental issue.

Research has shown that pulverized oyster and scallop shells heated to over 700

°C exhibit bactericidal activity due to the conversion of calcium carbonate ($CaCO_3$) to

calcium oxide (CaO) [9, 10]. Oikawa et al. (2000) conducted the first study investigating

the disinfection efficacy of heated oyster shells against *Staphylococcus aureus* (*S.

aureus*), *Escherichia coli* (*E. coli*), and *Pseudomonas aeruginosa*, achieving 0.6-log-

inactivation, 0.75-log-inactivation, and 3.8-log-inactivation with 1 g/L oyster shell

solution in 1 h, respectively [11]. Later, Sawai *et al.* conducted several studies

demonstrating that the heated scallop shells could effectively inactivate *S. aureus* and *E. coli* [12].

Advanced oxidation processes (AOP) have gained notice in recent years as effective means for decomposing organic pollutants and inactivating pathogens [13-16]. The procedures rely on the production of highly reactive oxygen-containing species (ROS) such as hydroxide radicals (OH·) and hydrogen peroxide (H_2O_2). These strong oxidants can degrade recalcitrant compounds through reactions involving, for example, Fenton catalysis [17, 18], ozonation [19], and sulfate radical-based reactions [20, 21]. Singlet oxygen ($^1O_2$) has been reported to be the most reactive ROS, with 94 kJ mol^{-1}($\Delta_G H°_{298}$) above the ground state triplet oxygen ($O_2(^3\Sigma_g^-)$) [22]. Other studies posited that singlet oxygen causes great damage to proteins located on bacterial membranes due to oxidation [23]. Indeed, singlet oxygen demonstrated greater suitability than other ROS as an oxidant for biological targets [24], suggesting that the presence of singlet oxygen is critical in disinfection mechanisms.

It has been proposed that the disinfection observed with the use of heated oyster-shell (HOS) is related to ROS generation and protein denaturation [25-29]. For example, Chen et al. (2015), Sadeghi et al. (2020), and Park et al. (2021) have suggested that the disinfection mechanism of shell-derived disinfectants is related to the generation of $HO_2^•$, $^•O_2$, and H_2O_2 [25, 28, 30]. In addition, several researchers have reported the presence of $HO_2^•$, $^•O_2$, and H_2O_2 in solutions containing shell-derived disinfectants [9, 31-34]. However, the presence of singlet oxygen has not been reported, and no direct mechanistic evidence has been provided; thus, the disinfection mechanism remains unclear. Nevertheless, knowing how or why a disinfectant deactivates microorganisms is critical

for understanding how efficiently the disinfectant removes viable microorganisms. It also provides information towards improvements in the production and efficacy of new disinfectants and prediction of types of organisms the disinfectant could inactivate.

Thus, this study aims to elucidate the mechanism by which HOS deactivates two bacteria: gram-positive *S. aureus* and gram-negative *E. coli*. *S. aureus* is one of the primary pathogens involved in nosocomial infections in medical institutions worldwide [35, 36]. *E. coli* is a well-known bioindicator of water and food contamination, inducing diarrhea and even hemolytic uremic syndrome [37, 38]. In this study, we hypothesize that the highly active singlet oxygen generated in the HOS suspension is the primary disinfection mechanism against bacteria. Singlet oxygen further attacks bacterial cells and alters cell permeability, leading to the leakage of cellular components and the collapse of the cell structure. To diagnose the change of biophysical properties in the disinfection process, we used atomic force microscopy (AFM) to characterize the 3D morphology and biophysical properties of inactivated bacteria in the disinfection process, including height, surface roughness, adhesion, and Derjaguin-Muller-Toporov (DMT) elastic modulus. Real-time observation and three-dimensional images of the living bacterial cells provide a better understanding of the disinfection processes. For example, Betancourt et al. (2019) showed the increasing bacterial roughness during sodium hypochlorite inactivation [39], and Pleskova et al. (2016) demonstrated decreasing bacterial height during TiO_2 inactivation [40]. Our research team has exhibited the potential of early diagnosis via AFM for the microbial inactivation processes (Tzeng et al., 2021). To gain insight into the disinfection mechanism, we also monitored cell morphology, cell wall ultrastructure, biophysical properties, and the changes in

intracellular substances (e.g., potassium ions) of the inactivated bacteria. Finally, an electron spin resonance (ESR) spectrometer was employed to identify the active ROS in the HOS suspension.

Thus, this study elaborates on the interaction between HOS and two different bacteria (*S. aureus* and *E. coli*) and the HOS impacts on bacterial permeability, morphology, and biophysical properties. The results increase our understanding of pathogen inactivation by HOS, supporting the application of oyster shell waste as the source of a low-cost, environmentally-friendly disinfectant.

6.3 Materials and Methods

6.3.1 Chemicals

Analytical grade 2,2,6,6-tetramethyl-1-piperidone (TEMP, 95%), furfuryl alcohol (FA, 98%), reagent grade sodium hypochlorite solution (NaClO, 10-15%), propidium iodide (PI), and diamidino-2-phenylindole (DAPI) were purchased from Sigma-Aldrich. 9,10-anthracenediyl-bis(methylene)dimalonic acid (ABDA) was purchased from FLUKA. Difco™ Nutrient Agar was purchased from BD Diagnostics for culturing the bacteria. Uranyl acetate (98-100%) purchased from Spectrum™ and led citrate from Sigma-Aldrich were used for bacterial sample staining.

6.3.2 Preparation and characterization of heated oyster shell (HOS)

Waste oyster shell (*Crassostrea gigas*) was obtained from Wong Gong fishery harbor in Taiwan. Upon reception, the waste shell was washed with tap water to remove surface impurities. It was then soaked in a 1% NaClO solution for 24 h and cleaned with deionized water. The treated shells were oven-dried at 105 °C for 18 h and then

pulverized with a grinder (Rong Tsong Precision Technology Co., RT-N12, Taiwan). The pulverized oyster shell was then heated in a furnace (Cherng Huei, CH-202045, Taiwan) at 105°C for 60 min and calcined by ramping to 1050°C for 120 min. Finally, the calcined powder was cooled to room temperature before grinding in a Planetary Ball Mill (Retsch, PM400, Germany) at 300 rpm for 60 min.

The HOS particle size was analyzed via the dynamic light scattering (DLS) with a Zetasizer (Nano ZS, Malvern, United Kingdom). The specific surface area was obtained by nitrogen adsorption according to the Brunauer-Emmett-Teller (BET) equation (Micromeritics ASAP 2020, USA). The crystal phases of the composites were analyzed by X-ray diffraction (XRD) (BRUKER, D8 SSS, USA) with Cu-Ka radiation ($\lambda =$ 1.54184 Å), which recorded the data over a 2θ range from 5° to 80°. The surface functional groups were identified using Fourier transform infrared spectroscopy (FTIR 4700, JASCO, Japan) coupled with attenuated total reflection (ATR) over the region 400-4000 cm^{-1} with 4 cm^{-1} spectral resolution.

6.3.3 Detection of generated reactive oxygen species (ROS)

The reactive oxygen species (ROS) were detected using an electron spin resonance (ESR) spectrometer (Bruker, ELEXSYS-II E580 FT/CW system) equipped with an X-band range of 9.49 – 9.88 GHz 8.02 mW power. A 0.05 M 2,2,6,6-tetramethyl-1-piperidone (TEMP, 7.8 mg/mL) solution was used to detect $^1O_2$ in the aqueous solution. HOS was dispersed in deionized water (1 mg/mL) by ultrasonication for 1 min before adding the trapping agent. The HOS suspension was immediately transferred to the ESR for measurement. The same HOS suspension was then prepared for scavenging experiments, with the addition of furfuryl alcohol (FA) as the scavenger for TEMP–$^1O_2$.

In order to quantify the yield of singlet oxygen generated from HOS during the disinfection process, 9,10-anthracenediyl-bis(methylene)dimalonic acid (ABDA) was used [41]. A 0.2 mg ABDA was dispersed in 0.1 mL dimethyl sulfoxide (DMSO) to form a 5 mM solution. Then a 5 µL aliquot of the ABDA solution was added to the 200 µL HOS suspension (500 ppm). The absorbance at a wavelength of 380 nm at 0 and 120 min was recorded by a microplate reader (Awareness Technology). The whole process was conducted without light exposure.

6.3.4 Disinfection experiments

Staphylococcus aureus (*S. aureus,* ATCC 6538P) and *Escherichia coli* (*E. coli,* ATCC 8739) were purchased from the Bioresource Collection and Research Center, Taiwan. The bacteria strains were cultured on nutrient agar plates for 18 h. The bacteria were washed three times with sterile, deionized water and then re-suspended in 9 mL sterile deionized water. *S. aureus* and *E. coli* were inoculated into polypropylene plastic vessels containing 100 mL sterile water to achieve a desired initial bacterial concentration (10^5 and 10^8 CFU/mL) [42]. The HOS dosage was maintained at 0.2 g/L in the suspension at a pH of 11.5 ± 0.1. A 0.1 mL bacterial suspension aliquot was from the bulk suspension at different reaction times and cultured on nutrient agar plates using a spread plate method. For comparison, bacterial suspension treated with 100 mL NaOH solution at pH of 11.5 ± 0.1 was prepared. Temperature-controlled (25 °C) stirring was maintained throughout the experiments. All agar plates, solutions, glassware, and pipette tips were sterilized in an autoclave at 121 °C for 40 min before use in each experiment.

The bacterial survival ratio and disinfection efficiency were calculated as follows:

$$\text{Survival Ratio (\%)} = (N_t/ N_0) \times 100 \tag{1}$$

$$\text{Disinfection efficiency (\%)} = (1- N_t/ N_0) \times 100 \tag{2}$$

where N_t and N_0 are bacteria concentrations (CFU/mL) at time t (min) and starting point (0 min), respectively.

6.3.5 Ultrastructure of bacteria and intracellular component leakage

For the transmission electron microscopy (TEM) analyses, the sample was prepared by fixing 5 mL of the bacterial suspensions with 2.5% (v/v) glutaraldehyde for 2 h. The samples were then postfixed with 1% (w/v) osmium tetroxide for 2 h at room temperature. After washing the samples three times with a phosphate buffer (pH 6.8), they were dehydrated in a graded series of ethanol (50%, 70%, 80%, 95%, and 100% v/v) before embedding in 300 μL LR white resin (London Resin Company Ltd). Next, thin sections of the specimens were cut with a diamond knife. The sectioned samples were double-stained with saturated uranyl acetate and lead citrate [43]. Finally, the grids were examined with a JEM-1400 transmission electron microscope (Hitachi, Tokyo, Japan) at an operating voltage of 12 kV.

To determine potassium ion (K^+) leakage from the bacterial cells during the disinfection process, 10 mL of bacterial suspension was collected at several reaction times: 0, 60, 120, 240, and 360 min. The suspensions were filtered through the 25 mm diameter nylon syringe filters (0.22 μm pore size, Millipore). After filtration, the K concentrations were measured by inductively coupled plasma optical emission spectrometry (ICP-OES) (Element 2, Thermo Scientific).

6.3.6 Measurement of cell wall permeability via fluorescence microscopy (FM)

To prepare the samples for analysis by FM, a 1-mL aliquot of the reaction suspension was sampled at each of the designed reaction times (0, 60, 120, 240, and 360 min). After the suspension aliquot was centrifuged at 1,000 × g for 5 min, 900 μL of supernatant was removed to get the bacteria pellet. Then, propidium iodide (PI) and diamidino-2-phenylindole (DAPI) were added to the bacteria pellet and mixed for 20 and 40 min, respectively [44]. PI is a red-fluorescent probe that does not permeate cell membranes and is commonly used to detect cell membrane injury. DAPI is a blue fluorescent probe that selectively binds to the minor groove of double-stranded DNA. The samples were analyzed with an inverted fluorescence microscope (IFM) (TH4-100, Olympus, Japan).

For each sample, five different locations were chosen randomly. Two images were taken at each location. The DAPI-stained cells were imaged using a filter with excitation 340-380 nm and suppression at 425 nm. The PI-stained cells were visualized using a filter with excitation at 515 - 560 nm and suppression at 590 nm. Cell counting was conducted with the image processing software (Image J, version 1.53).

Membrane permeability ratio (%)＝(N_{PI}/ N_{DAPI})×100 %　　　　　　　　(3)

where N_{PI} is the amount of PI-fluorescent bacteria (CFU), N_{DAPI} is the amount of DAPI-fluorescent bacteria (CFU).

6.3.7 Three-dimensional image and biophysical properties measurement

Following disinfection, the biophysical properties of the inactivated bacteria, including cell height, surface roughness, DMT modulus, and adhesion of the bacterial

surface, were measured by AFM (Dimension Icon, Bruker, USA) in Peak Force QNM

mode with ACTA cantilever from AppNano (Applied NanoStructures, Inc., USA). The

resonance frequency and spring constant of the ACTA cantilever were 200 - 400 kHz and

25 - 75 Nm^{-1}, respectively. Biophysical properties were measured and analyzed using the

instrument-equipped software, NanoScope 6.0. Bacterial surface roughness was

calculated from the bacterial surface height using the root-mean-square (R_{rms}) equation

Eq. (4).

$$R_{rms} = \sqrt{\sum_{i=1}^{N} \frac{(Z_i - Z_m)^2}{N-1}} \tag{4}$$

where N is the total number of data points, Z_i is the height of ith point, and Z_m is

the mean height [42, 45-48]. The DMT elastic modulus is shown in Eq. (5). DMT model

was used when surface deformation was lower than tip radius [49].

$$F_{tip,DMT} = \frac{4}{3} E^* \sqrt{Rd^3} + F_{adh} \tag{5}$$

where F_{tip} is the force on the tip, F_{adh} is the adhesion force, R is the tip radius, d is

the sample deformation, and E^* is the equivalent elastic modulus, $E^* = E/(1-\upsilon^2)$, where υ

is the Poisson ratio, and E is the elastic modulus [42, 49]. The bacterial suspension (10

μL) was dropped on the poly-L-lysine coated glass slice and then air-dried for 5 min

before conducting AFM scanning.

6.3.8 Statistical analyses

The disinfection experiments and the measurement of cell wall permeability were

conducted in triplicate. In addition, the biophysical properties of the bacterial cell were

calculated from ten random points on the bacterial surface using NanoScope 6.0 software. The results mentioned above are presented as mean ± SD.

6.4 Results and Disscusions

6.4.1 Characterizations

HOS has an average particle diameter of 1.8 ± 0.2 μm, which is much smaller than that of other shell-derived materials, such as scallop-shell-derived (30 μm) [33] and coral-derived (7.3 μm) [25] disinfectants. Such size differences likely arise from the preparation processes. As prepared, the HOS has a specific surface area of 7.9 $m^2\,g^{-1}$, which is higher than that of other conventional disinfectants, such as ZnO (4.5 $m^2\,g^{-1}$) [50], shown in Table 6-1. The higher surface area and smaller particle size of the HOS enhance disinfection efficiency by providing more active sites in contact with the bacteria.

Table 6-1. Comparison of disinfection performances and approaches for examining disinfection actions to other disinfectants.

Disinfectant	Dose (g/L)	Particle Size (µm)	Surface Area (m^2/g)	Initial Bacterial Concentration (CFU/mL)	Inactivation Performance	Inactivation Method	Approaches for Examining Disinfection Mechanism	References
Oyster shell derived disinfectant	0.2	1.8	7.9	1×10^5	5-log-inactivation in 1h for *E. coli*; 3-log-inactivation in 6 h for *S. aureus*	Suspension	Morphology, biophysical properties, K$^+$ leakage, cell wall permeability, and ROS detection (ESR)	This study
Scallop-shell derived disinfectant	5.0	30	NA	1×10^9	2-log-inactivation in 0.1 h for *E. coli*	Suspension	None	[33]
ZnO	0.4	0.31	4.5	9×10^6	0.8 log-inactivation in 10 min for *E. coli*; 0.6-log-inactivation in 10 min for *S. aureus*	Suspension	None	[50]
Scallop-shell derived disinfectant	1.0	NA	NA	7×10^7	2-log-inactivation in 1 h for *S. aureus*	Suspension	None	[52]
Oyster shell	1.0	NA	NA	1×10^6	0.75-log-inactivation in 1h for *E. coli*; 0.60-log-inactivation in 1h for *S. aureus*	Suspension	None	[11]
Nitrogen-doped TiO$_2$	1000	0.22	119.2	1.5×10^6	1-log-inactivation in 5 h for *E. coli*; 1-log-inactivation in 5 h for *S. aureus*	Suspension	None	[53]
Corals derived disinfectant	1.0	7.3	NA	1×10^8	38%-inactivation in 18 h for *E. coli*; 50%-inactivation in 18 h for *S. aureus*.	Plate diffusion	None	[25]

NA: Not available

FTIR analysis of the HOS (Fig. 6-1a) resulted in peaks at 3640 cm^{-1}, 1407 cm^{-1}, and 875 cm^{-1}, which are assigned to the O–H, C–O, and Ca–O bonds, respectively. The characteristic Ca–O bond peak in HOS is consistent with the FTIR spectra of calcined marine coral powders and calcium oxide [25, 51]. Oyster shells contain 95 to 99% calcium carbonate ($CaCO_3$), which is converted into calcium oxide (CaO) by calcination [32]. The presence of CaO is also supported by the XRD results. The XRD pattern of HOS (Fig. 6-1b) shows major diffraction peaks at 2θ angles of 32.2°, 37.4°, 53.9°, 64.2°, 67.4°, and 79.7°, corresponding to the (111), (200), (220), (311), (222), and (400) crystal faces of CaO (JCPDS Card No. 00-037-1497), respectively. Other minor diffraction peaks at 2θ angles of 18.0°, 28.7°, 34.1°, 47.1°, and 50.8° correspond to $Ca(OH)_2$ (JCPDS Card No. 00-044-1481). The appearance of $Ca(OH)_2$ is due to exposure of HOS to moisture in the air [25]. The SEM images (Fig. 6-1c) show that the ground oyster shell particles have a layered structure with a rough surface before heating; whereas, HOS has irregular, almost sintered, and shaped particles (Fig. 6-1d).
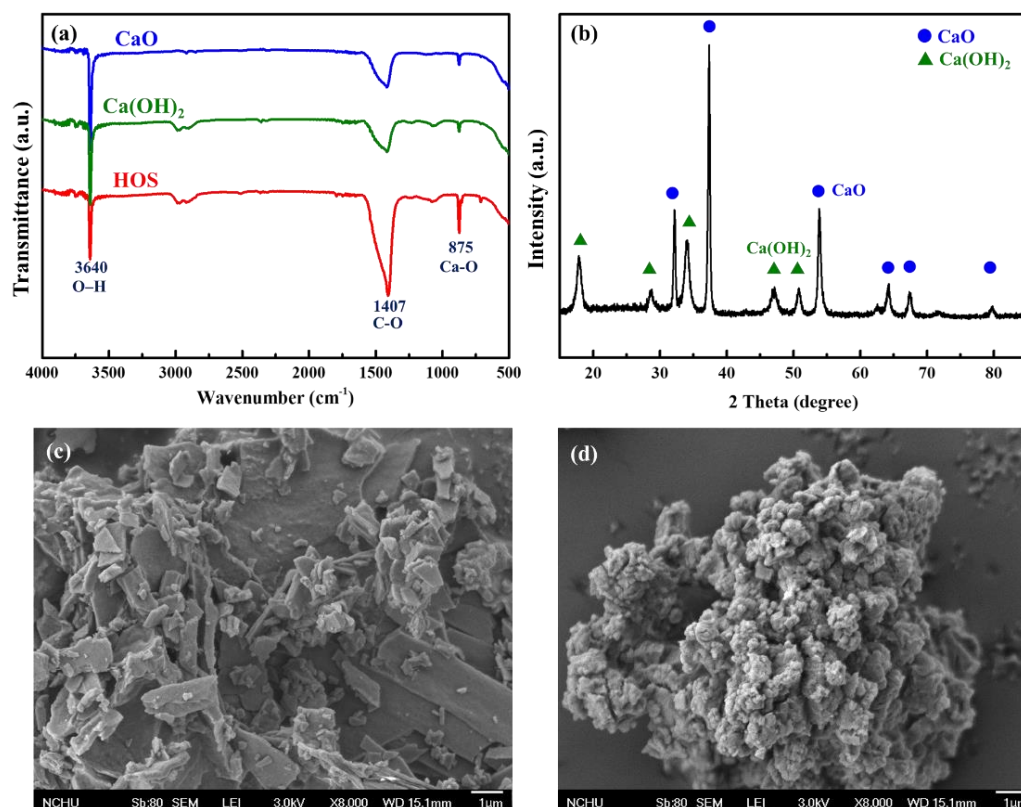
Figure 6-1. (a) FTIR spectra of CaO, Ca(OH)$_2$, and HOS and (b) XRD pattern of HOS. SEM images of (c) oyster shell and (d) HOS.

6.4.2 Disinfection performance and identifying reactive oxygen species

The efficacy of HOS disinfection was evaluated by comparing the inactivation rate of two different bacterial types: gram-positive bacteria (*S. aureus*) and gram-negative bacteria (*E. coli*). Figs. 6-2a and 6-2b show the inactivation kinetics of the two bacteria observed by culturing the bacterial suspensions in the presence of HOS at different reaction times. As shown in Fig. 6-2a, the survival of *E. coli* decreased dramatically from 1.07×10^5 CFU/mL to 1.40×10^3 CFU/mL after exposure to HOS for 30 min; complete inactivation was achieved within 60 min. In contrast to *E. coli*, a 99.9% inactivation rate was obtained for *S. aureus* only after 360 min. The disparate disinfection efficiency

between *E. coli* and *S. aureus* is related to differences in cell wall structures and the HOS

disinfection mechanism. It has been proposed that alkaline condition induced by shell-

derived disinfectants was one of the primary factors in the disinfection mechanism.

Therefore, we evaluate the effect of alkalinity on bacterial inactivation by using a NaOH

solution at the same pH (11.5 ± 0.1) as the HOS suspension. As shown in Fig. 6-2b.,

there was merely 0.85-log inactivation of *E. coli* and 0.59-log inactivation of *S. aureus*

after exposure to NaOH solution for 360 min. The disinfection performance of the NaOH

solution against bacteria is much lower than that of the HOS material, which indicates

that there is a critical factor in the HOS disinfection mechanism beyond alkalinity.

Although previous studies suggested that ROS might be the primary factor in the

inactivation mechanism of shell-derived disinfectants, no direct evidence was provided.

Herein, we use ESR to verify the presence of ROS species generated in the presence of

HOS.
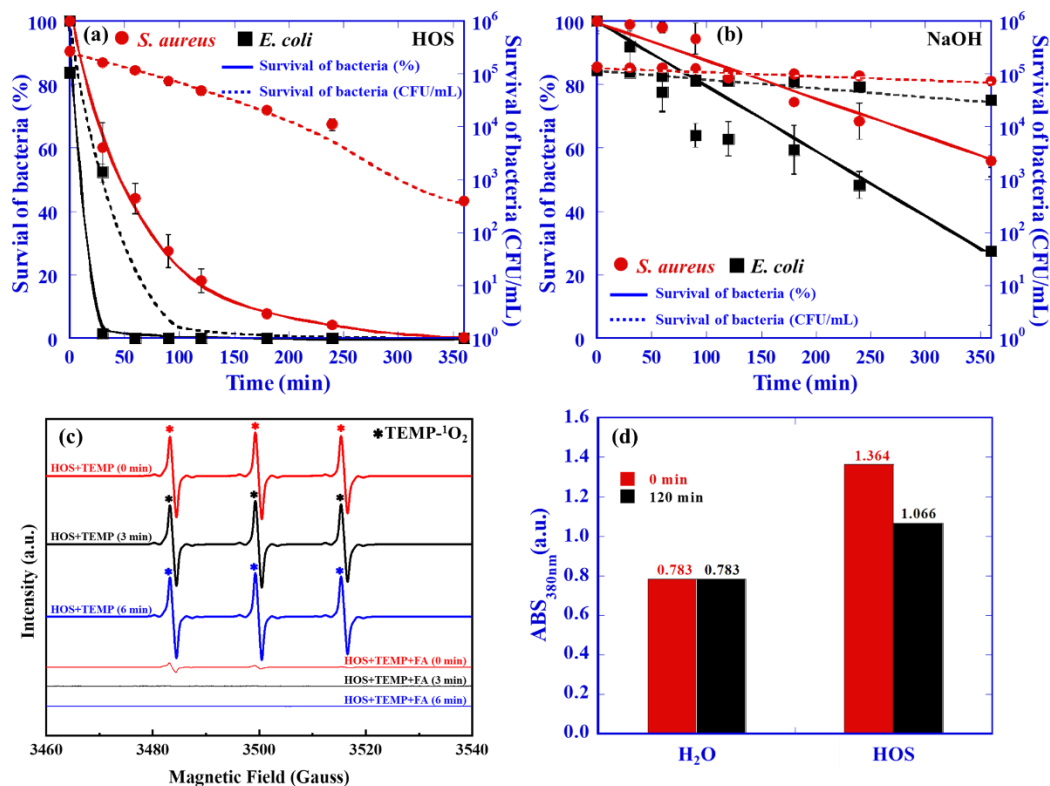
Figure 6-2. (a) HOS disinfection efficiency against *S. aureus* and *E. coli*. Experimental conditions: [HOS] 0.20 g/L, pH= 11.5 ± 0.1, [bacteria] 10^5 CFU/mL, T = 25 ± 1 °C. (b) NaOH disinfection efficiency against *S. aureus* and *E. coli*. Experimental conditions: pH 11.5 ± 0.1, [bacteria] 10^5 CFU/mL, T = 25 ± 1 °C. (c) ESR spectra of HOS obtained with TEMP as a spin-trapping agent and furfuryl alcohol (FA) as a quenching agent. Experimental conditions: [HOS] = 1 g/L, [FA] = 0.01 M, T = 25 ± 1 °C. (d) ABDA absorbance reduction at 380 nm of HOS at 0 and 120 min in the dark. Experimental conditions: [HOS] = 500 µg/mL, [ABDA] = 0.005 M, wavelength = 380 nm, T = 25 ± 1 °C.

Generation of $^1O_2$ in the HOS suspension was confirmed by ESR using TEMP as a spin-trapped agent. TEMP was selected to trap $^1O_2$ and form the stable TEMP-$^1O_2$ adduct, which can be identified by its typical ESR spectrum with three lines of equal

intensity (aN = 16 G). As shown in Fig. 6-2c, the characteristic 1:1:1 triplet signal of

TEMP$-^1$O$_2$ adducts was observed, indicating the presence of singlet oxygen in the HOS

suspension [54, 55]. To further confirm the formation of singlet oxygen, 0.01 M furfuryl

alcohol (FA) was added to the HOS sample to scavenge the singlet oxygen. The intensity

of the 1:1:1 peaks of TEMP$-^1$O$_2$ adducts was low in the presence of FA, confirming that

the singlet oxygen was produced in the system. Moreover, the yield of singlet oxygen

was quantified using the ABDA method. A 9,10-anthracenediyl-bis(methylene)dimalonic

acid (ABDA) solution has a strong absorption peak at 380 nm, which can be used to

detect singlet oxygen generated from HOS. ABDA reacts rapidly with singlet oxygen in

the solution, resulting in a decrease in absorbance at 380 nm. As shown in Fig. 6-2d, after

ABDA reacting with HOS for 120 min revealed a 21.8% reduction in the absorbance

compared with 0 min, which confirmed the generation of singlet oxygen. The methylene

blue (MB) at 50 ppm was used as a reference photosensitizer, which showed a 74.8%

reduction of absorbance (Fig. B5-3). According to Yu et al. (2015), the quantum yield of

singlet oxygen for MB molecules measured by the ABDA method is about 50% under

visible light exposure conditions [41]. Compared with the production of light-triggered

^{1}O$_2$ via 50 μg/mL MB, the 500 μg/mL HOS exhibited a 14.6% relative yield of singlet

oxygen in the dark.

This is the first direct evidence that a ROS species is generated by HOS. Sawai et

al. (2001) were the first to speculate that the formation of ROS from scallop shell waste

contributed to the inactivation of bacteria; however, they did not identify the ROS species

[12]. Since then, other researchers [25, 28, 30] have also suggested that shell waste

generated HO$_2$$^•$, $^•$O$_2$, and H$_2$O$_2$ contributed to its disinfection mechanism. To date, there is

no literature identifying singlet oxygen ($^1O_2$) in shell-derived disinfectants as a critical component in the disinfection process. Within the ROS, singlet oxygen ($^1O_2$) has been reported to be the most reactive ROS [22]. The production of $^1O_2$ using a photocatalyst remains the most popular and efficient method for photo-degradation applications. However, studies of nonphotochemical methods of generating $^1O_2$ from shell-derived disinfectants are still limited. Bokare & Choi (2015) reported the nonphotochemical generation of $^1O_2$ using potassium periodate (KIO_4) under alkaline conditions [54]. In addition, Persich et al. (2017) demonstrated the formation of $^1O_2$ without photolytic irradiation [56]. Moreover, Ikoma et al. (2001) investigated the ROS formation in CaO using ESR, and they proposed that ROSs were generated due to the trapped electrons (e^-) on the surface of CaO. The surface-trapped electrons resulted from the dislocations in the CaO crystal structure in the grinding process. Therefore, the contact between the organic compound and oxygen-rich surface would cause an electron transfer from O^{2-} to the organic substance [57]. The CaO crystal cleavage leads to the point vacancy defects and traps the electrons on its surface. In this study, the formation of $^1O_2$ in a HOS suspension in the dark was experimentally confirmed using ESR measurements in corroboration with a quenching experiment using furfuryl alcohol as a selective $^1O_2$ scavenger. The ABDA method also verified about 14.6% relative yield of singlet oxygen formed in HOS suspension in the dark. However, the formation pathway of singlet oxygen needs to be investigated in our future study.

Singlet oxygen ($^1O_2$) had been reported to react with proteins with a higher rate constant than other biological targets, such as DNA, RNA, and lipids [23, 58]. This feature of singlet oxygen can explain the higher HOS disinfection efficiency against *E.*

coli, which has a high proportion of protein in its cell wall than *S. aureus*. *S. aureus* is gram-positive bacteria with a thick cell wall consisting of peptidoglycan. The thick peptidoglycan layer (20 - 80 nm) could be a barrier to the oxidative disinfection material. In contrast, the structure of the gram-negative bacteria, *E. coli*, is more complex than that of gram-positive bacteria. The outer membrane of *E. coli* consists of lipopolysaccharides (LPS) with porin proteins inserted within them and covers a thin peptidoglycan layer. Although *E. coli* has a multilayer cellular membrane structure, its survival ratio is much lower than that of *S. aureus* with its simple cell wall structure. The differences are attributed to the thickness of the *E. coli* cell wall and the presence of the ROS-denatured proteins on the outer membrane, which may cause the lead to leakage of the intracellular components and cell structure collapse. Therefore, singlet oxygen generation and alkaline conditions induced by HOS result in membrane alteration and bacterial inactivation.

HOS exhibited higher disinfection efficiency against *S. aureus* and *E. coli* than other shell-derived disinfectants. A 5-log-inactivation *E. coli* was achieved within 1 h, and a 3-log-inactivation *S. aureus* was achieved within 6 h with 0.2 g/L HOS (Table 6-1). As shown in Table 6-1, Watanabe et al. (2014) reported a 2-log-inactivation *E. coli* using scallop-shell-derived disinfectant with a dose of 5 g/L [33]; Sawai et al. (2013) indicated a 2-log-inactivation within 1 h against *S. aureus* using scallop-shell-derived disinfectant with a dose of 1 g/L. Moreover, HOS has a higher specific surface area (7.94 m^2/g) and smaller particle size (1.8 ± 0.2 μm) than other shell-derived disinfectants, which provides more active sites on its surface, further enhancing HOS reaction efficiency and leading to improved disinfection performance.

6.4.3 Damage of bacterial cell wall and leakage of intracellular component

Damage to bacterial cell walls and the loss of bacterial intracellular components in the presence of HOS can be seen in the TEM images (Figs. 6-3 a-h) and plots of changes in K^+ ion concentration over time (Figs. 6-3 i-j), respectively. Before inactivation, the spherically-shaped *S. aureus* and rod-shaped *E. coli* were intact with clear cell walls and uniformly rendered cell interiors. After 120 min, the *S. aureus* cell was still intact (Fig. 6-3b), but the slight aggregation of intracellular components is apparent. By 360 min (Fig. 6-3d), the cell wall was decomposed, damaging the permeability and leading to leakage of the intracellular components. As for *E. coli*, the intracellular components aggregated, and the cell wall ruptured at 120 min (Fig. 6-3f). The blurred boundary and holes in the cell wall (Fig. 6-3g) indicate a damaged cell envelope at 240 min. Additionally, the intracellular components leaked out of the cells due to the change in permeability. Finally, the *E. coli* cell structure collapsed and completely flattened at 360 min (Fig. 6-3h), leaving only cell debris inside. The damaged bacterial ultrastructure observed in the TEM images is in agreement with the leakage of K^+ ions (Figs. 6-3i and 6-3j), which confirm that HOS induced an alteration in bacterial ultrastructure.
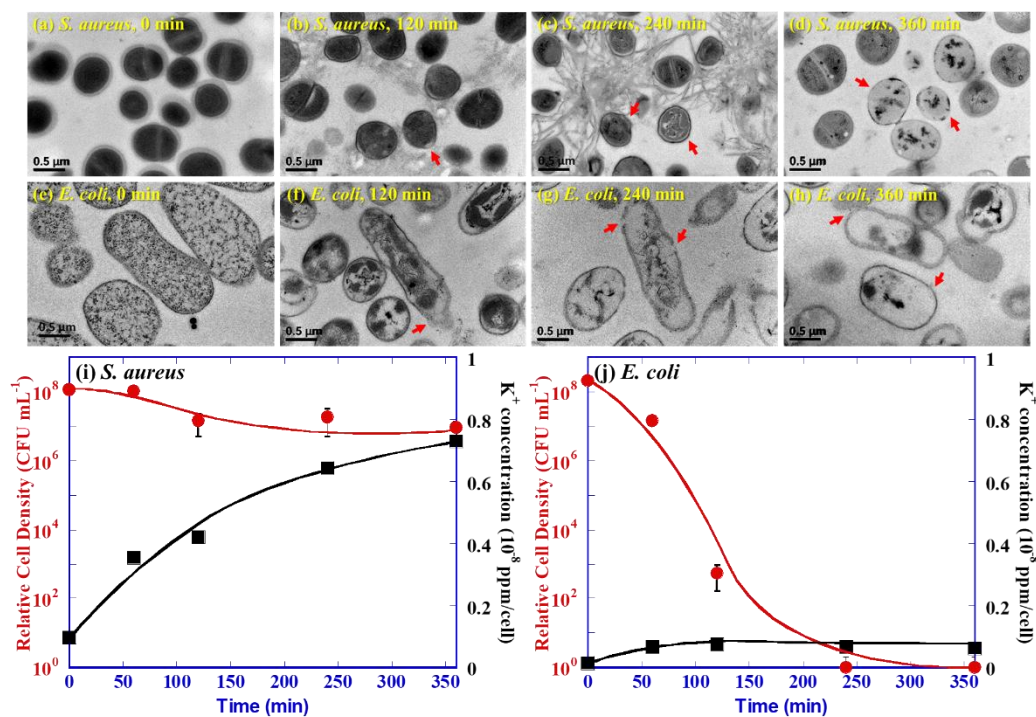
Figure 6-3. TEM images of *S. aureus* (a-d) with HOS treatment for (a) 0 min, (b) 120 min, (c) 240 min, and (d) 360 min; *E. coli* (e-h) with HOS treatment for (e) 0 min, (f) 120 min, (g) 240 min, and (h) 360 min. Comparison of the leakage of K^+ (10^{-8} ppm/cell) from (i) *S. aureus* and (j) *E. coli* cells during the treatment of HOS. Experimental conditions: [HOS] = 0.20 g/L, [bacteria] = 10^8 CFU/mL, T = 25 ± 1 °C.

To further confirm the destruction process of the bacteria, leakage of K^+ ions was investigated. K^+ ions are an essential intracellular component. Therefore, the leakage of K^+ ions was investigated to assess changes in cell permeability throughout the disinfection process. As shown in Figs. 6-3i and 6-3j, K^+ ion leakage in *S. aureus* increased from 0.10 to 0.35, 0.42, 0.64, and 0.73 10^{-8} ppm/cell with increasing reaction times of 60, 120, 240, and 360 min, respectively. As for *E. coli*, K^+ ion concentrations increased from 0.03 to 0.13 10^{-8} ppm/cell after reacting with HOS material for 120 min and stabilizing. Moreover, the different K^+ concentrations in *S. aureus* and *E. coli* could

be discerned. Grundling (2013) indicated that *S. aureus* maintains a higher K^+ concentration than *E. coli* since *S. aureus* contains two potassium-uptake systems, Ktr and Kdp [59]. Similar results were also reported by Bouhdid et al. (2009), who found a lower K^+ concentration in *Pseudomonas aeruginosa* (gram-negative bacteria) than *S. aureus* (gram-positive bacteria), while *Pseudomonas aeruginosa* was inactivated more quickly than *S. aureus* by origanum compactum essential oil [60].

The oxidative stress and alkaline conditions produced by shell-derived disinfectants would also alter bacterial metabolism, damage cell permeability, and impact cell structure. The unstable cell permeability would in turn lead to leakage of extracellular components, such as K^+ ions. K^+ ions participate in regulating polysome content and protein synthesis of bacterial cells [61-63]. Imbalances of K^+ ion in bacterial cells would then affect cell viability, resulting in cell dysfunction or death [61, 64, 65]. Therefore, the results in TEM images and K^+ ion leakage suggested that the cell wall and cell permeability have been damaged, thus leading to the inactivation of *S. aureus* and *E. coli*.

6.4.4 Cell wall permeability methods and comparison of inactivation

Permeability of the cell membrane is another indispensable indicator diagnosing the damage level over bacteria. In this work, the cell membrane permeability measurements were conducted by using an inverted fluorescence microscope (IFM). Propidium iodide (PI) and diamidino-2-phenylindole (DAPI) were used to distinguish intact bacteria from those with permeated cell membranes [66]. DAPI can pass through an intact cell membrane and bind to bacterial DNA, giving off a blue fluorescence. PI cannot pass through an intact cell membrane and can only bind with the DNA if the cell

membrane is damaged [67]. Experimentally, the blue fluorescence of DAPI will be detected in all the cells; whereas, the red fluorescence of PI will only be displayed in the permeated cells. Figs. 6-4a and 6-4e show that the intact cells of *S. aureus* and *E. coli* appeared with the blue fluorescence and no red fluorescence at 0 min. As seen in Figs. 6-4b and 6-4f, the red fluorescence rises over time as the cell membranes of *S. aureus* and *E. coli* are gradually altered with reaction time. The amount of red fluorescence stabilized within 240-360 min. Interestingly, the DAPI/PI double-stain results reveal that the cell membrane of *S. aureus* are permeable at 120 min, while the plate-counting results show the 92.5 % of the bacteria are still viable at that time. A general consensus is that the conventional agar plate method for counting the culturable bacteria includes different levels of damage to cell membranes [66, 68, 69]. Nevertheless, the degree of permeability damage to a cell membrane ought to be quantified to understand the physiological state of the bacterium. In this study, viable bacteria were counted at different reaction times by the plate counting method. Then, FM imaging was used to distinguish bacteria with intact cell membranes from those with permeated cell walls. The number of blue fluorescent bacteria indicated total bacteria because DAPI can be transmitted through both intact and damaged cell membranes. The number of red fluorescent bacteria indicated those with damaged or permeable cell membranes. The inactivation rates of the bacteria estimated by the two different methods, the plate counting method and the DAPI/PI double-stained method, were compared.
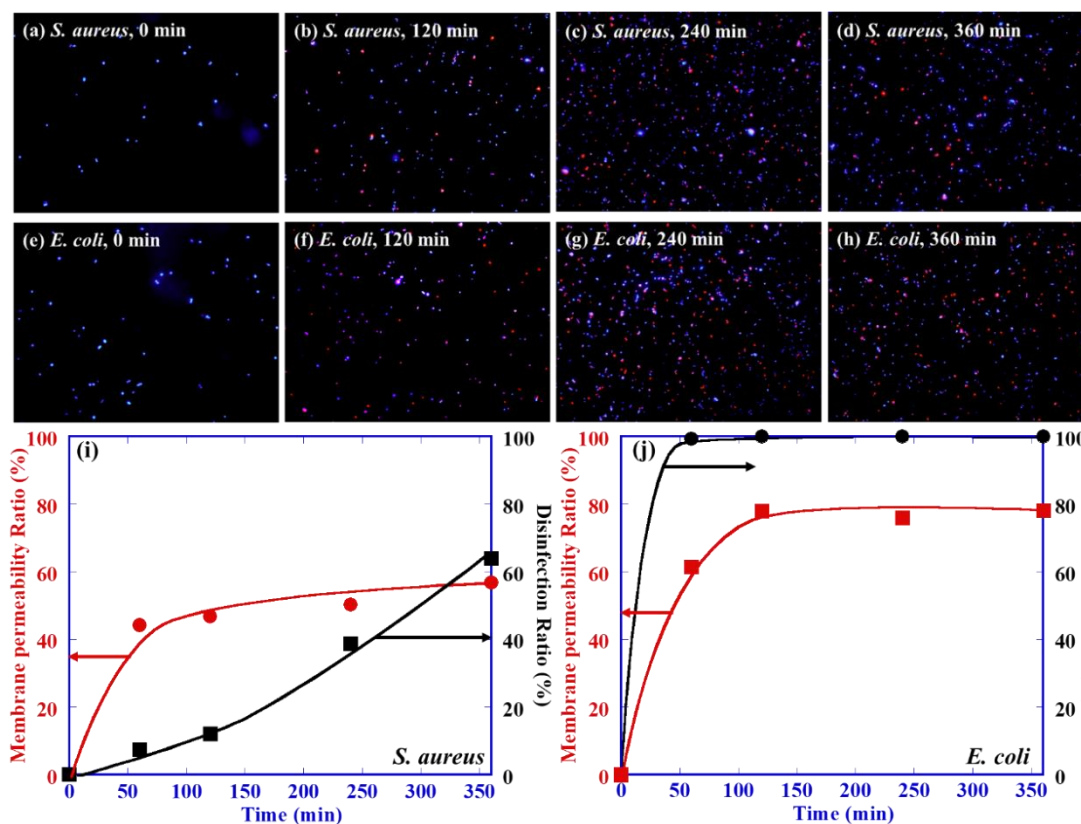
Figure 6-4. FM images of *S. aureus* (a-d) with HOS treatment for (a) 0 min, (b) 120 min, (c) 240 min, and (d) 360 min; *E. coli* (e-h) with HOS treatment for (e) 0 min, (f) 120 min, (g) 240 min, and (h) 360 min. Inactivation ratio of (i) *S. aureus* and (j) *E. coli* measured by two methods with HOS treatment. Experimental conditions: [HOS] = 0.20 g/L, [bacteria] = 10^8 CFU/mL, T = 25 ± 1 °C.

As shown in Figs. 6-4i and 6-4j, the cell-wall-permeability measurement and the percentage of viable bacteria determined with the agar plates showed that the number of red fluorescent bacteria did not correspond to the number of inactivated bacteria. This phenomenon occurred predominantly when determining the cell-membrane-permeability ratio of *S. aureus* (Fig. 6-4i) early in the course of the experiment. The cell-membrane-permeability measurements showed that the permeability of *S. aureus* was altered within

60 min of the reaction and by 120 min, its permeability ratio (red/blue fluorescence) had increased to 44.2%, while its inactivation rate (counting-plate method) remained at 7.5%. This indicates that changes in the permeability of *S. aureus* that appear in the early stages of the reaction, likely due to attack by singlet oxygen and the alkaline conditions, do not lead to the immediate death of *S. aureus*. On the other hand, the *E. coli* permeability ratio had risen to 62.5% by 120 min while its inactivation rate reached 99.3% within the same timeframe. These differences between the permeability ratios and inactivation rates of *S. aureus* and *E. coli* suggest that different inactivation phenomena occur between gram-positive and gram-negative bacteria. Exposure to the HOS quickly induced damage in *E. coli* cell permeability and structure, resulting in the leakage of intracellular components, including DNA. The DNA could then be decomposed by ROS and, therefore, was unable to bind with the PI dye, leading to the slow increase in the inactivation ratio quantified by the cell-membrane-permeability measurement. Thus the disparity between the results obtained using the two methods used to assess inactivation (inactivation ratio vs. permeability ratio) can provide insight into not only the mode of inactivation but also the definition of inactivation.

6.4.5 Biophysical properties of the bacterial cell

AFM is an outstanding technique for measuring live cells with various biophysical properties and imaging real-time disinfection processes. To understand the disinfection mechanism of HOS, the three-dimensional morphology and the biophysical properties of bacteria were investigated by using AFM. The bacterial cells were observed in hydrated conditions without any sample pretreatment, such as staining or dehydration. AFM three-dimensional images of both *S. aureus* (Fig. 6-5a) and *E. coli* (Fig. 6-5e)

showed the spherically-shaped and rod-shaped bacteria at 0 min, respectively. After

contact with HOS for 240 min, *S. aureus* remained relatively intact until a minor collapse

appeared in the cell wall at 360 min. In contrast to *S. aureus*, the rumpled bacterial

surface of *E. coli* appeared intact after reacting for 120 min, before structure collapse

occurred at 240 min. The formation of vesicle-like structures on the bacterial surface was

evident at 360 min. Thus, the three-dimensional AFM images offer valuable

morphological information about *S. aureus* and *E. coli* during the disinfection process

that surpasses the two-dimensional limitations of conventional methods, such as SEM.

The AFM images in Fig. 6-5h depict the striking effect of decomposition on the *E. coli*

cell wall structure. In contrast, there is merely minor damage to the structure of *S. aureus*.
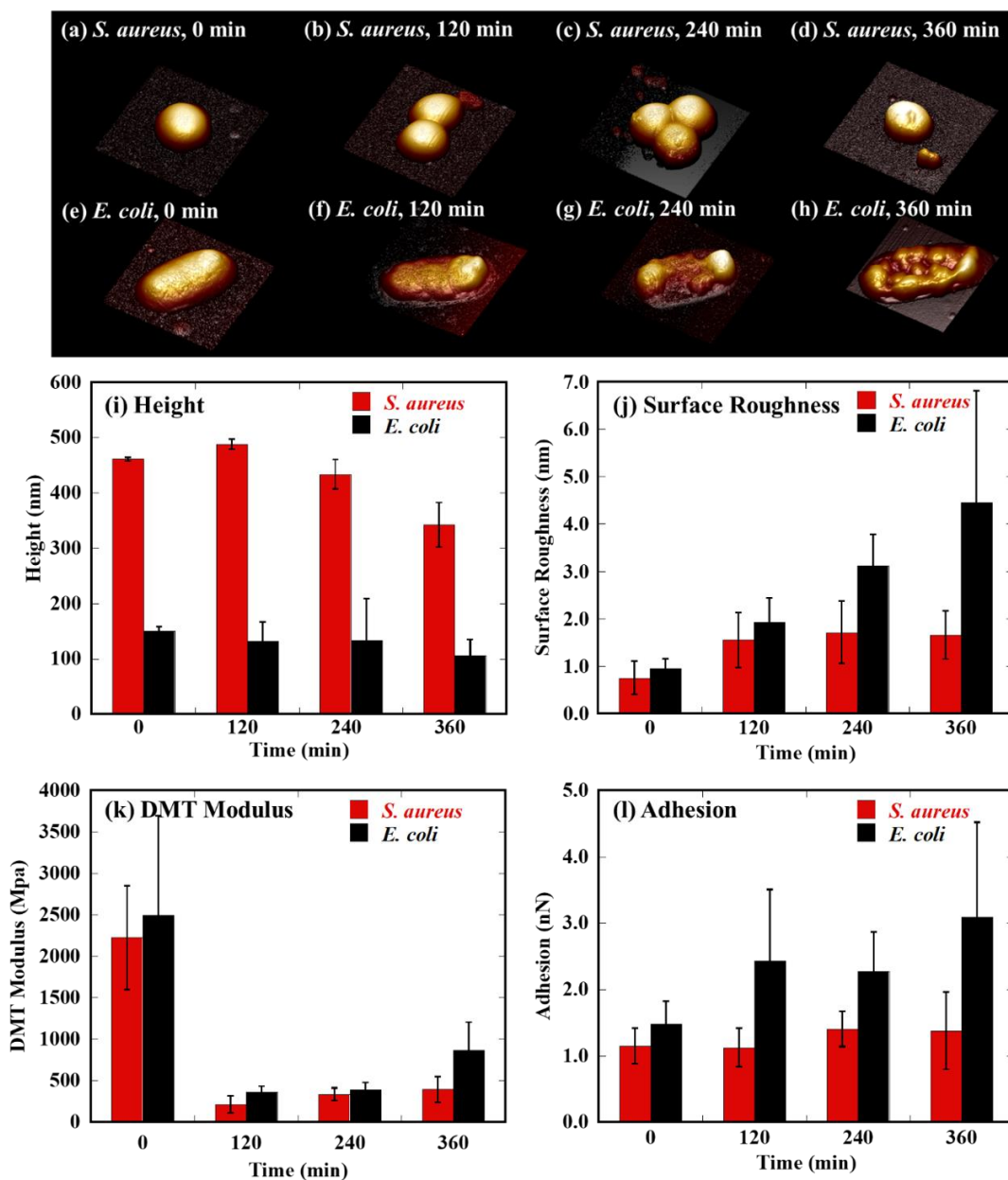
Figure 6-5. Comparison of the three-dimensional morphology of *S. aureus* (a-d) with HOS treatment for (a) 0 min, (b) 120 min, (c) 240 min, and (d) 360 min; *E. coli* (e-h) with HOS treatment for (e) 0 min, (f) 120 min, (g) 240 min, and (h) 360 min. Biophysical properties of *S. aureus* and *E. coli* with HOS treatment, including (i) height, (j) surface roughness, (k) DMT modulus, and (l) adhesion. Experimental conditions: [HOS] 0.20 g/L, [bacteria] 10^8 CFU/mL, T = 25 ± 1 °C.

To further analyze the cell wall biophysical properties, bacterial height, surface roughness, DMT modulus, and adhesion were described by the root-mean-square value obtained from AFM force measurements. As shown in Figs. 6-5 (i-l), when *S. aureus* reacted with HOS material for 120, 240, and 360 min, the bacterial cell height gradually dropped from 568.9 ± 15.6 nm to 342.2 ± 40.3 nm. The roughness of the *S. aureus* cell surface increased slightly from 1.34 ± 0.42 nm to 1.66 ± 0.51 nm, DMT modulus dropped from $2{,}223.0 \pm 623.7$ MPa to 394.1 ± 154.5 MPa, and adhesion increased from 1.15 ± 0.40 nN to 1.38 ± 0.59 nN. After reacting with HOS material for 120, 240, and 360 min, the *E. coli* bacterial height decreased from 150.4 ± 8.3 nm to 105.5 ± 29.1 nm. The surface roughness increased from 0.95 ± 0.21 nm to 4.46 ± 0.34 nm, DMT modulus dropped from $2{,}492.2 \pm 1202.9$ MPa to 866.9 ± 337.8 MPa, while the adhesion increased from 1.48 ± 0.34 nN to 3.10 ± 1.42 nN. According to the results, the alteration to the surface roughness, DMT modulus, and adhesion was time-dependent. Changes in the *S. aureus* and *E. coli* cell heights occurred due to the loss of intracellular components. The height of *S. aureus* dropped by 39.8%, whereas *E. coli* heights dropped by 29.8% as compared to the cell heights at time 0. The extensive destruction of the cell wall was also reflected in an increase in the surface roughness of the cells. The measured roughness of *S. aureus* and *E. coli* increased as much as 23.6% and 370%, respectively.

Alternation of the cell envelope composition of *S. aureus* and *E. coli* also resulted in a decreased elastic modulus. The DMT model is one of the elastic modulus models that reflected the contact and deformation between the AFM probe and the sample. Mathelie-Guinlet et al. (2020) revealed a decreased modulus value of treated *E. coli* cell, representing the softening *E. coli* cell envelope due to the lack of lipoprotein Lpp in the

outer membrane [70]. Moreover, Jin et al. (2010) reported that the photo-inactivated *S. aureus* and *E. coli* treated by hematoporphyrin monomethyl ether possessed lower modulus values indicating the cell envelope composition had changed [71]. Similarly, the decreased DMT modulus of *S. aureu*s and *E. coli* after being treated with HOS indicated the reduced stiffness of the cell envelope. Furthermore, the HOS-treated cell exhibited increasing adhesion force with the increasing reaction time. Adhesion of the bacterial cell surface, measured by AFM, results from the interaction between the probe tip and cell surface. It indicates that the probe tip interacted with the HOS-treated cell wall components more strongly than untreated cells. The permeated cell membrane and leakage of the intracellular components revealed that the chemical composition of the cell surfaces changed during the disinfection process. Therefore, the AFM probe-tip might have penetrated the decomposed cell wall and interacted with the peptidoglycan or lipopolysaccharide layer of the gram-positive and gram-negative bacteria, leading to the observed increase in the adhesion force [46].

6.4.6 Discrepancy disinfection efficiency between gram-positive and gram-negative bacteria

In view of the discrepancies between disinfection efficiencies reported in the literature in Table 1, it is necessary to adopt multiple approaches to investigate disinfection effects on bacteria, such as determining the changes in morphology, ultrastructure, cell permeability, and biophysical properties of the bacterium. The ultrastructure (TEM images) and three-dimensional (AFM images) micrographs show that *S. aureus* retains its spherical form throughout the disinfection process; whereas, rupture, alteration, and loss of cell wall structure are observed in *E. coli*. However,

leakage of essential potassium ions was detected in *S. aureus* at a higher rate than in *E. coli*. The FM images confirm the changes in the cell membranes, with a higher ratio of permeated cell membranes with *S. aureus* than inactivated cells measured by the plate-counting method. The cell ultrastructure obtained by TEM also indicated the loss of intracellular components in *S. aureus* after reacting with HOS for 360 min. By comparison, the cell envelope of *E. coli* was clearly damaged by 120 min. The *E. coli* cell membrane was decomposed with compromised permeability leading to the loss of intracellular components, such as potassium ions. The mechanical properties of the bacteria mainly consist of the cell membrane and the turgor pressure of the cell. The permeated cell membrane and leakage of the intracellular components affected the turgor pressure of the bacterium and cell growth [72].

The cell-membrane-permeability measurements show that there are significant differences between gram-positive and gram-negative bacteria due to their cell structures (Fig. 6-6). The cell wall of gram-positive bacteria is thick (20 - 80 nm) and composed of multilayered peptidoglycan (90%). The glycans are cross-linked to one another, forming a three-dimensional lattice. On the other hand, the cell wall of gram-negative bacteria is thinner (10-15 nm) but more complicated than that of gram-positive bacteria. The outer membrane (OM) is composed primarily of lipopolysaccharide (LPS) and a few layers of peptidoglycan (around 2 nm thick). The OM also contains many lipoproteins, including porins proteins that form pores in the outer membrane. Even though LPSs form a permeability barrier, the outer membrane is more permeable than the plasma membrane due to the presence of tube-shaped porin proteins in the outer membrane [73]. The disrupted outer membrane porins (OMPs) enhance cell lysis due to increased ROS levels

[74]. Furthermore, $^1O_2$ has been reported to damage the dominant and side chains of amino acids, peptides, and proteins [23, 58]. Therefore, the generation of singlet oxygen in HOS suspensions results in higher disinfection efficiency against *E. coli* than *S. aureus*. Or, in other words, *S. aureus* displays greater resistance to HOS due to its thick peptidoglycan layer and lower protein content in its cell wall [2].
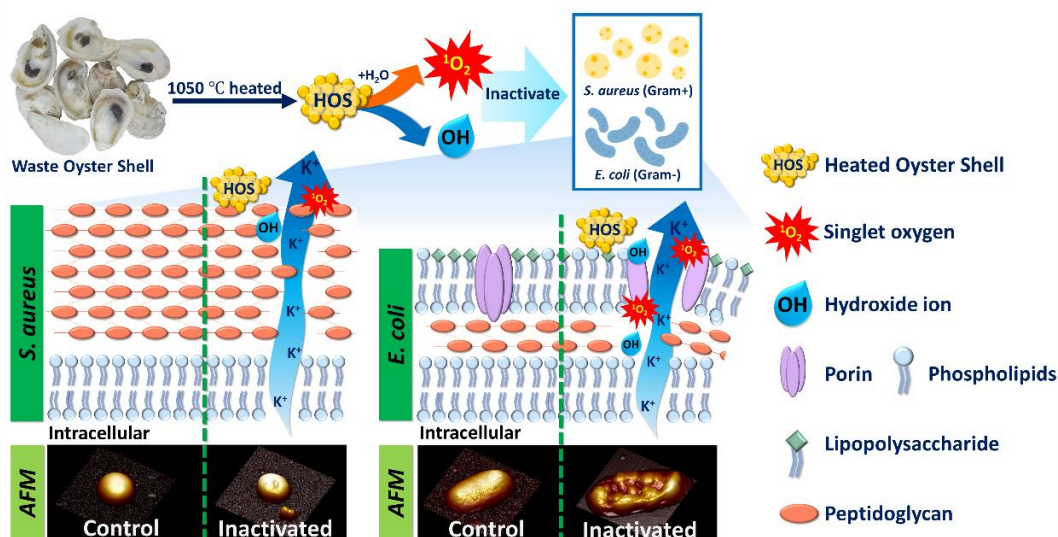
Figure 6-6. Schematic illustration of the disinfection mechanism of *S. aureus (Gram-positive)* and *E. coli (Gram-negative)* treated with HOS.

6.5 Conclusions

The HOS displayed high disinfection efficiency toward *E. coli* and *S. aureus*, achieving 99% inactivation in 30 min and 360 min, respectively. The different cell structures led to disparate disinfection efficiency rates between gram-positive and gram-negative bacteria. This study provides a template for the early assessment of altered bacterial cell structure and cell membrane permeability using FM, TEM, and quantification of K^+ that leaks from bacterial cells. The biophysical properties have

shown the damage to bacterial height, surface roughness, DMT modulus, and adhesion following HOS treatment. The three-dimensional AFM images also revealed the greater vulnerability of *E. coli* cellular structure relative to *S. aureus*. The findings provide evidence that cell permeability is crucial in the HOS disinfection process and that cell wall structure results in different levels of cell permeability damage between *S. aureus* and *E. coli*. Furthermore, analysis of the ROS induced by HOS treatment revealed that singlet oxygen plays an essential role in the disinfection mechanism. Overall, the HOS disinfectant, derived from natural resources, has the high potential to be applied as a universal disinfectant, as well as alleviating an aquaculture waste pollution problem.

6.6 References

[1] O. Jonas, Global Health Threats of the 21st Century, 2014.

[2] O.K. Dalrymple, E. Stefanakos, M.A. Trotz, D.Y. Goswami, A review of the mechanisms and modeling of photocatalytic disinfection, Appl. Catal. B 98 (2010) 27-38.

[3] M. Moazzami, L.L. Fernstrom, I. Hansson, Reducing Campylobacter jejuni, Enterobacteriaceae and total aerobic bacteria on transport crates for chickens by irradiation with 265-nm ultraviolet light (UV-C LED), Food Control 119 (2021) 107424.

[4] F. Abu-Shkara, I. Neeman, R. Sheinman, R. Armon, The effect of fatty acid alteration in coliform bacteria on disinfection resistance and/or adaptation, Water Sci. Technol. 38 (1998) 133-139.

[5] H. Childress, B. Sullivan, J. Kaur, R. Karthikeyan, Effects of ultraviolet light disinfection on tetracycline-resistant bacteria in wastewater effluents, J. Water Health 12 (2014) 404-409.

[6] I.L. Hsu, F.H. Yeh, Y.-C. Chin, C.I. Cheung, Z.C. Chia, L.-X. Yang, Y.-J. Chen, T.-Y. Cheng, S.-P. Wu, P.-J. Tsai, N.-Y. Lee, M.-Y. Liao, C.-C. Huang, Multiplex antibacterial processes and risk in resistant phenotype by high oxidation-state nanoparticles: New killing process and mechanism investigations, Chem. Eng. J. 409 (2021) 128266.

[7] FAO, FAO Online Query Panels, 2019.

[8] R. Botta, F. Asche, J.S. Borsum, E.V. Camp, A review of global oyster aquaculture production and consumption, Mar. Policy 117 (2020) 103952 .

[9] N. Shimamura, F. Irie, T. Yamakawa, M. Kikuchi, J. Sawai, Heated scallop-shell powder treatment for deactivation and removal of *Listeria sp* biofilm formed at a low temperature, Biocontrol Sci. 20 (2015) 153-157.

[10] R. Xing, Y. Qin, X. Guan, S. Liu, H. Yu, P. Li, Comparison of antifungal activities of scallop shell, oyster shell and their pyrolyzed products, Egypt. J. Aquat. Res. 39 (2013) 83-90.

[11] K. Oikawa, T. Asada, K. Yamamoto, H. Wakabayashi, M. Sasaki, M. Sato, J. Matsuda, Antibacterial activity of calcined shell calcium prepared from wild surf clam, J. Health Sci. 46 (2000) 98-103.

[12] J. Sawai, H. Shiga, H. Kojima, Kinetic analysis of the bactericidal action of heated scallop-shell powder, Int. J. Food Microbiol. 71 (2001) 211-218.

[13] L. Wang, J. Jiang, J. Ma, S. Pang, T. Zhang, A review on advanced oxidation processes homogeneously initiated by copper(II), Chem. Eng. J. 427 (2022) 131721.

[14] Z. Xiong, Y. Jiang, Z. Wu, G. Yao, B. Lai, Synthesis strategies and emerging mechanisms of metal-organic frameworks for sulfate radical-based advanced oxidation process: A review, Chem. Eng. J. 421 (2021) 127863.

[15] D. Venieri, A. Karapa, M. Panagiotopoulou, I. Gounaki, Application of activated persulfate for the inactivation of fecal bacterial indicators in water, J. Environ. Manage. 261 (2020) 110223.

[16] V.D. Dang, J. Adorna, T. Annadurai, T.A.N. Bui, H.L. Tran, L.-Y. Lin, R.-A. Doong, Indirect Z-scheme nitrogen-doped carbon dot decorated Bi_2MoO_6/g-C_3N_4 photocatalyst for enhanced visible-light-driven degradation of ciprofloxacin, Chem. Eng. J. 422 (2021) 130103.

[17] K. Roy, V.S. Moholkar, Sulfadiazine degradation using hybrid AOP of heterogeneous Fenton/persulfate system coupled with hydrodynamic cavitation, Chem. Eng. J. 386 (2020) 121294.

[18] A.Q. Wang, H. Wang, H. Deng, S. Wang, W. Shi, Z.X. Yi, R.L. Qiu, K. Yan, Controllable synthesis of mesoporous manganese oxide microsphere efficient for photo-Fenton-like removal of fluoroquinolone antibiotics, Appl. Catal. B 248 (2019) 298-308.

[19] Y. Guo, Y.X. Zhang, G. Yu, Y.J. Wang, Revisiting the role of reactive oxygen species for pollutant abatement during catalytic ozonation: The probe approach versus the scavenger approach, Appl. Catal. B 280 (2021) 119418.

[20] P. Gao, X. Tian, Y. Nie, C. Yang, Z. Zhou, Y. Wang, Promoted peroxymonosulfate activation into singlet oxygen over perovskite for ofloxacin degradation by controlling the oxygen defect concentration, Chem. Eng. J. 359 (2019) 828-839.

[21] S. Giannakis, K.-Y.A. Lin, F. Ghanbari, A review of the recent advances on the treatment of industrial wastewaters by Sulfate Radical-based Advanced Oxidation Processes (SR-AOPs), Chem. Eng. J. 406 (2021) 127083.

[22] J. Al-Nu'airat, B.Z. Dlugogorski, X.P. Gao, N. Zeinali, J. Skut, P.R. Westmoreland, I. Oluwoye, M. Altarawneh, Reaction of phenol with singlet oxygen, Phys. Chem. Chem. Phys. 21 (2019) 171-183.

[23] M.J. Davies, Singlet oxygen-mediated damage to proteins and its consequences, Biochem. Biophys. Res. Commun. 305 (2003) 761-770.

[24] J. Kim, H. Lee, J.-Y. Lee, K.-H. Park, W. Kim, J.H. Lee, H.-J. Kang, S.W. Hong, H.-J. Park, S. Lee, J.-H. Lee, H.-D. Park, J.Y. Kim, Y.W. Jeong, J. Lee, Photosensitized production of singlet oxygen via C60 fullerene covalently attached to functionalized silica-coated stainless-steel mesh: Remote bacterial and viral inactivation, Appl. Catal. B 270 (2020) 118862.

[25] K. Sadeghi, S. Thanakkasaranee, I.J. Lim, J. Seo, Calcined marine coral powders as a novel ecofriendly antimicrobial agent, Mater. Sci. Eng. C-Mater. Biol. Appl. 107 (2020) 6.

[26] J. Sawai, E. Kawada, F. Kanou, H. Igarashi, A. Hashimoto, T. Kokugan, M. Shimizu, Detection of active oxygen generated from ceramic powders having antibacterial activity, J. Chem. Eng. Jpn. 29 (1996) 627-633.

[27] Y. Sato, M. Ishihara, S. Nakamura, K. Fukuda, M. Kuwabara, T. Takayama, S. Hiruma, K. Murakami, M. Fujita, H. Yokoe, Comparison of various disinfectants on

bactericidal activity under organic matter contaminated environments, Biocontrol Sci. 24 (2019) 103-108.

[28] Y.C. Chen, C.L. Lin, C.T. Li, D.F. Hwang, Structural transformation of oyster, hard clam, and sea urchin shells after calcination and their antibacterial activity against foodborne microorganisms, Fish. Sci. 81 (2015) 787-794.

[29] I.H. Alsohaimi, A.M. Nassar, T.A.S. Elnasr, B. Cheba, A novel composite silver nanoparticles loaded calcium oxide stemming from egg shell recycling: A potent photocatalytic and antibacterial activities, J. Clean. Prod. 248 (2020) 119274.

[30] K. Park, K. Sadeghi, S. Thanakkasaranee, Y.I. Park, J. Park, K.H. Nam, H. Han, J. Seo, Effects of calcination temperature on morphological and crystallographic properties of oyster shell as biocidal agent, Int. J. Appl. Ceram. Technol. 18 (2021) 302-311.

[31] J. Sawai, H. Miyoshi, H. Kojima, Sporicidal kinetics of *Bacillus subtilis* spores by heated scallop shell powder, J. Food Prot. 66 (2003) 1482-1485.

[32] J. Sawai, Antimicrobial characteristics of heated scallop shell powder and its application, Biocontrol Sci. 16 (2011) 95-102.

[33] T. Watanabe, R. Fujimoto, J. Sawai, M. Kikuchi, S. Yahata, S. Satoh, Antibacterial characteristics of heated scallop-shell nano-particles, Biocontrol Sci. 19 (2014) 93-97.

[34] Y. Nomoto, S. Sawada, S. Abe, J. Wakazawa, M. Kikuchi, J. Sawai, Sorbitol minimizes calcium carbonate scale generation while maintaining the disinfection effect of heated scallop-shell powder for fresh produce, Biocontrol Sci. 23 (2018) 157-165.

[35] M.A. Argudin, M.C. Mendoza, M.R. Rodicio, Food poisoning and *Staphylococcus aureus* enterotoxins, toxins 2 (2010) 1751-U1342.

[36] H.F. Chambers, F.R. Deleo, Waves of resistance: *Staphylococcus aureus* in the antibiotic era, Nat. Rev. Microbiol. 7 (2009) 629-641.

[37] J.M. Spinale, R.L. Ruebner, L. Copelovitch, B.S. Kaplan, Long-term outcomes of Shiga toxin hemolytic uremic syndrome, Pediatr. Nephrol. 28 (2013) 2097-2105.

[38] T. Abuladze, M. Li, M.Y. Menetrez, T. Dean, A. Senecal, A. Sulakvelidze, Bacteriophages reduce experimental contamination of hard surfaces, tomato, spinach, broccoli, and ground beef by *Escherichia coli* O157 : H7, Appl. Environ. Microbiol 74 (2008) 6230-6238.

[39] P. Betancourt, A. Merlos, J.M. Sierra, O. Camps-Font, J. Arnabat-Dominguez, M. Vinas, Effectiveness of low concentration of sodium hypochlorite activated by Er,Cr:YSGG laser against *Enterococcus faecalis* biofilm, Lasers Med. Sci. 34 (2019) 247-254.

[40] S.N. Pleskova, I.S. Golubeva, Y.K. Verevkin, Bactericidal activity of titanium dioxide ultraviolet-induced films, Mater. Sci. Eng. C-Mater. Biol. Appl. 59 (2016) 807-817.

[41] J.S. Yu, C.H. Hsu, C.C. Huang, P.Y. Chang, Development of therapeutic au-methylene blue nanoparticles for targeted photodynamic therapy of cervical cancer cells, ACS Appl. Mater. Interfaces 7 (2015) 432-441.

[42] J.-H. Tzeng, C.-H. Weng, C.-C. Wang, M.-S. Ho, L.-T. Yen, J.-Y. Chen, G. Gaybullaev, C. Poonpakdee, Y.-T. Lin, A solution of identifying biophysical properties and 3D cellular structure of visible-light-driven photocatalytic inactivated *Staphylococcus aureus*, Chem. Eng. J. (2020) 127880.

[43] X.K. Zeng, D.T. McCarthy, A. Deletic, X.W. Zhang, Silver/reduced graphene oxide hydrogel as novel bactericidal filter for point-of-use water disinfection, Adv. Funct. Mater. 25 (2015) 4344-4351.

[44] D. Liu, L. Zhang, W. Xue, Y.P. Wang, J.S. Ju, B.H. Zhao, Knockout of the alanine racemase gene in *Aeromonas hydrophila* HBNUAh01 results in cell wall damage and enhanced membrane permeability, FEMS Microbiol. Lett. 362 (2015) 1-8.

[45] M. Girasole, G. Pompeo, A. Cricenti, A. Congiu-Castellano, F. Andreola, A. Serafino, B.H. Frazer, G. Boumis, G. Amiconi, Roughness of the plasma membrane as an independent morphological parameter to study RBCs: A quantitative atomic force microscopy investigation, Biochim Biophys Acta Biomembr 1768 (2007) 1268-1276.

[46] B. Ramalingam, T. Parandhaman, S.K. Das, Antibacterial effects of biosynthesized silver nanoparticles on surface ultrastructure and nanomechanical properties of gram-negative bacteria viz. *Escherichia coli* and *Pseudomonas aeruginosa*, ACS Appl. Mater. Interfaces 8 (2016) 4963-4976.

[47] H.N. Su, Z.H. Chen, X.Y. Song, X.L. Chen, M. Shi, B.C. Zhou, X. Zhao, Y.Z. Zhang, Antimicrobial peptide trichokonin VI-induced alterations in the morphological and nanomechanical properties of *Bacillus subtilis*, Plos One 7 (2012) e45818.

[48] S.K. Das, M. Mukherjee, A.K. Guha, Interaction of chromium with resistant strain *Aspergillus versicolor*: Investigation with atomic force microscopy and other physical studies, Langmuir 24 (2008) 8643-8650.

[49] G. Smolyakov, S. Pruvost, L. Cardoso, B. Alonso, E. Belamie, J. Duchet-Rumeau, AFM PeakForce QNM mode: Evidencing nanometre-scale mechanical properties of chitin-silica hybrid nanocomposites, Carbohydr. Polym. 151 (2016) 373-380.

[50] A. Stankovic, S. Dimitrijevic, D. Uskokovic, Influence of size scale and morphology on antibacterial properties of ZnO powders hydrothemally synthesized using different surface stabilizing agents, Colloids Surf. B-Biointerfaces 102 (2013) 21-28.

[51] M. Galvan-Ruiz, J. Hernandez, L. Banos, J. Noriega-Montes, M.E. Rodriguez-Garcia, Characterization of calcium carbonate, calcium oxide, and calcium hydroxide as starting point to the improvement of lime for their use in construction, J. Mater. Civ. Eng. 21 (2009) 694-698.

[52] J. Sawai, K. Nagasawa, M. Kikuchi, Ability of heated scallop-shell powder to disinfect *Staphylococcus aureus* biofilm, Food Sci. Technol. Res. 19 (2013) 561-568.

[53] J. Ananpattarachai, Y. Boonto, P. Kajitvichyanukul, Visible light photocatalytic antibacterial activity of Ni-doped and N-doped TiO$_2$ on *Staphylococcus aureus* and *Escherichia coli* bacteria, Environ. Sci. Pollut. Res. 23 (2016) 4111-4119.

[54] A.D. Bokare, W. Choi, Singlet-Oxygen Generation in Alkaline Periodate Solution, Environ. Sci. Technol. 49 (2015) 14392-14400.

[55] K. Nakamura, K. Ishiyama, H. Ikai, T. Kanno, K. Sasaki, Y. Niwano, M. Kohno, Reevaluation of analytical methods for photogenerated singlet oxygen, J. Clin. Biochem. Nutr. 49 (2011) 87-95.

[56] P. Persich, S. Hostyn, C. Joie, G. Winderickx, J. Pikkemaat, E.P. Romijn, B.U.W. Maes, "Dark" singlet oxygen and electron paramagnetic resonance spin trapping as convenient tools to assess photolytic drug degradation, J. Pharm. Sci. 106 (2017) 1310-1316.

[57] T. Ikoma, Q.W. Zhang, F. Saito, K. Akiyama, S. Tero-Kubota, T. Kato, Radicals in the mechanochemical dechlorination of hazardous organochlorine compounds using CaO nanoparticles, Bull. Chem. Soc. Jpn. 74 (2001) 2303-2309.

[58] F. Wilkinson, W.P. Helman, A.B. Ross, Rate constants for the decay and reactions of the lowest electronically excited singlet-state of molecular-oxygen in solution - an expanded and revised compilation, J. Phys. Chem. Ref. Data 24 (1995) 663-1021.

[59] A. Grundling, Potassium Uptake Systems in *Staphylococcus aureus*: New Stories about Ancient Systems, Mbio 4 (2013) e00784-13.

[60] S. Bouhdid, J. Abrini, A. Zhiri, M.J. Espuny, A.n. Manresa, Investigation of functional and morphological changes in *Pseudomonas aeruginosa* and *Staphylococcus aureus* cells induced by *Origanum compactum* essential oil, J. Appl. Microbiol. 106 (2009) 1558–1568.

[61] S. Das, S. Sinha, B. Das, R. Jayabalan, M. Suar, A. Mishra, A.J. Tamhankar, C.S. Lundborg, S.K. Tripathy, Disinfection of multidrug resistant *Escherichia coli* by solar-photocatalysis using Fe-doped ZnO nanoparticles, Sci. Rep. 7 (2017) 104.

[62] D.H. Wu, H. You, D.R. Jin, X.C. Li, Enhanced inactivation of *Escherichia coli* with Ag-coated TiO$_2$ thin film under UV-C irradiation, J. Photochem. Photobiol. A 217 (2011) 177-183.

[63] L.S. Zhang, K.H. Wong, H.Y. Yip, C. Hu, J.C. Yu, C.Y. Chan, P.K. Wong, Effective Photocatalytic Disinfection of *E. coli* K-12 Using AgBr-Ag-Bi$_2$WO$_6$ nanojunction system irradiated by visible light: The role of diffusing hydroxyl radicals, Environ. Sci. Technol 44 (2010) 1392-1398.

[64] Y.M. Chen, T.W. Ng, A.H. Lu, Y. Li, H.Y. Yip, T.C. An, G.Y. Li, H.J. Zhao, M.H. Gao, P.K. Wong, Comparative study of visible-light-driven photocatalytic inactivation of two different wastewater bacteria by natural sphalerite, Chem. Eng. J. 234 (2013) 43-48.

[65] T.Y. Leung, C.Y. Chan, C. Hu, J.C. Yu, P.K. Wong, Photocatalytic disinfection of marine bacteria using fluorescent light, Water Res. 42 (2008) 4827-4837.

[66] C. Pablos, R. van Grieken, J. Marugan, B. Moreno, Photocatalytic inactivation of bacteria in a fixed-bed reactor: Mechanistic insights by epifluorescence microscopy, Catal. Today 161 (2011) 133-139.

[67] T.-W. Chang, H. Ko, W.-S. Huang, Y.-C. Chiu, L.-X. Yang, Z.-C. Chia, Y.-C. Chin, Y.-J. Chen, Y.-T. Tsai, C.-W. Hsu, C.-C. Chang, P.-J. Tsai, C.-C. Huang, Tannic acid-induced interfacial ligand-to-metal charge transfer and the phase transformation of Fe_3O_4 nanoparticles for the photothermal bacteria destruction, Chem. Eng. J. 428 (2022) 131237.

[68] W.K. Jung, H.C. Koo, K.W. Kim, S. Shin, S.H. Kim, Y.H. Park, Antibacterial activity and mechanism of action of the silver ion in *Staphylococcus aureus* and *Escherichia coli*, Appl. Environ. Microbiol. 74 (2008) 2171-2178.

[69] L. Boulos, M. Prevost, B. Barbeau, J. Coallier, R. Desjardins, Live/Dead (R) BacLight (TM): Application of a new rapid staining method for direct enumeration of viable and total bacteria in drinking water, J. Microbiol. Methods 37 (1999) 77-86.

[70] M. Mathelie-Guinlet, A.T. Asmar, J.F. Collet, Y.F. Dufrene, *Lipoprotein Lpp* regulates the mechanical properties of the *E. coli* cell envelope, Nat. Commun. 11 (2020) 1789.

[71] H. Jin, X. Huang, Y. Chen, H.X. Zhao, H.Y. Ye, F.C. Huang, X.B. Xing, J.Y. Cai, Photoinactivation effects of hematoporphyrin monomethyl ether on gram-positive and -negative bacteria detected by atomic force microscopy, Appl. Microbiol. Biotechnol. 88 (2010) 761-770.

[72] M. Mathelie-Guinlet, C. Grauby-Heywang, A. Martin, H. Fevrier, F. Morote, A. Vilquin, L. Beven, M.H. Delville, T. Cohen-Bouhacina, Detrimental impact of silica nanoparticles on the nanomechanical properties of *Escherichia coli*, studied by AFM, J. Colloid Interface Sci. 529 (2018) 53-64.

[73] I. Shlar, S. Droby, R. Choudhary, V. Rodov, The mode of antimicrobial action of curcumin depends on the delivery system: monolithic nanoparticles vs. supramolecular inclusion complex, Rsc Advances 7 (2017) 42559-42569.

[74] R. Noor, Mechanism to control the cell lysis and the cell survival strategy in stationary phase under heat stress, SpringerPlus 4 (2015).

CHAPTER 7

Substantial improvement in photocatalysis performance of N-TiO₂ immobilized on PMMA: Exemplified by inactivation of *Staphylococcus aureus* and *Escherichia coli*

7.1 Abstract[2]

Photocatalysis is an efficient process for degrading organic pollutants and inactivating pathogenic microorganisms. However, this process constantly suffers from turbidity shading and particle aggregation in a catalyst suspension system, thereby reducing its photocatalytic activity. Immobilizing the photocatalyst on the light-transmissible surface is a viable solution to the obstacles. So far, the photo-inactivation efficacy between the immobilized photocatalyst and suspension systems has yet to be compared and investigated. In this study, N-TiO₂ (NT) immobilized on poly-methyl-methacrylate (PMMA) was fabricated via a dip-coating method, which has a high transmittance rate of 92% - better than all of the previous works (50%). By immobilizing N-TiO₂ on PMMA, up to 60% and 19% improvements in inactivation efficiencies against Gram-positive *Staphylococcus aureus* (*S. aureus*) and Gram-negative *Escherichia coli* (*E. coli*) are achieved, respectively, relative to a photocatalyst suspension. Notably, reactive oxygen species (ROSs) detection results indicate that 5 g L^{-1} NT coated PMMA ((NT-PMMA)$_5$) has higher intensities of singlet oxygen ($^1O_2$), hydroxyl radicals (HO$^•$), and higher concentration of hydrogen peroxide (H_2O_2) than the NT suspension. The as-made NT-PMMA sustains a 99.99% inactivation efficiency (5-log-inactivation) against *S. aureus*

---

[2] Yen, L.-T., Weng, C.-H., Tzeng, J.-H., Chen, Y.-C., Jacobson, A. R., & Lin, Y.-T. (2024). Substantial improvement in photocatalysis performance of N-TiO₂ immobilized on PMMA: Exemplified by inactivation of *Staphylococcus aureus* and *Escherichia coli*. *Separation and Purification Technology*, 345, 127298.

through five consecutive photocatalysis cycles of reuse. The inactivation kinetics of *S. aureus* and *E. coli* fit well with the modified Hom model. Atomic force microscopy observations indicate that the NT-PMMA inactivation causes more severe damage to *S. aureus'*s cell wall than *E. coli* due to the different susceptibility of cell wall structure to ROSs. This study paves a substantial way for scaling up the immobilizing catalyst on PMMA for the effective photocatalytic inactivation of pathogens under visible light.

Keywords: N-TiO$_2$, poly-methyl-methacrylate, hydrogen peroxide, hydroxyl radicals, immobilization, photocatalysis, singlet oxygen

7.2 Introduction

Chlorination, ozonation, and ultraviolet (UV) light are conventional techniques used to inactivate pathogenetic bacteria in water and wastewater treatment processes. However, they still have drawbacks, such as high operating costs and inadequate inactivation performance. Photocatalysis has the potential to serve as an alternative technology due to its emerging ability to degrade persistent organic pollutants and inactivate pathogens effectively (Tzeng et al., 2021; Yen et al., 2022). because of its large band gap, titanium dioxide (TiO$_2$), one of the most popular photocatalysts, can only be activated under radiation with wavelengths below 350 nm. Element doping of TiO$_2$, for example, nitrogen and carbon, can further narrow the bandgap, allowing it to utilize the full spectrum of visible light in sunlight for photocatalysis.

Photocatalysts have typically been used in suspension systems for photooxidation. However, such a TiO$_2$ suspension process often suffers from the adverse effects of particle aggregation and turbidity shading in the catalyst suspension, thereby reducing its

photocatalytic activity. Immobilizing photocatalysts on a surface offers a solution system to minimize such effects (Terra et al., 2023). The immobilization of photocatalysts by fixing the catalyst powder to a support material provides a long-term and cost-effective inactivation solution without additional post-treatment steps, thereby minimizing overall operational expenses (Goutham et al., 2019). Furthermore, the immobilized photocatalyst allows readily reusing immobilized photocatalysts without recovery or separation from suspension, thereby reducing ecotoxicity concerns (Wood et al., 2020; Zhang et al., 2023). Previous studies have shown that immobilized TiO_2 is capable of bacteria inactivation. Cantarella et al. (2016) embedded TiO_2 in polymethyl methacrylate (PMMA) with a dose of 150 g L^{-1}. They found 4.8-log inactivation of *E. coli* in 1 h under UV light irradiation. Varnagiris et al. (2021) immobilized carbon-doped TiO_2 on the surface of high-density polyethylene (HDPE) beads, which resulted in a 2.5-log photocatalytic inactivation of *Salmonella typhimurium* in 1 h under UV light irradiation (5 mW cm^{-2}). So far, the inactivation efficiency of immobilized photocatalysts against bacteria under visible light irradiation and the comparison with the suspension system have yet to be explored.

Poly-methyl-methacrylate (PMMA) has excellent impact strength, UV resistance, and high transparency to visible light and is the most frequently used commercial polymer in architecture, electronics, and furniture (El-Newehy et al., 2022; Khaled et al., 2007). By sprinkling a layer of TiO_2 on PMMA fabricating a TiO_2/PMMA film, Ounas et al. (2020) showed that the photocatalytic degradation of methylene blue with UV light irradiation remained merely only 60% after 250 min because the sprinkling method reduced PMMA light transmittance by 50%. To improve the light transmittance, other researchers have adopted methods to functionalize the PMMA polymer matrix with the minimum influence

on its original properties, including dip-coating (Wu et al., 2022), vapor-deposition (Peng et al., 2022), and magnetron sputtering (Hao et al., 2022). Dip-coating is an economical and facile approach to fabricating nanocoating on a polymer matrix that is easy to scale up with a uniform thickness (Wu et al., 2022). However, an immobilized catalyst with high transmittance properties responsive to visible light is still needed. So far, studies have yet to successfully immobilize photocatalysts, maintain ultra-transmittance, and evaluate the bacterial inactivation efficiency under visible light.

This study fabricated a high transmittance, surface-functionalized TiO_2-coated PMMA composite (NT-PMMA) using a dip-coating technique to enhance photocatalytic activity via immobilization. For the first time, the inactivation efficiency of NT immobilized PMMA composite against gram-positive *S. aureus* and gram-negative *E. coli* bacteria was explored under visible light. The test adopted two bacterial strains due to their different cell structures and varying susceptibility to photooxidation reactions. Noteworthy, a comparison of inactivation efficiency and the reactive oxygen species (ROSs) intensity between immobilized $NT-TiO_2$ and $NT-TiO_2$ suspension was investigated in this study. A modified Hom (MH) inactivation kinetic model was used to simulate the inactivation process and determine the light intensity and NT-PMMA dose effects on photocatalytic inactivation. The durability of the photocatalysts was evaluated by subjecting the NT-PMMA to five cycles of photoinactivation reaction. Lastly, the early changes in the biophysical properties of inactivated *S. aureus* and *E. coli* strains were observed using atomic force microscopy (AFM) analysis. This study provides insight into pathogen inactivation by NT-PMMA and supports the application of a photocatalyst-immobilized polymer as an environmentally friendly inactivation approach.

7.3 Materials and Methods

7.3.1 Chemicals

Small sheets of PMMA (5 cm × 5 cm × 0.5 cm) were obtained from Tzy Feng Tech Co. Ltd, Taiwan. Strains of *S. aureus* (ATCC 6538P) and *E. coli* (ATCC 8739) were obtained from the Bioresource Collection and Research Center in Taiwan. Reagent grade ethanol (99.9%), ammonium hydroxide (28-30%), and titanium isopropoxide (97%) were purchased from J.T. Baker (United States) and Invitrogen (United States), respectively.

7.3.2 Preparation of NT-PMMA

NT was synthesized using a modified sol-gel method, as described by Lin et al. (2015). In brief, a triple-necked round bottom flask was filled with 200 mL of ethanol, followed by 50 mL of deionized water and 150 mL of ammonium hydroxide. The solution was stirred at 350 rpm and placed in a low-temperature thermostatic water bath to maintain the temperature at 4 °C. Over a period of 4 min, 10 mL of titanium tetra-isopropoxide was added dropwise, and stirring was continued for 4 h. The solution was left to stir overnight, after which the solid particles were allowed to settle, and the supernatant was decanted. The resulting precipitate was washed twice with distilled water, dried in an oven at 105 °C overnight, and then calcined in a vacuum furnace for 1 h at 500 °C.

NT-coating solutions were prepared by mixing NT powder with isobutyl alcohol (99%, Sigma-Aldrich) at concentrations of 0.1, 0.75, 1, 2.5, 5, 10, and 20 g L^{-1}. The solutions were ultrasonicated at 40 kHz for 10 min before use. NT was coated onto the

PMMA surface using a dip coater (Bungard, RCD15, Germany). To ensure that the

thickness of NT on the PMMA surface was coated uniformly, the dipping speed was

fixed at 1.2 cm min^{-1} for 5 sec in the NT coating solution, and then the PMMA was

pulled up at a stable speed of 1.2 cm min^{-1}. NT-PMMA was dried in an oven at 80 °C for

2 min and stored in a clean petri dish ready for use. The light transmittance of NT-

PMMA was measured using a full-spectrum transmittance measuring instrument

(Rainbow light, TSM-02, Taiwan) following ASTM standards (ASTM D1003-13). The

analysis was performed first with plain PMMA as a reference, followed by the 0.1-20 g

L^{-1} NT-PMMA.

7.3.3 Characteristics of NT and NT-PMMA

The X-ray Diffraction (XRD) measurements of the NT-PMMA composite were

carried out using a BRUKER D8 SSS instrument (USA) with Cu-Kα radiation to

determine its phase composition and crystallite size. Dynamic Light Scattering (DLS)

with a Zetasizer (Malvern, U.K.) was used to analyze the particle size. The optical

absorption response of the composite was measured with a UV-Vis spectrometer

(Hitachi, Japan) equipped with an integrated sphere, with $BaSO_4$ as a reference. The

specific surface area was determined using the Brunauer-Emmett-Teller (BET) method

on a Micromeritics ASAP 2020 instrument (USA). The morphology of NT on the PMMA

surface was observed with a scanning electron microscope (JEOL, Japan). The

transmittance of the NT-PMMA was measured by full spectrum transmittance using a

transmittance measuring equipment (TSM-02; Rainbow Light Technology, Taiwan),

following the standard method ASTM D 1003. The methods for photoelectrochemical

characterization, including electrochemical impedance spectroscopy (EIS), transient

photocurrent (TPC), photoluminescence spectroscopy (PL), and UV–vis diffuses reflectance spectra were shown in Supplemental Information (text S1).

7.3.4 Detection of generated ROSs

Reactive oxygen species (ROSs) were identified using an electron spin resonance (ESR) spectrometer (Bruker, USA) operating within the X-band frequency range of 9.49 – 9.88 GHz with an output power of 8.02 mW. For the detection of singlet oxygen ($^1O_2$), a 0.05 M solution of 2,2,6,6-tetramethylpiperidine (TEMP) was employed, while a 0.05 M solution of 5,5-dimethyl-1-pyrroline N-oxide (DMPO) was used to identify hydroxyl radicals (HO$^\bullet$) and superoxide ions ($O_2^{\bullet-}$) in the aqueous solution. One mL NT suspension and (NT-PMMA)$_5$ reaction suspension were immediately transferred to the measuring cuvette, respectively. Another 1 mL trapping agent was added directly to the cuvette before the ESR measurement. The same suspensions were employed for scavenging experiments, with the inclusion of 0.01 M furfuryl alcohol (FA) as the scavenger for TEMP–$^1O_2$, 0.01 M tert-butanol (TBA) as the scavenger for DMPO– HO$^\bullet$, and 0.01 M p-benzoquinone (BQ) as the scavenger for DMPO−$O_2^{\bullet-}$. The production of H_2O_2 was quantified using a triiodide method. Detailed procedures for this analysis is illustrated in the literature (Diesen & Jonsson, 2014).

7.3.5 Inactivation Efficacy of NT-PMMA

This study employed the ISO 22196 standard method to measure the antibacterial activity on non-porous surfaces. Prior to the experiment, *E. coli* and *S. aureus* were cultured on nutrient agar for 18 h at 37 °C, resulting in a bacterial suspension of 10^5 CFU mL^{-1} obtained by mixing bacteria with 1/500 NB (*E. coli*) or 1/500 TSB (*S. aureus*). The 0.4 mL

bacterial suspension was then dropped onto the surface of NT-PMMA, which was covered with a sterilized polyethylene cover film (5×5 cm^2) and kept at a controlled humidity by adding 1 mL of deionized water on a cotton pad. Visible light irradiation was conducted in a reaction box equipped with fluorescent lamps (T5 8W 6000 K, Kanjin, Taiwan), with light intensity ranging from 0.24–1.74 mW cm^{-2}. The samples were exposed to visible light for 0, 30, 60, 180, 360, 720, 900, 1080, and 1440 min. After exposure, the bacterial cells on the surface of NT-PMMA and the polyethylene cover film were flushed with 10 mL of soya casein digest lecithin polysorbate broth (SCDLP), and 1 mL of the SCDLP bacterial suspension was serially diluted and cultured on nutrient agar for 18 h at 37 °C.

A comparison was conducted to assess the inactivation efficiencies between immobilized NT-PMMA and NT suspension. *S. aureus* and *E. coli* were cultured on nutrient agar plates for 18 h. After rinsing three times with sterilized deionized water, the bacterial pellets were resuspended in 9 mL of sterilized deionized water. Then, 100 mL of sterilized water was added to polypropylene plastic vessels, and the bacterial strains were inoculated to achieve an initial bacterial concentration of 10^5 CFU mL^{-1}. Subsequently, 0.5 g NT was added. The suspension was exposed to visible light with an intensity of 0.54 mW cm^{-2}. At increasing reaction intervals (0, 60, 180, 360, 720, and 1440 min), bacterial suspension with volume of 0.1 mL was serial-diluted and cultured on agar plates. The bacterial survival ratio and inactivation efficiency were calculated using the following formulas:

Survival ratio (%) $= (N_t/ N_0) \times 100$ (1)

Inactivation efficiency (%) $= (1 - N_t/ N_0) \times 100$ (2)

where N_t represents the bacterial concentration (CFU mL^{-1}) at time t (min); N_0 represents the bacterial concentration (CFU mL^{-1}) at the starting point (0 min).

The durability of the photocatalysts was evaluated by subjecting them to five cycles. After each cycle, NT-PMMA was washed several times with ethanol and water to eliminate residual organic compounds produced from the degradation of bacteria. The NT-PMMA was then dried at 80 °C, irradiated by UV light for 2 h to remove the residual organic compound on the surface, and reused for four subsequent tests.

7.3.6 Inactivation kinetic model

The MH model is utilized for analyzing the kinetics of photocatalytic bacterial inactivation processes. The model fitting involves simulating inactivation profiles with three independent rate constants corresponding to a shoulder region, log-linear region, and final tail inactivation (Ganguly et al., 2018; Yemmireddy & Hung, 2015). The MH model has been successfully used for describing bacterial inactivation kinetics by double-layer ZnO/Al$_2$O$_3$ thin film (Meznaric et al., 2022) and spinel ferrite CuFe$_2$O$_4$ (Ozkal, 2022) nanocomposites. The three rate constants illustrate three inactivation phases in a photocatalytic process, i.e., accumulation of ROSs in the surrounding bacteria, rapid log-linear bacterial inactivation due to the ROSs attack, and the deceleration of cell damage.

$$log \frac{N_t}{N_0} = -k_1[1 - \exp(-k_2 t)]^{k_3} \tag{3}$$

where k_1, k_2, and k_3 are the empirical rate constants corresponding to shoulder, log-linear reduction, and tailing distinct regions; log (N_t/N_0) is the bacterial log reduction unit, N_t is the bacterial population at the time (t), and N_0 is the initial bacterial concentration. The

KaleidaGraph 4.0 software was used to fit the experimental data to the MH model. The accuracy of the model's quantitative predictions was assessed using the root mean square error (RMSE), as shown in Eq. (4).

$$RMSE = \sqrt{\frac{\Sigma\left[\left(log\frac{C}{C0}\right)_{pred} - \left(log\frac{C}{C0}\right)_{exp}\right]^2}{n}} \tag{4}$$

7.3.7 Identifying the biophysical properties of the damaged bacteria

The inactivated bacteria's biophysical properties were measured using AFM in Peak Force Quantitative Nanomechanical Mapping (QNM) mode after being exposed to visible light irradiation on NT-PMMA. The measurement was conducted using an ACTA cantilever with a resonance frequency of 200–400 kHz and a spring constant of 25–75 Nm^{-1}. The equipment used for the measurement was Dimension Icon from Bruker in the USA, and the cantilever was from AppNano in the USA. To conduct the AFM scanning, a bacterial suspension of 10 µL was dropped on a sheet of glass coated with poly-L-lysine and air-dried for 5 min. The photo-inactivation experiments were repeated three times. The biophysical characteristics of bacterial cells were determined by analyzing ten distinct locations on the bacterial surface with NanoScope 6.0 software. The roughness of the bacterial surface was assessed by root-mean-square (R_{rms}) (Eq. 5) (Girasole et al., 2007; Tzeng et al., 2020).

$$R_{rms} = \sqrt{\Sigma_{i=1}^{N} \frac{(Z_i - Z_m)^2}{N-1}} \tag{5}$$

where N stands for the total number of data points, Z_i represents the height of the ith point, and Z_m signifies the mean height.

7.4 Results and Discussions

7.4.1 Characterization of N-TiO₂

Table B6-1 summarizes the characterization results of NT. XRD analysis confirmed that NT was 100% anatase phase, with significant diffraction peaks observed at 2θ angles of 25.5°, 38.0°, 48.2°, 54.5°, 55.3°, and 63.06°, corresponding to the (101), (104), (200), (105), (211), and (204) planes, respectively (Fig. S7-1). The anatase phase of TiO_2 has been found to be the most effective for generating ROSs (Joost et al., 2015). The crystallite size of NT was determined to be 37 nm using the Scherrer formula. The specific surface area of NT is 45.3 m^2/g, with a pore size of 6.9 nm and a pore volume of 0.13 cm^3/g. The bandgap energy of NT, calculated from the plot of $(\alpha h\nu)^{1/2}$ versus photon energy, was found to be 2.4 eV (Lin et al., 2015). The nitrogen dopant in TiO_2 lowered the bandgap from 3.2 eV (pure anatase TiO_2) to 2.4 eV, making NT more photoactive under visible light irradiation. The photoelectrochemical characterization, including electrochemical impedance spectroscopy (EIS), transient photocurrent (TPC), photoluminescence spectroscopy (PL), and UV–vis diffuses reflectance spectra for NT used in this study were shown in Figs. B6-2, B6-3, S8-4, and B6-5. NT showed an absorption threshold at approximately 415 nm (Fig. B6-2). As shown in Fig. B6-3, NT has a smaller radius compared to the pure anatase TiO_2, suggesting the electron transfer process of NT is faster.

7.4.2 Transmittance measurement of NT-PMMA

PMMA is widely used in commercial products due to its excellent light transmittance feature with potential as an alternative to glass. It is important to determine

whether the coating of NT onto PMMA would affect light transmittance. As shown in the SEM images (Figs. 7-1a and 7-1b), the dip-coated NT particles are uniformly distributed on the PMMA surfaces with minimal aggregation. PMMA without coating exhibited a transmittance of 94%, while PMMA coated with NT suspensions still maintained high transmittances of 93-88% in the NT coating concentration ranging from 0.1 g L^{-1} to 20 g L^{-1} (Fig. 8-1c). These transmittances of NT-PMMA are far superior to the 50% transmittance obtained using the sprinkle method (Ounas et al., 2020). No noticeable screening effect of the NT coating of NT-PMMA was detected (Fig. 7-1d). The excellent transmittance results suggest that PMMA is a promising substitute for glass for coating NT.
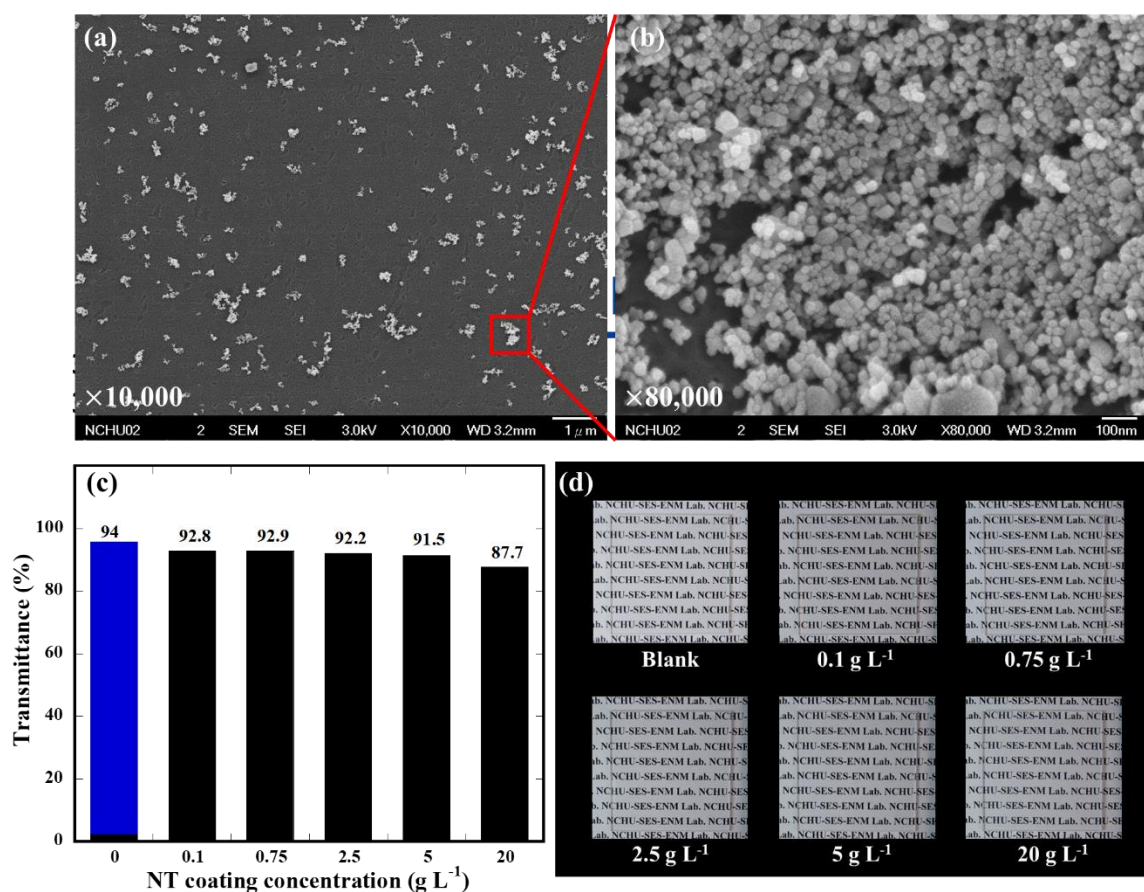
Figure 7-1. SEM images of (NT-PMMA)$_5$ with resolutions of (a) ×10,000 and (b) ×80,000. (c) Effect of NT coating concentration on the transmittance of NT-PMMA and (d) NT-PMMA transmission images.

7.4.3 Comparison of inactivation efficiency between NT-PMMA and NT suspension

To compare the inactivation efficiencies of *S. aureus* and *E. coli* between the immobilization (NT-PMMA) and suspension (NT) systems, (NT-PMMA)$_5$ and 5 g L^{-1} NT in suspension were tested under the same visible light condition. As shown in Figs. 7-2a and 7-2b, PMMA without a NT coating demonstrates a stable bacterial survival rate of approximately 91-105% for *S. aureus* and 97-119% for *E. coli* during 24 h. This indicates that in the absence of any disinfectant coating, there is steady bacterial growth on the plain PMMA surface. NT-PMMA exhibits significantly higher inactivation efficiency than the NT suspensions for both bacteria. For *S. aureus*, the NT-PMMA demonstrates a 96% inactivation efficiency (t = 360 min), whereas the inactivation efficiency of the NT suspension is 36%. As for *E. coli*, the NT-PMMA resulted in 62% inactivation efficiency (t = 360 min), which decreased to 43% in the NT suspension. After 24 h, the NT-PMMA achieved complete inactivation, whereas the NT suspension only achieved 81% and 72% inactivation efficacy for *S. aureus* and *E. coli*, respectively. Ananpattarachai et al. (2016) reported that a 1000 g L^{-1} dose of NT suspension irradiated with visible light for 24 h resulted in only a 1-log-inactivation of *S. aureus* and *E. coli*, indicating the low photooxidation efficacy of the catalyst powder in suspension systems. It can be realized that such discrepancy is due mainly to the suffering of particle aggregation and light shading effect in a suspension system, consequently resulting in a decrease in inactivation efficiency. The production of $^1O_2$ in both (NT-PMMA)$_5$ and NT suspension was verified

through ESR analysis using TEMP as a spin-trapped agent. TEMP was specifically chosen to capture $^1O_2$ and create the stable TEMP-$^1O_2$ adduct, identifiable by its characteristic ESR spectrum featuring three lines of equal intensity (aN = 16 G). As illustrated in Fig. 7-2c, the distinct 1:1:1 triplet signal indicative of TEMP$-^1O_2$ adducts was observed, confirming the presence of $^1O_2$ in both the NT suspension and (NT-PMMA)$_5$. The presence of hydroxyl radicals in both systems was identified based on the observation of the typical 1:2:2:1 signal of DMPO-HO$^•$ shown in Fig. 7-2d. However, the signal of $O_2^{•-}$ was not found in the ESR spectra (Fig. B6-6). A similar result is shown in Fig. 7-2e, the H_2O_2 generated from (NT-PMMA)$_5$ showed a 1.5-fold higher concentration (0.92 mol L^{-1}) than that in NT suspension (0.63 mol L^{-1}). It is evidenced that the intensities of $^1O_2$, HO$^•$, and H_2O_2 concentration of (NT-PMMA)$_5$ system are greater than in the NT suspension, corresponding to the greater inactivation efficiency of (NT-PMMA)$_5$ shown in Figs. 7-2a and 7-2b.
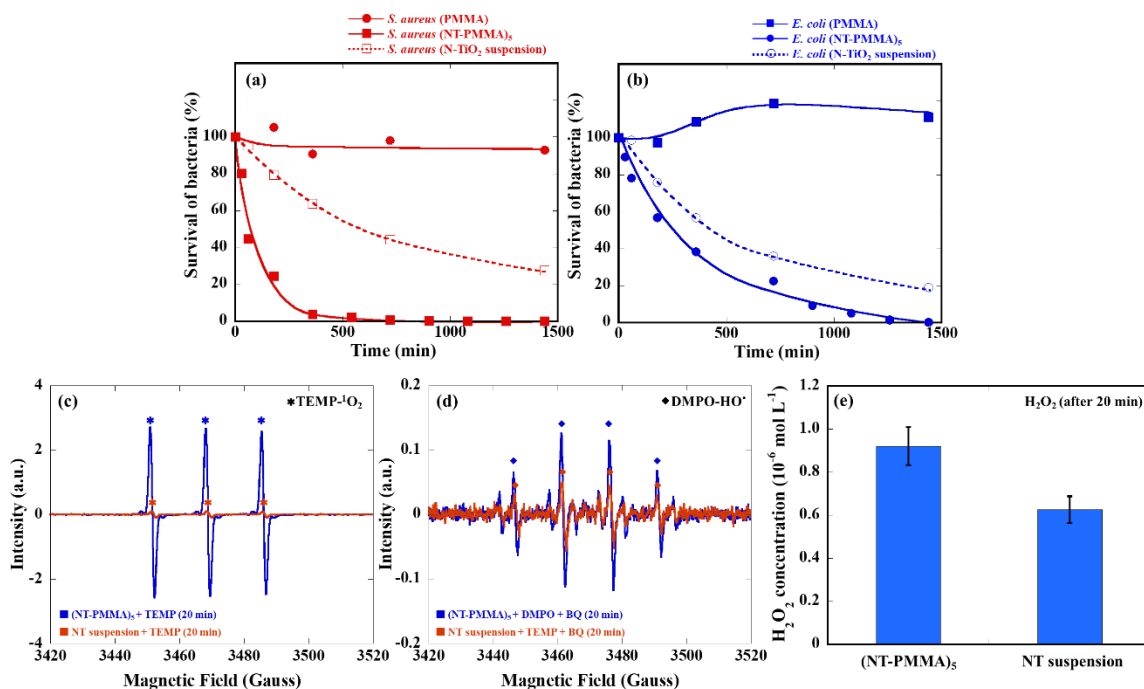
Figure 7-2. (a) The comparison of inactivation efficiency against *S. aureus* between plain PMMA, NT-PMMA, and NT suspension with the dose of 5 g L^{-1} under visible-light intensity of 0.54 mW cm^{-2}. Conditions: [bacteria] = 10^5 CFU mL^{-1}. (b) The comparison of inactivation efficiency against *E. coli* between plain PMMA, NT-PMMA, and NT suspension with the dose of 5 g L^{-1} under visible-light intensity of 0.54 mW cm^{-2}. Conditions: [bacteria] = 10^5 CFU mL^{-1}. (c) ESR spectra of (NT-PMMA)$_5$ and NT suspension. Conditions: [NT-PMMA] = 5 g L^{-1}, [NT suspension] = 5 g L^{-1}, T = 25 ± 1 °C. (d) ESR spectra of (NT-PMMA)$_5$ and NT suspension, and BQ as a quenching agent for O$_2$$^{\bullet-}$. Conditions: [NT-PMMA] = 5 g L^{-1}, [NT suspension] = 5 g L^{-1}, T = 25 ± 1 °C. (e) H$_2$O$_2$ concentrations of (NT-PMMA)$_5$ and NT suspension. Conditions: [NT-PMMA] = 5 g L^{-1}, [NT suspension] = 5 g L^{-1}, T = 25 ± 1 °C.

7.4.4 Effects of NT dosage and visible light intensity on inactivation efficiency

The inactivation kinetics of the *S. aureus* and *E. coli* were compared by culturing the bacteria flushed from the NT-PMMA surface at various reaction times (Figs. 7-3a and 7-3b). In Fig. 7-3a, 5-log-inactivation of *S. aureus* treated with 1, 5, and 10 g L^{-1} NT-PMMA under 0.54 mW cm^{-2} visible light irradiation was achieved at 720, 540, and 60 min, respectively. On the other hand, 5-log-inactivation of *E. coli* treated with the same concentrations of NT-PMMA was achieved with longer reaction times, which are 900, 900, and 360 min. The disparity in inactivation efficiencies between the two bacterial types is attributed to the differences in their cell wall structures. Gram-positive bacteria have a thick cell wall (20-80 nm) made up of multilayered peptidoglycan (90%) that forms a three-dimensional lattice, while gram-negative bacteria have a thinner (10–15 nm) but more complex cell wall composed primarily of lipopolysaccharide (LPS) and a

few layers of peptidoglycan (around 2 nm thick) (Liu et al., 2023; Yen et al., 2022). As Figs. 7-2c and 7-2d showed that the photooxidation reaction of NT-PMMA was predominately driven by $^1O_2$. Valduga et al. (1993) indicated that gram-negative bacteria exhibited higher resistance to externally produced $^1O_2$ compared to gram-positive bacteria. Moreover, the outer membrane of gram-negative bacteria contains LPS, a compound comprising lipids and polysaccharides, which significantly limits the $^1O_2$ infiltration (Kim et al., 2019).

In Figs. 7-3c and 7-3d, it is evident that *S. aureus* achieved a 99.99% photo-inactivation efficiency after 720 min with the light intensity of 0.54 mW cm^{-2}, whereas *E. coli* achieved a 99.99% photo-inactivation efficiency after 1080 min with light intensity of 1.74 mW cm^{-2}. With the same light intensity of 0.54 mW cm^{-2}, *S. aureus* showed a 99.99% inactivation efficiency at 720 min, but it took *E. coli* 1260 min to achieve the same efficiency. The rapid photocatalytic reaction occurred on the surface of NT-PMMA, causing extensive damage to the bacteria. Overall, the inactivation efficiency against *S. aureus* and *E. coli* increases proportionally with increasing the coating of NT dosage and visible light intensity. A greater light intensity for *E. coli* inactivation is needed because *E. coli* is susceptible to the penetration damage of singlet oxygen. Table 8-1 summarizes similar studies and reveals that as-made NT-PMMA in this study showed excellent inactivation efficiency with a lower photocatalytic concentration under visible light irradiation than in other studies. For instance, Cantarella et al. (2016) embedded TiO_2 in PMMA with a 30-times higher dose of 150 g L^{-1} and achieved 4.8-log-inactivation of *E. coli* in 1 h using UV light. Tangudom et al. (2018) used a 3-times higher concentration of TiO_2 to achieve the same 5-log inactivation in 24 h, also with UV light irradiation.

Pascagaza-Rubio et al. (2022) immobilized TiO_2 on the HDPE surface with a dose of 46.7 g L^{-1}, showing only a 3-log inactivation of *E. coli* in 8 h under UVA light irradiation. However, there has been no notable advancement in the disinfection efficiency of TiO_2-immobilized matrices since the study conducted by Pascagaza-Rubio et al. (2022). The photooxidation efficiency of (NT-PMMA)$_5$ surpassed that of previous studies at a lower dose of only 5 g L^{-1} and proved effective under visible light exposure.
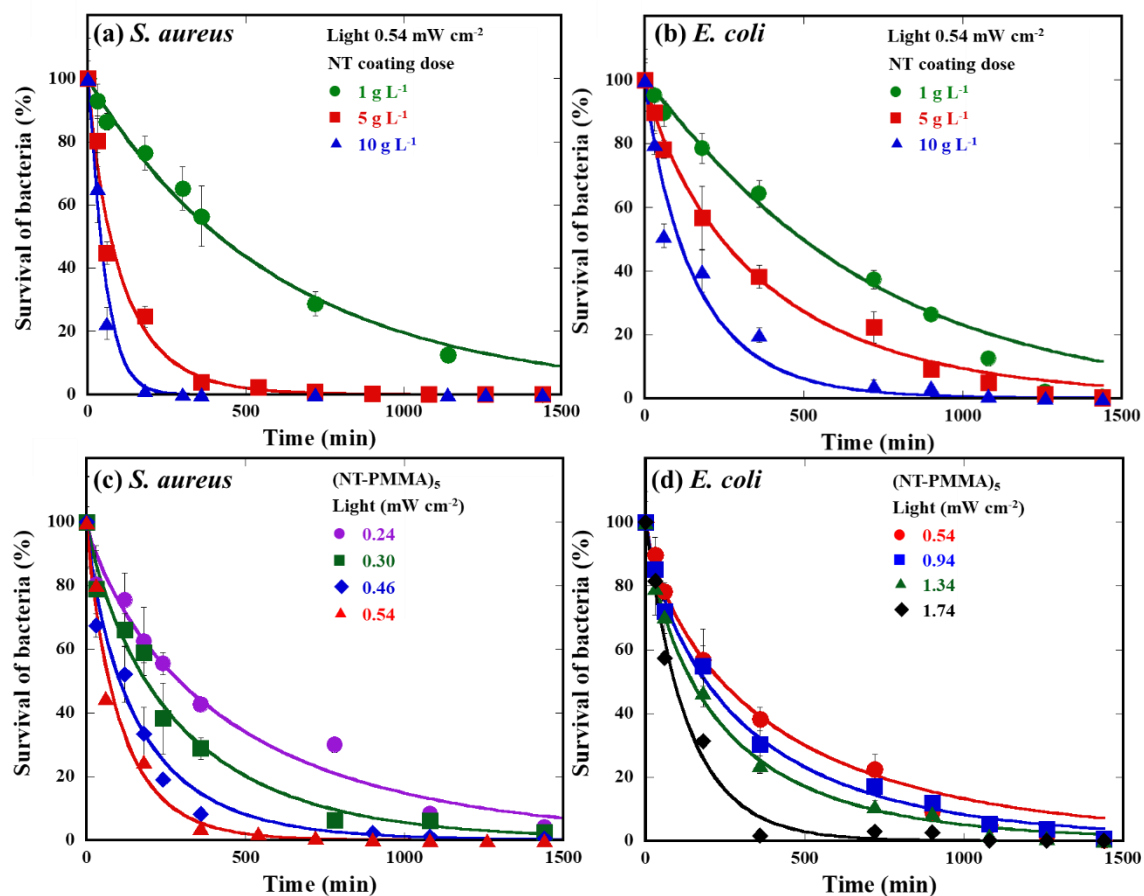
Figure 7-3. The NT coating concentration on PMMA and its effect on the survival rates of (a) *S. aureus* and (b) *E. coli*. The visible light intensity affects on the survival ratio of (NT-PMMA)$_5$ against (c) *S. aureus* and (d) *E. coli*. Conditions: [NT] = 1 - 10 g L^{-1}, [bacteria] = 10^5 CFU mL^{-1}, visible light intensity = 0.24 - 1.74 mW cm^{-2}, 25 ± 2 °C.

Table 7-1. The comparison of inactivation performance and the examination of inactivation actions with other disinfectants.

	Band gap	Particle Size	Dose	Light Source	Light Intensity	Inactivation Method	Initial Bacterial Concentration	Inactivation Performance	Ref.
	eV	nm	g L^{-1}	-	mW cm^{-2}	-	CFU mL^{-1}	-	
NT-PMMA	2.4	20	5	Visible light	0.54	Immobilization	1×10^5	5-log-inactivation of *E. coli* in 24 h; 5-log-inactivation of *S. aureus* in 24 h	**This study**
TiO$_2$-PMMA	NA	<50 nm	150	UV light	2.00	Immobilization	1×10^5	4.8-log-inactivation of *E. coli* in 1 h	(Cantarella et al., 2016)
C-TiO$_2$-HDPE	2.2-2.4	38	100	UV light	5.00	Immobilization	3×10^9	1-log-inactivation of *Salmonella typhimurium* in 1 h	(Varnagiris et al., 2021)
TiO$_2$-HDPE	NA	NA	46.7	UVA LED light	NA	Immobilization	1×10^4	3-log-inactivation of *E. coli* in 8 h	(Pascagaza-Rubio et al., 2022)
acrylic rubber-TiO$_2$/PMMA	NA	400	15	UV light	7.70	Immobilization	1×10^5	5-log-inactivation of *E. coli* in 24 h; 5-log-inactivation of *S. aureus* in 24 h	(Tangudom et al., 2018)
N-TiO$_2$	2.4	20	1	Visible light	0.76	Suspension	1×10^5	4-log-inactivation of *S. aureus* in 24 h	(Tzeng et al., 2021)
N-TiO$_2$	3.0	18	0.1	UV light	0.0013	Suspension	1×10^6	6-log-inactivation of *E. coli* in 1 h	(Makropoulou et al., 2018)

NA: Not available

PMMA= Polymethyl methacrylate

HDPE= High density polyethylene

1 **7.4.5 Reusability (stability) of NT-PMMA**

2 On the other hand, durability is an important factor for photocatalysts in practical

3 applications. The resilience of NT-PMMA against both bacterial strains was assessed

4 over five consecutive cycles using a visible light intensity of 1.74 mW cm^{-2} (as shown in

5 Fig. 7-4a) and a 24-hour duration for each cycle. Throughout the five cycles, the

6 inactivation efficiency for *S. aureus* remained high at 99.99%, but it declined to

7 approximately 76% for *E. coli*. The findings are in line with data from Figs. 7-2a and 7-

8 2b further confirm that *S. aureus* is more susceptible to inactivation than *E. coli* due to

9 varying resistance levels against the $^1O_2$-driven inactivation reaction. Another possible

10 cause is that the extracellular polymeric substances (EPS) produced by *E. coli* under

11 environmental stress will reduce the photooxidation capacity (Wang et al., 2023). In

12 order to overcome this issue, the coating concentration of NT-PMMA was increased to

13 20 g L^{-1} ((NT-PMMA)$_{20}$). Subsequent results, depicted in Fig. 8-4b, show that

14 inactivation efficiency against *E. coli* was 99.99% in the first cycle and maintained a

15 level of 99.4% throughout the subsequent four cycles. Notably, the performance of NT-

16 PMMA surpasses previous research. For comparison, a study by (Ye et al., 2013)

17 highlighted a 22% reduction in photooxidation efficiency for Rhodamine B using a TiO$_2$

18 thin film with 250 g L^{-1} after only four cycles under xenon lamp irradiation.
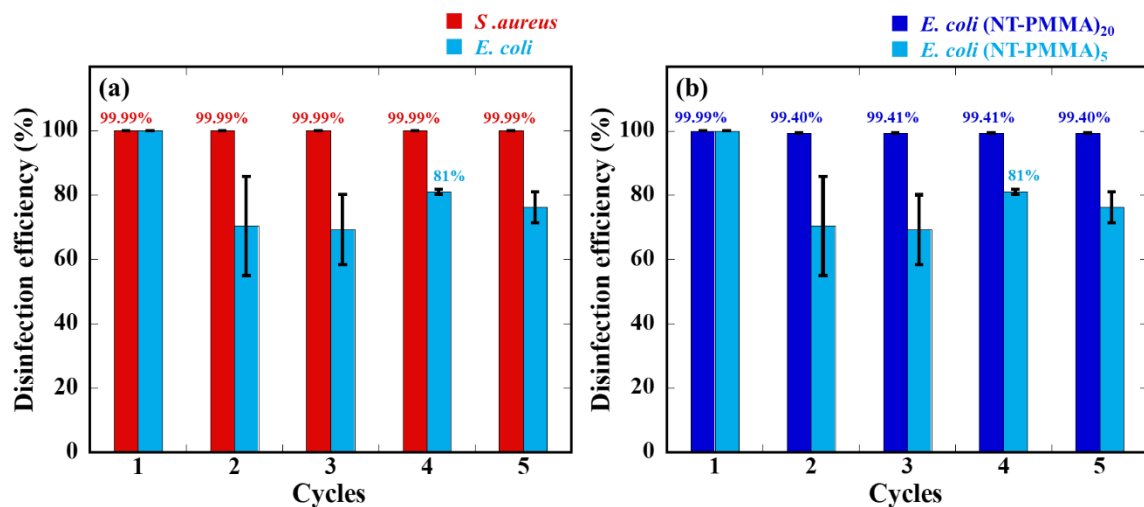
Figure 7-4. (a) Reusability (stability) experiment of (NT-PMMA)$_5$ for the photooxidation of *S. aureus* and *E. coli*. Conditions: [NT] = 5 g L^{-1}, [bacteria] = 10^5 CFU mL^{-1}, visible light intensity = 1.74 mW cm^{-2}, 25 ± 2 °C. (b) Reusability (stability) experiment of (NT-PMMA)$_5$ and (NT-PMMA)$_{20}$ for the photooxidation of *E. coli*. Conditions: [NT] = 5 and 20 g L^{-1}, [bacteria] = 10^5 CFU mL^{-1}, visible light intensity = 1.74 mW cm^{-2}, 25 ± 2 °C.

7.4.6 Modified Hom (MH) kinetic inactivation model

The photo-inactivation process usually comprises three phases, i.e., the lag (shoulder), log-linear, and tail phases, which are based on the concentration of bacteria under different damaged levels. To describe the variation of these inactivation phases, MH model has been developed, which has successfully simulated the photocatalytic inactivation of *E. coli* by CuFe$_2$O$_4$-Ti-GO (Ozkal, 2022), *S. aureus* and *E. coli* by double-layer ZnO/Al$_2$O$_3$, and *Klebsiella pneumonia*e by N/C-doped and N-tourmaline/palladium-C-codoped TiO$_2$ (Huang et al., 2020). In this study, two critical parameters, NT coating dosage and light intensity, were evaluated in determining the inactivation kinetics of NT-PMMA via the MH model. Fig. 7-5 shows the fitting curves

1   of the MH model for the inactivation of *S. aureus* and *E. coli* affected by these two

2   parameters. Table 7-2 summarizes that the experimental results fit well with the MH

3   model with low RMSE values. The MH model is useful in assessing the impact of

4   photocatalyst dosage and light intensity on the photo-inactivation performance of

5   bacteria. The constants k_1 (shoulder region), k_2 (log-linear region), and k_3 (tailing region),

6   which describe the inactivation of *S. aureus* and *E. coli*, decrease with increasing NT

7   coating concentrations and light intensity. The constant k_1 (shoulder region) can illustrate

8   the sequential process, where cellular damage accumulates over time instead of inducing

9   immediate lethality (Huang et al., 2019). In this study, the value of constant k_1 (shoulder

10   region) positively correlates with initial inactivation efficiency (the first 480 min). At the

11   NT doses of 5 and 10 g L^{-1}, *E. coli* showed higher k_1 values than *S. aureus* because of the

12   higher resistance to the ROSs attack. Similarly, *E. coli* showed a higher k_1 value than *S.*

13   *aureus* with the same visible light intensity of 0.54 mW cm^{-2}, corresponding to the results

14   in Figs. 7-2a and 7-2b that *E. coli* has greater resistance than *S. aureus* to the $^1O_2$

15   dominant system.
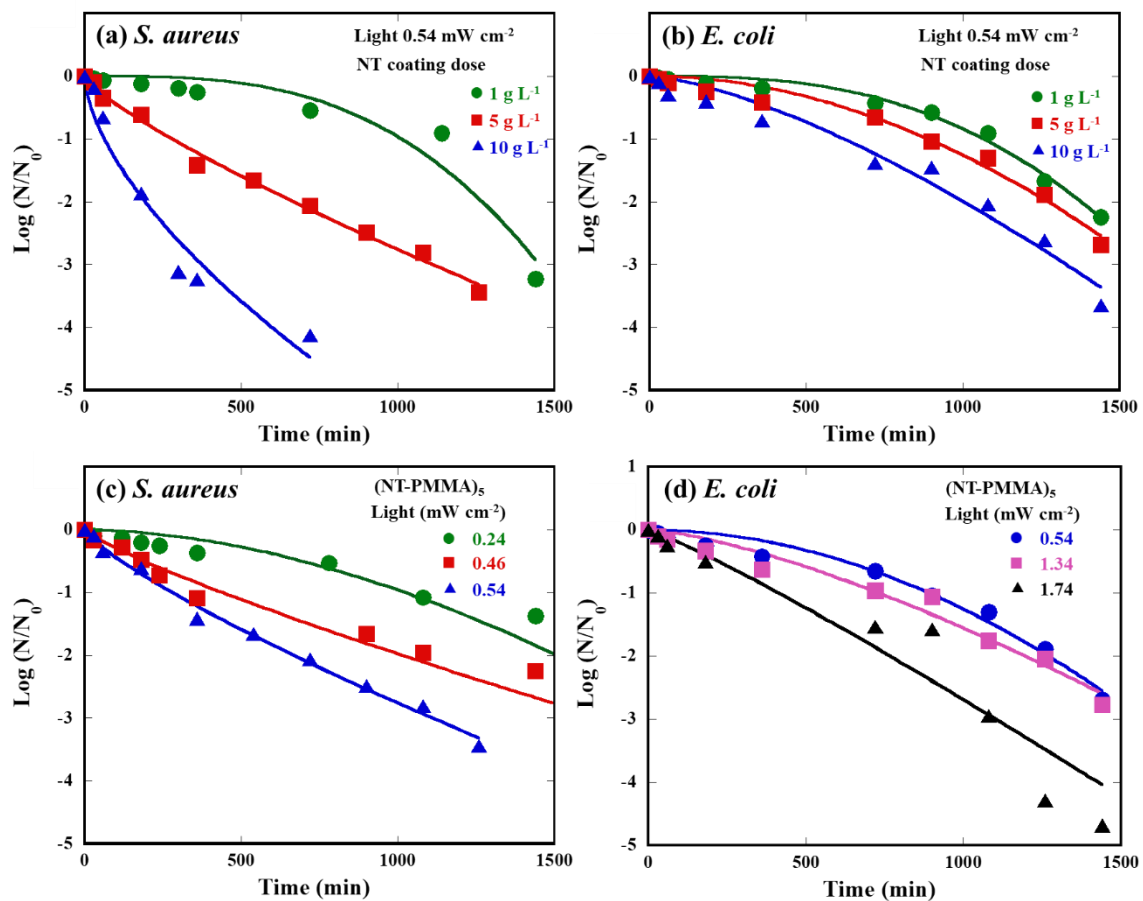
Figure 7-5. The fitting parameters of the MH kinetic model for NT coating concentration effect on PMMA against (a) *S. aureus* and (b) *E. coli*. The fitting parameters of the MH kinetic model for visible light intensity effect on (NT-PMMA)$_5$ against (c) *S. aureus* and (d) *E. coli*. Conditions: [NT] = 1 - 10 g L^{-1}, [bacteria] = 10^5 CFU mL^{-1}, visible light intensity = 0.24 - 1.74 mW cm^{-2}, 25 ± 2 °C.

Table 7-2. MH model fitting parameters for disinfection kinetics of *S. aureus* and *E. coli*.

		S. aureus							*E. coli*				
	g L^{-1}	k_1	k_2	k_3	RMSE	R^2		g L^{-1}	k_1	k_2	k_3	RMSE	R^2
NT coating concentrations, with light intensity of 0.54 mW cm^{-2}	**1**	1821.0	10.37×10^{-5}	3.26	0.24	0.94	**NT coating concentrations, with light intensity of 0.54 mW cm^{-2}**	**1**	1172.0	8.33×10^{-5}	2.85	0.09	0.99
	5	64.6	2.01×10^{-5}	0.80	0.10	0.99		**5**	467.8	5.34×10^{-5}	2.00	0.13	0.98
	10	24.0	9.87×10^{-5}	0.63	0.33	0.95		**10**	417.2	2.63×10^{-5}	1.46	0.21	0.97
	mW cm^{-2}	k_1	k_2	k_3	RMSE	R^2		mW cm^{-2}	k_1	k_2	k_3	RMSE	R^2
Light intensities, with NT coating concentration of 5 g L^{-1}	**0.24**	416.2	3.67×10^{-5}	1.83	0.20	0.94	**Light intensities, with NT coating concentration of 5 g L^{-1}**	**0.54**	467.8	5.34×10^{-5}	2.00	0.13	0.98
	0.46	97.8	0.93×10^{-5}	0.83	0.18	0.95		**1.34**	365.6	2.21×10^{-5}	1.43	0.16	0.97
	0.54	64.6	2.01×10^{-5}	0.80	0.10	0.99		**1.74**	214.4	2.10×10^{-5}	1.13	0.44	0.93

[a] Root mean square error (RMSE)

1 **7.4.7 Biophysical properties of the damaged bacteria**

2   The biophysical properties of the inactivated bacteria on NT-PMMA

3 composite were examined using atomic force microscopy (AFM). The AFM was used to

4 observe cells in real time under hydrated conditions without staining or dehydration. At 0

5 min, *S. aureus* appeared spherical (Fig. 7-6a), and *E. coli* appeared rod-shaped (Fig. 7-

6 6c). After 24 h of contact with NT-PMMA, *S. aureus*'s cell structure decomposed due to

7 ROSs attacks, whereas *E. col*i remained largely intact, consistent with the inactivation

8 performance results shown in Figs. 7-2a and 7-2b. After 24 h, *S. aureus*'s bacterial cell

9 height on NT-PMMA decreased by 42%, from 292.6 ± 27.8 nm to 170.5 ± 39.7 nm, and

10 the surface roughness increased by 91%, from 6.65 ± 2.18 nm to 12.7 ± 3.9 nm.

11 Conversely, the height of *E. coli* experienced a significant reduction of 53%, decreasing

12 from an initial measurement of 187.6 ± 9.9 nm to 89.2 ± 14.3 nm. In parallel, there was a

13 notable 97% increase in surface roughness, rising from 6.35 ± 2.2 nm to 12.5 ± 4.8 nm.

14 These alterations in bacterial height and surface roughness can be ascribed to the

15 oxidative attack from $^1O_2$, $HO^{\bullet}$, and H_2O_2 generated by $(NT\text{-}PMMA)_5$ on the bacterial

16 membranes. This attack leads to the depletion of intracellular components, including the

17 loss of potassium ions (K^+) (Yen et al., 2022) and protein (Liu et al., 2023). As

18 mentioned in section 7.4.4, the major component, LPS, in the cell wall of Gram-negative

19 bacteria plays a major role in reducing the penetration of singlet oxygen. Therefore, the

20 photooxidation reaction of NT-PMMA was predominately driven by $^1O_2$, resulting in

21 more severe damage on gram-positive bacteria than on gram-negative bacteria. The

22 defensive ability of LPS against $^1O_2$ can be observed in the cellular morphology in Figs.

1 7-6b and 7-6d, showing the relatively significant alternation of *S. aureus* and miner

2 impact on *E. coli* after 24 h.
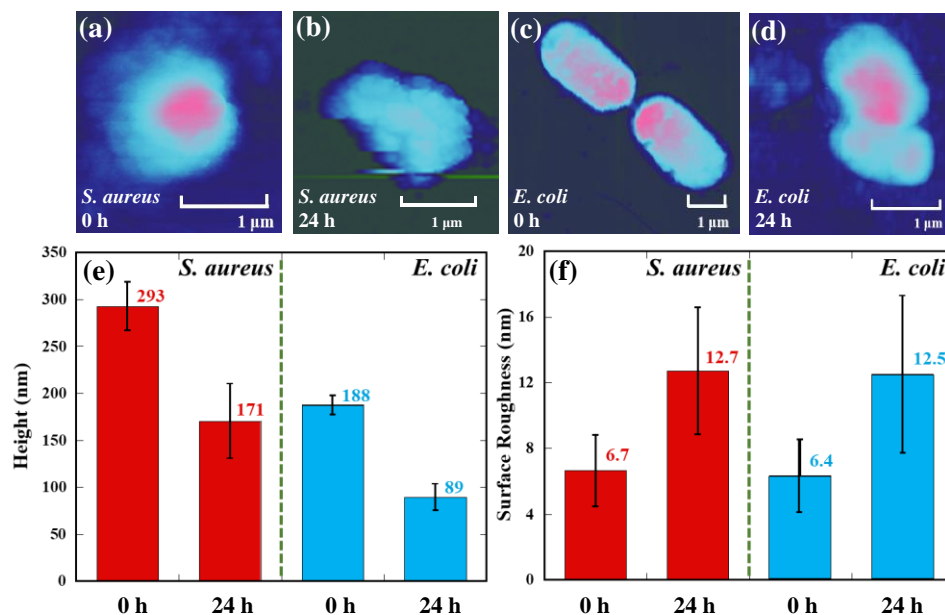
3

4 Figure 7-6. AFM images of *S. aureus* after reacting with NT-PMMA for (a) 0 h, (b) 24 h;

5 *E. coli* after reacting with NT-PMMA for (c) 0 h, (d) 24 h. The (e) bacterial height and (f)

6 surface roughness of *S. aureus* and *E. coli* after reacting with NT-PMMA for 0 h and 24

7 h. Conditions: [NT] = 5 g L^{-1}, [bacteria] = 10^8 CFU mL^{-1}, visible light intensity = 0.54

8 mW cm^{-2}, 25 ± 2 °C.

9 **7.4.8 Photo-inactivation mechanism of NT-PMMA**

10 Fig. 7-7 illustrates the photocatalytic inactivation mechanism of NT-PMMA

11 against *S. aureus* and *E. coli*. The generation of ROSs under visible light irradiation via

12 the route of reaction equations is shown in Eqs. 6-11. These reactions involve photons

13 with a compatible wavelength bombarding the photocatalyst's surface, exciting electrons

14 (e^-) from the valence band to the conduction band (e_{CB}^-) and leaving a positive hole

1 (h_{VB}^+). The electron-hole pair then reacts with a water molecule in the environment, with

2 the positive hole (h_{VB}^+) splitting the water and generating HO$^\bullet$ and hydrogen ions (H$^+$)

3 (Chen et al., 2020; Lin et al., 2015) (Eqs. (7)-(8)). The electron in the conduction band

4 (e_{CB}^-) reacts with oxygen and H$_2$O$_2$, resulting in the formation of a positive hole (h_{aq}^+),

5 ^{1}O$_2$, and HO$^\bullet$ radicals (Eqs. (10)-(11)). As such, ^{1}O$_2$, HO$^\bullet$, and H$_2$O$_2$ play a dominant role

6 in the photo-inactivation mechanism, the same as the findings in Tzeng et al. (2022).

7 Differently, Tzeng et al. (2022) only examined ROSs in the NT suspension system

8 instead of comparing the suspension and immobilization systems. In this work,

9 immobilization of NT on PMMA can substantially minimize the reactant turbidity and

10 exclude particle aggregation, subsequently the light is fully utilized and improving

11 photocatalytic efficiency. The ROSs generated on the (NT-PMMA)$_5$ surface were proved

12 to have a stronger intensity than NT suspension (Figs. 7-2c and 7-2d), which can

13 decompose the target bacteria more efficiently because of the lack of turbidity

14 interference, uniform distribution of NT, and the shorter diffusion distance for ROSs

15 directly reacting with the bacteria.

16 $\text{NT-PMMA} + hv \rightarrow e_{CB}^- + h_{VB}^+$ (6)

17 $h_{VB}^+ + 2\text{H}_2\text{O} \rightarrow \text{H}_2\text{O}_2 + 2\text{H}^+$ (7)

18 $h_{VB}^+ + \text{H}_2\text{O} \rightarrow \text{HO}^\bullet + \text{H}^+$ (8)

19 $2\,\text{HO}^\bullet \rightarrow \text{H}_2\text{O}_2$ (9)

20 $e_{CB}^- + \text{O}_2 \rightarrow h_{aq}^+ + {}^1\text{O}_2$ (10)

21 $e_{CB}^- + \text{H}_2\text{O}_2 \rightarrow \text{HO}^\bullet + \text{OH}^-$ (11)
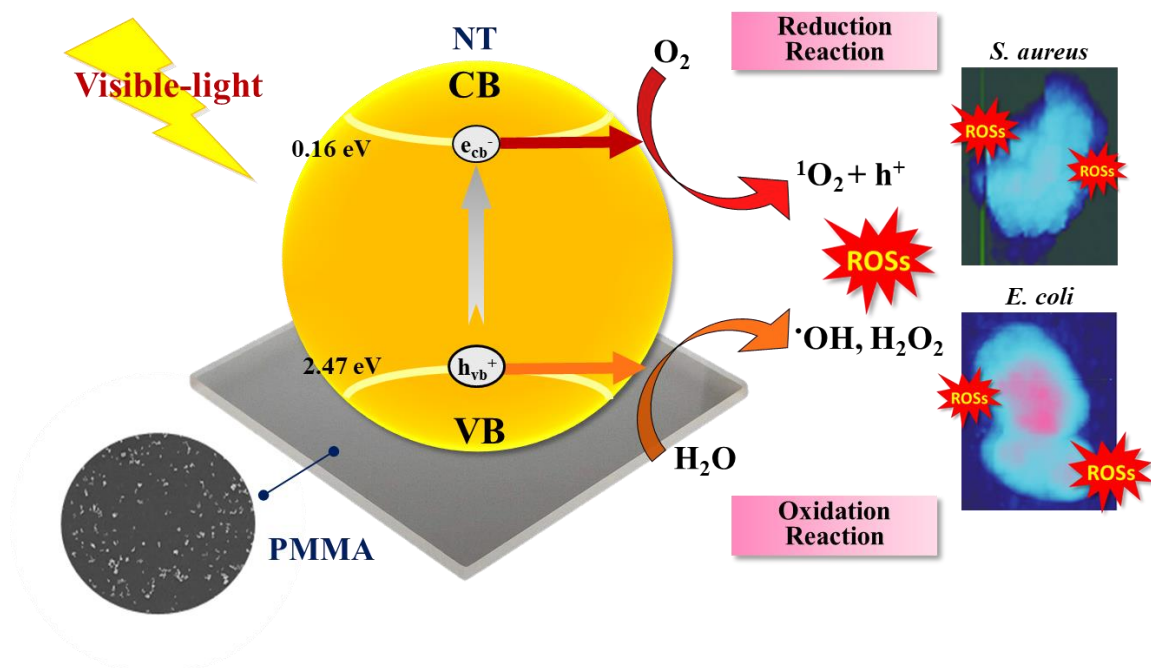
1

2 Figure 7-7. Proposed photo-inactivation mechanism of NT-PMMA against *S. aureus*

3 (Gram-positive bacteria) and *E. coli* (Gram-negative bacteria).

4 **7.5 Conclusions**

5 This study demonstrated that NT-PMMA could effectively eliminate both *S.*

6 *aureus* and *E. coli* bacteria under visible light irradiation. The transmittance of the (NT-

7 PMMA)$_5$ remained high at 92%, even when equipped with a self-inactivation film,

8 suggesting that it is a promising alternative to glass. The inactivation efficiency of (NT-

9 PMMA)$_5$ against *S. aureus* and *E. coli* reached 99.9% within 24 h under various visible

10 light intensities. NT-PMMA showed higher intensities of $^1O_2$, HO$^\bullet$, and higher

11 concentration of H_2O_2 than NT suspension, implying the greater inactivation efficiency of

12 immobilized NT on PMMA than in NT-suspension. The immobilization approach

13 enhanced the inactivation performances of NT-PMMA, making it superior to NT

14 suspension due to the absence of turbidity interference and the uniform distribution of

1   NT. Remarkably, NT-PMMA sustained a 99.99% inactivation rate against *S. aureus* over

2   five cycles of photooxidation due to cell disruption induced by $^1O_2$, $HO^•$, and H_2O_2

3   attacks. Thus, the above results indicate that the inactivation efficiency of NT-PMMA has

4   been substantially improved by immobilization and has a potential for bacterial

5   inactivation. Future research will further explore the structural characterization of NT-

6   PMMA after repeated use, investigate the presence of bacterial biofilm residues on its

7   surface, and assess their impact on disinfection efficiency.

7.6 References

1. Ananpattarachai, J., Boonto, Y., & Kajitvichyanukul, P. (2016). Visible light photocatalytic antibacterial activity of Ni-doped and N-doped TiO_2 on *Staphylococcus aureus* and *Escherichia coli* bacteria. *Environmental Science and Pollution Research*, *23*(5), 4111-4119. DOI: 10.1007/s11356-015-4775-1

2. Cantarella, M., Sanz, R., Buccheri, M. A., Ruffino, F., Rappazzo, G., Scalese, S., Impellizzeri, G., Romano, L., & Privitera, V. (2016). Immobilization of nanomaterials in PMMA composites for photocatalytic removal of dyes, phenols and bacteria from water. *Journal of Photochemistry and Photobiology a-Chemistry*, *321*, 1-11. DOI: 10.1016/j.jphotochem.2016.01.020

3. Chen, D., Cheng, Y., Zhou, N., Chen, P., Wang, Y., Li, K., Huo, S., Cheng, P., Peng, P., Zhang, R., Wang, L., Liu, H., Liu, Y., & Ruan, R. (2020). Photocatalytic degradation of organic pollutants using TiO_2-based photocatalysts: A review. *Journal of Cleaner Production*, *268*, 121725. DOI: 10.1016/j.jclepro.2020.121725

4. Diesen, V., & Jonsson, M. (2014). Formation of H_2O_2 in TiO_2 photocatalysis of oxygenated and deoxygenated aqueous systems: A probe for photocatalytically produced hydroxyl radicals. *The Journal of Physical Chemistry C*, *118*(19), 10083-10087. DOI: 10.1021/jp500315u

5. El-Newehy, M. H., Kim, H. Y., Khattab, T. A., & El-Naggar, M. E. (2022). Production of photoluminescent transparent poly(methyl methacrylate) for smart windows. *Luminescence*, *37*(1), 97-107. DOI: 10.1002/bio.4150

6. Ganguly, P., Byrne, C., Breen, A., & Pillai, S. C. (2018). Antimicrobial activity of photocatalysts: Fundamentals, mechanisms, kinetics and recent advances. *Applied Catalysis B-Environmental*, *225*, 51-75. DOI: 10.1016/j.apcatb.2017.11.018

7. Girasole, M., Pompeo, G., Cricenti, A., Congiu-Castellano, A., Andreola, F., Serafino, A., Frazer, B. H., Boumis, G., & Amiconi, G. (2007). Roughness of the plasma membrane as an independent morphological parameter to study RBCs: A quantitative atomic force microscopy investigation. *Biochimica et Biophysica Acta (BBA) - Biomembranes*, *1768*(5), 1268-1276. DOI: 10.1016/j.bbamem.2007.01.014

8. Goutham, R., Badri Narayan, R., Srikanth, B., & Gopinath, K. P. (2019). Supporting materials for immobilisation of nano-photocatalysts. In Inamuddin, G. Sharma, A. Kumar, E. Lichtfouse, & A. M. Asiri (Eds.), *Nanophotocatalysis and Environmental Applications : Materials and Technology* (pp. 49-82). Springer International Publishing. DOI: 10.1007/978-3-030-10609-6_2

9. Hao, B., Guo, J., Zhang, L., & Ma, H. (2022). Cr-doped TiO2/CuO photocatalytic nanofilms prepared by magnetron sputtering for wastewater treatment. *Ceramics International*, *48*(5), 7106-7116. DOI: 10.1016/j.ceramint.2021.11.270

10. Huang, S.-M., Weng, C.-H., Tzeng, J.-H., Huang, Y.-Z., Anotai, J., Yen, L.-T., Chang, C.-J., & Lin, Y.-T. (2019). Kinetic study and performance comparison of TiO_2-mediated visible-light-responsive photocatalysts for the inactivation of

Aspergillus niger. *Science of the Total Environment*, *692*. DOI: 10.1016/j.scitotenv.2019.07.329

11. Huang, S. M., Weng, C. H., Tzeng, J. H., Huang, Y. Z., Anotai, J., Yen, L. T., Chang, C. J., & Lin, Y. T. (2020). Photocatalytic inactivation of *Klebsiella pneumoniae* by visible-light-responsive N/C-doped and N-tourmaline/palladium-C-codoped TiO_2. *Chemical Engineering Journal*, *379*, 122345. DOI: 10.1016/j.cej.2019.122345

12. Joost, U., Juganson, K., Visnapuu, M., Mortimer, M., Kahru, A., Nommiste, E., Joost, U., Kisand, V., & Ivask, A. (2015). Photocatalytic antibacterial activity of nano-TiO_2 (anatase)-based thin films: Effects on *Escherichia coli* cells and fatty acids. *Journal of Photochemistry and Photobiology B-Biology*, *142*, 178-185. DOI: 10.1016/j.jphotobiol.2014.12.010

13. Khaled, S. M., Sui, R., Charpentier, P. A., & Rizkalla, A. S. (2007). Synthesis of TiO_2−PMMA nanocomposite: using methacrylic acid as a coupling agent. *Langmuir*, *23*(7), 3988-3995. DOI: 10.1021/la062879n

14. Kim, H.-S., Cha, E. J., Kang, H.-J., Park, J.-H., Lee, J., & Park, H.-D. (2019). Antibacterial application of covalently immobilized photosensitizers on a surface. *Environmental Research*, *172*, 34-42. DOI: 10.1016/j.envres.2019.01.002

15. Lin, Y.-H., Weng, C.-H., Srivastav, A. L., Lin, Y.-T., & Tzeng, J.-H. (2015). Facile synthesis and characterization of N-doped TiO_2 photocatalyst and its visible-light activity for photo-oxidation of ethylene. *Journal of Nanomaterials*, 807394. DOI: 10.1155/2015/807394

16. Liu, C., He, D., Yang, H., Zhang, K., Zhou, X., Zhang, T., & Qu, J. (2023). Selective generation of H_2O_2 by Cu-modified graphitic carbon nitride for rapid water disinfection via intracellular Fenton reaction. *Chemical Engineering Journal*, *477*, 146835. DOI: 10.1016/j.cej.2023.146835

17. Makropoulou, T., Panagiotopoulou, P., & Venieri, D. (2018). N-doped TiO2 photocatalysts for bacterial inactivation in water. *Journal of Chemical Technology & Biotechnology*, *93*(9), 2518-2526. DOI: 10.1002/jctb.5639

18. Meznaric, S., Badovinac, I. J., Saric, I., Peter, R., Markovic, M. K., Ambrozic, G., & Gobin, I. (2022). Superior UVA-photocatalytic antibacterial activity of a double-layer ZnO/Al_2O_3 thin film grown on cellulose by atomic layer deposition (ALD). *Journal of Environmental Chemical Engineering*, *10*(3), 108095. DOI: 10.1016/j.jece.2022.108095

19. Ounas, O., El Foulani, A. A., Lekhlif, B., & Jamal-Eddine, J. (2020). Immobilization of TiO_2 into a poly methyl methacrylate (PMMA) as hybrid film for photocatalytic degradation of methylene blue. *Materials Today: Proceedings*, *22*, 35-40. DOI: 10.1016/j.matpr.2019.08.068

20. Ozkal, C. B. (2022). Synthesis of $CuFe_2O_4$-Ti and $CuFe_2O_4$-Ti-GO nanocomposite photocatalysts using green-synthesized CuFe2O4: determination of photocatalytic activity, bacteria inactivation and antibiotic degradation potentials under visible

light. *Journal of Chemical Technology and Biotechnology*, *97*(7), 1842-1859. DOI: 10.1002/jctb.7058

21. Pascagaza-Rubio, H. D., Godbout, S., Palacios, J. H., Cinq-Mars, D., Côté, C., Rousseau, A. N., & Fournel, S. (2022). Disinfection of outdoor livestock water troughs: Effect of TiO$_2$-based coatings and UV-A LED. *Water*, *14*(23), 3808. DOI: 10.3390/w14233808

22. Peng, X., Lv, Y., & Zhao, S. (2022). Chemical vapor deposition and thermal oxidation of cuprous phosphide nanofilm. *Coatings*, *12*(1), 68. DOI: 10.3390/coatings12010068

23. Tangudom, P., Wimolmala, E., Prapagdee, B., & Sombatsompop, N. (2018). Material formulations for AR/PMMA and AR-TiO$_2$/PMMA blends and effects of UV radiation and TiO$_2$ loading on mechanical and antibacterial performances. *Polymer-Plastics Technology and Engineering*, *57*, 1963 - 1976. DOI: 10.1080/03602559.2018.1447131

24. Terra, J. C. S., Desgranges, A., Amara, Z., & Moores, A. (2023). Photocatalysis on magnetic supports for singlet oxygen generation: Role of immobilization and photobleaching. *Catalysis Today*, *407*, 52-58. DOI: 10.1016/j.cattod.2022.05.042

25. Tzeng, J.-H., Weng, C.-H., Chang, C.-J., Yen, L.-T., de Luna, M. D. G., Huang, J.-W., & Lin, Y.-T. (2022). N-Schorl TiO$_2$ nanocomposite for visible-light photocatalysis deactivation yeast exemplified by Candida albicans. *Chemical Engineering Journal*, *435*, 134294. DOI: 10.1016/j.cej.2021.134294

26. Tzeng, J.-H., Weng, C.-H., Wang, C.-C., Ho, M.-S., Yen, L.-T., Chen, J.-Y., Gaybullaev, G., Poonpakdee, C., & Lin, Y.-T. (2020). A solution of identifying biophysical properties and 3D cellular structure of visible-light-driven photocatalytic inactivated Staphylococcus aureus. *Chemical Engineering Journal*, 127880. DOI: 10.1016/j.cej.2020.127880

27. Tzeng, J.-H., Weng, C.-H., Yen, L.-T., Gaybullaev, G., Chang, C.-J., de Luna, M. D. G., & Lin, Y.-T. (2021). Inactivation of pathogens by visible light photocatalysis with nitrogen-doped TiO$_2$ and tourmaline-nitrogen co-doped TiO$_2$. *Separation and Purification Technology*, *274*, 118979. DOI: 10.1016/j.seppur.2021.118979

28. Valduga, G., Bertoloni, G., Reddi, E., & Jori, G. (1993). Effect of extracellularly generated singlet oxygen on Gram-positive and Gram-negative bacteria. *Journal of Photochemistry and Photobiology B: Biology*, *21*(1), 81-86. DOI: 10.1016/1011-1344(93)80168-9

29. Varnagiris, S., Urbonavicius, M., Sakalauskaite, S., Demikyte, E., Tuckute, S., & Lelis, M. (2021). Photocatalytic inactivation of Salmonella typhimurium by floating carbon-doped TiO$_2$ photocatalyst. *Materials*, *14*(19), 5681. DOI: 10.3390/ma14195681

30. Wang, M., Xu, Z., Qi, Z., Cai, Y., Li, G., Choi, W., & An, T. (2023). Repeated photocatalytic inactivation of E. coli by UV + Ni foam@TiO$_2$: Performance and photocatalyst deactivation. *Chemical Engineering Journal*, *468*, 143680. DOI: 10.1016/j.cej.2023.143680

31. Wood, D., Shaw, S., Cawte, T., Shanen, E., & Van Heyst, B. (2020). An overview of photocatalyst immobilization methods for air pollution remediation. *Chemical Engineering Journal*, *391*, 123490. DOI: 10.1016/j.cej.2019.123490

32. Wu, T.-T., Guo, S., Li, B., Li, J.-Y., Zhang, H.-S., Ma, P.-Z., Zhang, X., Shen, C.-Y., Liu, X.-H., & Cao, A.-M. (2022). Facile construction of nanofilms from a dip-coating process to enable high-performance solid-state batteries. *ACS Applied Materials & Interfaces*, *14*(28), 32026-32034. DOI: 10.1021/acsami.2c07292

33. Ye, L. Q., Chen, J. N., Tian, L. H., Liu, J. Y., Peng, T. Y., Deng, K. J., & Zan, L. (2013). BiOI thin film via chemical vapor transport: Photocatalytic activity, durability, selectivity and mechanism. *Applied Catalysis B-Environmental*, *130*, 1-7. DOI: 10.1016/j.apcatb.2012.10.011

34. Yemmireddy, V. K., & Hung, Y. C. (2015). Effect of food processing organic matter on photocatalytic bactericidal activity of titanium dioxide (TiO_2). *International Journal of Food Microbiology*, *204*, 75-80. DOI: 10.1016/j.ijfoodmicro.2015.03.019

35. Yen, L.-T., Weng, C.-H., Than, N. A. T., Tzeng, J.-H., Jacobson, A. R., Iamsaard, K., Dang, V. D., & Lin, Y.-T. (2022). Mode of inactivation of *Staphylococcus aureus* and *Escherichia coli* by heated oyster-shell powder. *Chemical Engineering Journal*, *432*, 134386. DOI: 10.1016/j.cej.2021.134386

36. Zhang, L. X., Rao, L., Wang, P. F., & Shi, Z. Y. (2023). Durable, strong, and flexible superhydrophobic N-TiO_2 silicone composite aerogels with unique air-liquid-solid triphase photocatalytic properties. *Applied Surface Science*, *609*, Article 155348. DOI: 10.1016/j.apsusc.2022.155348

CHAPTER 8

CONCLUSIONS

MetaVT has been historically applied to plants in calcareous soil to mitigate Fe chlorosis, although past studies have reported its extremely low solubility in electrolyte solutions. This study expands on previous research by evaluating the effectiveness of nano-metaVT and nano-CT-metaVT under various conditions, as detailed across three chapters. In Chapter 2, results show that nano-CT-metaVT-KCl has a lower total soluble iron (Fe) concentration than nano-metaVT-KCl, attributed to the slow-release properties of the CT coating. Conversely, in SPE suspensions, nano-CT-metaVT exhibits higher total soluble Fe than nano-metaVT, contradicting findings from previous research. Additionally, inoculation with *Pp* Pf-5 enhances total soluble Fe concentrations and lowers pH in both nano-metaVT-SPE and nano-CT-metaVT-SPE compared to treatments without microbes, highlighting the influential role of soil microbes. However, the total soluble Fe concentrations in both nano formulations in SPE are still lower than those observed in KCl suspensions, highlighting factors such as CT coating, microbial inoculation, and the presence of organic/inorganic ligands that affect solubility.

In Chapter 3, the study explores the performance of these nano-formulations with winter wheat grown in silica sand amended with a modified ½HS (pH 8.4). Although results are inconclusive within a 14-day growth period, *Pp* Pf-5 inoculation appears to mitigate salinity stress by increasing plant transpiration rates, without interference from nano-metaVT or nano-CT-metaVT on root colonization. Chapter 4 extends this investigation to wheat and beans grown in calcareous and salt-affected soils. Here, nano-CT-metaVT treatments significantly enhance bean root dry mass, and nano-metaVT

1 treatments improve chlorophyll content within a 28-day growth period. After 50 days,

2 both treatments led to an increase in the number of flowers and buds in beans compared

3 to controls, demonstrating their potential to enhance growth and productivity.

4 Furthermore, these nano-fertilizers exhibit lower environmental impacts by minimizing

5 Fe leaching, confirming their stability and reduced environmental footprint. Overall, the

6 effectiveness of nano-metaVT and nano-CT-metaVT is influenced by various factors,

7 including plant type, growth conditions, the presence of abiotic stresses, and the time

8 necessary for mineral weathering, which provide insight to research further investigating

9 the mechanism in agricultural settings in the future.

10 Chapters 7 and 8 examine the disinfection efficiency of HOS and NT-PMMA.

11 The research findings from Chapter 6 indicate that cell permeability plays a pivotal role

12 in the HOS disinfection process. The structural differences in cell walls lead to varying

13 levels of permeability damage between *S. aureus* and *E. coli*. Additionally, the analysis

14 revealed that singlet oxygen is a critical component in the disinfection mechanism

15 induced by HOS treatment. In Chapter 7, immobilization proved to enhance the

16 antibacterial activity of NT-PMMA, making it more effective than NT suspension. This

17 high level of bacterial inactivation was achieved through cellular disruption caused by

18 attacks from ROSs such as $^1O_2$, $HO^{\bullet}$, and H_2O_2. Consequently, these results indicate that

19 the inactivation efficiency of NT-PMMA has been significantly improved through

20 immobilization, indicating the potential for effective bacterial inactivation in various

21 applications.

22

1   Lastly, Chapters 7 and 8 assess the disinfection efficiency of heated oyster shells

2   (HOS) and nitrogen-doped titanium dioxide-coated polymethyl methacrylate (NT-

3   PMMA). The findings in Chapter 6 provide evidence that cell permeability is crucial in

4   the HOS disinfection process and that cell wall structure results in different levels of cell

5   permeability damage between *S. aureus* and *E. coli*. Furthermore, analysis of the ROS

6   induced by HOS treatment revealed that singlet oxygen plays an essential role in the

7   disinfection mechanism. In Chapter 7, the immobilization approach enhanced the

8   inactivation performances of NT-PMMA, making it superior to NT suspension due to the

9   absence of turbidity interference and the uniform distribution of NT. Remarkably, NT-

10   PMMA sustained a 99.99% inactivation rate against *S. aureus* over five cycles of

11   photooxidation due to cell disruption induced by $^1O_2$, $HO^{\bullet}$, and H_2O_2 attacks. Thus, the

12   above results indicate that the inactivation efficiency of NT-PMMA has been

13   substantially improved by immobilization and has a potential for bacterial inactivation.

14

1

2

3

4

5

6

7

8

9

10   APPENDICES

1   **Appendix A. Copyrights**

2

3   Figure A-1. Copyright clearance for the published article in Chapter 6.

Figure A-2. Copyright clearance for the published article in Chapter 7.

1 **Appendix B. Supplemental information**

2 **B.1 Supplemental information for Chapter 1**
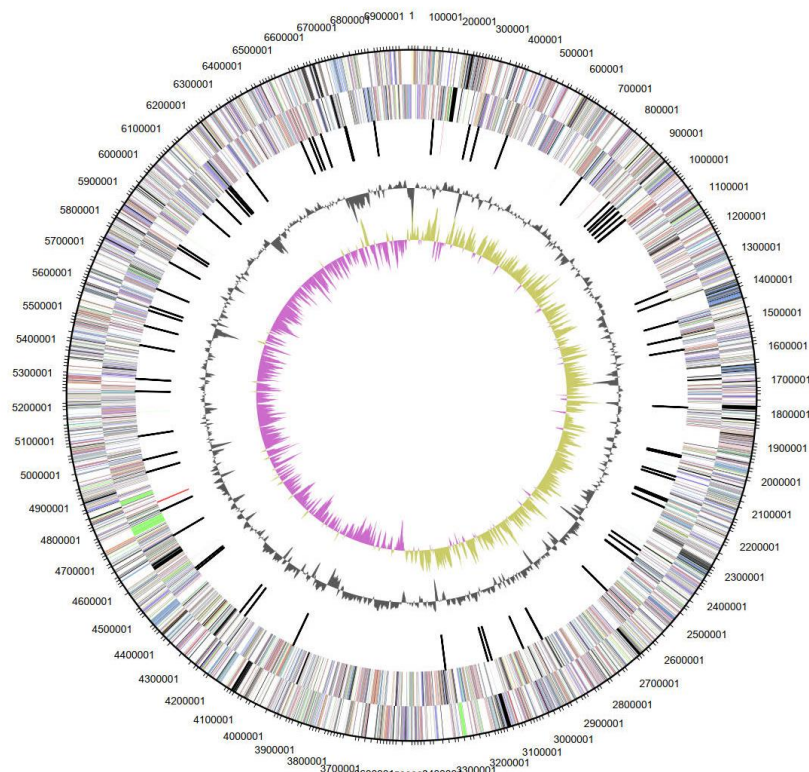
3

4 Figure B1-1. Graphical map of the *Pseudomonas chlororaphis* O6 (*Pc*O6) genome. From

5 the outside to the center: Genes on forward strand and Genes on reverse strand (color by

6 Clusters of Orthologous Group (COG) categories), RNA genes (tRNAs green, rRNAs

7 red, other RNAs black), guanine-cytosine (GC) content, GC skew. Data are obtained

8 from the National Center for Biotechnology Information's Entrez database and the

9 EzGenome database.
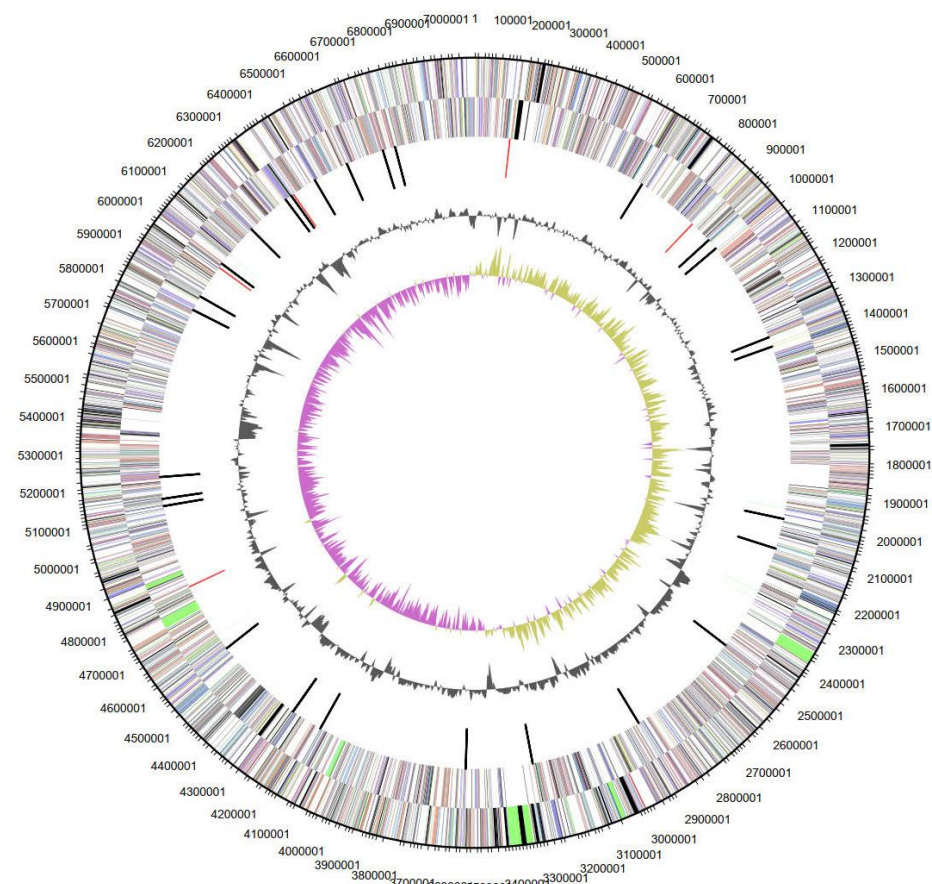
1

2　Figure B1-2. Graphical map of the *Pseudomonas protegens* Pf-5 (*Pp* Pf-5) genome. From

3　the outside to the center: Genes on forward strand and Genes on reverse strand (color by

4　Clusters of Orthologous Group (COG) categories), RNA genes (tRNAs green, rRNAs

5　red, other RNAs black), guanine-cytosine (GC) content, GC skew. Data are obtained

6　from the National Center for Biotechnology Information's Entrez database and the

7　EzGenome database.

8

1   **B.2 Supplemental information for Chapter 2**

2   Table B2-1. Total soluble elemental analysis of various KCl suspensions after 7 days.

	Day 7	
Total soluble elements	metaVT-KCl	CT-metaVT- KCl
Al (μg L^{-1})	5.36 ± 1.51	4.22 ± 3.02
As (μg L^{-1})	<DL	<DL
Ba (μg L^{-1})	0.25 ± 0.14	<DL
Ca (mg L^{-1})	0.10 ± 0.02	0.10 ± 0.03
Cd (μg L^{-1})	<DL	<DL
Co (μg L^{-1})	0.16 ± 0.07	0.18 ± 0.04
Cr (μg L^{-1})	0.04 ± 0.04	0.07 ± 0.06
Cu (μg L^{-1})	0.28 ± 0.16	0.29 ± 0.14
Fe (μg L^{-1})	1147 ± 103	654 ± 88
K (mg L^{-1})	137.9 ± 6.5	134.5 ± 7.5
Mg (mg L^{-1})	0.02 ± 0.01	0.02 ± 0.01
Mn (μg L^{-1})	21.6 ± 2.5	29.0 ± 3.2
Na (mg L^{-1})	0.22 ± 0.01	0.18 ± 0.04
Ni (μg L^{-1})	0.32 ± 0.39	0.25 ± 0.08
P (μg L^{-1})	630 ± 49	699 ± 55
Pb (μg L^{-1})	<DL	<DL
Sb (μg L^{-1})	0.6 ± 0.3	0.5 ± 0.2
Si (mg L^{-1})	0.27 ± 0.02	0.24 ± 0.01
Sr (μg L^{-1})	0.6 ± 0.3	0.5 ± 0.1
Tl (μg L^{-1})	0.016 ± 0.013	0.008 ± 0.002
V (μg L^{-1})	< DL	< DL
Zn (μg L^{-1})	11.8 ± 3.7	10.7 ± 2.1

3   < DL: lower than the detection limit
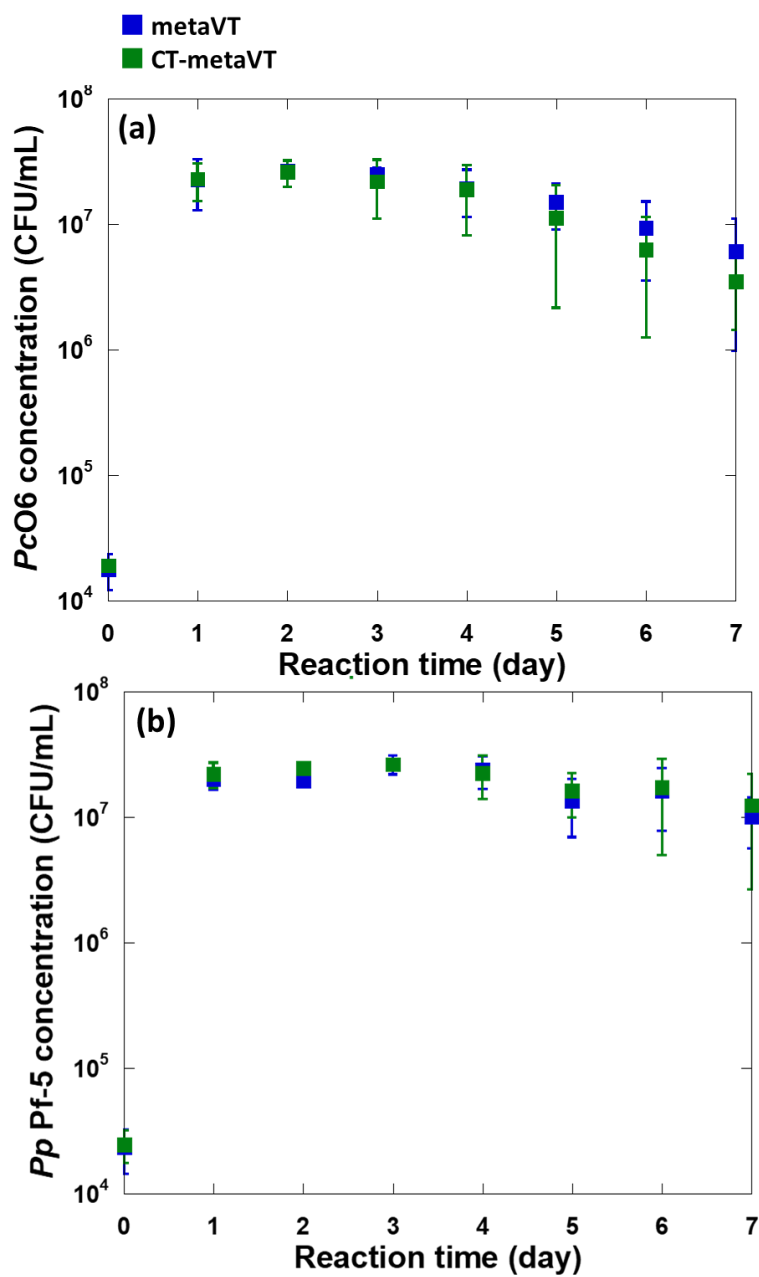
Figure B2-1. *Pc*O6 (a) and *Pp* Pf-5 (b) concentrations (CFU mL^{-1}) in nano-metaVT-SPE

and nano-CT-metaVT-SPE suspensions.

B.3 Supplemental information for Chapter 3

Table B3-1. Composition of the modified half-strength Hoagland solution.

Component		Final Concentration
Potassium nitrate	KNO_3	0.2525 g/L
Calcium nitrate	$Ca(NO_3)_2 \cdot 4H_2O$	0.59 g/L
Magnesium sulfate	$MgSO_4 \cdot 7H_2O$	0.2465 g/L
Ammonium nitrate	NH_4NO_3	0.04 g/L
Monopotassium phosphate	KH_2PO_4	0.034 g/L
Boric acid	H_3BO_3	0.00143 g/L
Manganese chloride	$MnCl_2 \cdot 4H_2O$	0.000905 g/L
Zinc sulfate	$ZnSO_4 \cdot 7H_2O$	0.00011 g/L
Copper sulfate	$CuSO_4 \cdot 5H_2O$	0.0000255 g/L
Sodium molybdate	$Na_2MoO_4 \cdot 2H_2O$	0.00006 g/L
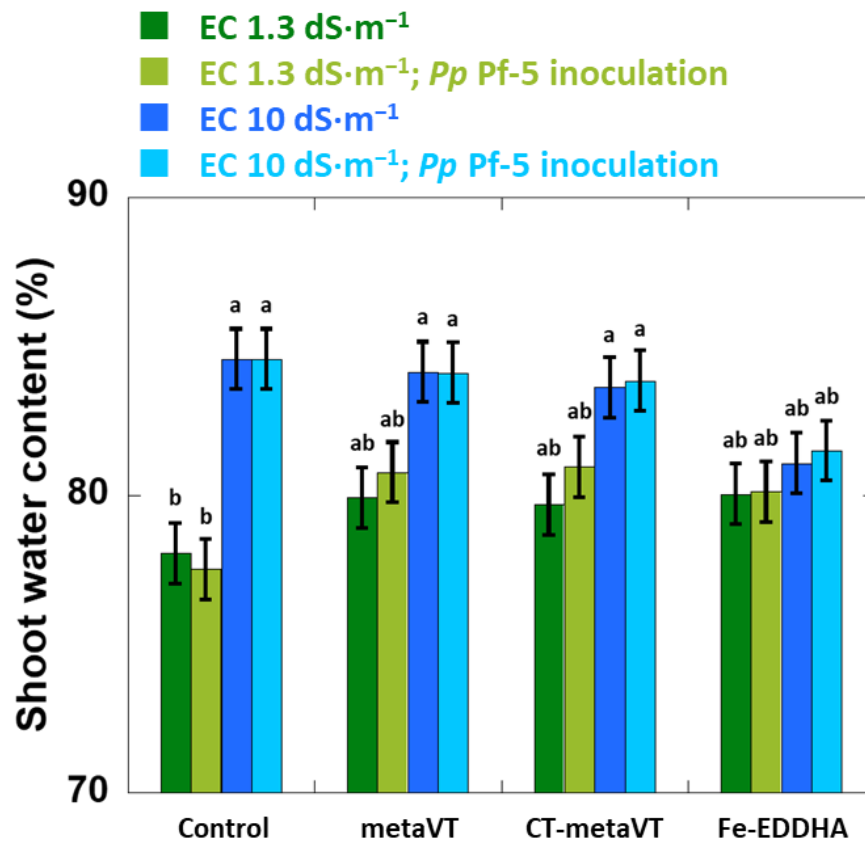
Figure B3-1. The shoot water content (%) wheat grown in the sand with the four Fe

treatments (control, nano-metaVT, nano-CT-metaVT, and Fe-EDDHA) without salinity

stress and under salinity stress. A three-way ANOVA was performed. Different letters

above columns represent significant differences between treatments based on the Tukey-

Kramer test ($\alpha \le 0.05$). Error bars represent the standard error calculated with the

statistical mix model.
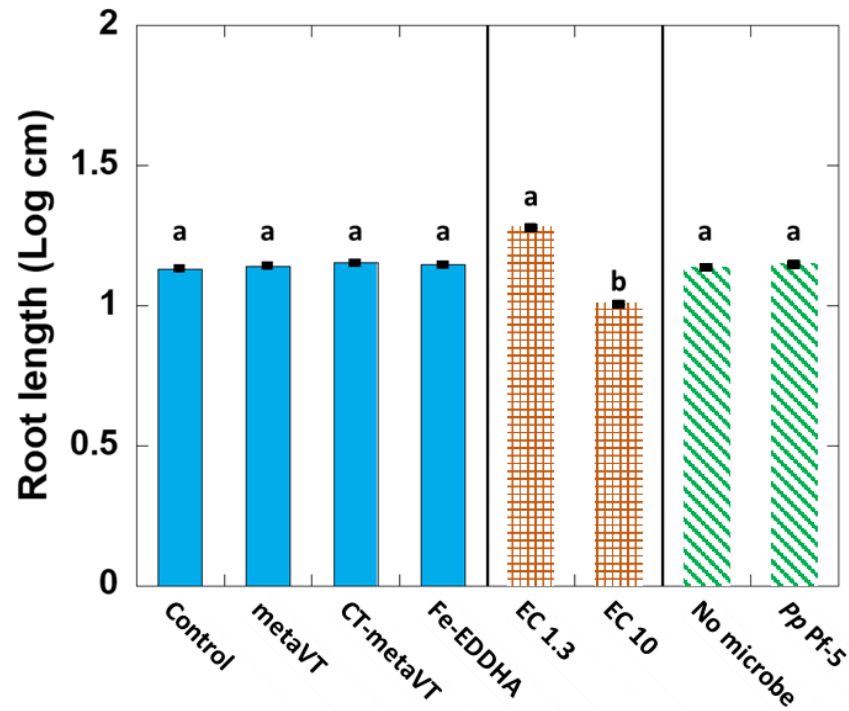
Figure B3-2. The root length of wheat grown in the sand with the four Fe treatments

(control, nano-metaVT, nano-CT-metaVT, and Fe-EDDHA) without salinity stress and

under salinity stress. A three-way ANOVA was performed. Different letters above

columns represent significant differences between treatments based on the Tukey-Kramer

test ($\alpha \leq 0.05$). Error bars represent the standard error calculated with the statistical mix

model.
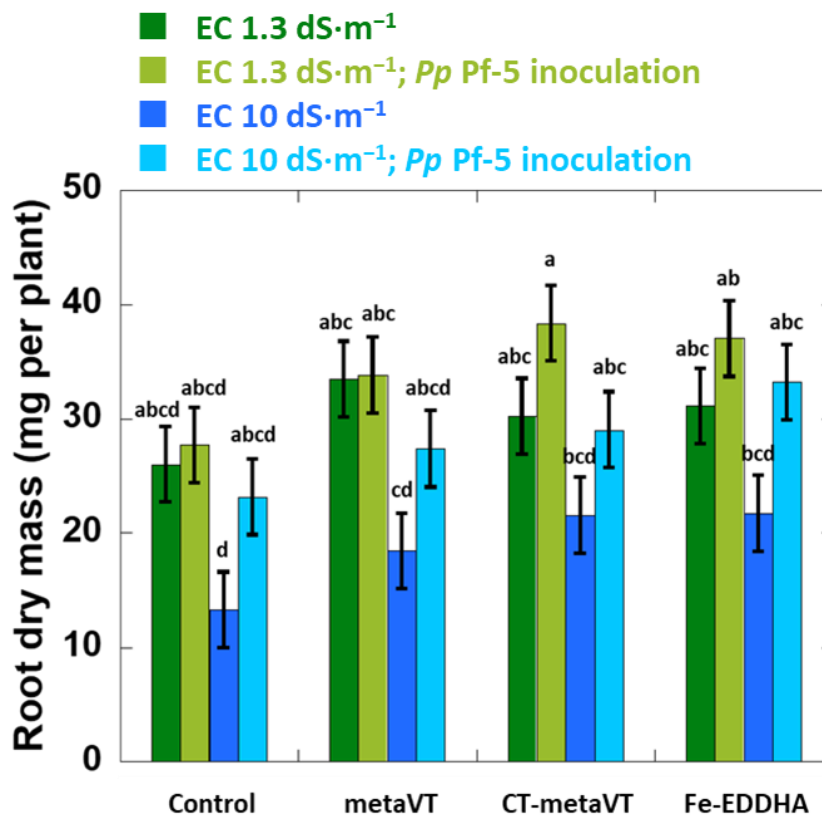
Figure B3-3. The root dry mass of wheat grown in the sand with the four Fe treatments (control, nano-metaVT, nano-CT-metaVT, and Fe-EDDHA) without salinity stress and under salinity stress. A three-way ANOVA was performed. Different letters above columns represent significant differences between treatments based on the Tukey-Kramer test ($\alpha \leq 0.05$). Error bars represent the standard error calculated with the statistical mix model.
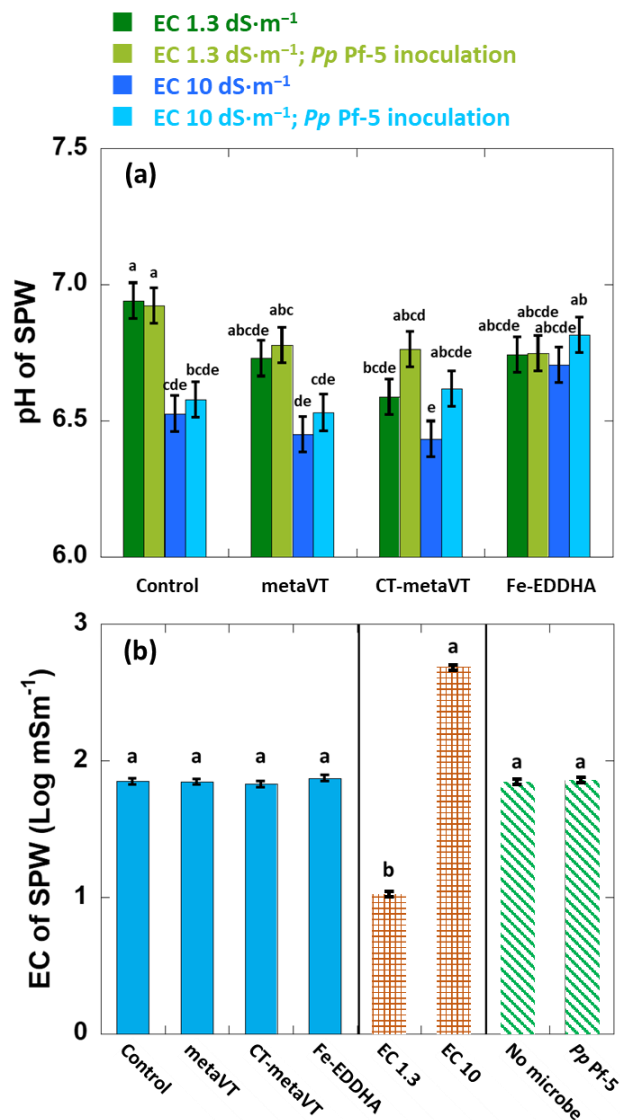
Figure B3-4. The pH (a) and EC (b) of sand pore water (SPW) after wheat grown in the sand with the four Fe treatments (control, nano-metaVT, nano-CT-metaVT, and Fe-EDDHA) without salinity stress and under salinity stress. A three-way ANOVA was performed. Different letters above columns represent significant differences between treatments based on the Tukey-Kramer test ($\alpha \leq 0.05$). Error bars represent the standard error calculated with the statistical mix model.
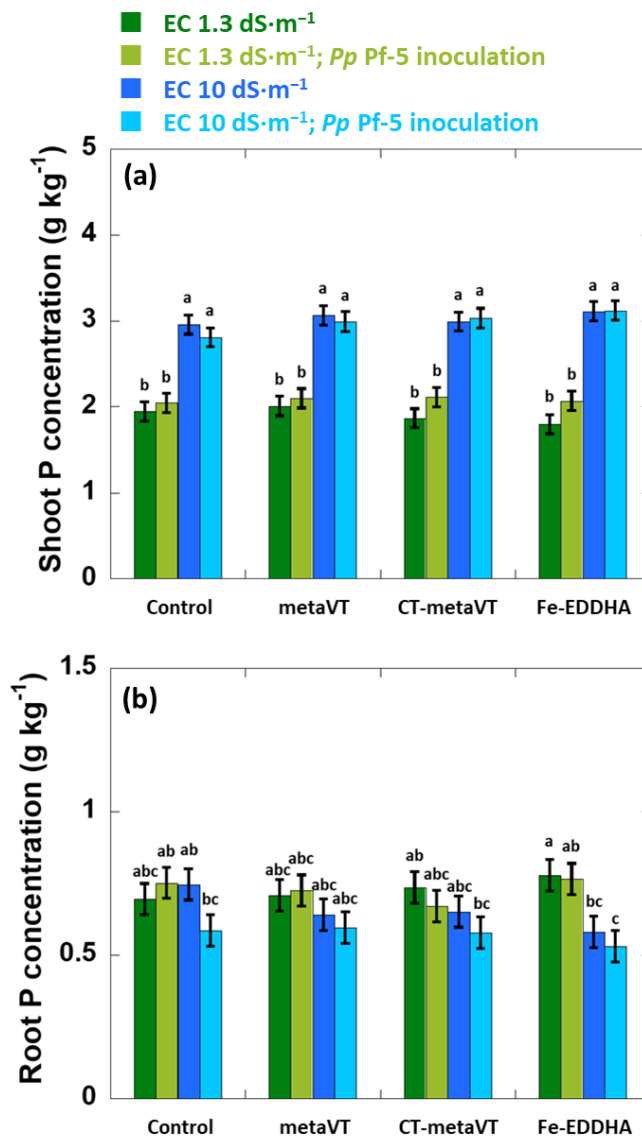
Figure B3-5. The shoot P (a) and root P (b) concentrations of wheat grown in the sand with the four Fe treatments (control, nano-metaVT, nano-CT-metaVT, and Fe-EDDHA) without salinity stress and under salinity stress. A three-way ANOVA was performed. Different letters above columns represent significant differences between treatments based on the Tukey-Kramer test ($\alpha \leq 0.05$). Error bars represent the standard error calculated with the statistical mix model.
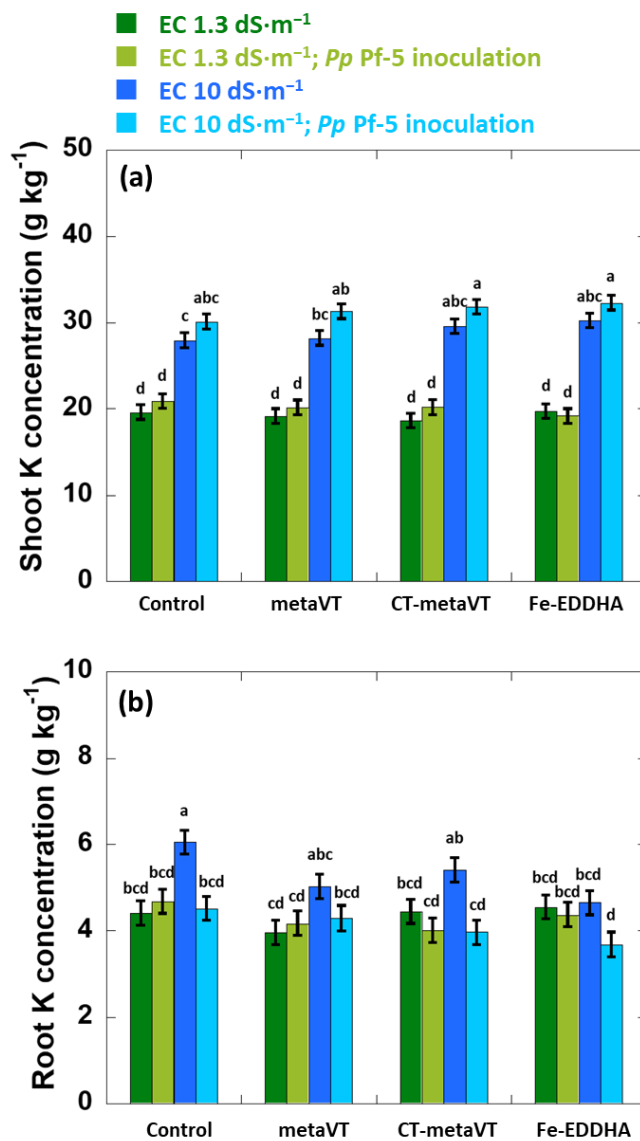
Figure B3-6. The shoot K (a) and root K (b) concentrations of wheat grown in the sand with the four Fe treatments (control, nano-metaVT, nano-CT-metaVT, and Fe-EDDHA) without salinity stress and under salinity stress. A three-way ANOVA was performed. Different letters above columns represent significant differences between treatments based on the Tukey-Kramer test ($\alpha \leq 0.05$). Error bars represent the standard error calculated with the statistical mix model.
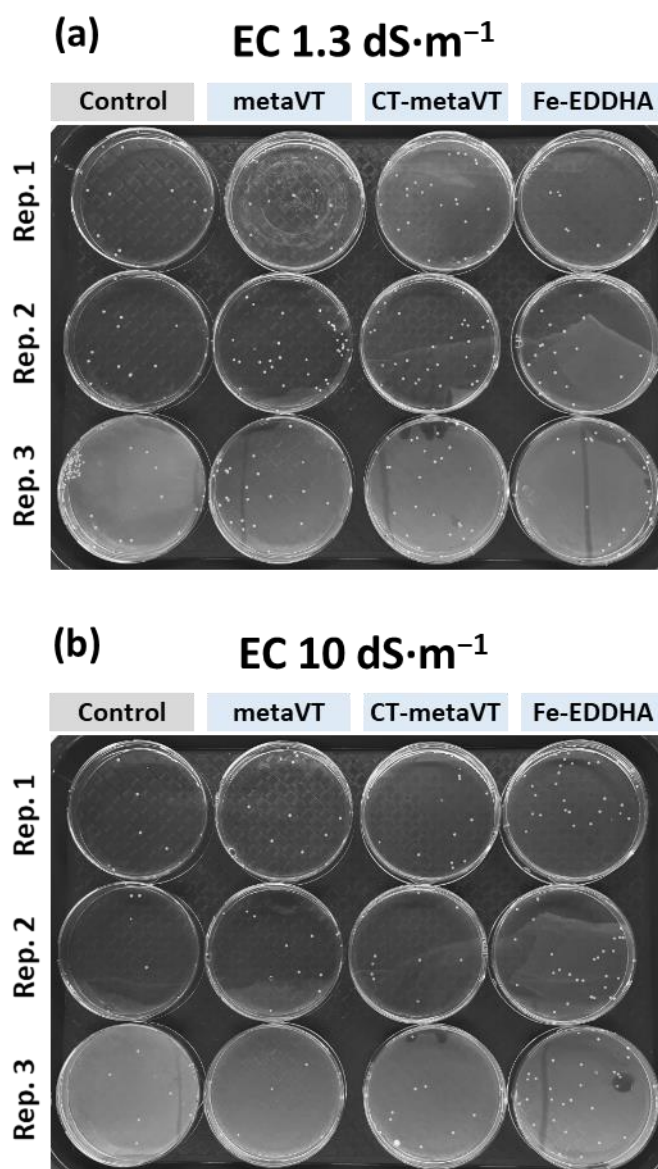
Figure B3-7. Pictures of *Pp* Pf-5 from sand pore water extraction cultured on TSA

medium without salinity stress (b) (EC = 1.3 dS·m^{-1}) and under salinity stress (c) (EC =

10 dS·m^{-1}).

B.4 Supplemental information for Chapter 4
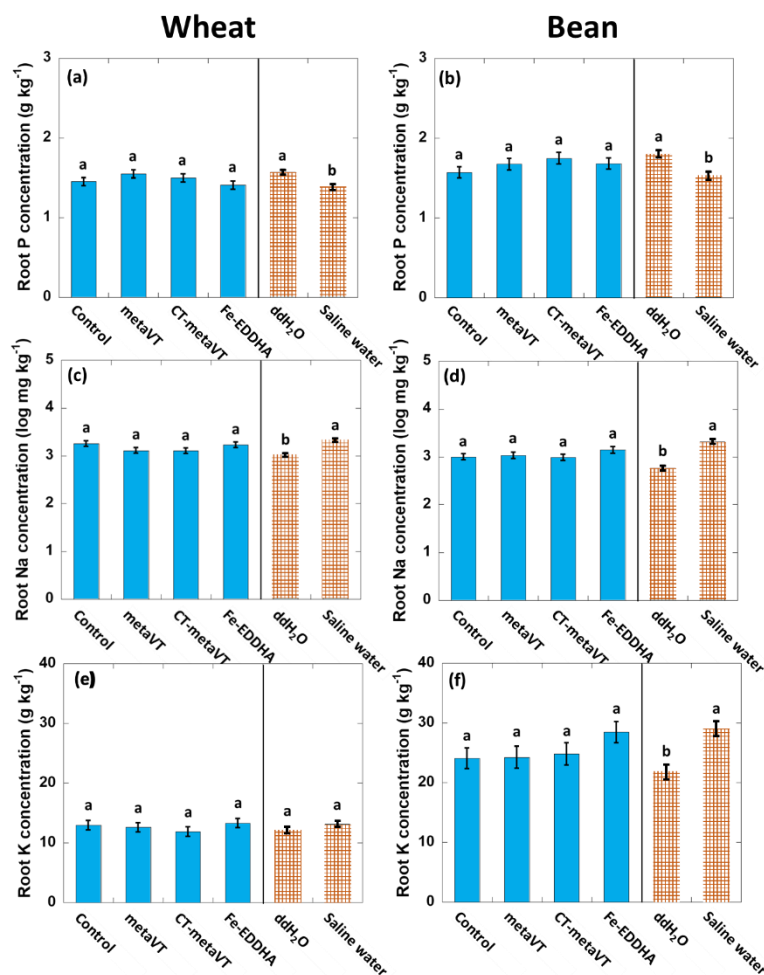
Figure B4-1. Root-associate P (a, b), Na (c, d), and K (e, f) of wheat (a, c, e) and beans

(b, d, f) grown in the sand with four Fe treatments, control, nano-metaVT, nano-CT-

metaVT, and Fe-EDDHA, and irrigated with ddH_2O and saline water (EC = 4 dS·m^{-1}). A

two-way ANOVA was performed. Different letters above columns represent significant

differences between treatments based on the Tukey-Kramer test ($\alpha \leq 0.05$). Error bars

represent the standard error calculated with the statistical mix model.
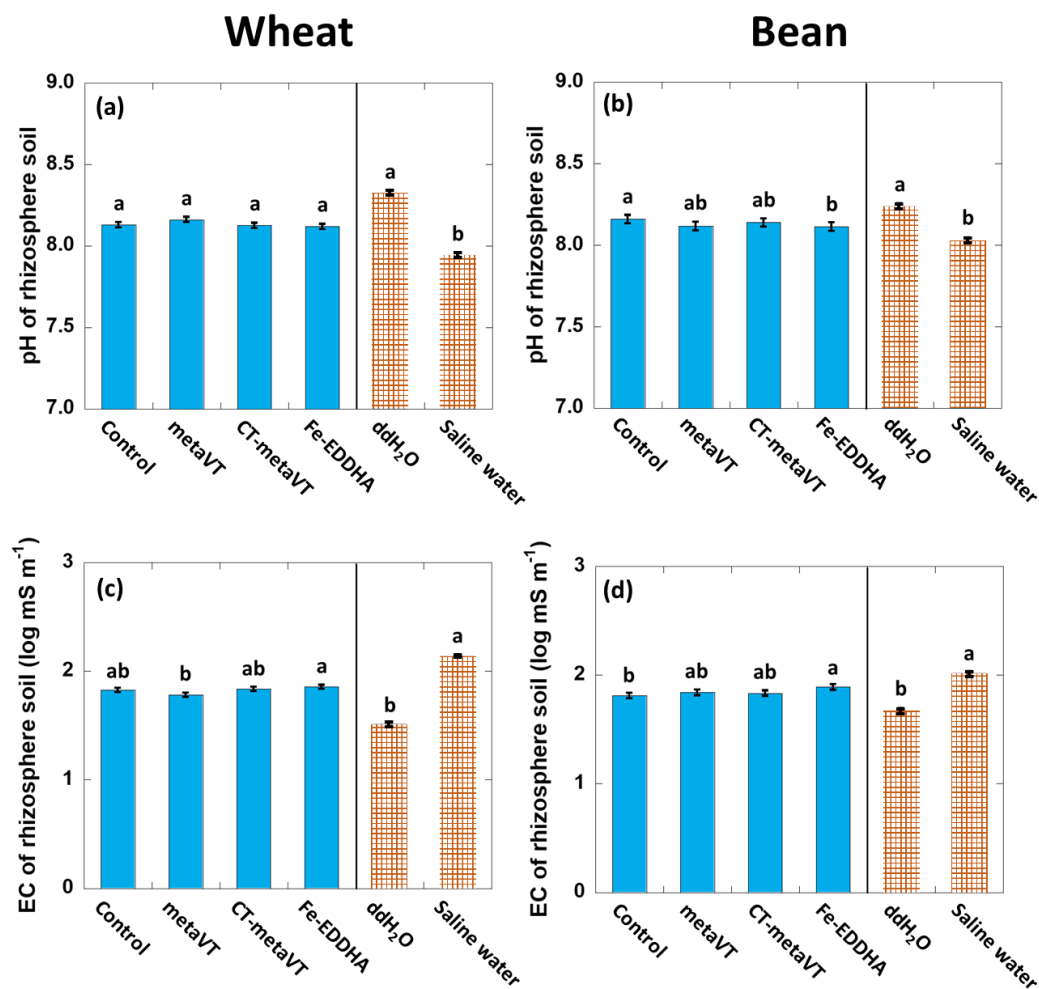
Figure B4-2. Rhizosphere soil pH (a, b) and EC (c, d) of wheat and beans grown with four Fe treatments, control, nano-metaVT, nano-CT-metaVT, and Fe-EDDHA, and irrigated with ddH$_2$O and saline water (EC = 4 dS·m^{-1}). Experimental condition: pH and EC were measured soil extract prepared with a soil-to-water ratio of 1:1. A two-way ANOVA was performed. Different letters above columns represent significant differences between treatments based on the Tukey-Kramer test ($\alpha \leq 0.05$). Error bars represent the standard error calculated with the statistical mix model.
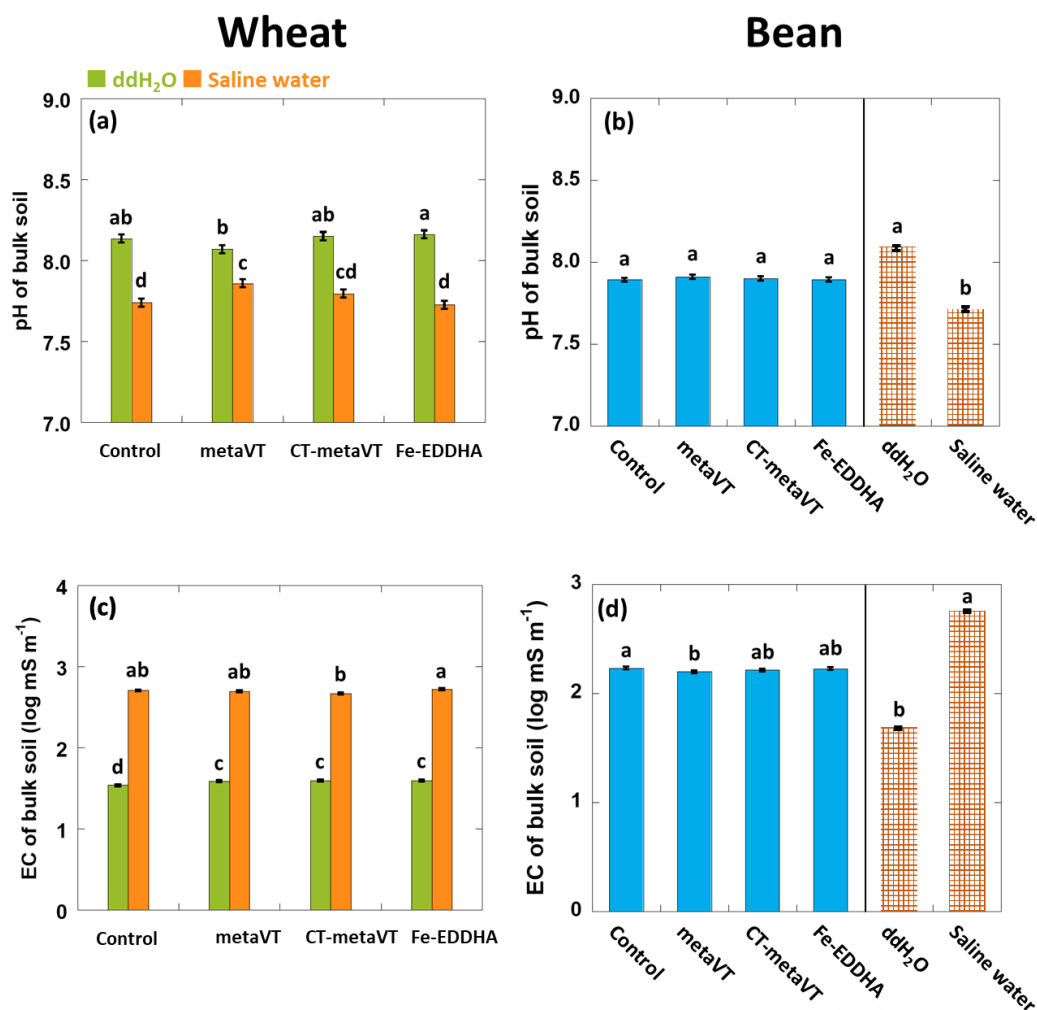
Figure B4-3. Bulk soil pH (a, b) and EC (c, d) of wheat and beans grown with four Fe treatments, control, nano-metaVT, nano-CT-metaVT, and Fe-EDDHA, and irrigated with ddH$_2$O and saline water (EC = 4 dS·m^{-1}). Experimental condition: pH and EC were measured with saturated soil paste extract. A two-way ANOVA was performed. Different letters above columns represent significant differences between treatments based on the Tukey-Kramer test ($\alpha \leq 0.05$). Error bars represent the standard error calculated with the statistical mix model.
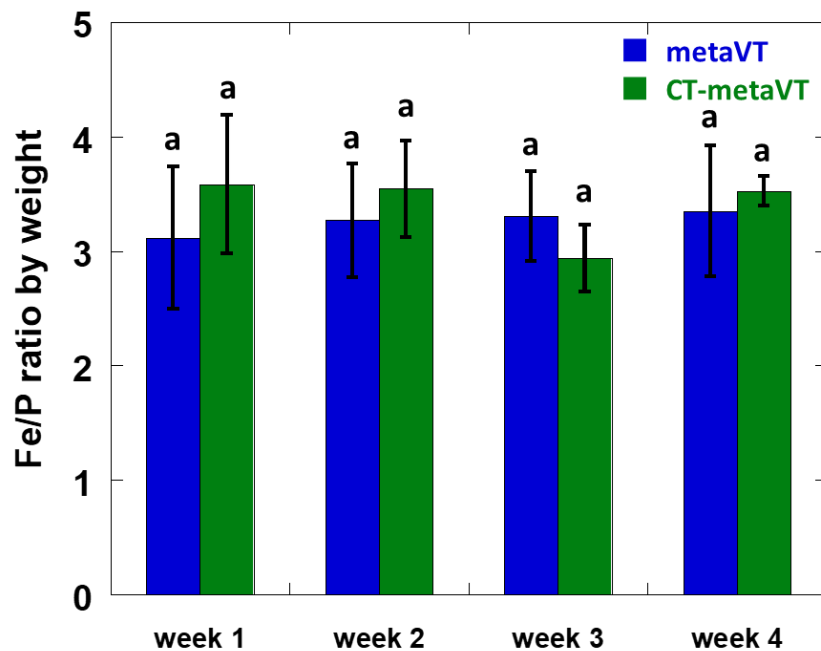
Figure B4-4. EDS semi-quantitative results of nano-metaVT and nano-CT-metaVT weathering in soil with wheat growing from one to four weeks. Three nano-metaVT/nano-CT-metaVT particles were analyzed each time. A two-way ANOVA was performed. Different letters above columns represent significant differences between treatments based on the Tukey-Kramer test ($\alpha \leq 0.05$). Error bars represent the standard deviation of the three replicates.

Table B4-1. The mobility of DTPA-extractable Fe in the soil columns without wheat. A two-way ANOVA was performed. Different letters above columns represent significant differences between treatments based on the Tukey-Kramer test ($\alpha \leq 0.05$). Error bars represent the standard deviation of the three replicates.

unit: mg kg^{-1}	control	metaVT	CT- metaVT	Fe-EDDHA
Initial DTPA-Fe concentrations in the top layers (0.4 cm; 160 mg Fe kg^{-1})	6.0 ± 0.2	10.0 ± 0.7	10.6 ± 0.3	114.7 ± 10.9
Layer 1	6.1 ± 0.4^c	7.8 ± 0.7^{ab}	7.9 ± 0.4^a	7.1 ± 0.6^{abc}
Layer 2	5.9 ± 0.2^c	6.7 ± 0.5^{abc}	7.2 ± 0.5^{abc}	6.8 ± 0.5^{abc}
Layer 3	5.9 ± 0.3^c	6.6 ± 0.4^{abc}	7.1 ± 0.5^{abc}	7.2 ± 0.6^{abc}
Layer 4	6.2 ± 0.5^{bc}	6.5 ± 0.5^{abc}	6.8 ± 0.6^{abc}	7.1 ± 0.7^{abc}
Layer 5	6.3 ± 0.4^{bc}	6.5 ± 0.8^{abc}	7.4 ± 0.3^{abc}	7.0 ± 0.6^{abc}

B.5 Supplemental information for Chapter 6

Table B5-1. Metal element analysis of HOS using inductively coupled plasma-optical

emission spectrometry (ICP-OES).

Element	ppm
Cu	0.1
Ag	0.1
Ca	18,094
Fe	5.0
Zn	0.3
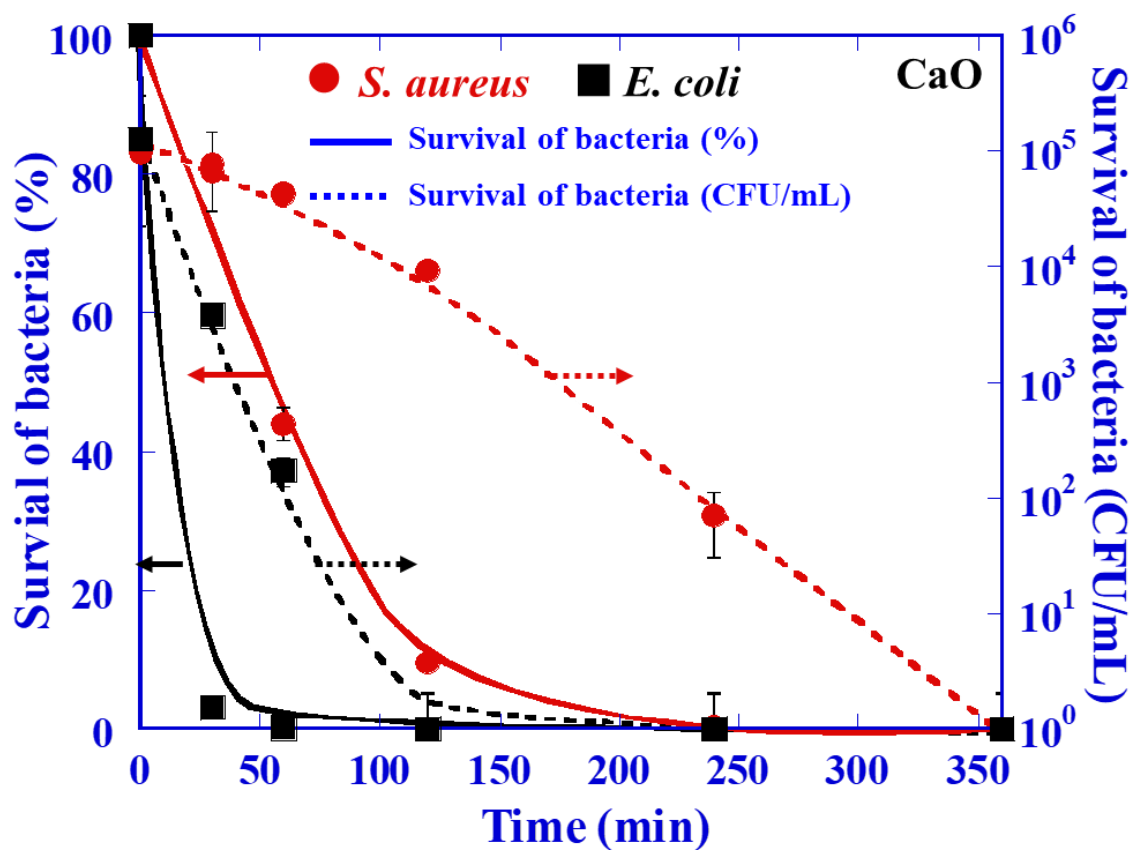
Figure B5-1. CaO disinfection efficiency against *S. aureus* and *E. coli*. Experimental

conditions: [CaO] 0.20 g/L, pH= 12.0 ± 0.1, [bacteria] 10^5 CFU/mL, T = 25 ± 1 °C.
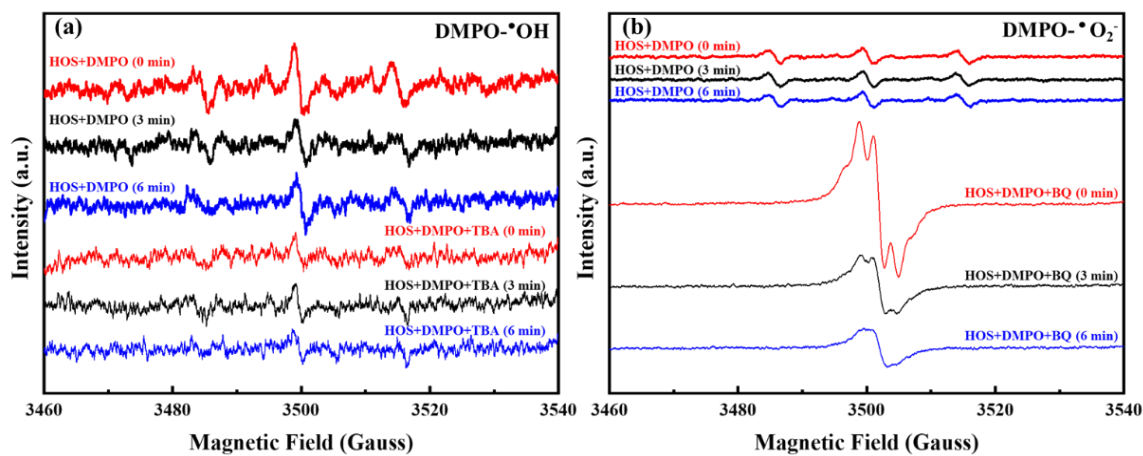
Figure B5-2. (a) ESR spectra of HOS obtained with DMPO as a spin-trapping agent and tert-Butanol (TBA) as a quenching agent. (b) ESR spectra of HOS obtained with DMPO as a spin-trapping agent and p-Benzoquinone (BQ) as a quenching agent. Experimental conditions: [HOS] = 1 g/L, [TBA] = 0.01 M, [BQ] = 0.01 M, T = 25 ± 1 °C.
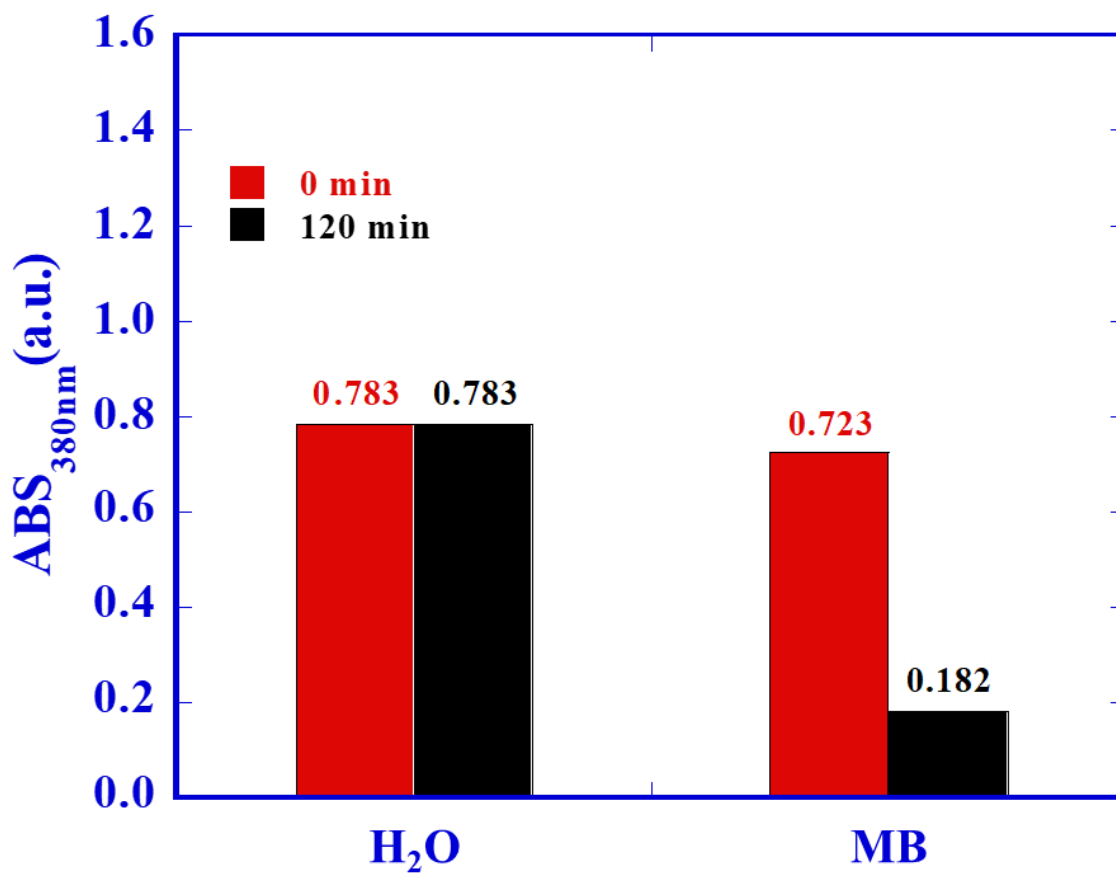
Figure B5-3. ABDA absorbance reduction at 380 nm of MB at 0 and 30 min under white light irradiation (30 mW). Experimental conditions: [MB] = 50 μg/mL, [ABDA] = 0.005 M, wavelength = 380 nm, T = 25 ± 1 °C.

B.6 Supplemental information for Chapter 7
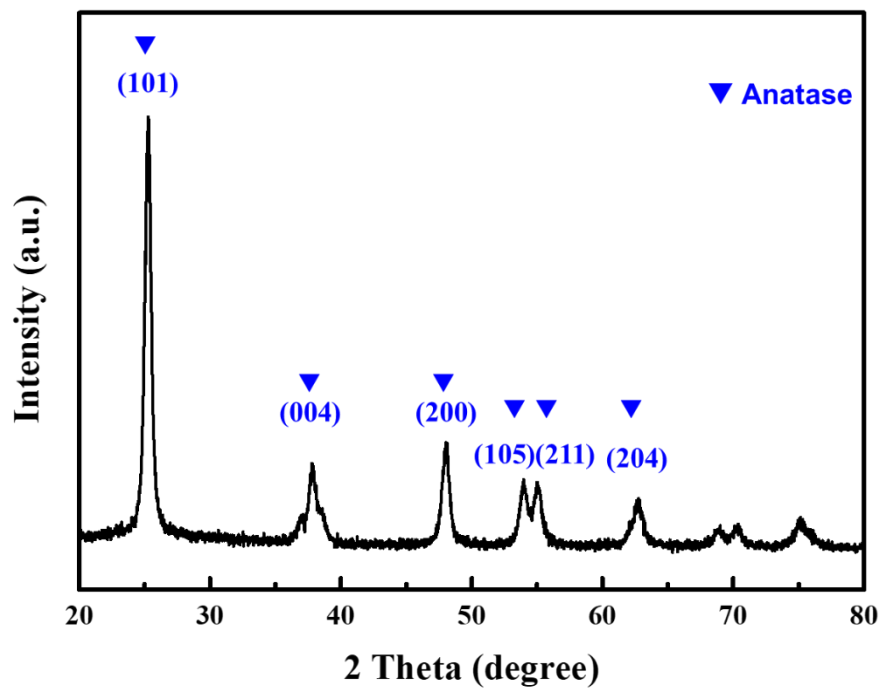
Figure B6-1. XRD pattern of N-TiO$_2$-coated PMMA.
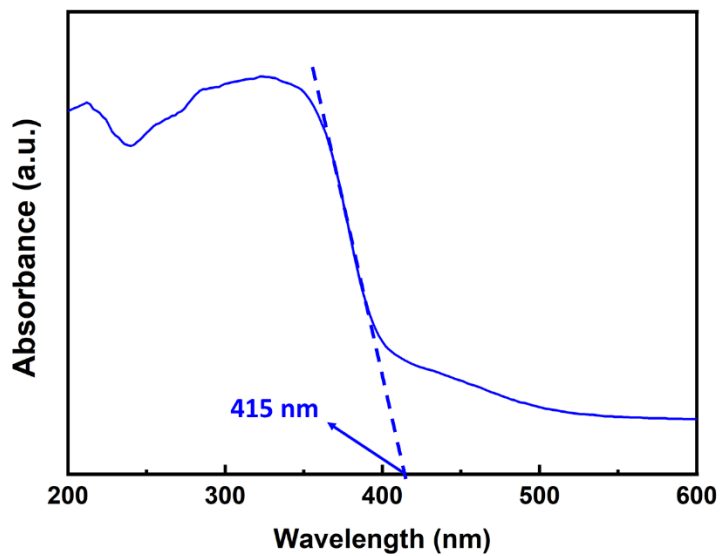
1

2   Figure B6-2. UV–vis diffuses reflectance spectra of NT.
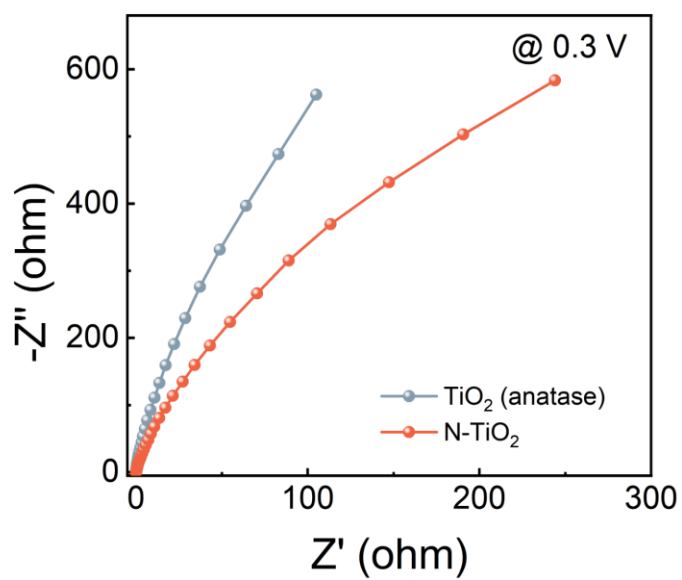
3

4   Figure B6-3. Nyquist plots of EIS for the TiO_2 (anatase) and N-TiO_2.

5
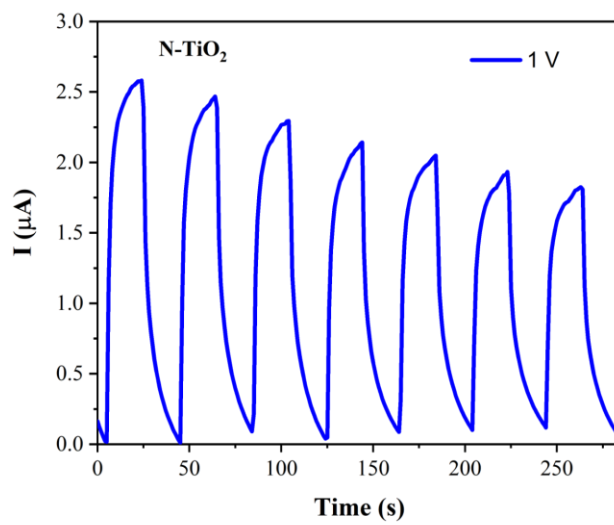
1

2   Figure B6-4. TPC responses of N-TiO$_2$.

3
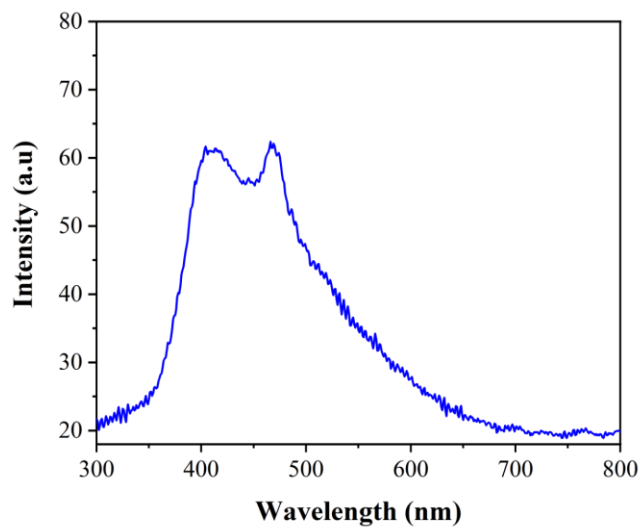
4

5   Figure B6-5. PL spectra of N-TiO$_2$.

6
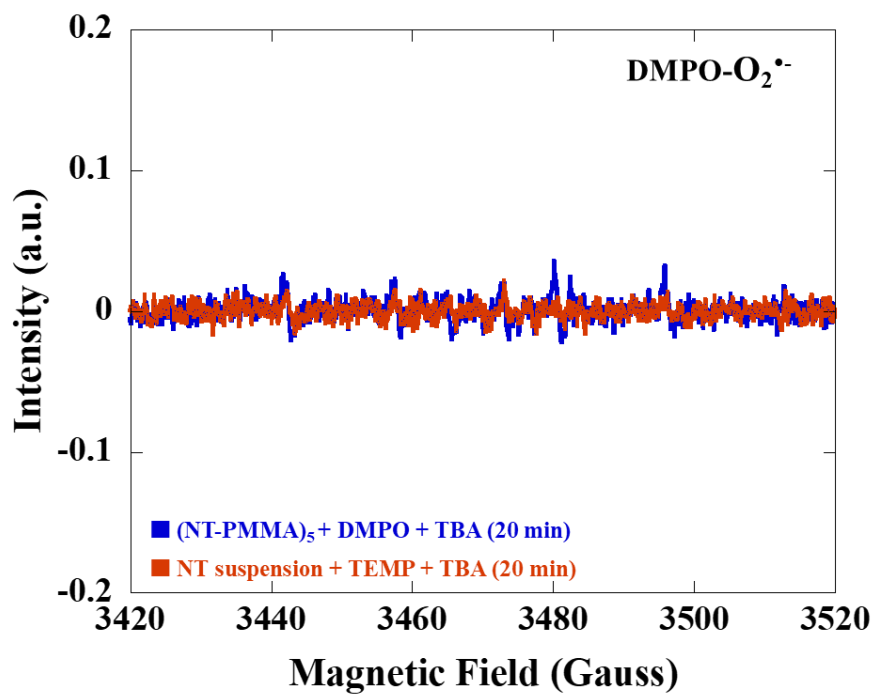
Figure B6-6. ESR spectra of (NT-PMMA)$_5$ and NT suspension, and TBA as a quenching agent for HO$^\bullet$. Conditions: [NT-PMMA] = 5 g L^{-1}, [NT suspension] = 5 g L^{-1}, T = 25 ± 1 °C.

Table B6-1. Characterization of N-TiO$_2$.

	XRD		SEM	UV-vis		BET		
	Phase content[a]	Crystalline size[b]	Particle size	Band gap[c]	Specific surface area	Pore size	Pore volume	Adsorption type[d]
	A/R/B (%)	nm	nm	eV	m^2/g	nm	cm^3/g	cm^3/g
NT	100/00/0	37	20	2.4	45.3	6.9	0.13	IV

[a] A, R, and B denote anatase, rutile, and brookite, respectively.

[b] The crystalline size was determined using the Scherer formula.

[c] The band gap is determined by the plot of $(\alpha h\nu)^{1/2}$ versus photon energy.

[d] Adsorption isotherm type & hysteresis loop were based on the IUPAC manual.

Appendix C. ANOVA tables

C.1 ANOVA tables for Chapter 2

Table C1-1. ANOVA table of total soluble Fe concentration in 0.003 mol L^{-1} KCl

suspension (Figure 2-3a).

Covariance Parameter Estimates				
Cov Parm	**Subject**	**Group**	**Estimate**	**Standard Error**
Intercept	block		1941.75	2217.79
time	rep*material	material CT-metaVT	2790.02	486.77
time	rep*material	material metaVT	9802.53	1665.30
Solutions for Fixed Effects						
Effect	**material**	**Estimate**	**Standard Error**	**DF**	**t Value**	**Pr > |t|**
Intercept		789.85	33.1824	2	23.80	0.0018
material	CT-metaVT	-293.03	24.1452	138	-12.14	<.0001
material	metaVT	0	.	.	.	.
day		57.6272	5.0924	138	11.32	<.0001
day*material	CT-metaVT	-34.3039	5.7718	138	-5.94	<.0001
day*material	metaVT	0	.	.	.	.
Type III Tests of Fixed Effects				
Effect	**Num DF**	**Den DF**	**F Value**	**Pr > F**
material	1	138	147.29	<.0001
day	1	138	196.71	<.0001
day*material	1	138	35.32	<.0001

Table C1-2. ANOVA table of total soluble Fe concentration in SPE suspension (Figure 2-3b and Figure 2-9a).

Covariance Parameter Estimates				
Cov Parm	**Subject**	**Group**	**Estimate**	**Standard Error**
Intercept	block		7.3159	7.4853
time	rep*material	material CT-metaVT	6.1208	1.0528
time	rep*material	material metaVT	10.3181	1.7788
Solutions for Fixed Effects						
Effect	**material**	**Estimate**	**Standard Error**	**DF**	**t Value**	**Pr > |t|**
Intercept		30.1875	1.7077	2	17.68	0.0032
material	CT-metaVT	2.3722	0.8724	138	2.72	0.0074
material	metaVT	0	.	.	.	.
day		0.1889	0.1652	138	1.14	0.2548
day*material	CT-metaVT	0.1400	0.2085	138	0.67	0.5033
day*material	metaVT	0	.	.	.	.
Type III Tests of Fixed Effects				
Effect	**Num DF**	**Den DF**	**F Value**	**Pr > F**
material	1	138	7.39	0.0074
day	1	138	6.17	0.0142
day*material	1	138	0.45	0.5033

Table C1-3. ANOVA table of total soluble P concentration in 0.003 mol L^{-1} KCl

suspension (Figure 2-3c).

Covariance Parameter Estimates				
Cov Parm	**Subject**	**Group**	**Estimate**	**Standard Error**
Intercept	block		382.80	480.14
time	rep*material	material CT-metaVT	4699.88	830.91
time	rep*material	material metaVT	3923.86	679.19
Solutions for Fixed Effects							
Effect	**material**	**Estimate**	**Standard Error**	**DF**	**t Value**	**Pr > |t|**
Intercept		392.15	17.5858	2	22.30	0.0020
material	CT-metaVT	15.9527	19.9812	138	0.80	0.4260
material	metaVT	0	.	.	.	.
day		39.5811	3.2219	138	12.29	<.0001
day*material	CT-metaVT	9.1991	4.7764	138	1.93	0.0562
day*material	metaVT	0	.	.	.	.
Type III Tests of Fixed Effects				
Effect	**Num DF**	**Den DF**	**F Value**	**Pr > F**
material	1	138	0.64	0.4260
day	1	138	342.23	<.0001
day*material	1	138	3.71	0.0562

Table C1-4. ANOVA table of total soluble P concentration in SPE suspension (Figure 2-3d and Figure 2-9c).

Covariance Parameter Estimates				
Cov Parm	**Subject**	**Group**	**Estimate**	**Standard Error**
Intercept	block		156.07	216.30
time	rep*material	material CT-metaVT	3122.00	549.90
time	rep*material	material metaVT	2800.16	484.65
Solutions for Fixed Effects						
Effect	**material**	**Estimate**	**Standard Error**	**DF**	**t Value**	**Pr > |t|**
Intercept		543.98	13.4782	2	40.36	0.0006
material	CT-metaVT	72.1274	16.5582	138	4.36	<.0001
material	metaVT	0	.	.	.	.
day		0.7897	2.7217	138	0.29	0.7721
day*material	CT-metaVT	3.5393	3.9582	138	0.89	0.3728
day*material	metaVT	0	.	.	.	.
Type III Tests of Fixed Effects				
Effect	**Num DF**	**Den DF**	**F Value**	**Pr > F**
material	1	138	18.97	<.0001
day	1	138	1.67	0.1981
day*material	1	138	0.80	0.3728

Table C1-5. ANOVA table of pH of 0.003 mol L^{-1} KCl suspension changed over time (Figure 2-4a).

Covariance Parameter Estimates				
Cov Parm	**Subject**	**Group**	**Estimate**	**Standard Error**
Intercept	block		0.000957	0.001087
time	rep*material	material CT-metaVT	0.005974	0.001017
time	rep*material	material metaVT	0.006524	0.001108

Solutions for Fixed Effects						
Effect	**material**	**Estimate**	**Standard Error**	**DF**	**t Value**	**Pr > |t|**
Intercept		5.3136	0.02492	2	213.24	<.0001
material	CT-metaVT	0.3593	0.02405	138	14.94	<.0001
material	metaVT	0	.	.	.	.
day		-0.02107	0.004154	138	-5.07	<.0001
day*material	CT-metaVT	0.007553	0.005750	138	1.31	0.1912
day*material	metaVT	0	.	.	.	.

Type III Tests of Fixed Effects				
Effect	**Num DF**	**Den DF**	**F Value**	**Pr > F**
material	1	138	223.06	<.0001
day	1	138	36.19	<.0001
day*material	1	138	1.73	0.1912

Table C1-6. ANOVA table of pH of SPE suspension changed over time (Figure 2-4b and Figure 2-10a).

Covariance Parameter Estimates				
Cov Parm	**Subject**	**Group**	**Estimate**	**Standard Error**
Intercept	block		0.01146	0.01201
Residual			0.02669	0.003213
Solutions for Fixed Effects						
Effect	**material**	**Estimate**	**Standard Error**	**DF**	**t Value**	**Pr > |t|**
Intercept		8.0290	0.07109	2	112.93	<.0001
material	CT-metaVT	-0.04574	0.04971	138	-0.92	0.3591
material	metaVT	0	.	.	.	.
day		0.03243	0.008403	138	3.86	0.0002
day*material	CT-metaVT	-0.00705	0.01188	138	-0.59	0.5540
day*material	metaVT	0	.	.	.	.
Type III Tests of Fixed Effects				
Effect	**Num DF**	**Den DF**	**F Value**	**Pr > F**
material	1	138	0.85	0.3591
day	1	138	23.67	<.0001
day*material	1	138	0.35	0.5540

Table C1-7. ANOVA table of EC of 0.003 mol L^{-1} KCl suspension changed over time (Figure 2-4c).

Covariance Parameter Estimates				
Cov Parm	**Subject**	**Group**	**Estimate**	**Standard Error**
Intercept	block		0	.
time	rep*material	material CT-metaVT	0.000041	6.949E-6
time	rep*material	material metaVT	0.000040	6.689E-6
Solutions for Fixed Effects							
Effect	**material**	**Estimate**	**Standard Error**	**DF**	**t Value**	**Pr > |t|**
Intercept		0.4238	0.001354	2	313.08	<.0001
material	CT-metaVT	0.003320	0.001933	138	1.72	0.0880
material	metaVT	0	.	.	.	.
day		0.002149	0.000324	138	6.64	<.0001
day*material	CT-metaVT	-0.00048	0.000462	138	-1.04	0.3002
day*material	metaVT	0	.	.	.	.
Type III Tests of Fixed Effects				
Effect	**Num DF**	**Den DF**	**F Value**	**Pr > F**
material	1	138	2.95	0.0880
day	1	138	68.28	<.0001
day*material	1	138	1.08	0.3002

Table C1-8. ANOVA table of EC of SPE suspension changed over time (Figure 2-4d and Figure 2-10c).

Covariance Parameter Estimates				
Cov Parm	**Subject**	**Group**	**Estimate**	**Standard Error**
Intercept	block		0.000200	0.000208
time	rep*material	material CT- metaVT	0.000461	0.000078
time	rep*material	material metaVT	0.000346	0.000059
Solutions for Fixed Effects						
Effect	**material**	**Estimate**	**Standard Error**	**DF**	**t Value**	**Pr > |t|**
Intercept		0.4021	0.009097	2	44.21	0.0005
material	CT-metaVT	0.002954	0.006115	138	0.48	0.6298
material	metaVT	0	.	.	.	.
day		-0.00276	0.000957	138	-2.89	0.0045
day*material	CT-metaVT	0.001064	0.001462	138	0.73	0.4678
day*material	metaVT	0	.	.	.	.
Type III Tests of Fixed Effects				
Effect	**Num DF**	**Den DF**	**F Value**	**Pr > F**
material	1	138	0.23	0.6298
day	1	138	9.33	0.0027
day*material	1	138	0.53	0.4678

Table C1-9. ANOVA table of effects of *Pc*O6 inoculation on total soluble Fe concentration in nano-metaVT-SPE suspension (Figure 2-5a).

Covariance Parameter Estimates				
Cov Parm	**Subject**	**Group**	**Estimate**	**Standard Error**
Intercept	block		0.2151	1.0439
time	rep*microbe	microbe *Pc*O6	17.9635	4.6126
time	rep*microbe	microbe no	17.0840	5.0474

Solutions for Fixed Effects						
Effect	**material**	**Estimate**	**Standard Error**	**DF**	**t Value**	**Pr > |t|**
Intercept		30.1875	0.9288	2	32.50	0.0009
microbe	*Pc*O6	1.8008	1.2738	138	1.41	0.1597
microbe	no	0	.	.	.	.
day		0.1889	0.2126	138	0.89	0.3757
day*microbe	*Pc*O6	0.2505	0.3045	138	0.82	0.4122
day*microbe	no	0	.	.	.	.

Type III Tests of Fixed Effects				
Effect	**Num DF**	**Den DF**	**F Value**	**Pr > F**
microbe	1	138	2.00	0.1597
day	1	138	4.26	0.0409
day*microbe	1	138	0.68	0.4122

Table C1-10. ANOVA table of effects of *Pc*O6 inoculation on total soluble Fe concentration in nano-CT-metaVT-SPE suspension (Figure 2-5b).

Covariance Parameter Estimates				
Cov Parm	**Subject**	**Group**	**Estimate**	**Standard Error**
Intercept	block		1.58E-17	.
time	rep*microbe	microbe *Pc*O6	18.6162	3.1694
time	rep*microbe	microbe no	9.5043	1.6065
Solutions for Fixed Effects						
Effect	**material**	**Estimate**	**Standard Error**	**DF**	**t Value**	**Pr > |t|**
Intercept		32.5597	0.6633	2	49.08	0.0004
microbe	*Pc*O6	2.5682	1.1525	137	2.23	0.0275
microbe	no	0	.	.	.	.
day		0.3289	0.1586	137	2.07	0.0399
day*microbe	*Pc*O6	0.05905	0.2743	137	0.22	0.8299
day*microbe	no	0	.	.	.	.
Type III Tests of Fixed Effects				
Effect	**Num DF**	**Den DF**	**F Value**	**Pr > F**
microbe	1	137	4.97	0.0275
day	1	137	6.83	0.0100
day*microbe	1	137	0.05	0.8299

Table C1-11. ANOVA table of effects of *Pc*O6 inoculation on total soluble Pconcentration in nano-metaVT-SPE suspension (Figure 2-5c).

Covariance Parameter Estimates				
Cov Parm	**Subject**	**Group**	**Estimate**	**Standard Error**
Intercept	block		483.59	559.86
time	rep*microbe	microbe *Pc*O6	2650.11	490.75
time	rep*microbe	microbe no	2996.62	541.96
Solutions for Fixed Effects						
Effect	**material**	**Estimate**	**Standard Error**	**DF**	**t Value**	**Pr > |t|**
Intercept		543.98	17.3185	2	31.41	0.0010
microbe	*Pc*O6	-32.6709	16.1686	138	-2.02	0.0453
microbe	no	0	.	.	.	.
day		0.7897	2.8156	138	0.28	0.7795
day*microbe	*Pc*O6	12.9521	3.8650	138	3.35	0.0010
day*microbe	no	0	.	.	.	.
Type III Tests of Fixed Effects				
Effect	**Num DF**	**Den DF**	**F Value**	**Pr > F**
microbe	1	138	4.08	0.0453
day	1	138	14.14	0.0003
day*microbe	1	138	11.23	0.0010

Table C1-12. ANOVA table of effects of *Pc*O6 inoculation on total soluble P concentration in nano-CT-metaVT-SPE suspension (Figure 2-5d).

Covariance Parameter Estimates				
Cov Parm	**Subject**	**Group**	**Estimate**	**Standard Error**
Intercept	block		174.63	254.68
time	rep*microbe	microbe *Pc*O6	3132.64	606.67
time	rep*microbe	microbe no	3474.54	649.65
Solutions for Fixed Effects						
Effect	**material**	**Estimate**	**Standard Error**	**DF**	**t Value**	**Pr > |t|**
Intercept		616.11	14.8009	2	41.63	0.0006
microbe	*Pc*O6	-32.8692	17.4897	138	-1.88	0.0623
microbe	no	0	.	.	.	.
day		4.3290	3.0318	138	1.43	0.1556
day*microbe	*Pc*O6	4.1904	4.1808	138	1.00	0.3180
day*microbe	no	0	.	.	.	.
Type III Tests of Fixed Effects				
Effect	**Num DF**	**Den DF**	**F Value**	**Pr > F**
microbe	1	138	3.53	0.0623
day	1	138	9.44	0.0026
day*microbe	1	138	1.00	0.3180

Table C1-13. ANOVA table of effects of *Pc*O6 inoculation on pH in nano-metaVT-SPE suspension (Figure 2-6a).

Covariance Parameter Estimates				
Cov Parm	**Subject**	**Group**	**Estimate**	**Standard Error**
Intercept	block		0.008345	0.009335
time	rep*microbe	microbe *Pc*O6	0.08043	0.01608
time	rep*microbe	microbe no	0.03053	0.006064

Solutions for Fixed Effects						
Effect	**material**	**Estimate**	**Standard Error**	**DF**	**t Value**	**Pr > |t|**
Intercept		8.0290	0.06477	2	123.97	<.0001
microbe	*Pc*O6	0.005093	0.07167	138	0.07	0.9435
microbe	no	0	.	.	.	.
day		0.03243	0.008987	138	3.61	0.0004
day*microbe	*Pc*O6	-0.01503	0.01713	138	-0.88	0.3820
day*microbe	no	0	.	.	.	.

Type III Tests of Fixed Effects				
Effect	**Num DF**	**Den DF**	**F Value**	**Pr > F**
microbe	1	138	0.01	0.9435
day	1	138	8.46	0.0042
day*microbe	1	138	0.77	0.3820

Table C1-14. ANOVA table of effects of *Pc*O6 inoculation on pH in nano-CT-metaVT-SPE suspension (Figure 2-6b).

Covariance Parameter Estimates				
Cov Parm	**Subject**	**Group**	**Estimate**	**Standard Error**
Intercept	block		0.009626	0.01044
time	rep*microbe	microbe *Pc*O6	0.04910	0.009180
time	rep*microbe	microbe no	0.03152	0.005877
Solutions for Fixed Effects						
Effect	**material**	**Estimate**	**Standard Error**	**DF**	**t Value**	**Pr > |t|**
Intercept		7.9832	0.06832	2	116.85	<.0001
microbe	*Pc*O6	0.05204	0.06110	138	0.85	0.3958
microbe	no	0	.	.	.	.
day		0.02538	0.009132	138	2.78	0.0062
day*microbe	*Pc*O6	0.002156	0.01460	138	0.15	0.8829
day*microbe	no	0	.	.	.	.
Type III Tests of Fixed Effects				
Effect	**Num DF**	**Den DF**	**F Value**	**Pr > F**
microbe	1	138	0.73	0.3958
day	1	138	13.13	0.0004
day*microbe	1	138	0.02	0.8829

Table C1-15. ANOVA table of effects of *Pc*O6 inoculation on EC in nano-metaVT-SPE
suspension (Figure 2-6c).

Covariance Parameter Estimates				
Cov Parm	**Subject**	**Group**	**Estimate**	**Standard Error**
Intercept	block		0.000034	0.000045
time	rep*microbe	microbe *Pc*O6	0.000506	0.000093
time	rep*microbe	microbe no	0.000414	0.000078

Solutions for Fixed Effects						
Effect	**material**	**Estimate**	**Standard Error**	**DF**	**t Value**	**Pr > |t|**
Intercept		0.4021	0.005512	2	72.96	0.0002
microbe	*Pc*O6	0.001453	0.006526	138	0.22	0.8242
microbe	no	0	.	.	.	.
day		-0.00276	0.001046	138	-2.64	0.0092
day*microbe	*Pc*O6	0.000167	0.001560	138	0.11	0.9151
day*microbe	no	0	.	.	.	.

Type III Tests of Fixed Effects				
Effect	**Num DF**	**Den DF**	**F Value**	**Pr > F**
microbe	1	138	0.05	0.8242
day	1	138	11.82	0.0008
day*microbe	1	138	0.01	0.9151

Table C1-16. ANOVA table of effects of *Pc*O6 inoculation on EC in nano-CT-metaVT-SPE suspension (Figure 2-6d).

Covariance Parameter Estimates				
Cov Parm	**Subject**	**Group**	**Estimate**	**Standard Error**
Intercept	block		0.000024	0.000037
time	rep*microbe	microbe *Pc*O6	0.000537	0.000096
time	rep*microbe	microbe no	0.000550	0.000102

Solutions for Fixed Effects						
Effect	**material**	**Estimate**	**Standard Error**	**DF**	**t Value**	**Pr > |t|**
Intercept		0.4051	0.005796	2	69.89	0.0002
microbe	*Pc*O6	0.000162	0.007093	138	0.02	0.9818
microbe	no	0	.	.	.	.
day		-0.00170	0.001206	138	-1.41	0.1609
day*microbe	*Pc*O6	-0.00011	0.001695	138	-0.06	0.9496
day*microbe	no	0	.	.	.	.

Type III Tests of Fixed Effects				
Effect	**Num DF**	**Den DF**	**F Value**	**Pr > F**
microbe	1	138	0.00	0.9818
day	1	138	4.28	0.0405
day*microbe	1	138	0.00	0.9496

Table C1-17. ANOVA table of effects of *Pp* Pf-5 inoculation on total soluble Fe concentration in nano-metaVT-SPE suspension (Figure 2-7a).

Covariance Parameter Estimates				
Cov Parm	**Subject**	**Group**	**Estimate**	**Standard Error**
Intercept	block		0	.
time	rep*microbe	microbe *Pp* Pf-5	12.9205	2.1828
time	rep*microbe	microbe no	18.1032	3.0627
Solutions for Fixed Effects						
Effect	**material**	**Estimate**	**Standard Error**	**DF**	**t Value**	**Pr > |t|**
Intercept		30.1875	0.9155	2	32.97	0.0009
microbe	*Pp* Pf-5	6.8335	1.1984	138	5.70	<.0001
microbe	no	0	.	.	.	.
day		0.1889	0.2188	138	0.86	0.3895
day*microbe	*Pp* Pf-5	0.03275	0.2865	138	0.11	0.9091
day*microbe	no	0	.	.	.	.
Type III Tests of Fixed Effects				
Effect	**Num DF**	**Den DF**	**F Value**	**Pr > F**
microbe	1	138	32.51	<.0001
day	1	138	2.05	0.1541
day*microbe	1	138	0.01	0.9091

Table C1-18. ANOVA table of effects of *Pp* Pf-5 inoculation on total soluble Fe concentration in nano-CT-metaVT-SPE suspension (Figure 2-7b).

Covariance Parameter Estimates				
Cov Parm	**Subject**	**Group**	**Estimate**	**Standard Error**
Intercept	block		0	.
time	rep*microbe	microbe *Pp* Pf-5	14.4711	2.4461
time	rep*microbe	microbe no	9.5043	1.6065
Solutions for Fixed Effects						
Effect	**material**	**Estimate**	**Standard Error**	**DF**	**t Value**	**Pr > |t|**
Intercept		32.5597	0.6633	2	49.08	0.0004
microbe	*Pp* Pf-5	9.5106	1.0536	138	9.03	<.0001
microbe	no	0	.	.	.	.
day		0.3289	0.1586	138	2.07	0.0399
day*microbe	*Pp* Pf-5	-0.1391	0.2518	138	-0.55	0.5816
day*microbe	no	0	.	.	.	.
Type III Tests of Fixed Effects				
Effect	**Num DF**	**Den DF**	**F Value**	**Pr > F**
microbe	1	138	81.49	<.0001
day	1	138	4.24	0.0413
day*microbe	1	138	0.31	0.5816

Table C1-19. ANOVA table of effects of *Pp* Pf-5 inoculation on total soluble Pconcentration in nano-metaVT-SPE suspension (Figure 2-7c).

Covariance Parameter Estimates				
Cov Parm	**Subject**	**Group**	**Estimate**	**Standard Error**
Intercept	block		47.2831	88.6538
time	rep*microbe	microbe *Pp* Pf-5	1527.95	259.33
time	rep*microbe	microbe no	2752.53	473.45
Solutions for Fixed Effects						
Effect	**material**	**Estimate**	**Standard Error**	**DF**	**t Value**	**Pr > |t|**
Intercept		543.98	11.9663	2	45.46	0.0005
microbe	*Pp* Pf-5	17.8508	14.0773	138	1.27	0.2069
microbe	no	0	.	.	.	.
day		0.7897	2.6985	138	0.29	0.7702
day*microbe	*Pp* Pf-5	2.8294	3.3651	138	0.84	0.4019
day*microbe	no	0	.	.	.	.
Type III Tests of Fixed Effects				
Effect	**Num DF**	**Den DF**	**F Value**	**Pr > F**
microbe	1	138	1.61	0.2069
day	1	138	1.72	0.1923
day*microbe	1	138	0.71	0.4019

Table C1-20. ANOVA table of effects of *Pp* Pf-5 inoculation on total soluble P concentration in nano-CT-metaVT-SPE suspension (Figure 2-7d).

Covariance Parameter Estimates				
Cov Parm	**Subject**	**Group**	**Estimate**	**Standard Error**
Intercept	block		130.69	171.61
time	rep*microbe	microbe *Pp* Pf-5	1363.14	234.66
time	rep*microbe	microbe no	3158.26	554.39
Solutions for Fixed Effects						
Effect	**material**	**Estimate**	**Standard Error**	**DF**	**t Value**	**Pr > |t|**
Intercept		616.11	13.7761	2	44.72	0.0005
microbe	*Pp* Pf-5	39.6104	14.4680	138	2.74	0.0070
microbe	no	0	.	.	.	.
day		4.3290	2.8905	138	1.50	0.1365
day*microbe	*Pp* Pf-5	-7.7835	3.4585	138	-2.25	0.0260
day*microbe	no	0	.	.	.	.
Type III Tests of Fixed Effects				
Effect	**Num DF**	**Den DF**	**F Value**	**Pr > F**
microbe	1	138	7.50	0.0070
day	1	138	0.06	0.8008
day*microbe	1	138	5.06	0.0260

Table C1-21. ANOVA table of effects of *Pp* Pf-5 inoculation on pH in nano-metaVT-SPE

suspension (Figure 2-8a).

Covariance Parameter Estimates				
Cov Parm	**Subject**	**Group**	**Estimate**	**Standard Error**
Intercept	block		0.008582	0.009220
time	rep*microbe	microbe *Pp* Pf-5	0.02780	0.005417
time	rep*microbe	microbe no	0.02958	0.005435
Solutions for Fixed Effects						
Effect	**material**	**Estimate**	**Standard Error**	**DF**	**t Value**	**Pr > |t|**
Intercept		8.0290	0.06504	2	123.45	<.0001
microbe	*Pp* Pf-5	-0.2762	0.05297	132	-5.21	<.0001
microbe	no	0	.	.	.	.
day		0.03243	0.008846	132	3.67	0.0004
day*microbe	*Pp* Pf-5	-0.01709	0.01244	132	-1.37	0.1720
day*microbe	no	0	.	.	.	.
Type III Tests of Fixed Effects				
Effect	**Num DF**	**Den DF**	**F Value**	**Pr > F**
microbe	1	132	27.19	<.0001
day	1	132	14.74	0.0002
day*microbe	1	132	1.89	0.1720

Table C1-22. ANOVA table of effects of *Pp* Pf-5 inoculation on pH in nano-CT-metaVT-SPE suspension (Figure 2-8b).

Covariance Parameter Estimates				
Cov Parm	**Subject**	**Group**	**Estimate**	**Standard Error**
Intercept	block		0.008054	0.008937
time	rep*microbe	microbe *Pp* Pf-5	0.06689	0.01208
time	rep*microbe	microbe no	0.02858	0.004997
Solutions for Fixed Effects						
Effect	**material**	**Estimate**	**Standard Error**	**DF**	**t Value**	**Pr > |t|**
Intercept		7.9832	0.06331	2	126.11	<.0001
microbe	*Pp* Pf-5	-0.3424	0.06911	132	-4.95	<.0001
microbe	no	0	.	.	.	.
day		0.02538	0.008695	132	2.92	0.0041
day*microbe	*Pp* Pf-5	-0.00098	0.01612	132	-0.06	0.9515
day*microbe	no	0	.	.	.	.
Type III Tests of Fixed Effects				
Effect	**Num DF**	**Den DF**	**F Value**	**Pr > F**
microbe	1	132	24.55	<.0001
day	1	132	9.54	0.0025
day*microbe	1	132	0.00	0.9515

Table C1-23. ANOVA table of effects of *Pp* Pf-5 inoculation on EC in nano-metaVT-SPE

suspension (Figure 2-8c).

Covariance Parameter Estimates				
Cov Parm	**Subject**	**Group**	**Estimate**	**Standard Error**
Intercept	block		0.000284	0.000293
time	rep*microbe	microbe *Pp* Pf-5	0.000203	0.000044
time	rep*microbe	microbe no	0.000564	0.000113

Solutions for Fixed Effects						
Effect	**material**	**Estimate**	**Standard Error**	**DF**	**t Value**	**Pr > |t|**
Intercept		0.4021	0.01099	2	36.59	0.0007
microbe	*Pp* Pf-5	-0.05190	0.006049	132	-8.58	<.0001
microbe	no	0	.	.	.	.
day		-0.00276	0.001221	132	-2.26	0.0252
day*microbe	*Pp* Pf-5	0.004220	0.001432	132	2.95	0.0038
day*microbe	no	0	.	.	.	.

Type III Tests of Fixed Effects				
Effect	**Num DF**	**Den DF**	**F Value**	**Pr > F**
microbe	1	132	73.63	<.0001
day	1	132	0.84	0.3624
day*microbe	1	132	8.69	0.0038

Table C1-24. ANOVA table of effects of *Pp* Pf-5 inoculation on EC in nano-CT-metaVT-SPE suspension (Figure 2-8d).

Covariance Parameter Estimates				
Cov Parm	**Subject**	**Group**	**Estimate**	**Standard Error**
Intercept	block		0.000199	0.000209
time	rep*microbe	microbe *Pp* Pf-5	0.000294	0.000061
time	rep*microbe	microbe no	0.000622	0.000119

Solutions for Fixed Effects						
Effect	**material**	**Estimate**	**Standard Error**	**DF**	**t Value**	**Pr > |t|**
Intercept		0.4051	0.009746	2	41.56	0.0006
microbe	*Pp* Pf-5	-0.04815	0.006635	132	-7.26	<.0001
microbe	no	0	.	.	.	.
day		-0.00170	0.001283	132	-1.32	0.1875
day*microbe	*Pp* Pf-5	0.002498	0.001568	132	1.59	0.1134
day*microbe	no	0	.	.	.	.

Type III Tests of Fixed Effects				
Effect	**Num DF**	**Den DF**	**F Value**	**Pr > F**
microbe	1	132	52.66	<.0001
day	1	132	0.33	0.5662
day*microbe	1	132	2.54	0.1134

Table C1-25. ANOVA table of total soluble Fe concentrations in nano-metaVT-SPE and nano-CT-metaVT-SPE suspensions with *Pp* Pf-5 inoculation (Figure 2-9b).

Covariance Parameter Estimates				
Cov Parm	**Subject**	**Group**	**Estimate**	**Standard Error**
Intercept	block		5.3985	5.6158
time	rep*material	material CT- metaVT	9.3286	1.6177
time	rep*material	material metaVT	10.9106	1.8781
Solutions for Fixed Effects							
Effect	**material**	**Estimate**	**Standard Error**	**DF**	**t Value**	**Pr > |t|**
Intercept		37.0210	1.5181	2	24.39	0.0017
material	CT-metaVT	5.0493	0.9680	138	5.22	<.0001
material	metaVT	0	.	.	.	.
day		0.2217	0.1699	138	1.30	0.1941
day*material	CT-metaVT	-0.03189	0.2314	138	-0.14	0.8906
day*material	metaVT	0	.	.	.	.
Type III Tests of Fixed Effects				
Effect	**Num DF**	**Den DF**	**F Value**	**Pr > F**
material	1	138	27.21	<.0001
day	1	138	3.16	0.0776
day*material	1	138	0.02	0.8906

Table C1-26. ANOVA table of total soluble P concentrations in nano-metaVT-SPE and nano-CT-metaVT-SPE suspensions with *Pp* Pf-5 inoculation (Figure 2-9d).

Covariance Parameter Estimates				
Cov Parm	**Subject**	**Group**	**Estimate**	**Standard Error**
Intercept	block		0	.
time	rep*material	material CT-metaVT	1403.06	237.09
time	rep*material	material metaVT	1537.80	260.03
Solutions for Fixed Effects						
Effect	**material**	**Estimate**	**Standard Error**	**DF**	**t Value**	**Pr > |t|**
Intercept		561.83	8.4377	2	66.59	0.0002
material	CT-metaVT	93.8870	11.6684	138	8.05	<.0001
material	metaVT	0	.	.	.	.
day		3.6190	2.0170	138	1.79	0.0750
day*material	CT-metaVT	-7.0736	2.7893	138	-2.54	0.0123
day*material	metaVT	0	.	.	.	.
Type III Tests of Fixed Effects				
Effect	**Num DF**	**Den DF**	**F Value**	**Pr > F**
material	1	138	64.74	<.0001
day	1	138	0.00	0.9531
day*material	1	138	6.43	0.0123

Table C1-27. ANOVA table of pH in nano-metaVT-SPE and nano-CT-metaVT-SPE suspensions with *Pp* Pf-5 inoculation (Figure 2-10b).

Covariance Parameter Estimates				
Cov Parm	**Subject**	**Group**	**Estimate**	**Standard Error**
Intercept	block		0.01452	0.01528
time	rep*material	material CT-metaVT	0.06262	0.01112
time	rep*material	material metaVT	0.02371	0.004260
Solutions for Fixed Effects						
Effect	**material**	**Estimate**	**Standard Error**	**DF**	**t Value**	**Pr > |t|**
Intercept		7.7584	0.07788	2	99.62	0.0001
material	CT-metaVT	-0.1103	0.06671	126	-1.65	0.1009
material	metaVT	0	.	.	.	.
day		0.01454	0.008085	126	1.80	0.0745
day*material	CT-metaVT	0.008819	0.01542	126	0.57	0.5683
day*material	metaVT	0	.	.	.	.
Type III Tests of Fixed Effects				
Effect	**Num DF**	**Den DF**	**F Value**	**Pr > F**
material	1	126	2.73	0.1009
day	1	126	6.04	0.0154
day*material	1	126	0.33	0.5683

Table C1-28. ANOVA table of EC in nano-metaVT-SPE and nano-CT-metaVT-SPE suspensions with *Pp* Pf-5 inoculation (Figure 2-10d).

Covariance Parameter Estimates				
Cov Parm	**Subject**	**Group**	**Estimate**	**Standard Error**
Intercept	block		0.000441	0.000446
time	rep*material	material CT-metaVT	0.000246	0.000044
time	rep*material	material metaVT	0.000166	0.000030

Solutions for Fixed Effects						
Effect	**material**	**Estimate**	**Standard Error**	**DF**	**t Value**	**Pr > |t|**
Intercept		0.3508	0.01248	2	28.12	0.0013
material	CT-metaVT	0.007075	0.004609	126	1.54	0.1273
material	metaVT	0	.	.	.	.
day		0.001370	0.000677	126	2.02	0.0451
day*material	CT-metaVT	-0.00071	0.001065	126	-0.67	0.5061
day*material	metaVT	0	.	.	.	.

Type III Tests of Fixed Effects				
Effect	**Num DF**	**Den DF**	**F Value**	**Pr > F**
material	1	126	2.36	0.1273
day	1	126	3.63	0.0591
day*material	1	126	0.44	0.5061

C.2 ANOVA tables for Chapter 3

Table C2-1. ANOVA table of bacterial culturability of *Pp* Pf-5 with various Fe sources with a dose of 33.3 mg Fe L^{-1} without salinity stress (EC = 1.3 dS·m^{-1}) (Figure 3-1a).

Type III Tests of Fixed Effects				
Effect	**Num DF**	**Den DF**	**F Value**	**Pr > F**
Fe source	3	16	38.35	<.0001
time	1	16	1046.25	<.0001
Fe source*time	3	16	20.76	<.0001

Fe source* time Least Squares Means						
Fe source	**time**	**Estimate**	**Standard Error**	**DF**	**t Value**	**Pr > |t|**
CT-metaVT	0	6.0644	0.06847	16	88.57	<.0001
CT-metaVT	72	7.3654	0.06847	16	107.57	<.0001
Fe-EDDHA	0	6.2546	0.06847	16	91.34	<.0001
Fe-EDDHA	72	8.3016	0.06847	16	121.24	<.0001
metaVT	0	6.1221	0.06847	16	89.41	<.0001
metaVT	72	7.9404	0.06847	16	115.96	<.0001
control	0	6.0754	0.06847	16	88.73	<.0001
control	72	7.1737	0.06847	16	104.77	<.0001
Tukey-Kramer Grouping for Fe source*time Least Squares Means (Alpha=0.05)						
LS-means with the same letter are not significantly different.						
Fe source	**time**	**Estimate**				
Fe-EDDHA	72	8.3016		A		EDDHA
metaVT	72	7.9404		B		VT
CT-metaVT	72	7.3654		C		CTVT
				C		
control	72	7.1737		C		con
EDDHA	0	6.2546		D		EDDHA
				D		
metaVT	0	6.1221		D		VT

			D	
control	0	6.0754	D	con
			D	
CT-metaVT	0	6.0644	D	CTVT

Table C2-2. ANOVA table of bacterial culturability of *Pp* Pf-5 with various Fe sources with a dose of 33.3 mg Fe L^{-1} under salinity stress (EC = 10 dS·m^{-1}) (Figure 3-1b).

Type III Tests of Fixed Effects				
Effect	**Num DF**	**Den DF**	**F Value**	**Pr > F**
Fe source	3	16	71.28	<.0001
time	1	16	99.35	<.0001
Fe source*time	3	16	66.02	<.0001

Fe source* time Least Squares Means						
Fe source	**time**	**Estimate**	**Standard Error**	**DF**	**t Value**	**Pr > |t|**
CT-metaVT	0	5.7402	0.07217	16	79.53	<.0001
CT-metaVT	72	6.8838	0.07217	16	95.38	<.0001
Fe-EDDHA	0	6.1854	0.07217	16	85.70	<.0001
Fe-EDDHA	72	6.8644	0.07217	16	95.11	<.0001
metaVT	0	6.0555	0.07217	16	83.90	<.0001
metaVT	72	6.9699	0.07217	16	96.57	<.0001
control	0	5.9617	0.07217	16	82.60	<.0001
control	72	5.2594	0.07217	16	72.87	<.0001

Tukey-Kramer Grouping for Fe source*time Least Squares Means (Alpha=0.05)				
LS-means with the same letter are not significantly different.				
Fe source	**time**	**Estimate**		
metaVT	72	6.9699		A
				A
CT-metaVT	72	6.8838		A
				A
Fe-EDDHA	72	6.8644		A
Fe-EDDHA	0	6.1854		B
				B
metaVT	0	6.0555	C	B
			C	B
control	0	5.9617	C	B
			C	
CT-metaVT	0	5.7402	C	
control	72	5.2594		D

Table C2-3. ANOVA table of shoot length of wheat grown in the sand with the four Fe treatments (control, nano-metaVT, nano-CT-metaVT, and Fe-EDDHA) (Figure 3-2a).

Covariance Parameter Estimates		
Cov Parm	Estimate	Standard Error
block	0.5686	0.6176
Residual	2.3498	0.2972
Type III Tests of Fixed Effects				
Effect	Num DF	Den DF	F Value	Pr > F
Fe source	3	125	10.23	<.0001
salt	1	125	403.31	<.0001
microbe	1	125	13.77	0.0003
Fe source*microbe	3	125	0.11	0.9555
Fe source*salt	3	125	0.65	0.5846
microbe*salt	1	125	3.30	0.0718
Fe sourc*microbe*salt	3	125	0.05	0.9837

salt Least Squares Means					
salt	Estimate	Standard Error	DF	t Value	Pr > |t|
10	17.3448	0.4719	125	36.76	<.0001
1.3	22.4958	0.4714	125	47.73	<.0001
Tukey-Kramer Grouping for salt Least Squares Means (Alpha=0.05)					
LS-means with the same letter are not significantly different.					
salt		Estimate			
1.3		22.4958		A	
10		17.3448		B	

Fe source Least Squares Means					
Fe source	Estimate	Standard Error	DF	t Value	Pr > |t|
CT-metaVT	20.2028	0.5048	125	40.02	<.0001
EDDHA	20.8139	0.5048	125	41.23	<.0001
metaVT	19.7980	0.5068	125	39.06	<.0001
control	18.8667	0.5048	125	37.38	<.0001
Tukey-Kramer Grouping for Fesource Least Squares Means (Alpha=0.05)					

LS-means with the same letter are not significantly different.			
Fe source	**Estimate**		
Fe-EDDHA	20.8139		A
			A
CT-metaVT	20.2028	B	A
		B	
metaVT	19.7980	B	C
			C
control	18.8667		C

microbe Least Squares Means					
microbe	**Estimate**	**Standard Error**	**DF**	**t Value**	**Pr > |t|**
Pp Pf-5	20.3962	0.4719	125	43.22	<.0001
no	19.4444	0.4714	125	41.25	<.0001
Tukey-Kramer Grouping for microbe Least Squares Means (Alpha=0.05)					
LS-means with the same letter are not significantly different.					
microbe		**Estimate**			
Pp Pf-5		20.3962		A	
no		19.4444		B	

Table C2-4. ANOVA table of shoot dry mass of wheat grown in the sand with the four Fe

treatments (control, nano-metaVT, nano-CT-metaVT, and Fe-EDDHA) (Figure 3-2b).

Covariance Parameter Estimates		
Cov Parm	Estimate	Standard Error
block	0.000012	0.000012
Residual	8.414E-6	1.064E-6
Type III Tests of Fixed Effects				
Effect	Num DF	Den DF	F Value	Pr > F
Fe source	3	125	3.81	0.0119
salt	1	125	431.08	<.0001
microbe	1	125	2.07	0.1529
Fe source*microbe	3	125	0.15	0.9265
Fe source*salt	3	125	1.67	0.1770
microbe*salt	1	125	0.75	0.3894
Fe sourc*microbe*salt	3	125	0.31	0.8191

salt Least Squares Means					
salt	Estimate	Standard Error	DF	t Value	Pr > |t|
10	0.01524	0.002013	125	7.57	<.0001
1.3	0.02532	0.002013	125	12.58	<.0001
Tukey-Kramer Grouping for salt Least Squares Means (Alpha=0.05)					
LS-means with the same letter are not significantly different.					
salt		Estimate			
1.3		0.02532		A	
10		0.01524		B	

Fe source Least Squares Means					
Fe source	Estimate	Standard Error	DF	t Value	Pr > |t|
CT-metaVT	0.02045	0.002042	125	10.01	<.0001
Fe-EDDHA	0.02152	0.002042	125	10.54	<.0001
metaVT	0.01982	0.002043	125	9.70	<.0001
control	0.01934	0.002042	125	9.47	<.0001
Tukey-Kramer Grouping for Fesource Least Squares Means (Alpha=0.05)					
LS-means with the same letter are not significantly different.					

Fe source	Estimate		
Fe-EDDHA	0.02152		A
			A
CT-metaVT	0.02045	B	A
		B	A
metaVT	0.01982	B	A
		B	
control	0.01934	B	

microbe Least Squares Means					
microbe	Estimate	Standard Error	DF	t Value	Pr > |t|
Pp Pf-5	0.02063	0.002013	125	10.25	<.0001
No	0.01993	0.002013	125	9.90	<.0001
Tukey-Kramer Grouping for microbe Least Squares Means (Alpha=0.05)					
LS-means with the same letter are not significantly different.					
microbe		Estimate			
Pp Pf-5		0.02063		A	
				A	
no		0.01993		A	

Table C2-5. ANOVA table of plant transpiration of wheat grown in the sand with the four

Fe treatments (control, nano-metaVT, nano-CT-metaVT, and Fe-EDDHA) (Figure 3-2c).

Covariance Parameter Estimates		
Cov Parm	Estimate	Standard Error
block	0.02034	0.01606
Residual	0.05671	0.007232
Type III Tests of Fixed Effects				
Effect	Num DF	Den DF	F Value	Pr > F
Fe source	3	123	1.93	0.1284
salt	1	123	70.49	<.0001
microbe	1	123	58.46	<.0001
Fe source*microbe	3	123	1.24	0.2966
Fe source*salt	3	123	0.19	0.9047
microbe*salt	1	123	17.57	<.0001
Fe sourc*microbe*salt	3	123	2.44	0.0679

Fe source*microbe*salt Least Squares Means							
Fe source	microbe	salt	Estimate	Standard Error	DF	t Value	Pr > |t|
CT-metaVT	*Pp* Pf-5	10	0.6981	0.1144	123	6.10	<.0001
CT-metaVT	*Pp* Pf-5	1.3	1.5427	0.1144	123	13.49	<.0001
CT-metaVT	no	10	0.2456	0.1144	123	2.15	0.0337
CT-metaVT	no	1.3	1.3697	0.1144	123	11.98	<.0001
Fe-EDDHA	*Pp* Pf-5	10	0.7076	0.1144	123	6.19	<.0001
Fe-EDDHA	*Pp* Pf-5	1.3	1.6972	0.1144	123	14.84	<.0001
Fe-EDDHA	no	10	0.3109	0.1144	123	2.72	0.0075
Fe-EDDHA	no	1.3	1.4239	0.1144	123	12.45	<.0001
metaVT	*Pp* Pf-5	10	0.7734	0.1179	123	6.56	<.0001
metaVT	*Pp* Pf-5	1.3	1.6885	0.1144	123	14.76	<.0001
metaVT	no	10	0.2624	0.1144	123	2.29	0.0235
metaVT	no	1.3	1.4184	0.1144	123	12.40	<.0001
control	*Pp* Pf-5	10	0.8314	0.1144	123	7.27	<.0001
control	*Pp* Pf-5	1.3	1.5471	0.1144	123	13.53	<.0001
control	no	10	0.3046	0.1144	123	2.66	0.0088
control	no	1.3	1.7127	0.1144	123	14.98	<.0001

Tukey-Kramer Grouping for Fe sourc*microbe*salt Least Squares Means (Alpha=0.05)					
LS-means with the same letter are not significantly different.					
Fe source	microbe	salt	Estimate		
control	no	1.3	1.7127		A
					A
Fe-EDDHA	*Pp Pf-5*	1.3	1.6972		A
					A
metaVT	*Pp Pf-5*	1.3	1.6885		A
					A
control	*Pp Pf-5*	1.3	1.5471		A
					A
CT-metaVT	*Pp Pf-5*	1.3	1.5427		A
					A
Fe-EDDHA	no	1.3	1.4239		A
					A
metaVT	no	1.3	1.4184		A
					A
CT-metaVT	no	1.3	1.3697	B	A
				B	
control	*Pp Pf-5*	10	0.8314	B	C
					C
metaVT	*Pp Pf-5*	10	0.7734		C
					C
Fe-EDDHA	*Pp Pf-5*	10	0.7076		C
					C
CT-metaVT	*Pp Pf-5*	10	0.6981	D	C
				D	
Fe-EDDHA	no	10	0.3109	D	E
					E
control	no	10	0.3046		E
					E
metaVT	no	10	0.2624		E
					E
CT-metaVT	no	10	0.2456		E

Table C2-6. ANOVA table of shoot Fe concentrations of wheat grown in the sand with four Fe treatments, control, nano-metaVT, nano-CT-metaVT, and Fe-EDDHA with and without inoculation by *Pp* Pf-5, with EC of 1.3 and 10 dS·m^{-1} (Figure 3-3a).

Covariance Parameter Estimates		
Cov Parm	**Estimate**	**Standard Error**
block	3.2982	3.7391
Residual	21.0956	2.6791
Type III Tests of Fixed Effects					
Effect	**Num DF**	**Den DF**	**F Value**	**Pr > F**	
Fe source	3	124	49.35	<.0001	
salt	1	124	272.32	<.0001	
microbe	1	124	15.86	0.0001	
Fe source*microbe	3	124	0.63	0.6001	
Fe source*salt	3	124	3.03	0.0320	
microbe*salt	1	124	2.28	0.1333	
Fe sourc*microbe*salt	3	124	1.09	0.3550	
Fe source*microbe*salt Least Squares Means							
Fe source	**microbe**	**salt**	**Estimate**	**Standard Error**	**DF**	**t Value**	**Pr > |t|**
CT-metaVT	*Pp* Pf-5	10	55.2814	1.8556	124	29.79	<.0001
CT-metaVT	*Pp* Pf-5	1.3	42.4938	1.8556	124	22.90	<.0001
CT-metaVT	no	10	52.4157	1.8556	124	28.25	<.0001
CT-metaVT	no	1.3	38.5649	1.8556	124	20.78	<.0001
Fe-EDDHA	*Pp* Pf-5	10	64.7928	1.9340	124	33.50	<.0001
Fe-EDDHA	*Pp* Pf-5	1.3	53.0290	1.8556	124	28.58	<.0001
Fe-EDDHA	no	10	66.5612	1.8556	124	35.87	<.0001
Fe-EDDHA	no	1.3	48.1552	1.8556	124	25.95	<.0001
metaVT	*Pp* Pf-5	10	57.2478	1.9340	124	29.60	<.0001
metaVT	*Pp* Pf-5	1.3	43.0874	1.8556	124	23.22	<.0001
metaVT	no	10	52.2234	1.8556	124	28.14	<.0001
metaVT	no	1.3	39.0986	1.8556	124	21.07	<.0001
control	*Pp* Pf-5	10	51.9579	1.8556	124	28.00	<.0001
control	*Pp* Pf-5	1.3	44.3996	1.8556	124	23.93	<.0001
control	no	10	50.4516	1.8556	124	27.19	<.0001
control	no	1.3	40.2358	1.8556	124	21.68	<.0001

Tukey-Kramer Grouping for Fe sourc*microbe*salt Least Squares Means (Alpha=0.05)							
LS-means with the same letter are not significantly different.							
Fe source	microbe	salt	Estimate				
Fe-EDDHA	no	10	66.5612			A	
						A	
Fe-EDDHA	*Pp* Pf-5	10	64.7928	B		A	
				B			
metaVT	*Pp* Pf-5	10	57.2478	B		C	
						C	
CT-metaVT	*Pp* Pf-5	10	55.2814	D		C	
				D		C	
Fe-EDDHA	*Pp* Pf-5	1.3	53.0290	D		C	
				D		C	
CT-metaVT	no	10	52.4157	D		C	
				D		C	
metaVT	no	10	52.2234	D		C	
				D		C	
control	*Pp* Pf-5	10	51.9579	D		C	E
				D		C	E
control	no	10	50.4516	D	F	C	E
				D	F		E
Fe-EDDHA	no	1.3	48.1552	D	F	G	E
					F	G	E
control	*Pp* Pf-5	1.3	44.3996	H	F	G	E
				H	F	G	
metaVT	*Pp* Pf-5	1.3	43.0874	H	F	G	
				H		G	
CT-metaVT	*Pp* Pf-5	1.3	42.4938	H		G	
				H			
control	no	1.3	40.2358	H			
				H			
metaVT	no	1.3	39.0986	H			
				H			
CT-metaVT	no	1.3	38.5649	H			

Table C2-7. ANOVA table of shoot Na concentrations of wheat grown in the sand with four Fe treatments, control, nano-metaVT, nano-CT-metaVT, and Fe-EDDHA with and without inoculation by *Pp* Pf-5, with EC of 1.3 and 10 dS·m^{-1} (Figure 3-3b).

Covariance Parameter Estimates		
Cov Parm	**Estimate**	**Standard Error**
block	0.007209	0.007550
Residual	0.01589	0.002018
Type III Tests of Fixed Effects					

Effect	**Num DF**	**Den DF**	**F Value**	**Pr > F**
Fe source	3	124	7.10	0.0002
salt	1	124	4039.98	<.0001
microbe	1	124	4.85	0.0295
Fe source*microbe	3	124	0.25	0.8612
Fe source*salt	3	124	8.78	<.0001
microbe*salt	1	124	19.12	<.0001
Fe sourc*microbe*salt	3	124	0.00	0.9998

Fe source*microbe*salt Least Squares Means							
Fe source	**microbe**	**salt**	**Estimate**	**Standard Error**	**DF**	**t Value**	**Pr > |t|**
CT-metaVT	*Pp* Pf-5	10	3.0829	0.06457	124	47.75	<.0001
CT-metaVT	*Pp* Pf-5	1.3	1.7739	0.06457	124	27.47	<.0001
CT-metaVT	no	10	3.2245	0.06457	124	49.94	<.0001
CT-metaVT	no	1.3	1.7319	0.06457	124	26.82	<.0001
Fe-EDDHA	*Pp* Pf-5	10	3.1054	0.06628	124	46.85	<.0001
Fe-EDDHA	*Pp* Pf-5	1.3	2.0372	0.06457	124	31.55	<.0001
Fe-EDDHA	no	10	3.2174	0.06457	124	49.83	<.0001
Fe-EDDHA	no	1.3	1.9663	0.06457	124	30.45	<.0001
metaVT	*Pp* Pf-5	10	3.1088	0.06628	124	46.91	<.0001
metaVT	*Pp* Pf-5	1.3	1.7667	0.06457	124	27.36	<.0001
metaVT	no	10	3.2773	0.06457	124	50.76	<.0001
metaVT	no	1.3	1.7431	0.06457	124	27.00	<.0001
control	*Pp* Pf-5	10	3.1142	0.06457	124	48.23	<.0001
control	*Pp* Pf-5	1.3	1.8193	0.06457	124	28.18	<.0001
control	no	10	3.2491	0.06457	124	50.32	<.0001
control	no	1.3	1.7719	0.06457	124	27.44	<.0001

Tukey-Kramer Grouping for Fe sourc*microbe*salt Least Squares Means (Alpha=0.05)					
LS-means with the same letter are not significantly different.					
Fe source	microbe	salt	Estimate		
metaVT	no	10	3.2773		A
					A
control	no	10	3.2491		A
					A
CT-metaVT	no	10	3.2245		A
					A
Fe-EDDHA	no	10	3.2174		A
					A
control	*Pp* Pf-5	10	3.1142		A
					A
metaVT	*Pp* Pf-5	10	3.1088		A
					A
Fe-EDDHA	*Pp* Pf-5	10	3.1054		A
					A
CT-metaVT	*Pp* Pf-5	10	3.0829		A
Fe-EDDHA	*Pp* Pf-5	1.3	2.0372		B
					B
Fe-EDDHA	no	1.3	1.9663	C	B
				C	
control	*Pp* Pf-5	1.3	1.8193	C	D
				C	D
CT-metaVT	*Pp* Pf-5	1.3	1.7739	C	D
				C	D
control	no	1.3	1.7719	C	D
				C	D
metaVT	*Pp* Pf-5	1.3	1.7667	C	D
					D
metaVT	no	1.3	1.7431		D
					D
CT-metaVT	no	1.3	1.7319		D

Table C2-8. ANOVA table of root Fe concentrations of wheat grown in the sand with four Fe treatments, control, nano-metaVT, nano-CT-metaVT, and Fe-EDDHA with and without inoculation by *Pp* Pf-5, with EC of 1.3 and 10 dS·m^{-1} (Figure 3-3c).

Covariance Parameter Estimates		
Cov Parm	**Estimate**	**Standard Error**
block	35009	35492
Residual	23091	2932.53
Type III Tests of Fixed Effects					
Effect	**Num DF**	**Den DF**	**F Value**	**Pr > F**	
Fe source	3	124	15.40	<.0001	
salt	1	124	35.92	<.0001	
microbe	1	124	3.63	0.0592	
Fe source*microbe	3	124	1.25	0.2962	
Fe source*salt	3	124	4.42	0.0055	
microbe*salt	1	124	0.51	0.4773	
Fe sourc*microbe*salt	3	124	0.26	0.8523	
Fe source*microbe*salt Least Squares Means							
Fe source	**microbe**	**salt**	**Estimate**	**Standard Error**	**DF**	**t Value**	**Pr > |t|**
CT-metaVT	*Pp* Pf-5	10	704.85	119.31	124	5.91	<.0001
CT-metaVT	*Pp* Pf-5	1.3	800.31	119.31	124	6.71	<.0001
CT-metaVT	no	10	691.41	119.31	124	5.79	<.0001
CT-metaVT	no	1.3	760.13	119.31	124	6.37	<.0001
Fe-EDDHA	*Pp* Pf-5	10	719.96	120.67	124	5.97	<.0001
Fe-EDDHA	*Pp* Pf-5	1.3	1057.11	119.31	124	8.86	<.0001
Fe-EDDHA	no	10	753.71	119.31	124	6.32	<.0001
Fe-EDDHA	no	1.3	1043.41	119.31	124	8.75	<.0001
metaVT	*Pp* Pf-5	10	676.56	120.67	124	5.61	<.0001
metaVT	*Pp* Pf-5	1.3	839.37	119.31	124	7.04	<.0001
metaVT	no	10	672.87	119.31	124	5.64	<.0001
metaVT	no	1.3	736.76	119.31	124	6.18	<.0001
control	*Pp* Pf-5	10	671.36	119.31	124	5.63	<.0001
control	*Pp* Pf-5	1.3	760.76	119.31	124	6.38	<.0001
control	no	10	533.11	119.31	124	4.47	<.0001
control	no	1.3	650.01	119.31	124	5.45	<.0001

Tukey-Kramer Grouping for Fe source*microbe*salt Least Squares Means (Alpha=0.05)						
LS-means with the same letter are not significantly different.						
Fe source	microbe	salt	Estimate			
Fe-EDDHA	*Pp* Pf-5	1.3	1057.11		A	
					A	
Fe-EDDHA	no	1.3	1043.41	B	A	
				B	A	
metaVT	*Pp* Pf-5	1.3	839.37	B	A	C
				B		C
CT-metaVT	*Pp* Pf-5	1.3	800.31	B		C
						C
control	*Pp* Pf-5	1.3	760.76		D	C
					D	C
CT-metaVT	no	1.3	760.13		D	C
					D	C
Fe-EDDHA	no	10	753.71		D	C
					D	C
metaVT	no	1.3	736.76		D	C
					D	C
Fe-EDDHA	*Pp* Pf-5	10	719.96		D	C
					D	C
CT-metaVT	*Pp* Pf-5	10	704.85		D	C
					D	C
CT-metaVT	no	10	691.41		D	C
					D	C
metaVT	*Pp* Pf-5	10	676.56		D	C
					D	C
metaVT	no	10	672.87		D	C
					D	C
control	*Pp* Pf-5	10	671.36		D	C
					D	C
control	no	1.3	650.01		D	C
					D	
control	no	10	533.11		D	

Table C2-9. ANOVA table of root Na concentrations of wheat grown in the sand with four Fe treatments, control, nano-metaVT, nano-CT-metaVT, and Fe-EDDHA with and without inoculation by *Pp* Pf-5, with EC of 1.3 and 10 dS·m^{-1} (Figure 3-3d)

Covariance Parameter Estimates		
Cov Parm	**Estimate**	**Standard Error**
block	0.001892	0.002007
Residual	0.005476	0.000695
Type III Tests of Fixed Effects					
Effect	**Num DF**	**Den DF**	**F Value**	**Pr > F**
Fe source	3	124	30.82	<.0001
salt	1	124	474.09	<.0001
microbe	1	124	0.61	0.4362
Fe source*microbe	3	124	1.38	0.2535
Fe source*salt	3	124	35.04	<.0001
microbe*salt	1	124	1.04	0.3090
Fe sourc*microbe*salt	3	124	0.43	0.7326
Fe source*microbe*salt Least Squares Means							
Fe source	**microbe**	**salt**	**Estimate**	**Standard Error**	**DF**	**t Value**	**Pr > |t|**
CT-metaVT	*Pp* Pf-5	10	3.6886	0.03520	124	104.78	<.0001
CT-metaVT	*Pp* Pf-5	1.3	3.3905	0.03520	124	96.32	<.0001
CT-metaVT	no	10	3.7075	0.03520	124	105.32	<.0001
CT-metaVT	no	1.3	3.4004	0.03520	124	96.60	<.0001
Fe-EDDHA	*Pp* Pf-5	10	3.6956	0.03628	124	101.86	<.0001
Fe-EDDHA	*Pp* Pf-5	1.3	3.6387	0.03520	124	103.37	<.0001
Fe-EDDHA	no	10	3.7409	0.03520	124	106.27	<.0001
Fe-EDDHA	no	1.3	3.6918	0.03520	124	104.87	<.0001
metaVT	*Pp* Pf-5	10	3.7208	0.03628	124	102.55	<.0001
metaVT	*Pp* Pf-5	1.3	3.3746	0.03520	124	95.86	<.0001
metaVT	no	10	3.7273	0.03520	124	105.88	<.0001
metaVT	no	1.3	3.3480	0.03520	124	95.11	<.0001
control	*Pp* Pf-5	10	3.7610	0.03520	124	106.84	<.0001
control	*Pp* Pf-5	1.3	3.4301	0.03520	124	97.44	<.0001
control	no	10	3.7798	0.03520	124	107.37	<.0001
control	no	1.3	3.3818	0.03520	124	96.07	<.0001

Tukey-Kramer Grouping for Fe source*microbe*salt Least Squares Means (Alpha=0.05)					
LS-means with the same letter are not significantly different.					
Fe source	microbe	salt	Estimate		
control	no	10	3.7798		A
					A
control	*Pp* Pf-5	10	3.7610		A
					A
metaVT	no	10	3.7409	B	A
				B	A
metaVT	no	10	3.7273	B	A
				B	A
metaVT	*Pp* Pf-5	10	3.7208	B	A
				B	A
CT-metaVT	no	10	3.7075	B	A
				B	A
metaVT	*Pp* Pf-5	10	3.6956	B	A
				B	A
metaVT	no	1.3	3.6918	B	A
				B	A
CT-metaVT	*Pp* Pf-5	10	3.6886	B	A
				B	
metaVT	*Pp* Pf-5	1.3	3.6387	B	
control	*Pp* Pf-5	1.3	3.4301		C
					C
CT-metaVT	no	1.3	3.4004		C
					C
CT-metaVT	*Pp* Pf-5	1.3	3.3905		C
					C
control	no	1.3	3.3818		C
					C
metaVT	*Pp* Pf-5	1.3	3.3746		C
					C
metaVT	no	1.3	3.3480		C

Table C2-10. ANOVA table of bacterial culturability of *Pp* Pf-5 in sand pore water extraction without salinity stress (EC = 1.3 dS·m^{-1}) and under salinity stress (EC = 10 dS·m^{-1}) (Figure 3-5).

Covariance Parameter Estimates		
Cov Parm	Estimate	Standard Error
block	0	.
Residual	0.03098	0.005521
Type III Tests of Fixed Effects				
Effect	Num DF	Den DF	F Value	Pr > F
Fe source	3	62	6.21	0.0009
salt	1	62	25.91	<.0001
Fe source*salt	3	62	7.75	0.0002

Fe source*salt Least Squares Means						
Fe source	salt	Estimate	Standard Error	DF	t Value	Pr > |t|
CT-metaVT	10	7.2453	0.05867	62	123.48	<.0001
CT-metaVT	1.3	7.3993	0.05867	62	126.11	<.0001
Fe-EDDHA	10	7.4210	0.05867	62	126.48	<.0001
Fe-EDDHA	1.3	7.4297	0.05867	62	126.63	<.0001
metaVT	10	6.9706	0.06223	62	112.01	<.0001
metaVT	1.3	7.5238	0.05867	62	128.23	<.0001
control	10	7.1170	0.05867	62	121.30	<.0001
control	1.3	7.2524	0.05867	62	123.60	<.0001
Tukey-Kramer Grouping for Fe source*salt Least Squares Means (Alpha=0.05)						
LS-means with the same letter are not significantly different.						
Fe source	salt	Estimate				
metaVT	1.3	7.5238				A
						A
Fe-EDDHA	1.3	7.4297		B		A
				B		A
Fe-EDDHA	10	7.4210		B		A
				B		A
CT-metaVT	1.3	7.3993		B		A

			B	
control	1.3	7.2524	B	C
			B	C
CT-metaVT	10	7.2453	B	C
				C
control	10	7.1170	D	C
			D	
metaVT	10	6.9706	D	

C.3 ANOVA tables for Chapter 4

Table C3-1. ANOVA table of shoot dry mass of wheat grown with four Fe treatments, control, nano-metaVT, nano-CT-metaVT, and Fe-EDDHA, and irrigated with ddH_2O and saline water ($EC = 4$ dS·m^{-1}) (Figure 4-3a).

Covariance Parameter Estimates		
Cov Parm	**Estimate**	**Standard Error**
block	0.000034	0.000065
Residual	0.000599	0.000107
Type III Tests of Fixed Effects				
Effect	**Num DF**	**Den DF**	**F Value**	**Pr > F**
Fe source	3	63	2.97	0.0386
salt	1	63	75.63	<.0001
Fe source*salt	3	63	0.26	0.8508

salt Least Squares Means					
salt	**Estimate**	**Standard Error**	**DF**	**t Value**	**Pr > |t|**
saline water	0.1220	0.007285	63	16.75	<.0001
ddH$_2$O	0.1722	0.007285	63	23.64	<.0001
Tukey-Kramer Grouping for salt Least Squares Means (Alpha=0.05)					
LS-means with the same letter are not significantly different.					
salt		**Estimate**			
ddH$_2$O		0.1722			A
saline water		0.1220			B

Fe source Least Squares Means					
Fe source	**Estimate**	**Standard Error**	**DF**	**t Value**	**Pr > |t|**
CT-metaVT	0.1560	0.008348	63	18.68	<.0001
Fe-EDDHA	0.1380	0.008348	63	16.53	<.0001
metaVT	0.1555	0.008348	63	18.62	<.0001
control	0.1391	0.008348	63	16.66	<.0001
Tukey-Kramer Grouping for Fesource Least Squares Means (Alpha=0.05)					
LS-means with the same letter are not significantly different.					

Fe source	Estimate		
CT-metaVT	0.1560	A	
		A	
metaVT	0.1555	A	
		A	
control	0.1391	A	
		A	
Fe-EDDHA	0.1380	A	

Table C3-2. ANOVA table of shoot dry mass of beans grown with four Fe treatments, control, nano-metaVT, nano-CT-metaVT, and Fe-EDDHA, and irrigated with ddH_2O and saline water (EC = 4 dS·m^{-1}) (Figure 4-3b).

Covariance Parameter Estimates		
Cov Parm	**Estimate**	**Standard Error**
block	0	.
Residual	0.2559	0.04672
Type III Tests of Fixed Effects				
Effect	**Num DF**	**Den DF**	**F Value**	**Pr > F**
Fe source	3	59	1.92	0.1359
salt	1	59	44.15	<.0001
Fe source*salt	3	59	0.69	0.5647

salt Least Squares Means					
salt	**Estimate**	**Standard Error**	**DF**	**t Value**	**Pr > |t|**
saline water	1.1612	0.08854	59	13.12	<.0001
ddH_2O	1.9796	0.08562	59	23.12	<.0001
Tukey-Kramer Grouping for salt Least Squares Means (Alpha=0.05)					
LS-means with the same letter are not significantly different.					
salt		**Estimate**			
ddH_2O		1.9796		A	
saline water		1.1612		B	

Fe source Least Squares Means					
Fe source	**Estimate**	**Standard Error**	**DF**	**t Value**	**Pr > |t|**
CT-metaVT	1.6234	0.1275	59	12.74	<.0001
Fe-EDDHA	1.5519	0.1229	59	12.63	<.0001
metaVT	1.7541	0.1229	59	14.27	<.0001
control	1.3524	0.1192	59	11.34	<.0001
Tukey-Kramer Grouping for Fe source Least Squares Means (Alpha=0.05)					
LS-means with the same letter are not significantly different.					
Fe source		**Estimate**			
metaVT		1.7541		A	

		A	
CT-metaVT	1.6234	A	
		A	
Fe-EDDHA	1.5519	A	
		A	
control	1.3524	A	

Table C3-3. ANOVA table of root dry mass of wheat grown with four Fe treatments, control, nano-metaVT, nano-CT-metaVT, and Fe-EDDHA, and irrigated with ddH$_2$O and saline water (EC = 4 dS·m^{-1}) (Figure 4-3c).

Covariance Parameter Estimates		
Cov Parm	**Estimate**	**Standard Error**
block	0.002578	0.004141
Residual	0.01677	0.002989
Type III Tests of Fixed Effects				
Effect	**Num DF**	**Den DF**	**F Value**	**Pr > F**
Fe source	3	63	5.06	0.0034
salt	1	63	3.43	0.0687
Fe source*salt	3	63	4.47	0.0065

Fe source*salt Least Squares Means						
Fe source	**salt**	**Estimate**	**Standard Error**	**DF**	**t Value**	**Pr > |t|**
CT-metaVT	saline water	2.7464	0.05563	63	49.37	<.0001
CT-metaVT	ddH$_2$O	2.7680	0.05563	63	49.76	<.0001
Fe-EDDHA	saline water	2.6353	0.05563	63	47.37	<.0001
Fe-EDDHA	ddH$_2$O	2.8798	0.05563	63	51.77	<.0001
metaVT	saline water	2.7952	0.05563	63	50.25	<.0001
metaVT	ddH$_2$O	2.8046	0.05563	63	50.42	<.0001
control	saline water	2.6650	0.05563	63	47.91	<.0001
control	ddH$_2$O	2.6155	0.05563	63	47.02	<.0001
Tukey-Kramer Grouping for Fe source*salt Least Squares Means (Alpha=0.05)						
LS-means with the same letter are not significantly different.						
Fe source	**salt**	**Estimate**				
Fe-EDDHA	ddH$_2$O	2.8798				A
						A
metaVT	ddH$_2$O	2.8046	B			A
			B			A
metaVT	saline water	2.7952	B			A
			B			A
CT-metaVT	ddH$_2$O	2.7680	B			A

			B	A
CT-metaVT	saline water	2.7464	B	A
			B	
control	saline water	2.6650	B	
			B	
Fe-EDDHA	saline water	2.6353	B	
			B	
control	ddH$_2$O	2.6155	B	

Table C3-4. ANOVA table of root dry mass of beans grown with four Fe treatments, control, nano-metaVT, nano-CT-metaVT, and Fe-EDDHA, and irrigated with ddH$_2$O and saline water (EC = 4 dS·m^{-1}) (Figure 4-3d).

Covariance Parameter Estimates		
Cov Parm	**Estimate**	**Standard Error**
block	0	.
Residual	0.2823	0.05155
Type III Tests of Fixed Effects				
Effect	**Num DF**	**Den DF**	**F Value**	**Pr > F**
Fe source	3	59	3.21	0.0294
salt	1	59	1.05	0.3086
Fe source*salt	3	59	0.20	0.8973

salt Least Squares Means					
salt	**Estimate**	**Standard Error**	**DF**	**t Value**	**Pr > |t|**
saline water	1.1924	0.09299	59	12.82	<.0001
ddH$_2$O	1.3253	0.08993	59	14.74	<.0001
Tukey-Kramer Grouping for salt Least Squares Means (Alpha=0.05)					
LS-means with the same letter are not significantly different.					
salt		**Estimate**			
ddH$_2$O		1.3253		A	
				A	
saline water		1.1924		A	

Fe source Least Squares Means					
Fe source	**Estimate**	**Standard Error**	**DF**	**t Value**	**Pr > |t|**
CT-metaVT	1.5572	0.1339	59	11.63	<.0001
Fe-EDDHA	1.2350	0.1291	59	9.57	<.0001
metaVT	1.2542	0.1291	59	9.72	<.0001
control	0.9890	0.1252	59	7.90	<.0001
Tukey-Kramer Grouping for Fe source Least Squares Means (Alpha=0.05)					
LS-means with the same letter are not significantly different.					
Fe source	**Estimate**				
CT-metaVT	1.5572			A	

			A
metaVT	1.2542	B	A
		B	A
Fe-EDDHA	1.2350	B	A
		B	
control	0.9890	B	

Table C3-5. ANOVA table of shoot water content of wheat grown with four Fe treatments: control, nano-metaVT, nano-CT-metaVT, and Fe-EDDHA, and irrigated with ddH$_2$O or saline water (EC = 4 dS·m^{-1}) (Figure 4-4a).

Covariance Parameter Estimates		
Cov Parm	**Estimate**	**Standard Error**
block	0	.
Residual	1.3708	0.2423
Type III Tests of Fixed Effects				
Effect	**Num DF**	**Den DF**	**F Value**	**Pr > F**
Fe source	3	63	3.18	0.0299
salt	1	63	10.44	0.0020
Fe source*salt	3	63	1.57	0.2043

salt Least Squares Means					
salt	**Estimate**	**Standard Error**	**DF**	**t Value**	**Pr > |t|**
saline water	4	80.9204	0.1951	63	414.69
ddH$_2$O	no	80.0289	0.1951	63	410.12
Tukey-Kramer Grouping for salt Least Squares Means (Alpha=0.05)					
LS-means with the same letter are not significantly different.					
salt		**Estimate**			
ddH$_2$O		80.9204		A	
saline water		80.0289		B	

Fe source Least Squares Means					
Fe source	**Estimate**	**Standard Error**	**DF**	**t Value**	**Pr > |t|**
CT-metaVT	80.7298	0.2760	63	292.54	<.0001
Fe-EDDHA	79.8712	0.2760	63	289.43	<.0001
metaVT	80.9931	0.2760	63	293.49	<.0001
control	80.3044	0.2760	63	291.00	<.0001
Tukey-Kramer Grouping for Fe source Least Squares Means (Alpha=0.05)					
LS-means with the same letter are not significantly different.					
Fe source	**Estimate**				
metaVT	80.9931		A		

			A
CT-metaVT	80.7298	B	A
		B	A
control	80.3044	B	A
		B	
Fe-EDDHA	79.8712	B	

Table C3-6. ANOVA table of shoot water content of beans grown with four Fe

treatments: control, nano-metaVT, nano-CT-metaVT, and Fe-EDDHA, and irrigated with

ddH$_2$O or saline water (EC = 4 dS·m^{-1}) (Figure 4-4b).

Covariance Parameter Estimates		
Cov Parm	Estimate	Standard Error
block	0.7238	1.0972
Residual	2.3784	0.4379
Type III Tests of Fixed Effects				
Effect	Num DF	Den DF	F Value	Pr > F
Fe source	3	59	1.33	0.2737
salt	1	59	98.61	<.0001
Fe source*salt	3	59	0.82	0.4905

salt Least Squares Means					
salt	Estimate	Standard Error	DF	t Value	Pr > |t|
saline water	84.7517	0.5158	59	164.31	<.0001
ddH$_2$O	81.0231	0.5121	59	158.23	<.0001
Tukey-Kramer Grouping for salt Least Squares Means (Alpha=0.05)					
LS-means with the same letter are not significantly different.					
salt	Estimate				
ddH$_2$O	84.7517	A			
saline water	81.0231	B			

Fe source Least Squares Means					
Fe source	Estimate	Standard Error	DF	t Value	Pr > |t|
CT-metaVT	83.0028	0.5757	59	144.17	<.0001
Fe-EDDHA	82.2546	0.5889	59	139.68	<.0001
metaVT	83.0861	0.5783	59	143.66	<.0001
control	83.2061	0.5711	59	145.68	<.0001
Tukey-Kramer Grouping for Fe source Least Squares Means (Alpha=0.05)					
LS-means with the same letter are not significantly different.					
Fe source	Estimate				
CT-metaVT	83.2061	A			

		A	
metaVT	83.0861	A	
		A	
Fe-EDDHA	83.0028	A	
		A	
control	82.2546	A	

Table C3-7. ANOVA table of relative chlorophyll content of wheat grown with four Fe treatments: control, nano-metaVT, nano-CT-metaVT, and Fe-EDDHA, and irrigated with ddH$_2$O or saline water (EC = 4 dS·m^{-1}) (Figure 4-4c).

Covariance Parameter Estimates		
Cov Parm	Estimate	Standard Error
block	0.1712	0.9939
Residual	25.3654	4.5195
Type III Tests of Fixed Effects				
Effect	Num DF	Den DF	F Value	Pr > F
Fe source	3	63	0.27	0.8502
salt	1	63	0.26	0.6093
Fe source*salt	3	63	0.24	0.8711

salt Least Squares Means					
salt	Estimate	Standard Error	DF	t Value	Pr > |t|
saline water	35.6239	1.1054	63	32.23	<.0001
ddH$_2$O	36.2337	1.1054	63	32.78	<.0001
Tukey-Kramer Grouping for salt Least Squares Means (Alpha=0.05)					
LS-means with the same letter are not significantly different.					
salt	Estimate				
ddH$_2$O	36.2337			A	
				A	
saline water	35.6239			A	

Fe source Least Squares Means					
Fe source	Estimate	Standard Error	DF	t Value	Pr > |t|
CT-metaVT	36.6923	1.3880	63	26.44	<.0001
Fe-EDDHA	35.8184	1.3880	63	25.81	<.0001
metaVT	35.9978	1.3880	63	25.94	<.0001
control	35.2067	1.3880	63	25.37	<.0001
Tukey-Kramer Grouping for Fe source Least Squares Means (Alpha=0.05)					
LS-means with the same letter are not significantly different.					
Fe source	Estimate				
CT-metaVT	36.6923		A		

		A	
metaVT	35.9978	A	
		A	
Fe-EDDHA	35.8184	A	
		A	
control	35.2067	A	

Table C3-8. ANOVA table of relative chlorophyll content of beans grown with four Fe treatments: control, nano-metaVT, nano-CT-metaVT, and Fe-EDDHA, and irrigated with ddH$_2$O or saline water (EC = 4 dS·m^{-1}) (Figure 4-4d).

Covariance Parameter Estimates		
Cov Parm	**Estimate**	**Standard Error**
block	1.0985	1.7063
Residual	4.9361	0.9088
Type III Tests of Fixed Effects				
Effect	**Num DF**	**Den DF**	**F Value**	**Pr > F**
Fe source	3	59	3.29	0.0266
salt	1	59	72.48	<.0001
Fe source*salt	3	59	1.92	0.1364

salt Least Squares Means					
salt	**Estimate**	**Standard Error**	**DF**	**t Value**	**Pr > |t|**
saline water	39.8892	0.7366	59	54.15	<.0001
ddH$_2$O	44.4944	0.7311	59	60.86	<.0001
Tukey-Kramer Grouping for salt Least Squares Means (Alpha=0.05)					
LS-means with the same letter are not significantly different.					
salt	**Estimate**				
ddH$_2$O	44.4944			A	
saline water	39.8892			B	

Fe source Least Squares Means					
Fe source	**Estimate**	**Standard Error**	**DF**	**t Value**	**Pr > |t|**
CT-metaVT	42.6836	0.8240	59	51.80	<.0001
Fe-EDDHA	42.5614	0.8423	59	50.53	<.0001
metaVT	42.7662	0.8273	59	51.69	<.0001
control	40.7558	0.8169	59	49.89	<.0001
Tukey-Kramer Grouping for Fe source Least Squares Means (Alpha=0.05)					
LS-means with the same letter are not significantly different.					
Fe source	**Estimate**				
metaVT	42.7662			A	

			A
CT-metaVT	42.6836	B	A
		B	A
Fe-EDDHA	42.5614	B	A
		B	
control	40.7558	B	

Table C3-9. ANOVA table of shoot Fe concentrations of wheat grown in the sand with four Fe treatments, control, nano-metaVT, nano-CT-metaVT, and Fe-EDDHA, and irrigated with ddH_2O or saline water (EC = 4 dS·m^{-1}) (Figure 4-5a).

Covariance Parameter Estimates		
Cov Parm	**Estimate**	**Standard Error**
block	0	.
Residual	353.77	63.0323
Type III Tests of Fixed Effects				
Effect	**Num DF**	**Den DF**	**F Value**	**Pr > F**
Fe source	3	62	0.85	0.4733
salt	1	62	21.16	<.0001
Fe source*salt	3	62	1.80	0.1558

salt Least Squares Means					
salt	**Estimate**	**Standard Error**	**DF**	**t Value**	**Pr > |t|**
saline water	70.0599	3.1834	62	22.01	<.0001
ddH_2O	49.5074	3.1348	62	15.79	<.0001
Tukey-Kramer Grouping for salt Least Squares Means (Alpha=0.05)					
LS-means with the same letter are not significantly different.					
salt	**Estimate**				
ddH_2O	70.0599	A			
saline water	49.5074	B			

Fe source Least Squares Means					
Fe source	**Estimate**	**Standard Error**	**DF**	**t Value**	**Pr > |t|**
CT-metaVT	59.5552	4.4333	62	13.43	<.0001
Fe-EDDHA	58.2844	4.5697	62	12.75	<.0001
metaVT	65.4589	4.4333	62	14.77	<.0001
control	55.8361	4.4333	62	12.59	<.0001
Tukey-Kramer Grouping for Fe source Least Squares Means (Alpha=0.05)					
LS-means with the same letter are not significantly different.					
Fe source	**Estimate**				
metaVT	65.4589	A			

		A	
CT-metaVT	59.5552	A	
		A	
Fe-EDDHA	58.2844	A	
		A	
control	55.8361	A	

Table C3-10. ANOVA table of shoot Fe concentrations of beans grown in the sand with four Fe treatments, control, nano-metaVT, nano-CT-metaVT, and Fe-EDDHA, and irrigated with ddH$_2$O or saline water (EC = 4 dS·m^{-1}) (Figure 4-5b).

Covariance Parameter Estimates		
Cov Parm	Estimate	Standard Error
block	0	.
Residual	277.25	50.6184
Type III Tests of Fixed Effects				
Effect	Num DF	Den DF	F Value	Pr > F
Fe source	3	59	5.84	0.0015
salt	1	59	0.20	0.6555
Fe source*salt	3	59	0.22	0.8853

salt Least Squares Means					
salt	Estimate	Standard Error	DF	t Value	Pr > |t|
saline water	83.7710	2.9141	59	28.75	<.0001
ddH$_2$O	85.5886	2.8182	59	30.37	<.0001
Tukey-Kramer Grouping for salt Least Squares Means (Alpha=0.05)					
LS-means with the same letter are not significantly different.					
salt	Estimate				
ddH$_2$O	85.5886				A
					A
saline water	83.7710				A

Fe source Least Squares Means					
Fe source	Estimate	Standard Error	DF	t Value	Pr > |t|
CT-metaVT	79.1529	4.1956	59	18.87	<.0001
Fe-EDDHA	99.2975	4.0454	59	24.55	<.0001
metaVT	80.9519	4.0454	59	20.01	<.0001
control	79.3169	3.9246	59	20.21	<.0001
Tukey-Kramer Grouping for Fe source Least Squares Means (Alpha=0.05)					
LS-means with the same letter are not significantly different.					
Fe source	Estimate				
Fe-EDDHA	99.2975		A		

metaVT	80.9519	B	
		B	
control	79.3169	B	
		B	
CT-metaVT	79.1529	B	

Table C3-11. ANOVA table of shoot P concentrations of wheat grown in the sand with four Fe treatments, control, nano-metaVT, nano-CT-metaVT, and Fe-EDDHA, and irrigated with ddH$_2$O or saline water (EC = 4 dS·m^{-1}) (Figure 4-5c).

Covariance Parameter Estimates		
Cov Parm	**Estimate**	**Standard Error**
block	0	.
Residual	0.2941	0.05241
Type III Tests of Fixed Effects				
Effect	**Num DF**	**Den DF**	**F Value**	**Pr > F**
Fe source	3	62	2.60	0.0598
salt	1	62	2.28	0.1364
Fe source*salt	3	62	0.42	0.7392

salt Least Squares Means					
salt	**Estimate**	**Standard Error**	**DF**	**t Value**	**Pr > |t|**
saline water	2.8076	0.09179	62	30.59	<.0001
ddH$_2$O	3.0020	0.09039	62	33.21	<.0001
Tukey-Kramer Grouping for salt Least Squares Means (Alpha=0.05)					
LS-means with the same letter are not significantly different.					
salt	**Estimate**				
ddH$_2$O	3.0020				A
					A
saline water	2.8076				A

Fe source Least Squares Means					
Fe source	**Estimate**	**Standard Error**	**DF**	**t Value**	**Pr > |t|**
CT-metaVT	2.9888	0.1278	62	23.38	<.0001
Fe-EDDHA	2.6264	0.1318	62	19.93	<.0001
metaVT	3.1220	0.1278	62	24.42	<.0001
control	2.8820	0.1278	62	22.55	<.0001
Tukey-Kramer Grouping for Fe source Least Squares Means (Alpha=0.05)					
LS-means with the same letter are not significantly different.					
Fe source	**Estimate**				
metaVT	3.1220				A

			A
CT-metaVT	2.9888	B	A
		B	A
control	2.8820	B	A
		B	
Fe-EDDHA	2.6264	B	

Table C3-12. ANOVA table of shoot P concentrations of beans grown in the sand with four Fe treatments, control, nano-metaVT, nano-CT-metaVT, and Fe-EDDHA, and irrigated with ddH$_2$O or saline water (EC = 4 dS·m^{-1}) (Figure 4-5d).

Covariance Parameter Estimates		
Cov Parm	**Estimate**	**Standard Error**
block	0	.
Residual	0.4207	0.07681
Type III Tests of Fixed Effects				
Effect	**Num DF**	**Den DF**	**F Value**	**Pr > F**
Fe source	3	59	0.82	0.4865
salt	1	59	16.25	0.0002
Fe source*salt	3	59	0.09	0.9664

salt Least Squares Means					
salt	**Estimate**	**Standard Error**	**DF**	**t Value**	**Pr > |t|**
saline water	1.7501	0.1135	59	15.42	<.0001
ddH$_2$O	2.3866	0.1098	59	21.74	<.0001
Tukey-Kramer Grouping for salt Least Squares Means (Alpha=0.05)					
LS-means with the same letter are not significantly different.					
salt		**Estimate**			
ddH$_2$O		2.3866		A	
saline water		1.7501		B	

Fe source Least Squares Means					
Fe source	**Estimate**	**Standard Error**	**DF**	**t Value**	**Pr > |t|**
CT-metaVT	2.1020	0.1634	59	12.86	<.0001
Fe-EDDHA	2.0998	0.1576	59	13.32	<.0001
metaVT	1.8684	0.1576	59	11.86	<.0001
control	2.2030	0.1529	59	14.41	<.0001
Tukey-Kramer Grouping for Fe source Least Squares Means (Alpha=0.05)					
LS-means with the same letter are not significantly different.					
Fe source		**Estimate**			
control		2.2030		A	

		A	
CT-metaVT	2.1020	A	
		A	
Fe-EDDHA	2.0998	A	
		A	
metaVT	1.8684	A	

Table C3-13. ANOVA table of shoot Na concentrations of wheat grown in the sand with four Fe treatments, control, nano-metaVT, nano-CT-metaVT, and Fe-EDDHA, and irrigated with ddH$_2$O or saline water (EC = 4 dS·m^{-1}) (Figure 4-6a).

Covariance Parameter Estimates		
Cov Parm	Estimate	Standard Error
block	0.02375	0.03536
Residual	0.05849	0.01050
Type III Tests of Fixed Effects				
Effect	Num DF	Den DF	F Value	Pr > F
Fe source	3	62	2.14	0.1044
salt	1	62	472.75	<.0001
Fe source*salt	3	62	2.74	0.0507

Fe source*salt Least Squares Means						
Fe source	salt	Estimate	Standard Error	DF	t Value	Pr > |t|
CT-metaVT	saline water	2.1745	0.1060	62	20.51	<.0001
CT-metaVT	ddH$_2$O	1.1916	0.1060	62	11.24	<.0001
Fe-EDDHA	saline water	2.5706	0.1125	62	22.84	<.0001
Fe-EDDHA	ddH$_2$O	1.1863	0.1060	62	11.19	<.0001
metaVT	saline water	2.4047	0.1060	62	22.68	<.0001
metaVT	ddH$_2$O	1.1614	0.1060	62	10.95	<.0001
control	saline water	2.5285	0.1060	62	23.85	<.0001
control	ddH$_2$O	1.1422	0.1060	62	10.77	<.0001
Tukey-Kramer Grouping for Fe source*salt Least Squares Means (Alpha=0.05)						
LS-means with the same letter are not significantly different.						
Fe source	salt	Estimate				
Fe-EDDHA	saline water	2.5706				A
						A
control	saline water	2.5285		B		A
				B		A
metaVT	saline water	2.4047		B		A
				B		
CT-metaVT	saline water	2.1745		B		

CT-metaVT	ddH$_2$O	1.1916		C
				C
Fe-EDDHA	ddH$_2$O	1.1863		C
				C
metaVT	ddH$_2$O	1.1614		C
				C
control	ddH$_2$O	1.1422		C

Table C3-14. ANOVA table of shoot Na concentrations of beans grown in the sand with four Fe treatments, control, nano-metaVT, nano-CT-metaVT, and Fe-EDDHA, and irrigated with ddH$_2$O or saline water (EC = 4 dS·m^{-1}) (Figure 4-6b).

Covariance Parameter Estimates		
Cov Parm	Estimate	Standard Error
block	0.01826	0.02647
Residual	0.02103	0.003872
Type III Tests of Fixed Effects				
Effect	Num DF	Den DF	F Value	Pr > F
Fe source	3	59	1.59	0.2012
salt	1	59	112.12	<.0001
Fe source*salt	3	59	3.22	0.0290

Fe source*salt Least Squares Means						
Fe source	salt	Estimate	Standard Error	DF	t Value	Pr > |t|
CT-metaVT	saline water	1.4115	0.06746	59	20.92	<.0001
CT-metaVT	ddH$_2$O	0.9376	0.06427	59	14.59	<.0001
Fe-EDDHA	saline water	1.3945	0.06822	59	20.44	<.0001
Fe-EDDHA	ddH$_2$O	0.9462	0.06427	59	14.72	<.0001
metaVT	saline water	1.3431	0.06427	59	20.90	<.0001
metaVT	ddH$_2$O	1.1512	0.06651	59	17.31	<.0001
control	saline water	1.3350	0.06427	59	20.77	<.0001
control	ddH$_2$O	0.9537	0.06427	59	14.84	<.0001
Tukey-Kramer Grouping for Fe source*salt Least Squares Means (Alpha=0.05)						
LS-means with the same letter are not significantly different.						
Fe source		salt		Estimate		
CT-metaVT		saline water		1.4115		A
						A
Fe-EDDHA		saline water		1.3945		A
						A
metaVT		saline water		1.3431	B	A
					B	A
control		saline water		1.3350	B	A

			B	
metaVT	ddH$_2$O	1.1512	B	C
				C
control	ddH$_2$O	0.9537		C
				C
Fe-EDDHA	ddH$_2$O	0.9462		C
				C
CT-metaVT	ddH$_2$O	0.9376		C

Table C3-15. ANOVA table of shoot K concentrations of wheat grown in the sand with four Fe treatments, control, nano-metaVT, nano-CT-metaVT, and Fe-EDDHA, and irrigated with ddH$_2$O or saline water (EC = 4 dS·m^{-1}) (Figure 4-6c).

Covariance Parameter Estimates		
Cov Parm	Estimate	Standard Error
block	0	.
Residual	37.1684	6.6224
Type III Tests of Fixed Effects				
Effect	Num DF	Den DF	F Value	Pr > F
Fe source	3	62	2.81	0.0467
salt	1	62	7.13	0.0096
Fe source*salt	3	62	1.13	0.3430

salt Least Squares Means					
salt	Estimate	Standard Error	DF	t Value	Pr > |t|
saline water	40.1898	1.0319	62	38.95	<.0001
ddH$_2$O	36.3218	1.0161	62	35.75	<.0001
Tukey-Kramer Grouping for salt Least Squares Means (Alpha=0.05)					
LS-means with the same letter are not significantly different.					
salt	Estimate				
ddH$_2$O	40.1898			A	
saline water	36.3218			B	

Fe source Least Squares Means					
Fe source	Estimate	Standard Error	DF	t Value	Pr > |t|
CT-metaVT	40.3538	1.4370	62	28.08	<.0001
Fe-EDDHA	34.7835	1.4812	62	23.48	<.0001
metaVT	39.5441	1.4370	62	27.52	<.0001
control	38.3419	1.4370	62	26.68	<.0001
Tukey-Kramer Grouping for Fe source Least Squares Means (Alpha=0.05)					
LS-means with the same letter are not significantly different.					
Fe source	Estimate				
CT-metaVT	40.3538			A	

			A
metaVT	39.5441	B	A
		B	A
control	38.3419	B	A
		B	
Fe-EDDHA	34.7835	B	

Table C3-16. ANOVA table of shoot K concentrations of beans grown in the sand with four Fe treatments, control, nano-metaVT, nano-CT-metaVT, and Fe-EDDHA, and irrigated with ddH$_2$O or saline water (EC = 4 dS·m^{-1}) (Figure 4-6d).

Covariance Parameter Estimates		
Cov Parm	Estimate	Standard Error
block	0	.
Residual	19.1753	3.5009
Type III Tests of Fixed Effects				
Effect	Num DF	Den DF	F Value	Pr > F
Fe source	3	59	2.73	0.0516
salt	1	59	1.48	0.2290
Fe source*salt	3	59	0.56	0.6422

salt Least Squares Means					
salt	Estimate	Standard Error	DF	t Value	Pr > |t|
saline water	22.9923	0.7664	59	30.00	<.0001
ddH$_2$O	24.2881	0.7411	59	32.77	<.0001
Tukey-Kramer Grouping for salt Least Squares Means (Alpha=0.05)					
LS-means with the same letter are not significantly different.					
salt	Estimate				
ddH$_2$O	24.2881	A			
		A			
saline water	22.9923	A			

Fe source Least Squares Means					
Fe source	Estimate	Standard Error	DF	t Value	Pr > |t|
CT-metaVT	21.9624	1.1034	59	19.90	<.0001
Fe-EDDHA	23.0880	1.0639	59	21.70	<.0001
metaVT	23.4281	1.0639	59	22.02	<.0001
control	26.0822	1.0321	59	25.27	<.0001
Tukey-Kramer Grouping for Fe source Least Squares Means (Alpha=0.05)					
LS-means with the same letter are not significantly different.					
Fe source	Estimate				
control	26.0822		A		

			A
metaVT	23.4281	B	A
		B	A
Fe-EDDHA	23.0880	B	A
		B	
CT-metaVT	21.9624	B	

Table C3-17. ANOVA table of root-associate Fe of wheat grown with four Fe treatments, control, nano-metaVT, nano-CT-metaVT, and Fe-EDDHA, and irrigated with ddH$_2$O or saline water (EC = 4 dS·m^{-1}) (Figure 4-7a).

Covariance Parameter Estimates		
Cov Parm	**Estimate**	**Standard Error**
block	0.4093	0.7000
Residual	4.1044	0.7432
Type III Tests of Fixed Effects				
Effect	**Num DF**	**Den DF**	**F Value**	**Pr > F**
Fe source	3	61	4.12	0.0100
salt	1	61	14.10	0.0004
Fe source*salt	3	61	2.45	0.0719

salt Least Squares Means					
salt	**Estimate**	**Standard Error**	**DF**	**t Value**	**Pr > |t|**
saline water	10.4054	0.6300	61	16.52	<.0001
ddH$_2$O	8.5848	0.6357	61	13.51	<.0001
Tukey-Kramer Grouping for salt Least Squares Means (Alpha=0.05)					
LS-means with the same letter are not significantly different.					
salt	**Estimate**				
ddH$_2$O	10.4054			A	
saline water	8.5848			B	

Fe source Least Squares Means					
Fe source	**Estimate**	**Standard Error**	**DF**	**t Value**	**Pr > |t|**
CT-metaVT	10.3910	0.7247	61	14.34	<.0001
Fe-EDDHA	8.4276	0.7148	61	11.79	<.0001
metaVT	10.2697	0.7247	61	14.17	<.0001
control	8.8921	0.7148	61	12.44	<.0001
Tukey-Kramer Grouping for Fe source Least Squares Means (Alpha=0.05)					
LS-means with the same letter are not significantly different.					
Fe source	**Estimate**				
CT-metaVT	10.3910			A	

			A
metaVT	10.2697		A
			A
control	8.8921	B	A
		B	
Fe-EDDHA	8.4276	B	

Table C3-18. ANOVA table of root-associate Fe of beans grown with four Fe treatments, control, nano-metaVT, nano-CT-metaVT, and Fe-EDDHA, and irrigated with ddH$_2$O or saline water (EC = 4 dS·m^{-1}) (Figure 4-7b).

Covariance Parameter Estimates		
Cov Parm	Estimate	Standard Error
block	0.08210	0.1925
Residual	2.3996	0.4456
Type III Tests of Fixed Effects				
Effect	Num DF	Den DF	F Value	Pr > F
Fe source	3	58	1.80	0.1570
salt	1	58	26.26	<.0001
Fe source*salt	3	58	1.93	0.1354

salt Least Squares Means					
salt	Estimate	Standard Error	DF	t Value	Pr > |t|
saline water	5.9129	0.4505	58	13.13	<.0001
ddH$_2$O	3.9620	0.4437	58	8.93	<.0001
Tukey-Kramer Grouping for salt Least Squares Means (Alpha=0.05)					
LS-means with the same letter are not significantly different.					
salt	Estimate				
ddH$_2$O	5.9129		A		
saline water	3.9620		B		

Fe source Least Squares Means					
Fe source	Estimate	Standard Error	DF	t Value	Pr > |t|
CT-metaVT	5.5432	0.5227	58	10.60	<.0001
Fe-EDDHA	5.0562	0.5291	58	9.56	<.0001
metaVT	4.8265	0.5227	58	9.23	<.0001
control	4.3237	0.5132	58	8.43	<.0001
Tukey-Kramer Grouping for Fe source Least Squares Means (Alpha=0.05)					
LS-means with the same letter are not significantly different.					
Fe source	Estimate				
control	5.5432	A			

		A	
metaVT	5.0562	A	
		A	
Fe-EDDHA	4.8265	A	
		A	
CT-metaVT	4.3237	A	

Table C3-19. ANOVA table of flowers and buds of beans grown in soil with four Fe
treatments (control, nano-metaVT, nano-CT-metaVT, and Fe-EDDHA) for 50 days
(Figure 4-8a).

Source	DF	Sum of Squares	Mean Square	F Value	Pr > F
Model	3	88.2500000	29.4166667	12.61	0.0021
Error	8	18.6666667	2.3333333		
Corrected Total	11	106.9166667			
Source	DF	Type I SS	Mean Square	F Value	Pr > F
Fe source	3	88.25000000	29.41666667	12.61	0.0021
Source	DF	Type III SS	Mean Square	F Value	Pr > F
Fe source	3	88.25000000	29.41666667	12.61	0.0021

Fe source	LSMEAN	Standard Error	Pr > |t|
CT-metaVT	15.0000	0.8819171	<.0001
Fe-EDDHA	12.3333	0.8819171	<.0001
metaVT	16.0000	0.8819171	<.0001
control	9.0000	0.8819171	<.0001
Tukey-Kramer Grouping for Fe source Least Squares Means (Alpha=0.05)			
LS-means with the same letter are not significantly different.			

Fe source	Estimate			
metaVT	16.0000		A	
			A	
CT-metaVT	15.0000		A	
			A	
EDDHA	12.3333	B	A	
		B		
control	9.0000	B		

Table C3-20. ANOVA table of shoot length of beans grown in soil with four Fe treatments (control, nano-metaVT, nano-CT-metaVT, and Fe-EDDHA) for 50 days (Figure 4-8b).

Source	DF	Sum of Squares	Mean Square	F Value	Pr > F
Model	3	209.5219087	69.8406362	4.79	0.0340
Error	8	116.6894560	14.5861820		
Corrected Total	11	326.2113647			
Source	DF	Type I SS	Mean Square	F Value	Pr > F
Fe source	3	209.5219087	69.8406362	4.79	0.0340
Source	DF	Type III SS	Mean Square	F Value	Pr > F
Fe source	3	209.5219087	69.8406362	4.79	0.0340

Fe source	LSMEAN	Standard Error	Pr > |t|
CT-metaVT	34.2110000	2.2050081	<.0001
Fe-EDDHA	29.9726667	2.2050081	<.0001
metaVT	31.3563333	2.2050081	<.0001
control	22.8653333	2.2050081	<.0001
Tukey-Kramer Grouping for Fe source Least Squares Means (Alpha=0.05)			
LS-means with the same letter are not significantly different.			
Fe source	Estimate		
CT-metaVT	34.2110000		A
			A
metaVT	31.3563333	B	A
		B	A
Fe-EDDHA	29.9726667	B	A
		B	
control	22.8653333	B	

Table C3-21. ANOVA table of root dry mass of beans grown in soil with four Fe treatments (control, nano-metaVT, nano-CT-metaVT, and Fe-EDDHA) for 50 days (Figure 4-8c).

Source	DF	Sum of Squares	Mean Square	F Value	Pr > F
Model	3	0.51473638	0.17157879	5.05	0.0298
Error	8	0.27164321	0.03395540		
Corrected Total	11	0.78637960			
Source	**DF**	**Type I SS**	**Mean Square**	**F Value**	**Pr > F**
Fe source	3	0.51473638	0.17157879	5.05	0.0298
Source	**DF**	**Type III SS**	**Mean Square**	**F Value**	**Pr > F**
Fe source	3	0.51473638	0.17157879	5.05	0.0298

Fe source	LSMEAN	Standard Error	Pr > |t|
CT-metaVT	1.49012700	0.10638828	<.0001
Fe-EDDHA	1.54569005	0.10638828	<.0001
metaVT	1.42432770	0.10638828	<.0001
control	1.01881618	0.10638828	<.0001
Tukey-Kramer Grouping for Fe source Least Squares Means (Alpha=0.05)			
LS-means with the same letter are not significantly different.			
Fe source	**Estimate**		
Fe-EDDHA	1.54569005		A	
			A	
CT-metaVT	1.49012700	B	A	
		B	A	
metaVT	1.42432770	B	A	
		B		
control	22.8653333	B		

Table C3-22. ANOVA table of bean Fe concentration of beans grown in soil with four Fe treatments (control, nano-metaVT, nano-CT-metaVT, and Fe-EDDHA) for 50 days (Figure 4-8d).

Source	DF	Sum of Squares	Mean Square	F Value	Pr > F
Model	3	78753.1977	26251.0659	6.75	0.0139
Error	8	31102.2833	3887.7854		
Corrected Total	11	109855.4810			
Source	DF	Type I SS	Mean Square	F Value	Pr > F
Fe source	3	78753.19768	26251.06589	6.75	0.0139
Source	DF	Type III SS	Mean Square	F Value	Pr > F
Fe source	3	78753.19768	26251.06589	6.75	0.0139

Fe source	LSMEAN	Standard Error	Pr > |t|
CT-metaVT	127.000231	35.999007	0.0078
Fe-EDDHA	330.575493	35.999007	<.0001
metaVT	139.495989	35.999007	0.0047
control	182.121712	35.999007	0.0010
Tukey-Kramer Grouping for Fe source Least Squares Means (Alpha=0.05)			
LS-means with the same letter are not significantly different.			
Fe source	**Estimate**		
Fe-EDDHA	330.575493		A	
			A	
control	182.121712	B	A	
		B		
metaVT	139.495989	B		
		B		
CT-metaVT	127.000231	B		

Table C3-23. ANOVA table of shoot Fe concentration of beans grown in soil with four

Fe treatments (control, nano-metaVT, nano-CT-metaVT, and Fe-EDDHA) for 50 days

(Figure 4-8e).

Source	DF	Sum of Squares	Mean Square	F Value	Pr > F
Model	3	3888.646127	1296.215376	8.53	0.0098
Error	7	1063.940363	151.991480		
Corrected Total	10	4952.586490			
Source	DF	Type I SS	Mean Square	F Value	Pr > F
Fe source	3	3888.646127	1296.215376	8.53	0.0098
Source	DF	Type III SS	Mean Square	F Value	Pr > F
Fe source	3	3888.646127	1296.215376	8.53	0.0098

Fe source	LSMEAN	Standard Error	Pr > |t|
CT-metaVT	93.130672	7.117853	<.0001
Fe-EDDHA	101.054495	7.117853	<.0001
metaVT	138.737613	7.117853	<.0001
control	96.862923	8.717554	<.0001
Tukey-Kramer Grouping for Fe source Least Squares Means (Alpha=0.05)			
LS-means with the same letter are not significantly different.			
Fe source	**Estimate**		
metaVT	138.737613	A	
Fe-EDDHA	101.054495	B	
		B	
control	96.862923	B	
		B	
CT-metaVT	93.130672	B	

Table C3-24. ANOVA table of root-associated Fe concentration of beans grown in soil with four Fe treatments (control, nano-metaVT, nano-CT-metaVT, and Fe-EDDHA) for 50 days (Figure 4-8g).

Source	DF	Sum of Squares	Mean Square	F Value	Pr > F
Model	3	7195319.69	2398439.90	5.79	0.0210
Error	8	3311080.36	413885.05		
Corrected Total	11	10506400.06			
Source	**DF**	**Type I SS**	**Mean Square**	**F Value**	**Pr > F**
Fe source	3	7195319.692	2398439.897	5.79	0.0210
Source	**DF**	**Type III SS**	**Mean Square**	**F Value**	**Pr > F**
Fe source	3	7195319.692	2398439.897	5.79	0.0210

Fe source	LSMEAN	Standard Error	Pr > |t|
CT-metaVT	2761.59969	371.43193	<.0001
Fe-EDDHA	3826.30393	371.43193	<.0001
metaVT	2325.07863	371.43193	0.0002
control	1703.01291	371.43193	0.0018
Tukey-Kramer Grouping for Fe source Least Squares Means (Alpha=0.05)			
LS-means with the same letter are not significantly different.			
Fe source	**Estimate**		
Fe-EDDHA	3826.30393		A	
			A	
CT-metaVT	2325.07863	B	A	
		B	A	
metaVT	2325.07863	B	A	
		B		
control	1703.01291	B		

Table C3-25. ANOVA table of the mobility of DTPA-extractable Fe in the soil columns

with wheat. (Table 4-3)

Type III Tests of Fixed Effects				
Effect	Num DF	Den DF	F Value	Pr > F
Fe source	3	40	14.90	<.0001
Depth	4	40	22.85	<.0001
Fe source*Depth	12	40	1.84	0.0735

Fe source*Depth Least Squares Means						
Fe source	Depth	Estimate	Standard Error	DF	t Value	Pr > |t|
CT-metaVT	1	7.9009	0.2091	40	37.78	<.0001
CT-metaVT	2	6.6847	0.2091	40	31.97	<.0001
CT-metaVT	3	6.4655	0.2091	40	30.92	<.0001
CT-metaVT	4	6.7087	0.2091	40	32.08	<.0001
Fe-EDDHA	5	6.6126	0.2091	40	31.62	<.0001
Fe-EDDHA	1	7.4595	0.2091	40	35.67	<.0001
Fe-EDDHA	2	6.5165	0.2091	40	31.16	<.0001
Fe-EDDHA	3	6.6667	0.2091	40	31.88	<.0001
metaVT	4	7.3514	0.2091	40	35.15	<.0001
metaVT	5	7.4565	0.2091	40	35.66	<.0001
metaVT	1	8.1892	0.2091	40	39.16	<.0001
metaVT	2	6.4384	0.2091	40	30.79	<.0001
control	3	6.4024	0.2091	40	30.62	<.0001
control	4	6.6727	0.2091	40	31.91	<.0001
control	5	6.8829	0.2091	40	32.91	<.0001
control	1	6.9339	0.2091	40	33.16	<.0001
Tukey-Kramer Grouping for Fe source*Depth Least Squares Means (Alpha=0.05)						
LS-means with the same letter are not significantly different.						
Fe source	Depth	Estimate				
metaVT	1	8.1892			A	
					A	
CT-metaVT	1	7.9009	B		A	
			B		A	
Fe-EDDHA	1	7.4595	B		A	C

			B	A	C
Fe-EDDHA	5	7.4565	B	A	C
			B	A	C
Fe-EDDHA	4	7.3514	B	A	C
			B		C
no	1	6.9339	B	D	C
			B	D	C
metaVT	5	6.8829	B	D	C
				D	C
CT-metaVT	4	6.7087		D	C
				D	C
CT-metaVT	2	6.6847		D	C
				D	C
metaVT	4	6.6727		D	C
				D	C
Fe-EDDHA	3	6.6667		D	C
				D	C
CT-metaVT	5	6.6126		D	C
				D	C
Fe-EDDHA	2	6.5165		D	C
				D	C
CT-metaVT	3	6.4655		D	C
				D	C
metaVT	2	6.4384		D	C
				D	C
metaVT	3	6.4024		D	C
				D	
no	5	6.2072		D	
				D	
no	4	6.1471		D	
				D	
no	3	6.0270		D	
				D	
no	2	6.0000		D	

Table C3-26. ANOVA table of the soluble Fe leached from the soil columns with wheat accumulated from day 11 to day 15. (Figure 4-9)

Source	DF	Sum of Squares	Mean Square	F Value	Pr > F
Model	3	1178.640073	392.880024	7.47	0.0105
Error	8	420.952661	52.619083		
Corrected Total	11	1599.592733			
Source	DF	Type I SS	Mean Square	F Value	Pr > F
Fe source	3	1178.640073	392.880024	7.47	0.0105
Source	DF	Type III SS	Mean Square	F Value	Pr > F
Fe source	3	1178.640073	392.880024	7.47	0.0105

Fe source	LSMEAN	Standard Error	Pr > |t|
CT-metaVT	1.0131000	4.1880418	0.8149
Fe-EDDHA	23.5670750	4.1880418	0.0005
metaVT	0.5693083	4.1880418	0.8952
control	0.4707500	4.1880418	0.9133
Tukey-Kramer Grouping for Fe source Least Squares Means (Alpha=0.05)			
LS-means with the same letter are not significantly different.			

Fe source	Estimate			
Fe-EDDHA	23.5670750	A		
CT-metaVT	1.0131000	B		
		B		
metaVT	0.5693083	B		
		B		
control	0.4707500	B		

Appendix D. Standard Operating Procedures (SOPs)

D.1 Synthesis of nano-metaVT and nano-CT-metaVT

1. Nano-metaVT will be synthesized according to the protocols described by Ammari & Hattar (2011). The synthesis is conducted in an ice bath in an argon gas chamber to eliminate oxygen and allow ferrous ions to be present.

2. Five grams monoammonium phosphate $[(NH_4)H_2PO_4]$ is dissolved in 200 mL deionized water to form a solution with a PO_4^{3-} concentration of 0.217 M. After stirring for 30 min,

3. Fifteen grams ferrous sulfate $(FeSO_4 \cdot 7H_2O)$ is slowly added to the solution, to create a solution with a Fe concentration of 0.270 M.

4. The solution is kept stirring for 30 min. Then the pH of the suspension will be adjusted to pH 6.5 by dropwise additions of 1.25 mM NaOH. A pale-blue precipitate will appear.

5. The resulting vivianite precipitate will be washed several times with deionized water until the EC of the mixture is below $0.2\ dS \cdot m^{-1}$.

6. The precipitate will be centrifuged at 6,000 ×g for 15 min, the residual water will be removed, and the pellet will be dried in a freeze-dryer (FreeZone Benchtop Freeze Dryer, Labconco).

7. A chitosan (CT) solution will be prepared by dissolving 1 g CT in 200 mL 0.1 M acetic acid (CH_3COOH) solution while stirring.

8. After 12 h, 4 g of metavivianite powder is slowly added to the CT solution and stirred for an additional 30 min.

9. The pH of the suspension will be adjusted to 6.5 by adding 1.25 mM NaOH.

10. The nano-CT-metaVT precipitate is rinsed with deionized water until salt-free ($< 0.2\ dS \cdot m^{-1}$).

11. The precipitate is centrifuged at 6,000 ×g for 15 min, the residual water is removed, and the pellet is freeze-dried.

Note: The whole synthesis process is conducted in a Argon chamber to minimize the oxidation, and in an ice bath to keep at the temperature around 4°C.

D.2 Atomic Absorption Spectroscopy (Varian AA240)

1. Turn on the heater that is connected to Nitrous Oxide (N_2O).

2. The heater can prevent the ice from blocking the tube, which would pose an explosion hazard.

3. Take off the hinged door in front of the burner assembly. (Burner assembly drainage box)

4. Change the burner head to the one specific for N_2O.

5. Check whether the slot of the burner head is clean or not. If not, clean by using DI water and put the door back.

6. Turn on the power of AA, and followed by the computer and the SpectrAA software.

7. In the software:

    Add a new worksheet→add Fe (or other elements of interest)

    [Type/Mode] edit the sampling method Manual; flame type N2O/Acetylene; N2O flow 10.5

    [Measurement] edit read delay 5 sec

    [Optical] edit lamp position 1; lamp current 13 mA; background correction BC on

    [Standard] type in the concentration of standard solutions (not include 0 ppm); conc decimal places 4

    [Analysis]

8. Open the acetylene cylinder (Check the pressure of acetylene cylinder > 400 kPa, or the acetone in the bottom of the cylinder will go out from the tube and cause the hazard)

    Open N_2O (with heater is turned on)

9. Open the air valve

    →click optimize→optimize the lamp

    →Adjust the location of the stage (use a card)

    →Adjust the nob on the lamp to make the signal greater

    →Turn on the Flame

10. If finished, turn off the flame→AA→software→computer

D.3 Making Luria-Bertani (LB) Medium

1.   Place a large weigh boat on a balance and measure out 5 g of Tryptone 1. Add all of it to a volumetric flask 2.

2.   If any dust remains stuck to the weigh boat afterwards, use a spray bottle filled with double distilled water to remove it.

3.   Place a large weigh boat on a balance and measure out 2.5 g of Yeast Extract. Add all of it to the volumetric flask.

4.   If any dust remains stuck to the weigh boat afterwards, use a spray bottle filled with double distilled water to remove it.

5.   Add ddH_2O to the volumetric flask until it reaches 500 mL.

6.   Place the solution on a stir plate 3 until it is a bright gold color, which indicates that the solution is fully dissolved.

7.   After several minutes of mixing, remove the volumetric flask from the stir plate and place in a 1 Liter Erlenmeyer flask.

8.   If making solid media, add 10 g of agar and stir using a stir plate. This addition must be done after transferring to the Erlenmeyer flask.

9.   Cover the opening of all flasks with two layers of aluminum foil. Label each flask with labeling tape specifying the date and that it is LB medium.

10. Autoclave for 30 minutes 4, plus time to cool. Remove from autoclave after the cycle ends.

11. If making solid media, allow to cool slightly then pour into petri dishes. If making liquid media, allow to completely cool to room temperature before use.

Notes:
1.   Solids were added before any of the water for convenience based on our lab setup.
2.   The solution was mixed in a volumetric flask instead of an Erlenmeyer flask for convenience of working in our lab. It was then transferred to an Erlenmeyer flask to be autoclaved. Also, volumetric flasks are more accurate than graduated cylinders.
3.   We used our stir plate to stir all solutions to ensure a good mix and for convenience.
4.   This corresponds to the program we run on our autoclave for media solutions. We use this duration to assure that solutions are not overcooked.
5.   This method is based on a method provided by Matthew Potter.

D.4 Making Minimal Medium

1.   Measure out the following chemicals in the specified amounts [1] and add to a
      volumetric flask [2]. This is the **Salt Solution**.

	1 L	500 mL	200 mL
K_2HPO_4	10.5 g	5.25 g	2.1 g
KH_2PO_4	4.5 g	2.25 g	0.9 g
Na*Citrate*$2H_2O$	0.5 g	0.25 g	0.1 g
$(NH_4)_2SO_4$	1 g	0.5 g	0.2

2.   Add ddH2O to the volumetric flask until it reaches the desired volume[7]. Pour
      back into flask and stir using a stir plate [3].

3.   Add 2 g of sucrose and 0.125 g $MgSO_4$*ANHYDROUS (or 0.25 g
      $MgSO_4$*$7H_2O$) to a small Erlenmeyer flask. Add 10 mL of ddH$_2$O using an
      electrical pipette [4] and stir using a stir plate. This is the **C & Mg Solution**.

4.   Transfer the salt solution to a Erlenmeyer flask[2].

5.   Add 2 g of agar to the **Salt Solution** for every 100 mL of medium (see table
      below). Swirl to disperse and stir using stir plate [3].

	1 L	500 mL	200 mL
Agar	20 g	10 g	4 g

6.   Cover each flask with two layers of aluminum foil, label each flask, and auto
      clave[5] the **Salt Solution** and the **C & Mg Solution** for 30 minutes, plus time for
      cooling [6].

7.   Allow to cool slightly, then add 1 mL of the **C & Mg Solution** to the **Salt
      Solution** for every 100 mL of **Salt Solution** (see table below).

	1 L	500 mL	200 mL
C & Mg Solution	10 mL	5 mL	2 mL

8.   Wait until the flask is cool to the touch then pour the solution into petri dishes.

Notes:
1.   Salts were added before any of the water for convenience based on our lab setup.
2.   If making 1 liter, use a 2 liter Erlenmeyer flask. If making 500 mL or 200 mL, a 1 liter flask will work. The solution was mixed in a volumetric flask instead of an Erlenmeyer flask for convenience of working in our lab. It was then transferred to an Erlenmeyer flask to be autoclaved. Also, volumetric flasks are more accurate than graduated cylinders.
3.   We used a stir plate to stir all solutions to ensure a good mix and for convenience.
4.   Small measurements of liquids are made using an electrical pipette for accuracy.
5.   Do not autoclave volumetric glassware! Make sure that the solution was transferred to Erlenmeyer flask in step 4.
6.   This corresponds to the program we run on our autoclave for media solutions. We use this duration to assure that solutions are not overcooked.
7.   500 mL makes about 25 Petri dishes worth of media.
8.   This method is based on a method provided by Matthew Potter.

D.5 Method of for preparing *Pc*O6/*Pp* Pf-5 bacterial suspension

1. Place bullet tube of *Pc*O6 on minimal media agar plate; spread. Seal plate.
2. 36-48 hours later, flood the plate with 10 mL sterile ddH$_2$O [1].
3. Rotate plate and agitate gently to suspend mobile cells. If necessary, gently scrape the surface of the media with a sterile spatula. Do not penetrate the media surface.
4. Transfer 1 mL of cell suspension to a sterile centrifuge tube.
5. Using sterile centrifuge tubes, serially dilute cells by 1:10 in sterile ddH$_2$O 4 times, switching pipette tips each time a new solution is drawn from.
6. Add 1 mL from the final serial dilution to 99 mL sterile ddH$_2$O in a beaker.

7. The objective is to achieve a concentration of $1x10^4$. Confirm that this is the approximate concentration of the final solution using a spectrophotometer to measure optical density at the 600 nm wavelength. An OD 600 measurement of 0.1 A correlates to about 10^8 CFU/mL. According to this method, if the 1:100 solution (second serial dilution) reads approximately 0.1 A on OD 600, this method should achieve the correct concentration. If this is not the case, adjust the dilutions as needed to achieve the correct concentration.

Note: This method is based on a method provided by Josh Hortin.

D.6 Making Hoagland's Solution (Modified)

This recipe is for a full-strength solution. To prepare a half-strength solution, double the water that the stock solutions are added to (use 2 L of water instead of 1 L).

Component		Stock Solution (g/L)	Stock Solution (g/ 250 mL)	Stock/L solution	Final Concentration (g/L)
Potassium nitrate	KNO_3	101	25.25	5 mL	0.505
Calcium nitrate	$Ca(NO_3)_2*4H_2O$	236	59	5 mL	1.18
Magnesium sulfate	$MgSO_4*7H_2O$	246.5	61.63	2 mL	0.493
Ammonium nitrate	NH_4NO_3	80	20	1 mL	0.08
Monopotassium phosphate	KH_2PO_4	68	17	1 mL	0.068
Boric acid	H_3BO_3	2.86	0.715	1 mL	0.00286
Manganese chloride	$MnCl_2*4H_2O$	1.81	0.453	1 mL	0.00181
Zinc sulfate	$ZnSO_4*7H_2O$	0.22	0.055	1 mL	0.00022
Copper sulfate	$CuSO_4*5H_2O$	0.051	0.0128	1 mL	0.000051
Sodium molybdate	$Na_2MoO_4*2H_2O$	0.12	0.03	1 mL	0.00012

Mix each stock solution in a separate 250 mL sealable container. This is done by adding the appropriate amount of each chemical to the container, and then adding ddH_2O until a volume of 250 mL is reached. These stock solutions can be stored for 6 months in the refrigerator. Within three days of using the Hoagland's solution, add the appropriate amount of stock solution to ddH_2O according to the table above. Agitate the final solution before adding to pots.

Notes:

1. This concentration was listed in terms of half liters in Matthew Potter's original method[3]. It was converted to terms of Liters by Justin Deakin. Li-Ting Yen modified the concentrations of the stock solution, preventing the stock solution from precipitating out (11/26/2022).
2. The stock solutions cannot be stored premixed. Each salt solution must be mixed and stored separately or the salts will precipitate out.
3. The separate stock solutions can be stored in the refrigerator for up to 6 months.
4. All water added to the Hoagland solution should be double-deionized water (resistance >18 MΩ cm) to ensure that the chemical concentrations stated here are the actual concentrations of the final solution.
5. Working solution should be prepared immediately before use. Do not store working solution for more than 3 days.

---

[3] Potter, M., Deakin, J., Cartwright, A., Hortin, J., Sparks, D., Anderson, A. J., McLean, J. E., Jacobson, A., & Britt, D. W. (2021). Absence of nanoparticle-induced drought tolerance in nutrient sufficient wheat seedlings. *Environmental Science & Technology*, 55(20), 13541-13550. https://doi.org/10.1021/acs.est.1c00453

D.7 Wheat harvest instructions

Time Estimate: 6 - 9 hours

1. Record the weight of the magenta box.
2. Pour 45 mL DI water into the magenta box, and let it sit for 15 minutes.
   a. Take photos
3. Separate the shoots from the roots by cutting at upper part of the coleoptile
4. Measure and record the maximum length of shoots via a ruler
   a. Take photos
5. Pour the pot of sand with root on a new and clean zip bag
6. Pick and dip plant roots in a 250-mL beaker of water to remove extra sand via a tweezer, then place the plant on a paper towel.
   a. Replace root rinsing water between triplicates
   b. Acid rinse beaker between treatments
7. Measure and record the maximum length of roots and shoots via a ruler
   a. Stretch roots for maximum length
   b. Take photos
8. Add roots and shoots to a respective paper envelope
9. Measure and record the wet weight of root and envelope and shoots and envelope
10. Vacuum separates the sand/water mixture into a sterile centrifuge tube to extract the liquid fraction of the sample. Measure pH and EC of sand pore water.
11. The sand pore water will be centrifuged at $20,800 \times g$ for 30 minutes, filtered through a syringe filter (0.22 μm), and acidified after measuring pH and EC. The sand pore water will be stored in the refrigerator for later analysis.
12. The shoot and root tissue will be dried at 60 °C for 48 hours. Before measuring the dry weight, make sure they are cooled down.
13. After measuring the dry weight, two sterilized tweezers will be used to remove the sand grains held by the root.

D.8 Measurement of humic and fulvic acid

Chemical preparations

1. 0.1 M HCl (Mw=36.46 g/mol, 37%, Density: 1.2 g/L; 8.2 mL for making a 1 L solution) Make 2 L
2. 6 M HCl (4.927 mL for making a 10 mL solution) Make 10 mL
3. 0.1 M NaOH (Mw=40 g/mol; 4g / 1L) Make 2 L
4. 0.1 M KOH (Mw=56.11 g/mol; 5.611 g / 1L) Make 1 L

Resin cleaning

1. Every new resin batch was first cleaned to remove organic impurities with five 0.1 M HCl extractions (24 h). This cycle was repeated with 0.1 M NaOH.
2. The resin was thoroughly cleaned by Soxhlet extractions with acetonitrile and methanol, each for 24 h. The cleaned resin was stored in methanol.
3. The methanol was removed by placing the resin in a Buchner funnel with a Whatman 41 filter and washing under vacuum with water having a volume 20 times that of the resin.
4. The resin was similarly rinsed with 0.1 M HCl, having 10 times the resin volume. It was found that 250 g of resin could be cleaned sufficiently by rinsing with 2 L of demineralized water and 1 L of 0.1 M HCl.

Batch Procedure

1. About 50 mL of a sample solution (V1) was adjusted to pH 1 with 6 M HCl (V2) to precipitate the dissolved HA.
2. After standing overnight, the suspension was centrifuged (10 min, 3000g).
3. The supernatant was decanted (V3; the difference between V1 and V3 is the water volume retained in the HA pellet) and subsampled for DOC analysis (representing the sum of dissolved FA, Hy, and HON, $DOC_{FAHyHON}$)
4. A 10 g portion of cleaned DAX-8 resin was added to the remaining supernatant (V4,L; this is essentially V3 minus the volume taken for DOC analysis) to adsorb the FA (and HON) fraction.
5. After 1 h of equilibration by continuous tumbling, the suspension was filtered. The resin was equilibrated in four subsequent steps (1 h each) with 20 mL of 0.1 M KOH ($V_{11,i}$).
6. Meanwhile, the pellet of precipitated HA was dissolved in 0.1 M KOH (**V5**) and analyzed for DOC (**DOC_{HA}**).

Blank experiment

1. Ten grams of moist DAX-8 resin was added to 50 mL of 0.1 M HCl (**$V4_{BL}$**) after previous DOC analysis (DOC_{BL1}).

Reference: Van Zomeren, A., & Comans, R. N. J. (2007). Measurement of humic and fulvic Acid concentrations and dissolution properties by a rapid batch procedure. Environmental Science & Technology, 41(19), 6755-6761. DOI: 10.1021/es0709223

Appendix E. Safety and chemical hygiene

This revised safety and chemical hygiene plan are based on the standard lab safety regulations in Dr. Jacobson's laboratory.

E.1 Biological Hazards

All waste contaminated with *Pc*O6/*Pp* Pf-5 will be autoclaved before disposal, including Petri dishes, centrifuge tubes, gloves, and aluminum foil placed on countertops contacted with *Pc*O6/*Pp* Pf-5. The sand matrix inoculated with *Pc*O6/*Pp* Pf-5 or used to grow seeds was also autoclaved before discarding. To minimize contamination, gloves will be worn at all times during the whole experiment dealing with *Pc*O6/*Pp* Pf-5. In addition, all instruments and lab benches used to handle *Pc*O6/*Pp* Pf-5 will be sanitized with ethanol before and after use.

E.2 Chemical Hazards

Each prepared solution will be labeled with the name of the solution, the date, and the researcher's name (space permitting) or initials. Gloves, eye protection, and a lab coat will be worn at all times in the laboratory. The following chemicals to be used in the experiments require only gloves, eye protection, and a lab coat to handle: bleach (6%), hydrogen peroxide (30%), potassium nitrate, calcium nitrate, magnesium sulfate, ammonium nitrate, monopotassium phosphate, boric acid, manganese chloride, tryptone, yeast extract, agar, potassium phosphate dibasic, potassium phosphate monobasic, sodium citrate dihydrate, ammonium sulfate, sucrose, magnesium sulfate, copper sulfate, zinc sulfate, and sodium molybdate. These ingredients are used to prepare minimal medium, LB medium, and the modified, half-strength Hoagland's solution and sterilize the seeds. After use, the minimal and LB media will be disposed of as bio-waste, as they will be

contaminated with microbes. Bleach (6%) will also be used to sanitize pots and laboratory surfaces. Hydrogen peroxide solutions will be diluted to 10% before disposal, with additional water to ensure flushing and dilution.

All sand/soil to which NPs are added will be collected in 5-gallon buckets to be disposed of by USU Environmental Health and Safety (EHS). Gloves, weigh boats, and all other disposable lab supplies used to handle concentrated NPs will be stored in gallon zip lock bags, which will also be disposed of by EHS. Whenever concentrated NPs are handled, required PPE will include gloves, a lab coat, eye protection, and an N-95 dust mask. All areas and scales where NPs or sand/soil containing NPs are handled will be carefully cleaned with a brush immediately after use. NPs will be stored, protected from light, in a marked container.

When handling liquid nitrogen, extreme caution will be exercised. PPE will include a lab coat, insulated gloves, and eye protection. A face shield will be worn when pouring liquid nitrogen. Non-pliable plastic containers will not be exposed to liquid nitrogen, as they can explode at low temperatures. Liquid nitrogen will only be stored in the container in which it is delivered. This container will be left closed as much as possible to minimize the release of nitrogen gas into the air (nitrogen gas released by liquid nitrogen can displace oxygen, creating a suffocation hazard). It will only be used in well-ventilated areas of the laboratory.

Concentrated nitric acid will be handled with extreme caution. It will only be handled in a fume hood. When handling this acid, a lab coat, neoprene gloves, safety glasses, and a face shield will be worn at all times. These precautions will also be taken

when handling concentrated perchloric acid. In addition, perchloric acid will only be handled in a fume hood specifically designed for its use.

E.3 Physical Hazards

Electrical systems will not be "daisy-chained" (power strips will not be plugged into other power strips). In addition, the cloth used to block light from growth shelves will be breathable to prevent heat buildup. The temperature of these shelves will be monitored to ensure that temperatures never reach potentially hazardous levels.

Appendix F. Quality assurance and control

For all experiments, reagents used will be reagent grade or better. Concentrated acid reagents will be trace metal grade or better. In order to confirm the accuracy of measurements, all balances used in these experiments will be tested against standard weights. Pipettes will be tested for accuracy by comparing the mass of dd-H_2O dispensed to the expected mass for each volume. Class A volumetric glassware will be used to measure larger volumes within the recommended temperature ratings. A blank and a calibration curve verification will be tested for all instrumental analyses for every ten samples. The instrument will be recalibrated when conducting calibration curve verifications if the values measured are outside an acceptable range. A variation of up to 10 % from the known concentration will be considered acceptable for analyses of inorganic compounds. Where appropriate (i.e., ICP-MS measurements), a spiked sample will be included for every ten samples to check for matrix interference.

For tissue digests, 1 of each of the following checks will be taken through the digestion process for every ten samples digested to check for losses occurring due to the digestion procedure: one blank, one solution with a known concentration of element, and one sample containing a known mass of 1573a tomato leaves or 1547 peach leaves from the National Institute of Standards and Technology (NIST).

The pH probe will be calibrated with three pH buffer solutions before use. It will be confirmed that the millivolt reading at pH 7 is near 0 ± 25 mV and that the slope is within 90% of Nernstian. If the probe does not meet these standards, the electrode will be cleaned and the filling solution replaced before use. The EC probe will be calibrated before each use with solutions representative of the expected range of values for the measured

samples. If measurements fall outside the calibration range, a new calibration will be conducted before the samples are remeasured.

The *Pc*O6 stocks used for these experiments were created in 2016 by Dr. Astrid Jacobson and Dr. Anne Anderson from original (2003) freezer stocks checked for phenazine formation on rich LB medium. *P. protegens* Pf-5 (ATCC BAA-477), another beneficial soil bacterium, was purchased from American Type Culture Collection (ATCC) in June 2022 for its documented ability to produce chitinase (Loper et al., 2016). These stocks will be stored in a -80 °C freezer in 15% glycerol. When these stocks are defrosted, they will be observed to confirm that they are not gelatinous (which would indicate cell lysis). When preparing inoculation solutions, the approximate solution concentration will be checked using a spectrophotometer to measure optical density at the 600 nm wavelength. The measured values will be compared to previously measured spectrophotometer values correlated to colony-forming unit concentrations using serial dilutions. The inoculation solution will also be diluted by ten-fold serial dilutions, and three aliquots of 200 µL will from each dilution be placed on LB/TSA plates further to verify the concentration of *Pc*O6/*Pp* Pf-5 in the solution. The plates will be checked each day after the samples are added, and the number of aliquots that have formed colonies will be recorded. At the end of each growth study for which inoculation with *Pc*O6/*Pp* Pf-5 occurred, roots will be dabbed on LB/TSA plates and allowed to grow for three days to confirm that *Pc*O6/*Pp* Pf-5 is present (indicating successful inoculation) and to confirm that no visible colonies of other microbes are present (which would indicate unintentional contamination).

Appendix G. Curriculum vitae

Li-Ting Yen

EDUCATION

Ph.D. in Soil Science, Utah State University, UT, USA	2020 - 2024
Ph.D. in Environmental Science, National Chung Hsing University, Taichung, Taiwan	2017 - 2024
B.S. in Environmental Science, National Chung Hsing University, Taichung, Taiwan	2013 - 2017

EMPLOYMENT HISTORY

Graduate research assistant, Dept. of Plant, Soils and Climate, Utah State University, UT, USA	2020-2023
Teaching Assistant, Dept. of Plant, Soils and Climate, Utah State University, UT, USA	2023
Graduate research assistant, Dept. of Soil and Environmental Sciences, National Chung Hsing University, Taiwan	2017-2021
Co-Founder and Managing Director of Research, Agri-Tech Co., Ltd	2017-2021
Undergraduate Research Assistant, Dept. of Soil and Environmental Sciences, National Chung Hsing University, Taiwan	2014-2017

TEACHING EXPERIENCE AND MENTORSHIP

Research mentor, Utah State University, USA	2022-2023
• Led four students from Research Experiences for Undergraduates (REU) Program, National Science Foundation (NSF)	
Guest lecture, Utah State University, USA	2023/4
• Principles of Environmental Soil Chemistry, PSC5050/6050	
Teaching Assistant, Utah State University, USA	2023/1
• Prepared course notes and graded homework (PSC5050/6050)	
Research mentor, National Chung Hsing University, Taiwan	2016-2017
• Led three students from National Chang-Hua senior high school and participated in Taiwan High School Students Science Fair	

PUBLICATIONS

1. **Yen, L.-T.**, Weng, C.-H., Tzeng, J.-H., Chen, Y.-C., Jacobson, A. R., & Lin, Y.-T., Substantial improvement in photocatalysis performance of N-TiO$_2$ immobilized on PMMA: Exemplified by inactivation of *Staphylococcus aureus and Escherichia coli*. *Separation and Purification Technology*, 345, 127298. (**2024**)
(IF: 8.6; Chemical Engineering 14/158, 8.9%, Q1)

2. **Yen, L.-T.**, Weng, C.-H., Than, N. A. T., Tzeng, J.-H., Jacobson, A. R., Iamsaard, K., Dang, V. D., & Lin, Y.-T., Mode of inactivation of *Staphylococcus aureus* and *Escherichia coli* by heated oyster-shell powder. *Chemical Engineering Journal*, 432, 134386. (**2022**)
(IF: 15.1; Environmental Engineering 3/75, 4.0%; Q1)

3. Tzeng, J.-H., Weng, C.-H., Chang, C.-J., **Yen, L.-T.**, de Luna, M.D.G., Huang, J.-W., Lin, Y.-T., N-Schorl TiO$_2$ nanocomposite for visible-Light photocatalysis deactivation yeast exemplified by *Candida albicans*. *Chemical Engineering Journal*, 435, 134294. (**2022**)
(IF: 15.1; Environmental Engineering 3/75, 4.0%; Q1)

4. Iamsaard, K., Weng, C.-H., **Yen, L.-T.**, Tzeng, J.-H., Poonpakdee, C., & Lin, Y.-T., Adsorption of metal on pineapple leaf biochar: Key affecting factors, mechanism identification, and regeneration evaluation. *Bioresource Technology*, 344, 126131. (**2022**) (IF: 11.4; Agricultural Engineering 1/17, 5.9%; Q1)

5. Tzeng, J.-H., Weng, C.-H., **Yen, L.-T.**, Gaybullaev, G., Chang, C.-J., de Luna, M. D. G., & Lin, Y.-T., Inactivation of pathogens by visible light photocatalysis with nitrogen-doped TiO$_2$ and tourmaline-nitrogen co-doped TiO$_2$. *Separation and Purification Technology*, 274, 118979. (**2021**)
(IF: 8.6; Chemical Engineering 14/158, 8.9%; Q1)

6. Tzeng, J.-H.; Weng, C.-H.; Wang, C.-C.; Ho, M.-S.; **Yen, L.-T.**; Chen, J.-Y.; Gaybullaev, G.; Poonpakdee, C.; Lin, Y.-T., A solution of identifying biophysical properties and 3D cellular structure of visible-light-driven photocatalytic inactivated *Staphylococcus aureus*. *Chemical Engineering Journal*, 421, 127880. (**2021**)
(IF: 15.1; Environmental Engineering 3/75, 4.0%; Q1)

7. Huang, S. M.; Weng, C. H.; Tzeng, J. H.; Huang, Y. Z.; Anotai, J.; **Yen, L. T.**; Chang, C. J.; Lin, Y. T., Photocatalytic inactivation of *Klebsiella pneumoniae* by visible-light-responsive N/C-doped and N-tourmaline/palladium-C-codoped TiO$_2$. *Chemical Engineering Journal*, 379, 10. (2020)
(IF: 15.1; Environmental Engineering 3/75, 4.0%; Q1)

8. Huang, S.-M.; Weng, C.-H.; Tzeng, J.-H.; Huang, Y.-Z.; Anotai, J.; **Yen, L.-T.**; Chang, C.-J.; Lin, Y.-T., Kinetic study and performance comparison of TiO$_2$-mediated visible-light-responsive photocatalysts for the inactivation of *Aspergillus niger*. *Science of the Total Environment*, 692, 975-983. (**2019**)
(IF: 9.8; Environmental Sciences 20/330, 6.1%; Q1)

9. Tzeng, J.-H.; Weng, C.-H.; Lin, Y.-H.; Huang, S.-M.; **Yen, L.-T**.; Anotai, J.; Lin, Y.-T., Synthesis, characterization, and visible light induced photoactivity of tourmaline-N-TiO$_2$ composite for photooxidation of ethylene, 80, 376-384, *Journal of Industrial and Engineering Chemistry*. (**2019**)
(IF: 6.1; Chemical Engineering 28/158, 17.7%; Q1)

AWARDS AND RECOGNITION

Awards (International)
- 2rd Award, — 2023
2023 ASA, CSSA, SSSA Annual Meeting, 5-min Rapid Talk & Poster Students Competition in Soils and Environmental Quality Division, United States.
- 3rd Award, — 2020
Air & Waste Management Association 113th Annual Conference & Exhibition, Doctoral Students Poster Competition, United States.
- Outstanding Paper Award, — 2019
International Conference on Environmental Quality Concern, Control and Conservation - Student Oral Presentation Competition, Taiwan.
- 1st Award, — 2018
International Symposium on Advanced Chemistry - Student Poster Presentation Competition, Taiwan.
- Award of Recognition, — 2017
Synchrotron Radiation Research Center (NSRRC) and User Executive Committee (UEC) Annual Conference, Taiwan.
- Outstanding Paper Award, — 2017
International Conference on Environmental Quality Concern, Control and Conservation, Taiwan.
- 2nd Award, — 2016
Air & Waste Management Association 109th Annual Conference & Exhibition, Students Poster Competition, United States.

PATENTS
- Antibacterial Plastic Chopping Board Containing Discarded Oyster Shell Layer-Structure Modified Micron Powder, and the Producing Method — I725835
- Method for Preventing and Treating Cucumber Downy Mildew — I816143

PRESENTATIONS (Selected)

1. **Li-Ting Yen**, David W. Britt, Joan E. McLean, Anne J. Anderson, Astrid R. Jacobson, Exploring Meta-vivianite and Chitosan-coated Meta-vivianite as Alternative Iron Nanofertilizers for Plants in Calcareous Soil, ASA, CSSA, SSSA Annual Meeting, Oct. 29 - Nov. 1, 2023, MO, United States. — 2023

2. **Li-Ting Yen**, David W. Britt, Joan E. McLean, Anne J. Anderson, Yao-Tung Lin, Astrid R. Jacobson, Fe and P Phytoavailability from Novel Nano-sized, Chitosan-Coated, Meta-Vivianite Particles for Wheat under Salinity Stress in Quartz Sand, ASA, CSSA, SSSA Annual Meeting, Nov. 6-9, 2022, MD, United States. — 2022

3. **Li-Ting Yen**, David W. Britt, Joan E. McLean, Anne J. Anderson, Yao-Tung Lin, Astrid R. Jacobson, Fe Phytoavailability from Novel Nano-Sized, Chitosan-Coated, Meta-Vivianite Particles in Calcareous Soil Saturated Paste Extract and its Interaction with Soil Bacterium, *Pseudomonas chlororaphis* O6 (*Pc*O6), ASA, CSSA, SSSA Annual Meeting, Nov. 7-10, 2021, UT, United States. — 2021

4. **Li-Ting Yen**, Ying-Chen Chen, Jing-Hua Tzeng, Yao-Tung Lin, Kinetic Model of Disinfection using Novel Chitosan-N-Doped TiO_2 Photocatalyst derived from Agricultural Waste, The 5th International Conference on New Photocatalytic Materials for Energy, Environment and Sustainability (NPM-5) and 6th International Conference on Photocatalytic and Advanced Oxidation Technologies for Treatment of Water, Air, Soil and Surfaces (PAOT-6), Nov 8-11, 2020, Szeged, Hungary (Vitrual). — 2020

5. **Li-Ting Yen**, Than Thi Nhu Anh, Yao-Tung Lin, The Disinfection Performance and Mechanism of Bio-calcium Oxide Derivate from Aquaculture Waste, The Air & Waste Management Association's 113th Annual Conference & Exhibition, June 29-July 2, 2020, San Francisco, CA, United States. — 2020

6. **Li-Ting Yen**, Yao-Tung Lin, Development of the Key Technology and Process for Antibacterial Agent using Agricultural Waste, 2019 Annual Conference of Chinese Institute of Environmental Engineering, November 23, 2019, Taichung, Taiwan. — 2019

7. **Li-Ting Yen**, Chih-Huang Weng, Jing-Hua Tzeng, Kesinee Iamsaard, Yao-Tung Lin, Disinfection Performance and Mechanism of Chitosan-N-Doped TiO_2 Composite made from Fishery Waste against *S. aureus* and *E. coli*, 2019 International Conference on Environmental Quality Concern, Control and Conservation, May 23-25, 2019, Kaohsiung, Taiwan. — 2019

8. **Li-Ting Yen**, Chih-Huang Weng, Jing-Hua Tzeng, Kesinee Iamsaard, Yao-Tung Lin, Characteristics and Photocatalytic Disinfection Performance of Chitosan-C-Doped TiO_2 Composite, 256th American Chemical Society National Meeting, August 19-23, 2018, Boston, MA, United States. — 2018

9. **Li-Ting Yen**, Chih-Huang Weng, Jing-Hua Tzeng, Kesinee Iamsaard, Yao-Tung Lin, Characteristics and Disinfection Performance of Chitosan-N-Doped TiO_2 Composite made from Agricultural Waste, The Air & Waste — 2018

Management Association's 111th Annual Conference & Exhibition, June 25-28, 2018, Hartford, CT, United States.

10. **Li-Ting Yen**, Jing-Hua Tzeng, Kai-Fen Tu, Yao-Tung Lin, Synthesis Method and Characteristics of the Innovative Photo-disinfection Material Derived from Fishery Waste, 2018 International Symposium on Advanced Chemistry and Integration of Knowledge-Action, May 25-26, 2018, Taichung, Taiwan. 2018

11. **Li-Ting Yen**, Jing-Hua Tzeng, Chun-Chieh Wang, Chakkrit Poonpakdee1, Chih-Huang Weng, Yao-Tung Lin, 3D Nanoscale Imaging of *S. aureus* Using Transmission X-ray Microscopy, 2017 Synchrotron Radiation Research Center (NSRRC) and User Executive Committee (UEC) Annual Conference, September 5-8, 2017, Hsinchu, Taiwan. 2017

12. **Li-Ting Yen**, Jing-Hua Tzeng, Yao-Tung Lin, To modify polymethyl methacrylate surface by using photodisinfection technology, 2017 International Conference on Environmental Quality Concern, Control and Conservation, April 28-29, 2017, Kaohsiung, Taiwan. 2017

13. **Li-Ting Yen**, Jing-Hua Tzeng, Yao-Tung Lin; Synthesis of the Visible-light-responsive TiO_2 Polymethyl Methacrylate Composite for Photocatalytic-oxidation/photodisinfection of Acetaldehyde/bacteria, Air & Waste Management Association 109th Annual Conference & Exhibition, June 20-23, 2016, LA, United States. 2016

14. **Li-Ting Yen**, Yao-Tung Lin; Innovative visible-light-responsive TiO_2 polymethyl methacrylate composite for photocatalytic oxidation of indoor air pollutants, National Symposium on Advanced Chemistry and Integration of Knowledge-Action, May 20, 2016, Taichung, Taiwan. 2016

15. **Li-Ting Yen**, Yao-Tung Lin; Modified Antibacterial Surface of Polymethyl Methacrylate using Photodisinfection Technology, Annual Conference of Chinese Institute of Environmental Engineering, Nov. 13-14, 2015, Taoyuan, Taiwan. 2015

RESEARCH GRANTS

Graduate Research and Creative Opportunities (GRCO)	2023

- Fe and P Phytoavailability from Novel Nano-Sized, Chitosan-Coated, Meta-Vivianite Particles and Uptake in Winter Wheat Funded by Utah State University

National Science and Technology Council (NSTC) grant, researcher	2019-2022

- Study on the Application of Environmental-friendly Mulch Made from Modified Agricultural and Fishery Waste and Impacts on Soil Environment
  Grant # MOST-108-2221-E-005-048-MY3 (TW)

National Science and Technology Council (NSTC) grant, principal researcher	2017-2021

- Development of the Key Technology and Process for Antibacterial Agent using Agricultural Waste
  Grant #: MOST-109-2218-E-005-006; MOST-108-2218-E-005-004; MOST-107-2218-E-005-007; 106-3114-E-005-003 (TW)

National Science and Technology Council (NSTC) grant, researcher	2016-2019

- The Ultrastructural Alteration and Bio-physical Characteristics of Microbial Cell during Visible-light-responsive Photocatalytic Inactivation
  Grant #: MOST-105-2221-E-005-005-MY3 (TW)